Interferometry for Precision Measurement

Tutorial Texts Series

- *Ocean Sensing and Monitoring: Optics and Other Methods*, Weilin Hou, Vol. TT98
- *Laser Beam Quality Metrics*, T. Sean Ross, Vol. TT96
- *Military Displays: Technology and Applications*, Daniel D. Desjardins, Vol. TT95
- *Interferometry for Precision Measurement*, Peter Langenbeck, Vol. TT94
- *Aberration Theory Made Simple, Second Edition*, Virendra N. Mahajan, Vol. TT93
- *Modeling the Imaging Chain of Digital Cameras*, Robert D. Fiete, Vol. TT92
- *Bioluminescence and Fluorescence for* In Vivo *Imaging*, Lubov Brovko, Vol. TT91
- *Polarization of Light with Applications in Optical Fibers*, Arun Kumar, Ajoy Ghatak, Vol. TT90
- *Digital Fourier Optics: A MATLAB Tutorial*, David G. Voeltz, Vol. TT89
- *Optical Design of Microscopes*, George Seward, Vol. TT88
- *Analysis and Evaluation of Sampled Imaging Systems*, Richard H. Vollmerhausen, Donald A. Reago, Ronald Driggers, Vol. TT87
- *Nanotechnology: A Crash Course*, Raúl J. Martin-Palma and Akhlesh Lakhtakia, Vol. TT86
- *Direct Detection LADAR Systems*, Richard Richmond, Stephen Cain, Vol. TT85
- *Optical Design: Applying the Fundamentals*, Max J. Riedl, Vol. TT84
- *Infrared Optics and Zoom Lenses, Second Edition*, Allen Mann, Vol. TT83
- *Optical Engineering Fundamentals, Second Edition*, Bruce H. Walker, Vol. TT82
- *Fundamentals of Polarimetric Remote Sensing*, John Schott, Vol. TT81
- *The Design of Plastic Optical Systems*, Michael P. Schaub, Vol. TT80
- *Fundamentals of Photonics*, Chandra Roychoudhuri, Vol. TT79
- *Radiation Thermometry: Fundamentals and Applications in the Petrochemical Industry*, Peter Saunders, Vol. TT78
- *Matrix Methods for Optical Layout*, Gerhard Kloos, Vol. TT77
- *Fundamentals of Infrared Detector Materials*, Michael A. Kinch, Vol. TT76
- *Practical Applications of Infrared Thermal Sensing and Imaging Equipment, Third Edition*, Herbert Kaplan, Vol. TT75
- *Bioluminescence for Food and Environmental Microbiological Safety*, Lubov Brovko, Vol. TT74
- *Introduction to Image Stabilization*, Scott W. Teare, Sergio R. Restaino, Vol. TT73
- *Logic-based Nonlinear Image Processing*, Stephen Marshall, Vol. TT72
- *The Physics and Engineering of Solid State Lasers*, Yehoshua Kalisky, Vol. TT71
- *Thermal Infrared Characterization of Ground Targets and Backgrounds, Second Edition*, Pieter A. Jacobs, Vol. TT70
- *Introduction to Confocal Fluorescence Microscopy*, Michiel Müller, Vol. TT69
- *Artificial Neural Networks: An Introduction*, Kevin L. Priddy and Paul E. Keller, Vol. TT68
- *Basics of Code Division Multiple Access (CDMA),* Raghuveer Rao and Sohail Dianat, Vol. TT67
- *Optical Imaging in Projection Microlithography*, Alfred Kwok-Kit Wong, Vol. TT66
- *Metrics for High-Quality Specular Surfaces*, Lionel R. Baker, Vol. TT65
- *Field Mathematics for Electromagnetics, Photonics, and Materials Science*, Bernard Maxum, Vol. TT64
- *High-Fidelity Medical Imaging Displays*, Aldo Badano, Michael J. Flynn, and Jerzy Kanicki, Vol. TT63
- *Diffractive Optics–Design, Fabrication, and Test*, Donald C. O'Shea, Thomas J. Suleski, Alan D. Kathman, and Dennis W. Prather, Vol. TT62
- *Fourier-Transform Spectroscopy Instrumentation Engineering*, Vidi Saptari, Vol. TT61
- *The Power- and Energy-Handling Capability of Optical Materials, Components, and Systems*, Roger M. Wood, Vol. TT60
- *Hands-on Morphological Image Processing*, Edward R. Dougherty, Roberto A. Lotufo, Vol. TT59
- *Integrated Optomechanical Analysis*, Keith B. Doyle, Victor L. Genberg, Gregory J. Michels, Vol. TT58
- *Thin-Film Design: Modulated Thickness and Other Stopband Design Methods*, Bruce Perilloux, Vol. TT57
- *Optische Grundlagen für Infrarotsysteme*, Max J. Riedl, Vol. TT56
- *An Engineering Introduction to Biotechnology*, J. Patrick Fitch, Vol. TT55

(For a complete list of Tutorial Texts, see http://spie.org/tt.)

Interferometry for Precision Measurement

Peter Langenbeck

Tutorial Texts in Optical Engineering
Volume TT94

SPIE PRESS
Bellingham, Washington USA

Library of Congress Cataloging-in-Publication Data

Langenbeck, Peter, author.
Interferometry for precision measurement / Peter Langenbeck.
pages cm – (Tutorial texts in optical engineering ; volume TT 94)
Includes bibliographical references.
ISBN 978-0-8194-9140-4 (print) – ISBN 978-0-8194-9141-1 (ebook) (print) –
ISBN 978-0-8194-9142-8 (epub) 1. Interferometry. 2. Optical measurements.
3. Optical instruments–Testing. 4. Engineering instruments. I. Title. II. Series:
Tutorial texts in optical engineering ; v. TT 94.
QC411.L24 2014
535'.470287–dc23

2013031940

Published by

SPIE
P.O. Box 10
Bellingham, Washington 98227-0010 USA
Phone: +1.360.676.3290
Fax: +1.360.647.1445
Email: books@spie.org
Web: www.spie.org

Printed in the United States of America.
First printing

SPIE.

Introduction to the Series

Since its inception in 1989, the Tutorial Texts (TT) series has grown to cover many diverse fields of science and engineering. The initial idea for the series was to make material presented in SPIE short courses available to those who could not attend and to provide a reference text for those who could. Thus, many of the texts in this series are generated by augmenting course notes with descriptive text that further illuminates the subject. In this way, the TT becomes an excellent stand-alone reference that finds a much wider audience than only short course attendees.

Tutorial Texts have grown in popularity and in the scope of material covered since 1989. They no longer necessarily stem from short courses; rather, they are often generated independently by experts in the field. They are popular because they provide a ready reference to those wishing to learn about emerging technologies or the latest information within their field. The topics within the series have grown from the initial areas of geometrical optics, optical detectors, and image processing to include the emerging fields of nanotechnology, biomedical optics, fiber optics, and laser technologies. Authors contributing to the TT series are instructed to provide introductory material so that those new to the field may use the book as a starting point to get a basic grasp of the material. It is hoped that some readers may develop sufficient interest to take a short course by the author or pursue further research in more advanced books to delve deeper into the subject.

The books in this series are distinguished from other technical monographs and textbooks in the way in which the material is presented. In keeping with the tutorial nature of the series, there is an emphasis on the use of graphical and illustrative material to better elucidate basic and advanced concepts. There is also heavy use of tabular reference data and numerous examples to further explain the concepts presented. The publishing time for the books is kept to a minimum so that the books will be as timely and up-to-date as possible. Furthermore, these introductory books are competitively priced compared to more traditional books on the same subject.

When a proposal for a text is received, each proposal is evaluated to determine the relevance of the proposed topic. This initial reviewing process has been very helpful to authors in identifying, early in the writing process, the need for additional material or other changes in approach that would serve to strengthen the text. Once a manuscript is completed, it is peer reviewed to ensure that chapters communicate accurately the essential ingredients of the science and technologies under discussion.

It is my goal to maintain the style and quality of books in the series and to further expand the topic areas to include new emerging fields as they become of interest to our reading audience.

James A. Harrington
Rutgers University

Contents

Preface

With new material added to the English translation of Chapter 7 of the German *Wirtschaftliche Mikrobearbeitung* (Carl Hanser Verlag, 2009), the author presents developments in physical, optical, and mechanical engineering over the past 60 years. The enduring impetus for this work is owed to the late, great gentleman engineer, Gordon J. Watt, with his assertion that optical wavefronts used in interferometers are complementary to the surfaces used to build air bearings. A foremost example of this statement is the fact that a plano-convex lens is confined by surfaces that are equivalent to those defining the Watt air-bearing spindle. The spindle rotor consists of a truncated hemisphere, rigidly connected to a flat disk.

Soon after the author founded Intop Entwicklungen (Baden-Württemberg, Germany) in 1972, he and G. J. Watt witnessed a sudden growth in spindle-enabling applications and new machines whose performance relied completely on low-axial-error motion (less than 5 nm) and an angular error motion of less than 0.1 arcsec. The bearing's disk took on multiple integral functions: as a polygon wheel, as a polishing scaife for diamond tools, and as a chuck for thin substrates (memory substrates with memory scaling of 14.5). Interferometers for in-process quality control and final acceptance needed to be developed.

Increased interferometric sensitivity by multiple passes was adopted as a technique for measuring small departures from 90 deg, both for the metrology of corner cubes and for extremely sensitive tilt measurement (one of the three CCR mirrors being the front mirror on a problem spindle's nose). Interferometric techniques that facilitated the assembly of ultraprecision machining and metrology machines (3D orthogonal) were developed.

Likewise, decreasing interferometric sensitivity made possible the inspection of nonspecular surfaces. The cost for quality control of mass-produced components (for example, water faucet ceramic seals) was substantially reduced. The inspection technique in use at the time became the standard for expedient handling of samples with interferometric precision.

This relatively recent development focused on measuring tilt error motions of air-bearing spindles, as is amply covered in this book. Tasks that

occur every day in an optical shop—such as centering and homogeneity measurement—are also extensively discussed.

The author gladly shares his recollections and experience with students, scholars, and peers but also wants to give a warning: dealing with optics every day may turn a profession into an obsession!

The author appreciates SPIE for making this publication possible. He also expresses his warm thanks to Prof. Hans Tiziani for frequent, critical discussions.

Peter Langenbeck
May 2014

Chapter 1
Known Methods: An Assessment of the State of the Art—Newton and Fizeau

1.1 Introduction

The subject of this assessment is surfaces whose final production processes include lapping, polishing, or micromachining. The majority of these processes relate to optical components, and many of them carry optical specifications for mechanical applications such as air-bearing techniques. Measuring departures from flatness is a common denominator. A useful compendium of interferometric techniques and applications was assembled by D. Malacara, A. Cornejo, and A. V. R. K. Murty.[1]

One of the procedures involved in the practice of an optician is illustrated in Fig. 1.1: an optical glass, the reference, is placed onto the semifinished work. The reference is illuminated by a spectral lamp λ behind an extended diffusing screen and is observed. The observer sees a fringe pattern, the interpretation of which is explained in Fig. 1.2. Actual fringe patterns are shown in Figs. 1.5(a) and (b), and Fig. 2.1(b). Such patterns appear to be similar to cartographic contour lines. This assessment procedure, which creates what is known as Newton's rings, is as simple to handle as it is to comprehend; it is the last option using low-cost instrumentation for mechanical/optical metrology with sub-micrometric resolution before expensive hardware and software need to be introduced. In that sense, the importance of interferometry to the precision engineer can be compared to that of a stethoscope to the general medical practitioner. This is our starting point for the assessment of the fascinating methods and instruments of interferometry.

The distance t between the reference and the workpiece in Fig. 1.1 is governed by three factors:

1. the small amount of dust that appears virtually everywhere, even in clean boxes and in compressed air for air bearings,

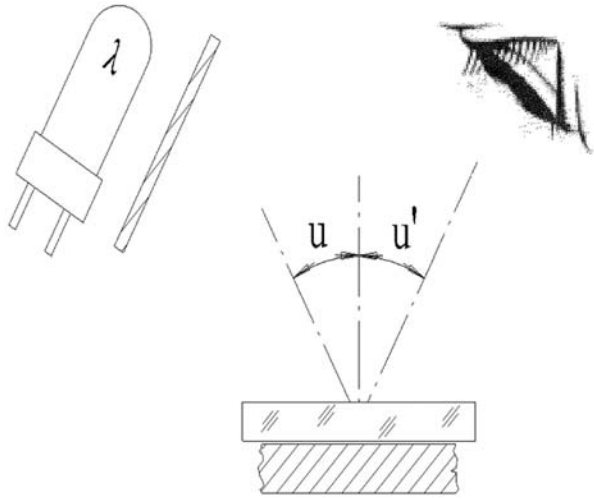

Figure 1.1 Assessment of the departure from flatness using Newton's interference method. The screen in front of the spectral lamp serves as an extended light source. The flat reference and the sample rest on each other. u' is the angle of observation (excidence between the sample's normal and the intuitively chosen line of sight), and u is the angle of incidence, where $u' = u$.

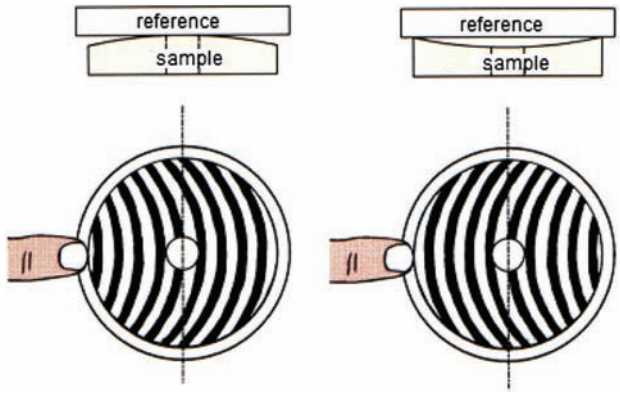

Figure 1.2 Common evaluation instructions for the interference flatness test. Here, manually symmetrizing pressure leads to closed annular fringes, known as Newton's rings, which can be either convex or concave. There would be two rings in the case sketched here. Rings are stable in the case of a concave sample and rather unstable in the case of a convex sample with a high spot in center.

2. three randomly occurring high spots on either one or both bulk surfaces, and
3. dust on the high spots of the surfaces. Most dust particles are compressible, and some are abrasive. The schematic representation of dust particles in Fig. 1.3 shows the typical dust that determines that distance t is in the same range as gaps in air-bearing techniques.

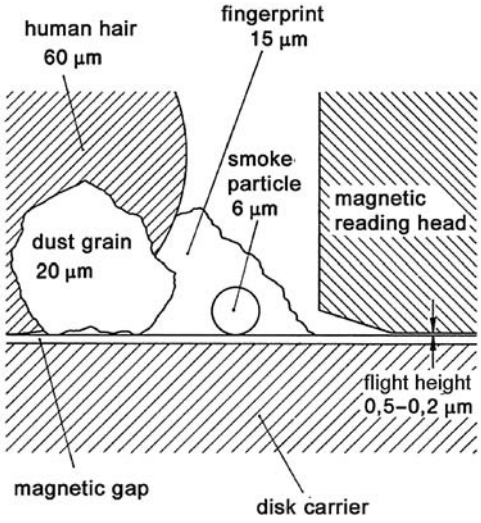

Figure 1.3 Omnipresent dust separating the testplate from the workpiece is thick enough to prevent contacting (wringing) and thin enough to allow scratching. This frequently cited illustration of unknown origin is entitled "Contamination of optical surfaces."[2]

Notes for the practitioner

1. An effective and inexpensive cleaning of the testplate/workpiece combination starts with a fine silk paper or an often-washed cotton cloth mildly pressed between the two and gently pulled out tangentially. However, this cleaning method can cause wringing.
2. Changing the pressure point from left to right in Fig 1.2 allows one to see two closed fringes, indicating a spherical surface with a very large radius of curvature. Figure 1.4 demonstrates the relationship between the spherical radius r of the cap, represented by fringe diameter d, sag h, and the wavelength.

In the production of optical lenses with very short radii of curvature, it is common to use spherical reference glasses, with the same squeezing treatment. The diameters, the interference rings, and the known wavelength determine the difference of radii of the cap.

Two closely tangential glass plates illuminated by sodium spectral light generate fringes like those in Fig. 1.5(a). Under a mild load, the direction and spacing P of the fringes can be varied prior to hard contact, the latter prevented by omnipresent dust. Thanks to the dust, for a convenient empirical interpretation, it is a common practice to squeeze the plates and thereby shift the fringes to delineate a defect. For visual inspection, the fringes are aligned either orthogonally or in parallel to the line of sight; five to seven fringes per diameter is a practical configuration.

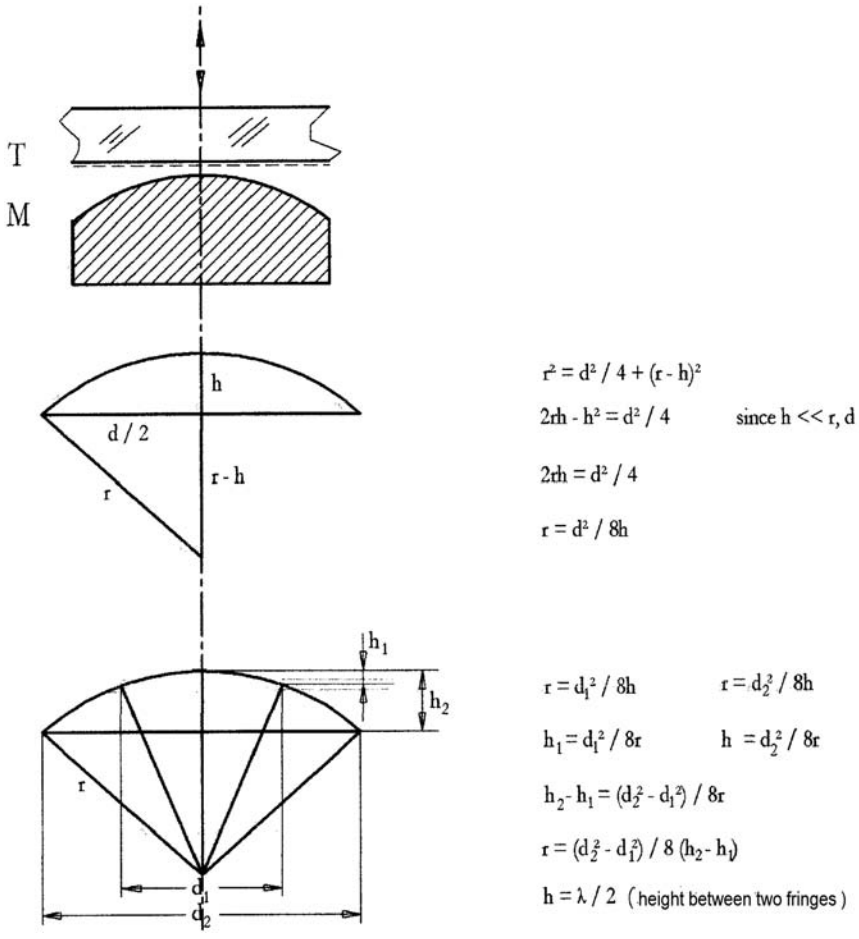

Figure 1.4 Annular closed fringes permit simple spherometry. T is the reference flat, and M is the part of the sample with a spherical surface (in many cases).

At this point either wringing occurs, or, as fringes are forcefully aligned, both surfaces become scratched. This is also the case with spherical reference glasses used in optical production of lenses. Wearing white gloves does not change the situation. These scratches are subject to rejection of optical components and are defined by scratch and dig specifications.[3]

Scratch quality assessment has become a somewhat controversial subject between users and suppliers. This book contains two sets of specifications for technical quantity products that include scratch and dig, corner-cube retroreflectors (CCRs) (Chapter 5), and polygon mirror wheels (Chapter 6). An informative account of detecting, avoiding, and accepting scratches is given by J. A. Slater and D. A. Cox in their paper "Scratches: At what price quality?"[4]

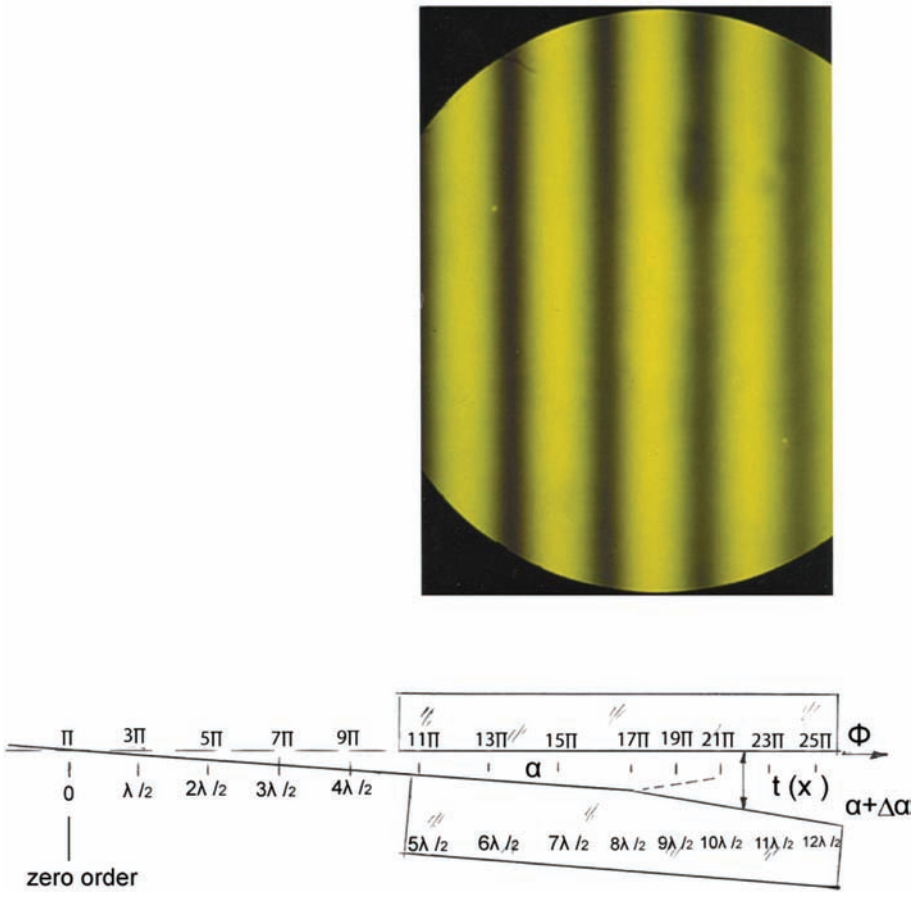

Figure 1.5(a) λ/2 interference fringes in yellow sodium light between two bare glass plate surfaces separated by omnipresent dust. The areas of almost complete surface contact appear darker and less dark with increasing gap *t*.

Measurement of fringe spacing P_1 (on an object-to-image scale of 1:1 and in the same dimension as λ) provides the included angle $\alpha_1 = (\lambda/2)/P_1$, with λ = the wavelength of light used. Above the minute wedge $\Delta\alpha$ on the workpiece, one sees fringes of a different spacing P_2 [as shown in Fig. 1.5(a)]: $(\alpha + \Delta\alpha) = (\lambda/2)/P_2$. The wedge angle ε on the surface is

$$\varepsilon = \frac{\lambda}{2}\left(\frac{1}{P_1} - \frac{1}{P_2}\right) = \alpha_1\left(\frac{\Delta P}{P_2}\right). \tag{1.1}$$

Narrowing the distance between the reference and the workpiece [Fig. 1.5(a)] by some load without changing α causes the fringes to "walk" parallel to themselves until the two surfaces come into contact, usually at the periphery. The contact zone is characterized by complete darkness and is the hinge or

apex of the angle wedge α between the plates. This is also the location of the optical zero, the zeroth order of interference. By narrowing the gap, fringes walk into the direction "away" from the zeroth order. The reason for the darkness sloping through a relative maximum in the zone of no gap, irrespective of contact pressure, is the $\lambda/2$ phase jump upon reflection at the glass/air interface. In transmission, contrast is reversed.

Much research has been reported on the gap thickness obtained by joining slip metallic or ceramic gauges by wringing, a customary practice in comparator metrology.[6] In this field, residual gaps are reported to range between 0.01 and 0.001 μm. This gap size appears to be sufficient to cause the phase jump on the inner glass surface (the dark center in Newton's rings).

The location of the zeroth-order fringe might be on the workpiece or, more commonly, far outside the workpiece for an unknown number n of orders. All that one knows is that n increases or decreases in integer numbers. The change Δt in distance between the test surface and the reference surface from one fringe to the next is given by

$$t_n - t_{n-1} = \frac{\lambda}{2}. \tag{1.2}$$

A mercury vapor lamp with distinct and dominant red, green, and blue spectral lines produces fringes equivalent to the monochromatic sodium

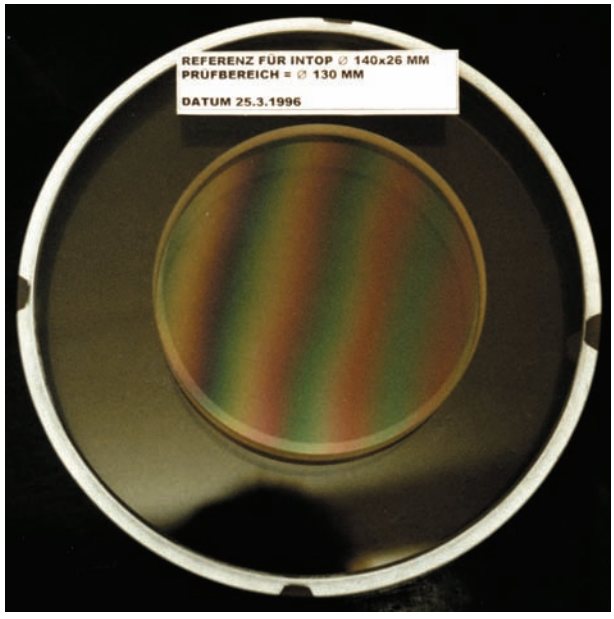

Figure 1.5(b) An acceptance protocol of a 140-mm-diameter Fizeau plate made of Zerodur with fringes as shown in Fig. 1.5(a) but illuminated by a tungsten point-discharge lamp (from Bulbtronics[5]). Included between the surfaces is some residual dust. Without any dust, the plates would be wrung to each other. Note that the darkest fringe is not identified on the sample.

fringes shown in Fig. 1.5(a), but multicolored, as shown in Figs. 1.5(b) and 1.7(a). Note that these are natural colors and not artificial coding colors. The darkest fringe appearing in the middle of the sample in Fig. 1.7(a) automatically calibrates the distance variation between the entire sample surface and the reference, both being monotonic. In terms of *any* optical wavelength, this calibration, which is chosen from spectral lamps, is called *absolute* because the wavelengths of these spectral lines are among the most accurate (and low-cost!) length standards in physics.

One tacitly assumes no departures from flatness on the reference. An often-overlooked fact is that the calibration applies to the total of the distance changes between the *two* surfaces, not of only one surface. In order to prove flatness beyond the commercially available quality of "flats," considerable effort was undertaken to verify flatness *absolutely* by successively comparing two or three flats. The interested reader will find a method developed by R. Schulz[7] and B. S. Fritz.[8] Note that taking a computer recording of an interferogram from a reference known to be "perfect" and subtracting the same from a sample interferogram is a step in the right direction but does not replace absolute measurement.

Figure 1.6 illustrates a quantitative interpretation of fringes seen between a flat reference glass and a flat sample with a rectangular relief profile (with a groove of depth Δt). The bottom of the groove is parallel to the ground, and distance t is unknown. In Fig. 1.6(b), the fringes are made to extend parallel to the groove and have the same spacing and direction above the sample surface and above the base of the groove, both partial surfaces being parallel. All that one can derive from such stationary fringe patterns is the angle between the plates, the flatness of the ground and groove, and the parallelism between the ground and groove. With the order-of-interference number on the ground before the groove unknown [$t_{ground} = n_1\ (\lambda/2)$], and for the first fringe in the groove [$t_{groove} = n_2\ (\lambda/2)$], which is likewise unknown, the difference $(n_2 - n_1) = \Delta n$ also remains unknown.

Changing the plates' wedge orientation from that shown in Fig. 1.6(a) to that shown in Fig. 1.6(b) causes the fringes to extend orthogonally to the groove, allowing them to be tracked; within one order, it becomes possible to determine $\Delta t = (\lambda/2)\ (\Delta P/P)$; at greater values of n,

$$\Delta t = \frac{\lambda}{2}\left(n + \frac{\Delta P}{P}\right). \tag{1.3}$$

Experimental use of the groove test for defining the direction of the zeroth-order location is illustrated in Fig. 3.4(c). The groove test using Eq. (1.3) in the schematic shown in Fig. 1.6 is useful for determining the thickness of thin vacuum-deposited layers. Detection of the uniformity of coating thickness within a few nanometers is an important application of interferometry.

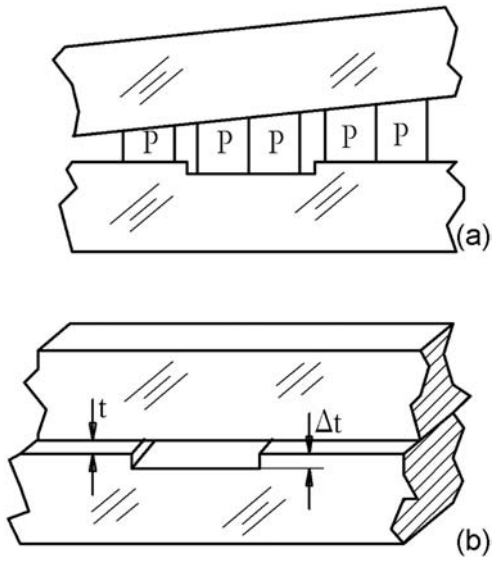

Figure 1.6 Fringe alignment of spacing and orientation to suit evaluation: (a) The apex of the wedge is parallel to the groove, with regular spacing P. At the entry and exit to the groove, P_1 changes to P_2 [$\Delta t = (\lambda/2)(n \pm (\Delta P/P)$], with factor n remaining unknown. (b) The apex of the wedge crossing the groove. The order-of-interference number n now becomes measurable [see Fig. 1.8(a)]. Identical reflectivity of groove bottoms and of the flat is assumed.

A note for the practitioner

The groove edge test, as shown in Fig. 1.6(b), is an indispensable tool in thin-layer technology (vacuum coatings) and lends itself to multipass interferometry. The direction of walkoff being parallel to the groove (see Chapter 10) results in approximately five times enhanced sensitivity (λ/10 fringes). Calibration masters are produced by diamond machining of a flat with a defined groove depth (see Section 1.6.2).

1.2 Limited Use of Newton's Method

At this point we can recognize the limitations of simple testplating, or Newton's method. Some of these limitations are listed here:

- It is a method, not an instrument.
- The distance between the sample and the reference is so small that alignment of fringes in any direction to suit evaluation is almost impossible [changing alignment between cases (a) and (b) in Fig. 1.6 might not be possible without undue force].
- Rapid sequential testing is not possible.

- As shims are inserted, interference patterns are lost; fringes are retained only when the shims are very thin, as in. e.g., cigarette paper or three thin spots of diluted Zapon lacquer.
- A wide variety of samples are either too large for the reference or too small for visual assessment; or they have "optical" surfaces on complex mechanical parts, or are too deformable (as are wafers). These samples need external auxiliary alignment.
- The advantageous feature of identifiable white-light interference allows one to follow a sample's topography, even if the surface is interrupted by long, empty intervals. However, white-light interferometry only works with narrow gaps; it eliminates the option of simple testplating and requires special instrumentation.

1.3 Other Methods of Interferometry

Classical interferometers provide solutions to dividing one (usually collimated) light bundle into two bundles of equal diameter, each having, for instance, 45% of the original luminance. The bundle that is returned unaltered into the instrument serves as the reference to the other bundle, which is returned in the same fashion after reflection at the sample. Recombination of the two bundles generates the interferogram, which is recorded on film or electronic camera at the location of the sample's image. The reader can find ample literature on interferometers in Ref. 7. For ordinary flat work, the interferometer results are equivalent to the testplated interferogram. However, instrumental solutions are much more costly than simple testplates, which might be selected cuts from low-cost float glass.[5]

Most interferometers are named after their inventors, well-known physicists such as Michelson or Fizeau. An experimental combination of a Fizeau (multiple-beam) and a Michelson (two-beam) interferometer was assembled in order to accompany the graphical vector display of interference, contrast, finesse, and contrast reversal, as shown in Fig. 3.24(a), with Fig. 3.24(b) being the corresponding representative interferogram.

A classic "old timer" of precision engineering and metrology interferometers is the Köster interferometer, whose basic configuration is based on the beam-dividing Köster prism, shown in Fig. 10.4(a). The classic application is in length metrology, which requires equalization of the length of the two bundles reflected at a sample and at a movable reference mirror. White-light interference with its dark center is observed [see Fig. 1.7(a)], indicating coplanarity between the longitudinally mobile reference and the top surface of the sample, for instance, a slip gauge resting on a slightly wider auxiliary mirror. That auxiliary mirror's coplanarity with the moveable reference mirror indicates the end of travel and represents the thickness of the slip gauge. Surface errors such as turned-down edges and wedge angles are seen in

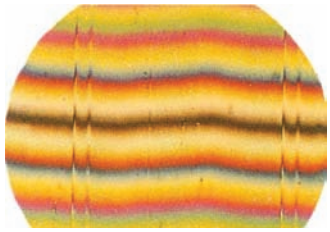

Figure 1.7(a) Interferogram from a dual-beam (Michelson) interferometer with white-light interference between two flat wavefronts that are slightly inclined toward each other. The apex is now in the center of the FOV and identified by a dark fringe (the zeroth-order interference). Such an interferogram can be recorded with an instrument similar to the one shown in the schematic in Fig. 1.9 or with equivalent optical hardware imbedded into a granite block (see Fig. 1.8).

the same interferogram as well. The length of travel between the two coplanarity positions is measured by counting the fringes obtained when using a long-coherence-length laser as a light source in addition to white light (compare with Fig. 1.17).

Another feature of the Köster prism is its angular null sensing around an axis parallel to the apex of the Köster prism (meaning no pyramidal error). For this to occur, only one mirror simultaneously returns both interferometer bundles; its nutation provides an opportunity to align the interferogram in Fig. 1.7(a) to show the dark white-light interference in the complete (50-mm diameter) field of view (FOV). This type of interference autocollimation defines an angular null to about 0.02 arcsec, a feature that will be discussed further in Chapter 3 [Fig. 3.7(d)] and Section 5.2.

Any instrumental interferometer allows for axial displacement of either the sample or the reference mirror in order to obtain the desired fringe alignment; this allowance is not offered by testplating. In Section 1.6.2 we look at different light sources that allow the resolution to be pushed to a range of 0.001 mm (white light) to 10,000 mm (laser) before losing interference contrast. In addition, the reference path can be conveniently inclined much farther than in testplating to align fringes to suit their interpretation.

Coincidence of two slightly tilted coherent white-light flat wavefronts is shown in Fig. 1.7(a). The apex with respect to the zeroth-order axis leads through the center of the image and can be turned around at will by alignment of either the reference or the sample mirror.

Note that in the classical Newton contact testplate setup, one of the two reflected wavefronts can be inclined as well, but only around an apex that is on the sample edge or is far outside the edge, and at the expense of inopportune squeezing.

Some technical workpieces have more than three, neither adjacent nor cohesive, partial surfaces that are specified to be coplanar. The interferometer's reference marks indicate the zones that are closest to the specified coplanarity.

A typical example is shown in Fig. 1.7(b). Coplanarity and departures thereof can be determined interferometrically but only with an ear-marked short-coherence-length light source (Section 1.3). It is not possible to follow the order number of interference with laser illumination [Fig. 1.7(c)]; however, white-light interference permits one to follow the ear-marked fringes (observing continuity of colored and zeroth-order fringes), ascertaining at least *some* coplanarity. The word *some* refers to another surprise: a minute axial displacement of the reference mirror makes the fringes walk. The walk in this example is away from the corner or from an edge that is tangent to the momentary best-fit spots.

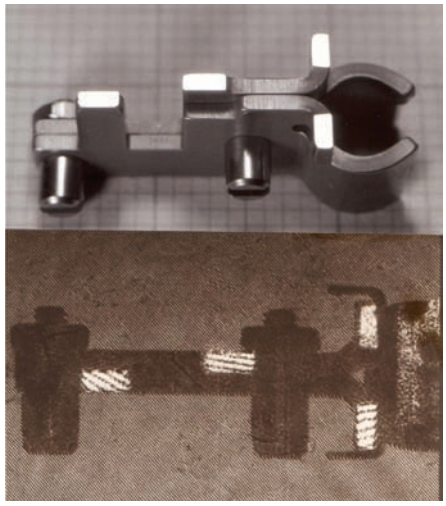

Figure 1.7(b) A 15-mm-long sample (part of the electrical relay) with four feet that have been precision lapped to be coplanar within 0.1 μm. It is not possible to measure height differences on this sample with laser illumination; only out-of-parallel samples can be measured.

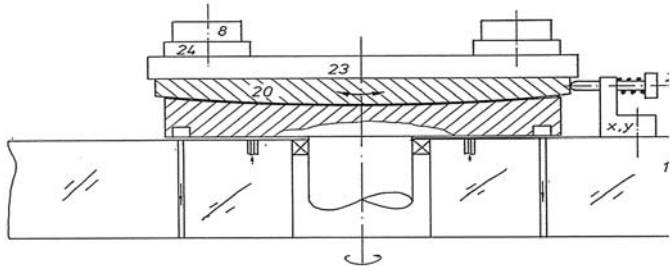

Figure 1.7(c) A typical white-light application: an interferometric test stand for slip gauge comparison. After charging the samples (by wringing) onto the air-bearing-supported reference base and after temperature balancing, all slip gauges should present the zeroth-order straight fringe interferogram [Fig. 1.7(a)]. Note the air-bearing table for positioning the multiple samples under the interferometer without need for realignment.

The specified coplanarity will certainly be fulfilled with fringes walking simultaneously in the same direction at the same speed (longitudinal scanning). Another typical white-light application is the slip gauge comparator mentioned above.

The monoblock instrument shown in Fig. 1.8 was specifically designed for combining two features: (1) employment of short-coherence-length light and

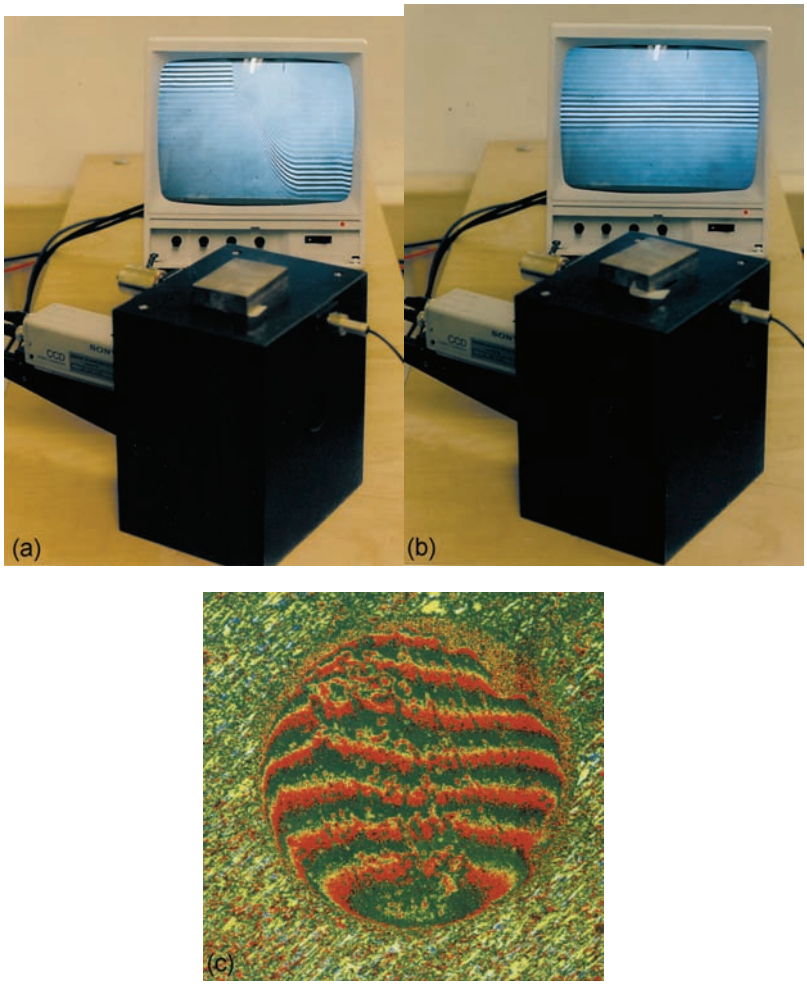

Figure 1.8 Micro-interferometer imbedded into a monolithic granite stone. The internal optical axis is orthogonal to the top surface, allowing scanning using air-bearing devices without losing focus. The sample shown is a micromachined brass plate for measuring surface quality as a function of depth of cut. The monitor exhibits a 0.3-mm FOV on the sample. Illumination is through a fiber cable connected to a short-coherence-length, white-light source or to a laser diode. (a) A diamond fly-cut sample that can be slid across until arriving at (b) without realigning (lateral scanning). (c) Interferogram showing the depth of a cut on a defective ceramic fiber optic connector. The center of the connector should be convex, not concave, for 0.2 μm, as seen here.

(2) generating lateral and/or rotary motion of a variety of air-bearing components, whose longitudinal error motion (orthogonal to the granite base) would be less than detectable by the interferometer integrated onto the granite. Lateral scanning of samples wider than the FOV of the micro-optics thus becomes possible. A channel underneath the air-bearing-quality flat stone contains a small reference flat [labelled L in Fig. 1.9(a)]. The same channel on the opposing end contains the small collimator.

The granite top surface serves as a base for simple X–Y sliding of a sample or, for an air-bearing slide of the type shown in Fig. 1.11(a), carrying samples facing downward and, thus, being moved strictly in a direction orthogonal to the optical axis. This alignment serves to guide the installation direction of the microscope's optical axis to be orthogonal to the instrument's axis; fringes of the air-bearing base show no lateral motion once orthogonality is found and fixed.

Centration measurement has become an important application of this micro-interferometer: the flat top of the granite block serves as a reference base for cylindrical disks rotating on a 2- to 3-μm air film. The cylindrical disk, airborne both on its axial surface facing the granite and at its periphery, can be centered to coincide with the optical axis by an iterative process of shifting both the removable sample holder on the spindle and the spindle itself. The latter is clamped in position by axial preload. Centration is indicated by an artifact, like the hole for the fiber in a ceramic pin. The hole's central position within the connector needs to be certified. The axis of rotation, being parallel to the optical axis, can be shifted to see the connector's periphery rotating through the image, thus enabling a measurement of mechanical centricity and determining the eccentricity of the fiber. Simultaneously, the micro-interferogram of the

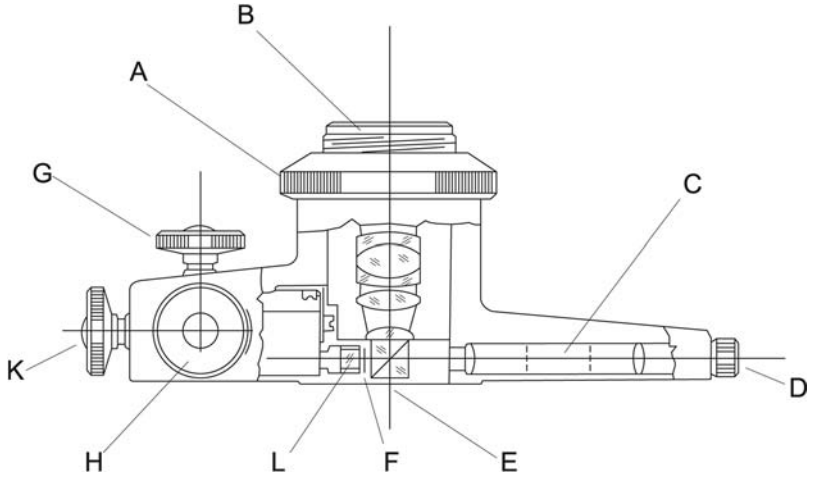

Figure 1.9(a) Design of a Michelson two-beam interferometer with a microscope attachment (adapted from Ref. 7).

well-polished cap of the ceramic pin must confirm the surface form, which is specified as two symmetric, convex fringes.

Optical components integrated into the rugged granite block use the same design as the very practical Watson two-beam Michelson interferometer serving as a microscope attachment [Fig. 1.9(a)].

A note for the practitioner

The task of interferometrically centering a small optical workpiece on an air-bearing spindle and fixing the same for subsequent center grinding of its periphery without changing the chuck/holder is made convenient using the rugged micro-interferometer shown in Fig. 1.9(a). This compact unit can be repeatedly removed and mounted to the air-bearing stator.

In Fig. 1.9(a), B is the RMS (Royal Microscopical Society) thread that connects the unit to a microscope with the knurled securing ring. A monochromatic light source (sodium or mercury lamp) is placed as close as is convenient to the illumination entry (D), which is a removable filter. E is the collimation system, which is a beamsplitter cube; F is a removable shutter; L is the reference mirror; K is the longitudinal alignment adjuster for the reference mirror; and G and H are the two adjusters for angular alignment of the reference mirror. The knurled ring (A) fixes the thread (B) to the microscope. C is the collimating optic, and F is the location for the filter.

Both the Watson dual-beam interferometer and the Integrated Topside (Intop, from the author's lab) monoblock micro-interferometer use collimated light reflected by a sample to measure the sample roughness profile. The vertical range of these two devices is limited to about 20 μm within the FOV. Flanks with a pitch equal to the axial wavefront departure from flatness in relation to lateral distance change can be measured with 0.015 μm/μm with 4× for the monoblock, and 0.04 μm/μm with 10× for the Watson, where the units μm/μm indicate the steepness of the flank of a deep groove divided by the width of the same. A thorough analysis of beam walkoff on steep flanks inspected by micro-interferometers is provided by H. Mykura.[9]

In order to make this measurement with white light, one must mechanically equalize the optical path lengths from the beamsplitter to the reference and, likewise, to the sample within one representative wavelength (e.g., green). The criterion for this balance is the dark zeroth-order interference fringe that passes extremely fast through the FOV upon alignment.

This and other microscopes (such as various Linnik microscopes) are typical. Figure E7 in Ref. 10 shows the use of fine threads for the control of mirror movement. (Note that the nanoscrew (Ref. 10, Fig. 1.9) is a useful device for such supersensitive alignment.)

A forewarning of the fast-approaching dark fringe is obtained by mixing white light with long-coherence-length light of an additional light source (laser). A description of this light mixing is found in Figs. 10.1(a) and (b). The process of aligning the length of an interferometer arm is made convenient when observing

the volatile light-mixing pattern in the FOV. Light mixing became useful and convenient with the Kollmorgen autocollimator (Section 5.2).

1.3.1 Tolansky: one experimenter's indispensable knowledge

Published in 1948, S. Tolansky's book on multiple-beam interferometry[11] teaches a wealth of optical testing essentials as it pursues crystallographic surface analysis. Tolansky cultivated the Fizeau multiple-beam reflection technique using split-mica membranes with semitransparent coatings (many of chemical silver). In this light, today's mundane interference microscopes appear as exuberantly expensive embellishments of the basic technique of thin (mica) membranes. These split-mica membranes of thicknesses under 0.1 mm and with a beamsplitter coating show crystalline flatness across areas wider than needed to cover the FOV of common metal microscopes; they were simply placed on the target and tweaked with a needle in order for the Fizeau fringes to suit evaluation.

Today, microscope substrate cover glasses or sections of large 0.1-mm-thick glass panels can be selected for flatness, wedge, and homogeneity before being coated with dielectric semitransparent and antireflective layers. In the author's laboratory, such plates were ordered by the dozens to serve as beamsplitters, replacing beamsplitter cubes, and for fast *in situ* inspection of micromachined metal mirrors.

In the translation of Ref. 11 (Part 6 on micromachining) are numerous examples of machine roughness inspection using the Tolansky method, cultivated for rapidly assessing the effects of changes in tool alignment. Instead of the flat reference from thin lamellar glass, we used a 10-mm^2 biprism with a 5-arcsec wedge and 50% beamsplitter coating. These were gently placed on the freshly diamond-machined surface. The biprism could then be inspected by a microscope mounted on the machine with a long-distance objective (Nikon) and with laser-diode illumination. This inspection provides instant microtopography,[12] as shown in Fig. 1.9(b).

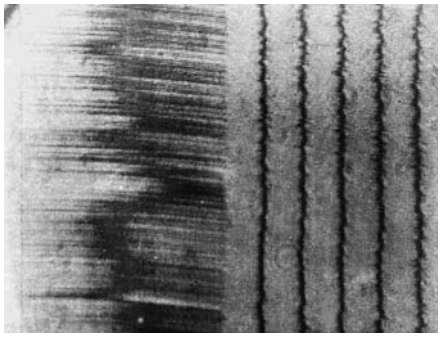

Figure 1.9(b) Tolansky-type multiple-beam interferogram using a 50% helium-neon (HeNe) laser beamsplitting coating on a 5-arcsec biprism. The long side of the printed record corresponds to 2 mm on the sample, which is an Al alloy fly cut with a badly worn diamond tool. This so-called roof-edge test provides fast, inexpensive, *in situ*, qualitative roughness measurement.[13]

1.4 Desirable Features for Safe, Applicable, and Economic Interferometry

1.4.1 Commercial coherent white light

From almost any thermal white-light source (e.g., a tungsten lamp), some small part of the emitted light can be made to behave coherently. To show this, Verdet set up the experimental parameters shown in Fig. 1.10(a), which demonstrates his coherence condition. With the notations in this figure, a lateral size a of a primary or secondary light source is required; a depends on F being the focal length of the collimating objective with its clear diameter d, and on x being the lateral distance within which coherence is desired (usually $d/2$).[14]

Verdet's criterion for coherence,

$$x\left(\frac{a}{F}\right) < \frac{\lambda}{4}, \tag{1.4}$$

allows one to estimate the useful dimension of a. If a represents the width of a fine controllable slit (a common element of instrumentation in an optical laboratory), then a 2- to 5-μm slit width or pinhole size suffices to produce quasi-coherent light from thermal white light focused on the back of the slit or pinhole. High-pressure spectral point discharge lamps (mercury) provide enough brilliance to allow a to be sufficiently small to satisfy the Verdet condition and transmit enough light for practical use.

With λ approximated as 6×10^{-4} mm and $b = 1000$ mm, we can apply a secondary light source of approximately 0.01 mm in diameter in order to obtain white-light interference across a beam, reflected by the two surfaces of an uncoated 0.5-mm-thick glass plate with no spectral filter applied. (Recall

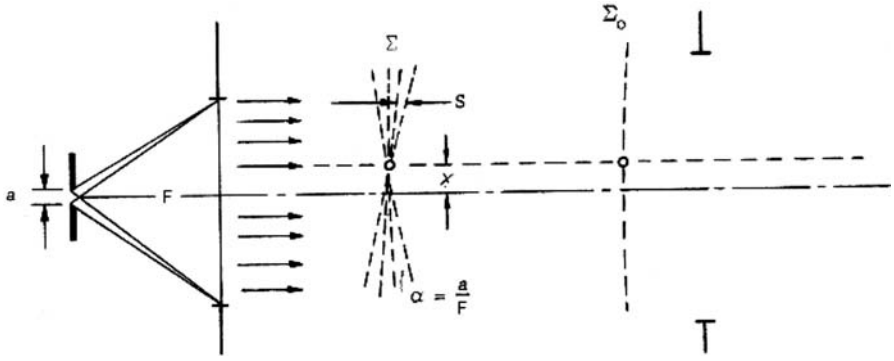

Figure 1.10(a) Diagram illustrating a collimated beam of coherent light that satisfies Verdet's criterion for coherence. Light from an extended light source—thermal white or monochromatic—is focused onto the back of an opaque stop, carrying a pinhole of diameter a [see Fig. 1.10(b)]. The fine control of focal distance (F, in this schematic figure) will be discussed in Sections 3.8 and 5.2.3.

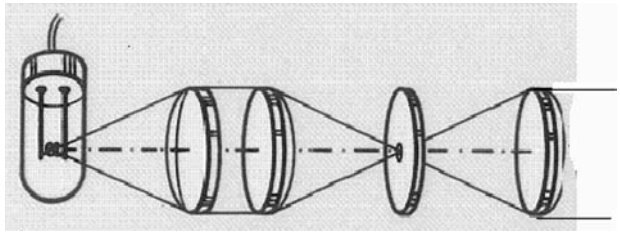

Figure 1.10(b) Transforming an extended light source into a 1D uniaxial collimated beam of interference-qualified light, or "more light through a smaller hole." The spectral lamp can be replaced by an LED device.

the beautiful colors in an oil film on the surface of a water puddle on a city street.) This secondary light source might be the end of a thin fiber optic cable, or a commercial pinhole illuminated from behind by an extended light source, as otherwise used for testplating. Figure 1.10(b) illustrates a common arrangement for focusing the light source onto the pinhole stop (secondary light source).

The following is a brief excursion for the experimenter: The transition from incoherent to coherent (or interference-qualified) thermal light source illumination will be illustrated in Section 8.1.3 and in the strioscopy setup shown in Fig. 8.4(b). The narrowing of the illumination slit allows interference to appear within in a so-called shadow image of a phase object [for instance, a flame, as in Fig. 8.4(b)]. Figure 1.10(c) illustrates the coherence behavior of this white-light illumination in relation to other types of illumination used for interferometry. Today's laser diodes can be electronically controlled between white-light short coherence length and gas-laser-like long coherence length. Long before lasers became available, this type of illumination was used in all interferometer configurations, some of which are still in use today.

1.4.2 Light sources for increased distance from reference to sample

White light does not produce interference with gaps dx between mirrors any larger than 0.002 mm. Simple experimentation allows one to find spectral-light lamps with well-established coherence lengths by inserting three small, equally sized bits of thin shim between the sample and the reference plate with successively increasing thicknesses. The yellow fringes of the sodium vapor lamp might still be visible; however, they have less contrast than those obtained with (shimless) direct contact. The green-mercury-lamp fringes tolerate thicker shims until the contrast disappears. Well-established coherence lengths are listed in Table 1.1.[15]

A very thin material/film that can be used as shims is Mylar® foils of 2-, 4-, 6-, 8-, 14-, and 18-μm thickness.[16] One problem encountered with shims is

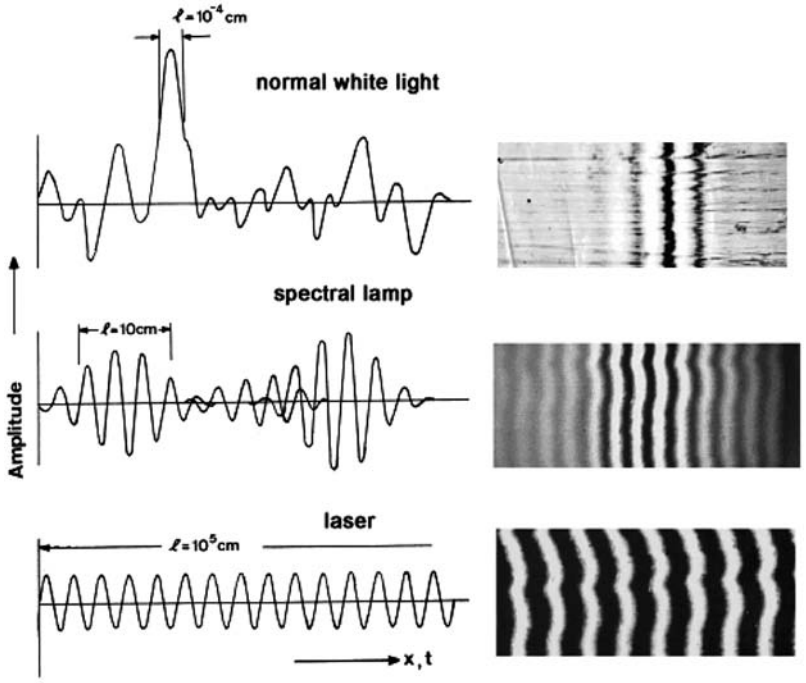

Figure 1.10(c) The coherence length of common light sources used for interferometry with the typical fringe pattern to the right of each diagram. (top) White light with green interference filter; the width of the surface seen on the sample is 0.3 mm. (middle) Green spectral lamp; the width of the surface seen on the sample is 1.3 mm. (bottom) HeNe gas laser; the width of the surface seen on the sample is 1.3 mm. (See also Section 10.4.) (Reprinted courtesy of H. Weber.[17])

Table 1.1 Coherence lengths for common light sources used in interferometry.[15]

Source	Wavelength (μm)	Useful coherence length
Visible white light	0.55	2 μm
Yellow, Na	0.59	600 μm
Green, Hg	0.55	11 mm
Gas laser, red, HeNe	0.63	several kilometers

cutting pieces without curling the edges. Packing the Mylar between sheets of paper and laser cutting helps to obtain clean edges.

The spectral wavelengths listed in Table 1.1 are among the most thoroughly researched natural constants. Their spectral properties and power supplies are unproblematic for operation, and their light sources are commercially available in great variety. The left side of Fig. 1.10(c) illustrates the typical coherence lengths of common light sources available for use in optical interferometry. With each of the three light sources, a typical

interferogram of the same micromachined aluminum flat sample was recorded and appears on the right side of the diagrams. One can easily select the most opportune type of illumination for a specific application. Needing the features of white light with a useful t (sufficiently large for convenient sample handling), one might select an illumination as shown in the middle section of Fig. 1.10(c).

The question arises: How far can the extension a of the secondary light source be increased before the observable fringe contrast begins to disappear due to coherent superpositions of the interferences? In an exaggerated, schematic way, the relation between the parameters at hand can be expressed as

$$\frac{\lambda}{4} > x\left(\frac{a}{F}\right), \tag{1.5}$$

where F is the focal length. Equating x with the collimator's diameter d gives

$$a < \left(\frac{\lambda}{4}\right)\left(\frac{F}{d}\right). \tag{1.6}$$

1.5 The Often-Neglected Angle of Light Incident to the Work

Changing the line of sight on a testplating assembly, i.e., the angle u of incidence, as in Fig. 1.1, quickly yields the following observation: Fringes change their spacing and orientation as a function of angle u. Angle u becomes the prolongation of the line of sight as it varies, as does the illumination angle u', as seen for the assessment.

Within certain instruments, angle u is the direction of the optical axis of target illumination and is a useful, if planned, design feature for testing technical surfaces. We argue against an unplanned, arbitrary choice of angle u'. Occasionally, one finds the effect of angular change, recommended for determining the sign of a deformation, to be convex or concave (consequently, even as a means of phase shifting for automatic evaluation).

The dependence of the interference pattern on angle u is demonstrated in Fig. 1.11(a). Shown is a planar air bearing composed of three equally thick stripes of glass contacted (wrung) onto a common base plate (glass). The essential coplanarity of the components of the bearing surface is to be tested. The left setting of the bearing assembly on the optical flat produces the information "not flat to specification and three components not coplanar." The same setting viewed from a slightly different direction, without the sample being touched by the technician, exhibits less fringe curvature (at both flanks of work), different fringe orientation, and different count per object length. The wedge angle and its orientation

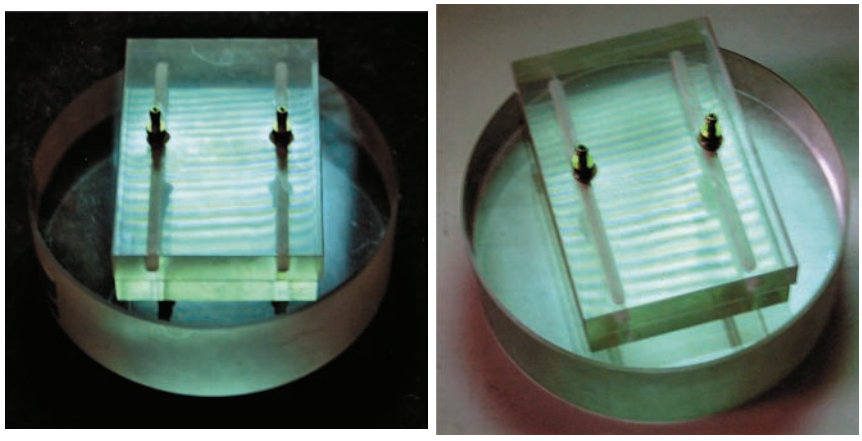

Figure 1.11(a) Workpiece (a planar air bearing made from glass) resting on an optical flat and viewed, as in Fig. 1.1, from two different, undefined directions: u_1 (left) and u_2 (right). Note the different fringe spacing and orientation.

relative to the work were initially adjusted for convenient fringe evaluation and rested in that position, enabled by omnipresent dust.

Air-bearing feet are expected to rest on the ground when not in operation, but how does one handle precious optical samples, which are not as tolerant to occasionally resting on the ground compared to air-bearing components of aluminum that have been hard anodized and polished? Safe handling requires an air gap between the reference and sample that is at least as large as an operational gap for air bearings (as in Fig. 1.3), if not larger. This constraint inevitably leads to the need for a longer coherence length than is offered by white light. Additionally, the desired larger gap calls for a light source with a coherence length that is much longer than an extended light source focused onto a pinhole stop can offer. Finally, the arbitrary viewing direction should be replaced by a fixed direction. Two independent observers should provide the same test results for quality control.

1.5.1 Selecting only one angle of incidence

The schematic in Fig. 1.11(b) serves to explain the obvious dependence of the interference pattern on nonorthogonal, oblique incidence. Two interfaces, separated by a gap of thickness t, are arranged under an illumination, as in Fig. 1.1 (an extended light source). U' is the line of sight, relative to the plate's normal. A partial light bundle is reflected at A, with 4% on the glass. The transmitted part of the bundle is reflected about 4% by the second surface, at B. The optical path difference ΔW between

the two reflected bundles, as a function of angle u and distance t, is derived from Fig. 1.11(b) as

$$\begin{aligned}\Delta W &= AB + BC - AD \\ &= \left(\frac{2t}{\cos u}\right) - 2t \tan u \cdot \sin u \\ &= 2t \cos u = n\lambda,\end{aligned} \tag{1.7}$$

with $\Delta W = 2t$, and only with $u = 0$, which is orthogonal incidence. If refractive index n is neglected, one may also operate with

$$\frac{\lambda_u}{2} = \frac{\lambda}{2\cos u}. \tag{1.8}$$

The value of λ_u is called the cartographic, or topographic, fringe equivalent. The relation between λ_u and angle u is represented by the curve in Fig. 1.13 for the HeNe laser wavelength of 632 nm.

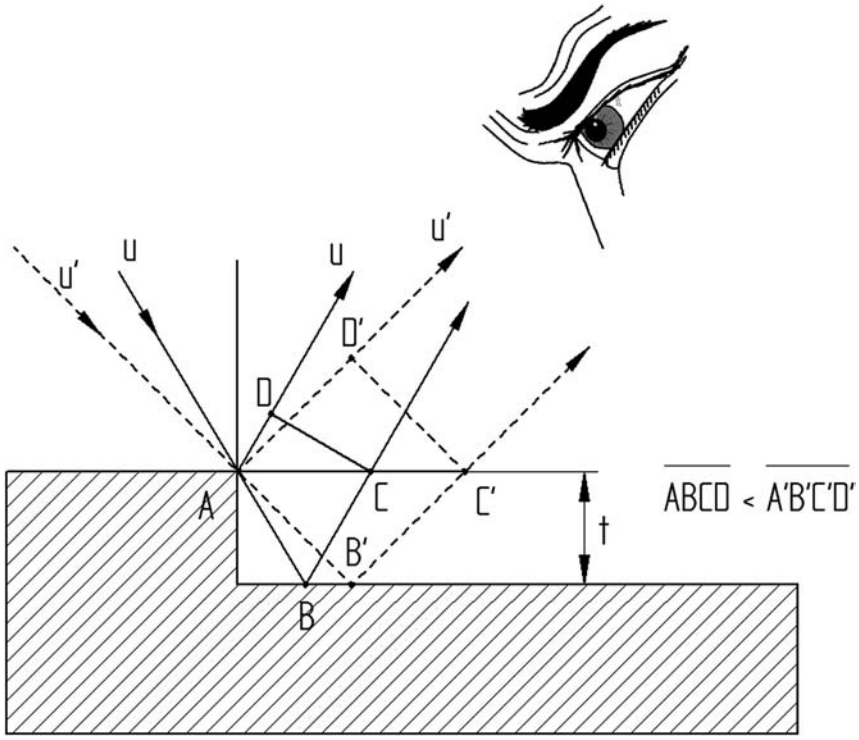

Figure 1.11(b) Deriving the optical path difference between two monochromatic light bundles reflected off of two parallel interfaces.

Equations for a small kink angle $\Delta\alpha$ on the sample and for a local change Δt of the distance between the sample and reference can be written as

$$\Delta\alpha = \frac{\lambda}{2P_1 \cos u}\left(\frac{\Delta P}{P_2}\right), \tag{1.9}$$

$$\Delta t = \frac{\lambda}{2\cos u}\left(\frac{\Delta P}{P}\right). \tag{1.10}$$

Many users (as in the lapping/polishing businesses) apply this simple test at an incidental variable oblique line of sight but determine the departure from flatness using $u = 0$. At $u = 30$ deg (cos 30 deg = 0.5), the fringe equivalent is not $\lambda/2$ but only λ, a difference that might be decisive in acceptance testing.

Surface errors on a specularly reflecting surface, represented by steps and by kink angles, modify the planar wavefront of a beam reflected at oblique incidence, as illustrated in Fig. 1.12. Their interference with a flat reference wavefront shows fringes whose fringe equivalent as a function of angle u can be read from Fig. 1.13.

Qualifying nonspecular, technical samples necessitates oblique incidence in order to obtain at least some quasi-specular reflection for meaningful interferometry. Most technical surfaces exhibit a reflectance as a function of oblique incidence, as in Fig. 1.14(a). We will see that partial specularity

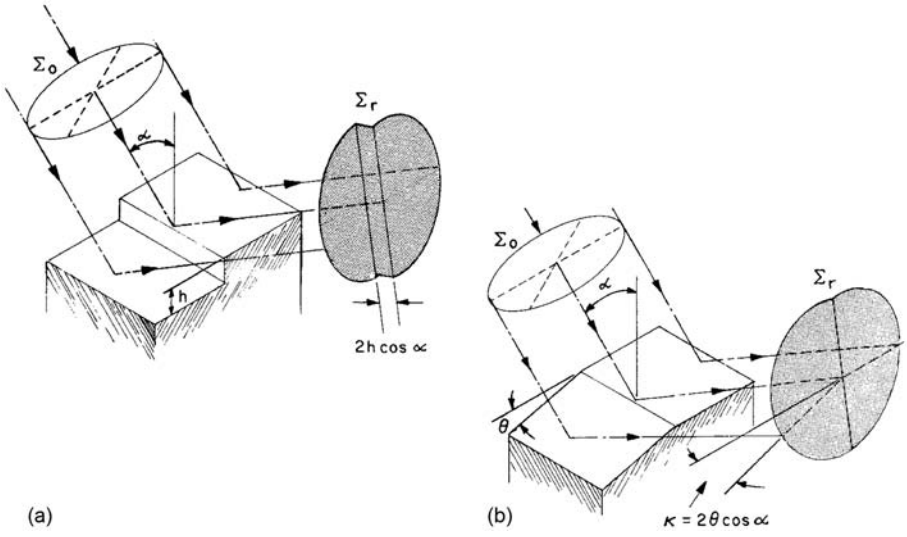

Figure 1.12 Planar wavefronts as supplied by a collimator (a) before and (b) after one reflection at oblique incidence on a sample with typical departures from flatness (a step or a kink angle).

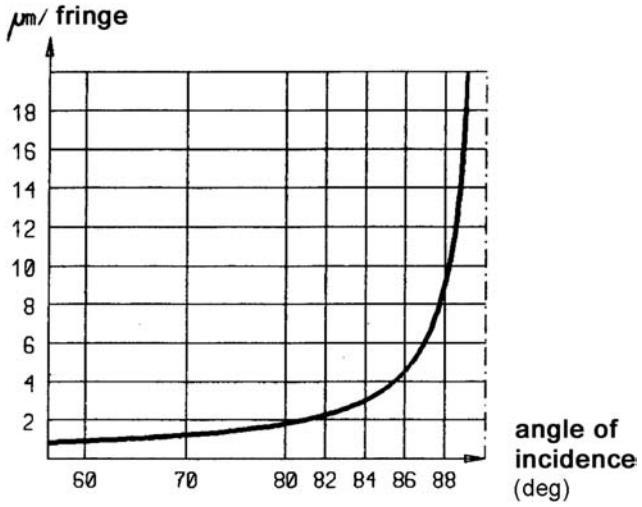

Figure 1.13 Fringe equivalent for $\lambda = 632$ nm as a function of angle u (valid for one reflection).

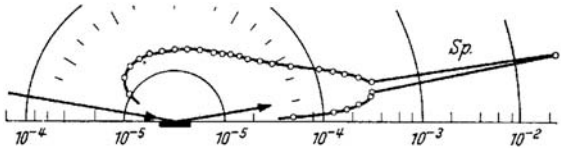

Figure 1.14(a) 2D cut through a global reflectance, characteristic of a technical (nonspecular) surface. (Reprinted from Ref. 14 with kind permission of Springer Science+Business Media.)

suffices for the generation of topographic interference fringes (see Section 9.1 on Lloyd interferometers). Incident angles between 80 and 87 deg result in 2- to 10-μm fringes.

1.5.2 Instrumental consequences

Certain coincidences have become quite favorable to applications in precision engineering and machining. Wanted are methods for measuring technical surfaces with the convenience of topographic information such as that provided by optical interferometry—with a reduced sensitivity; however:

- The range of so-called gloss angles of lapped, ground, and precision-machined surfaces is between 75 and 87 deg, covering the most-wanted 4- to 6-μm fringe equivalent.

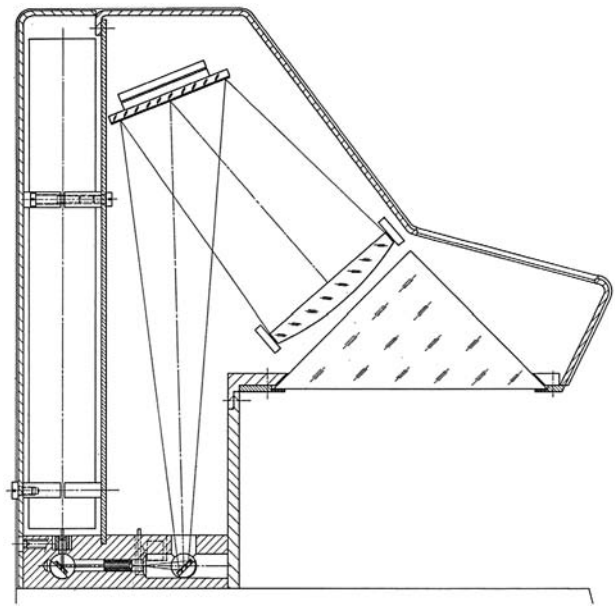

Figure 1.14(b) The 90-deg prism and collimator preset for 1-μm fringes on bottom-loaded samples. For sample/reference spacing see Chapter 2.

- Most technical substrates, metals, ceramics, prefinished glasses, and silicon wafers in all production stages have enough reflectance in that angular range to permit the application of unaltered, nondedicated optical inspection equipment.
- A majority of the technical surfaces ranging from microscopic to macroscopic and requiring stringent specifications are flat.
- A practical mass-produced optical component exists with a surface that simultaneously serves as a reference and beamsplitter without the need for special coating and, additionally, allows for adjustment of angles of excidence useful for sample illumination between grazing and 50-deg oblique incidence: the 90-deg prism. Figure 1.14(b) shows a practical implementation of a 90-deg prism for bottom-loading samples having 1-μm fringes.
- While the cross section of an obliquely reflected light bundle is unpractically oblong (elliptical), the same bundle is re-expanded at re-entry into the air/glass interface of the prism.

1.5.3 The multifunctionality of a prism's hypotenuse: beamsplitter, reference, and obliqueness provider

In order to replace the extended light source by interference-qualified illumination in a defined direction u, any collimator can be easily mounted,

as suggested in Fig. 1.14(c). A granite reference plate can serve as angular zero for the installation of the collimator. Simple, low-cost, home-made equipment as shown in Fig. 1.14(c) suffices. Hidden in the green box is the Z-folded version of a collimating optic.

Larger angles of incidence on non–fully specular surfaces, for instance, from 75 to 89 deg, are obtained by shining the collimated light through the cathede, one of the two identical short flanks of the right-angled prism, as shown in Fig. 1.14(b). A simple method allows one to incline the laboratory "do it yourself" collimator for use at zero, at oblique, and in combination with said 90-deg or Dove prism, at grazing incidence of the collimated light on the sample. Figure 1.14(d) shows the simple implementation and use of a 90-deg prism with its hypotenuse serving as a flatness reference. The flatness prism exhibits interference with a 1-μm fringe equivalent. Figure 2.1(d) illustrates the most primitive way of testing flatness, in violation of the noncontact measurement rule. In Section 9.1 we will see granite beds being tested for flatness with the grazing collimation direction set at approximately an 87-deg angle of incidence, which corresponds to a 6-μm fringe equivalent.

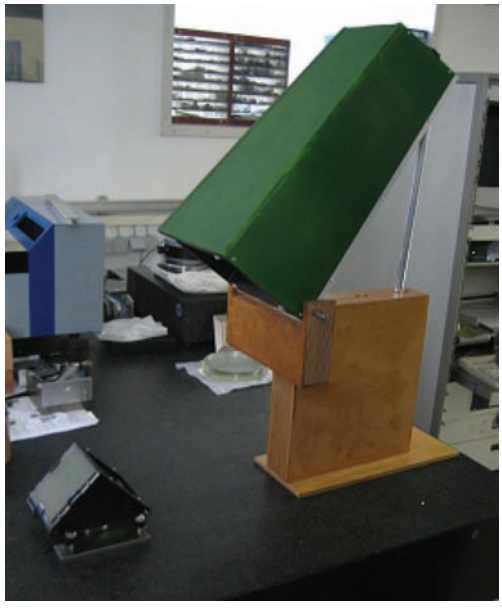

Figure 1.14(c) Collimator with Z-folded beam inclined to suit. The image is seen on a transparent paper or on ground glass [Fig. 1.14(d)]. Note that one surface, the prism's hypotenuse, serves as both the beamsplitter and the reference.

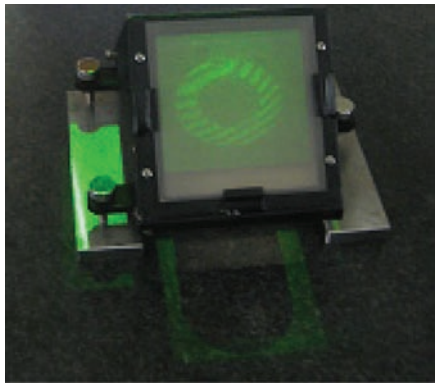

Figure 1.14(d) View of a sample at a defined angle of incidence with simple shop equipment. The stationary charge-coupled device (CCD) camera is not shown. Levelling screws on the reference holder allow precise alignment of the sample's distance and inclination. An alternative fixture for thick sample plates for use on a high-laboratory-grade granite surface plate is suggested in Fig. 2.1(c).

1.6 Knowing the Angle of Incidence with Respect to the Fringe Equivalent

Setting up a collimator to suit off-axis collimation, as suggested in Fig. 2.1, and having an unobstructed view of the sample needs no discussion; an angle of 10 deg suffices for applications in which testplating is replaced by contactless Fizeau interferometry. However, the easy-to-use flatness prism requires calibration to suit the application.

1.6.1 When the angle of total internal reflection is zero

The initial angular nulling alignment of the prism in Figs. 1.14(c) and (d) starts with finding the angle between the axis of collimation and the prism's hypotenuse, at which total internal reflection occurs. Less than 1 deg away from this position, light exits the hypotenuse nearly tangentially. With a choice of the angle of incidence to the prism, one can arrange the angle of excidence from the prism to range between 89 and ~35 deg, a range that is used in a wide variety of technical metrology tasks.

Any flat substrate (sample), glass or metal, brought to an arbitrary parallel distance of a few tenths of one millimeter, reflects the light at an angle of incidence equal to that of excidence from the prism. A minor nutation of the substrate creates a wedge, the direction and the size of which is indicated by the fringe pattern obtained. Obviously, the nutation of the substrate around an axis, orthogonal to the system's optical axis, increases the wedge angle in one direction, thereby reducing the fringe

equivalent, and vice versa. Quantitatively, these error contributions remain rather negligible in the 1- to 3-μm range of fringe equivalents but increase rapidly as the angle of incidence is preset to obtain a larger grazing incidence relative to the substrate, producing fringes desired to have about 3.5- to 8-μm fringe equivalent. In this range of very oblique (grazing) incidence, both the sample alignment and the sample departures from flatness entrain a built-in uncertainty in the amount and location of error. The distance between the sample and the reference will have a severe impact on the interferogram. In addition to pre-aligning the angle of incidence to the prism's cathede (starting where zero is the angle at which total internal reflection occurs), it has become common practice to employ calibration masters.

1.6.2 Calibration masters

Flatness calibration masters, which are precision-polished glass disks or testplates, are offered by different companies, quoting best usual flatness in the specification category of λ/20 and diameter to suit the application and the budget. Less costly are circular cuts (water jet) from selected float glass.[18] Process steps in the generation of a calibration master are shown in Fig. 1.15. In the center of the flat substrate, one polishes an artificial error in the form of a shallow spherical dish having a depth of, for instance, 3 μm and a diameter of ~10 mm.

The calibration master is made to have a peripheral zone(s) that represents the "flat" condition. For the prism, this means soft contact to the hypotenuse (the master and reference are parallel). Figure 1.16 shows a flat master with an artifact polished into the surface. The calibration follows the procedure shown in Fig. 1.15. The master is placed under a flatness prism interferometer [as in Fig. 1.14(b)].

Diamond micromachining of aluminum or brass makes possible the fabrication of a wedge with a mirror-like surface extending between two coplanar flanks (a wedge machined into a flat surface). Figure 1.17(a) shows an example of a linear wedge with 8.97-μm depth between the flat zones, recorded in a Michelson interferometer. The wedge presents 28 λ l/2 fringes. In order to calibrate a flatness prism to present 3-μm fringes, one would need to align the incident angle such that one obtains 8.97/3 fringes across the wedge. The dimension on the long side would be 70 mm.

In calibrating a prism interferometer to present 1-μm fringes, one would trim the angle of incidence to the prism's cathede to obtain 8.5 fringes across the wedge. The calibration master in Fig. 1.17(a) can be used in any interferometer operating with normal incidence due to the coplanar flat zones flanking the wedge.

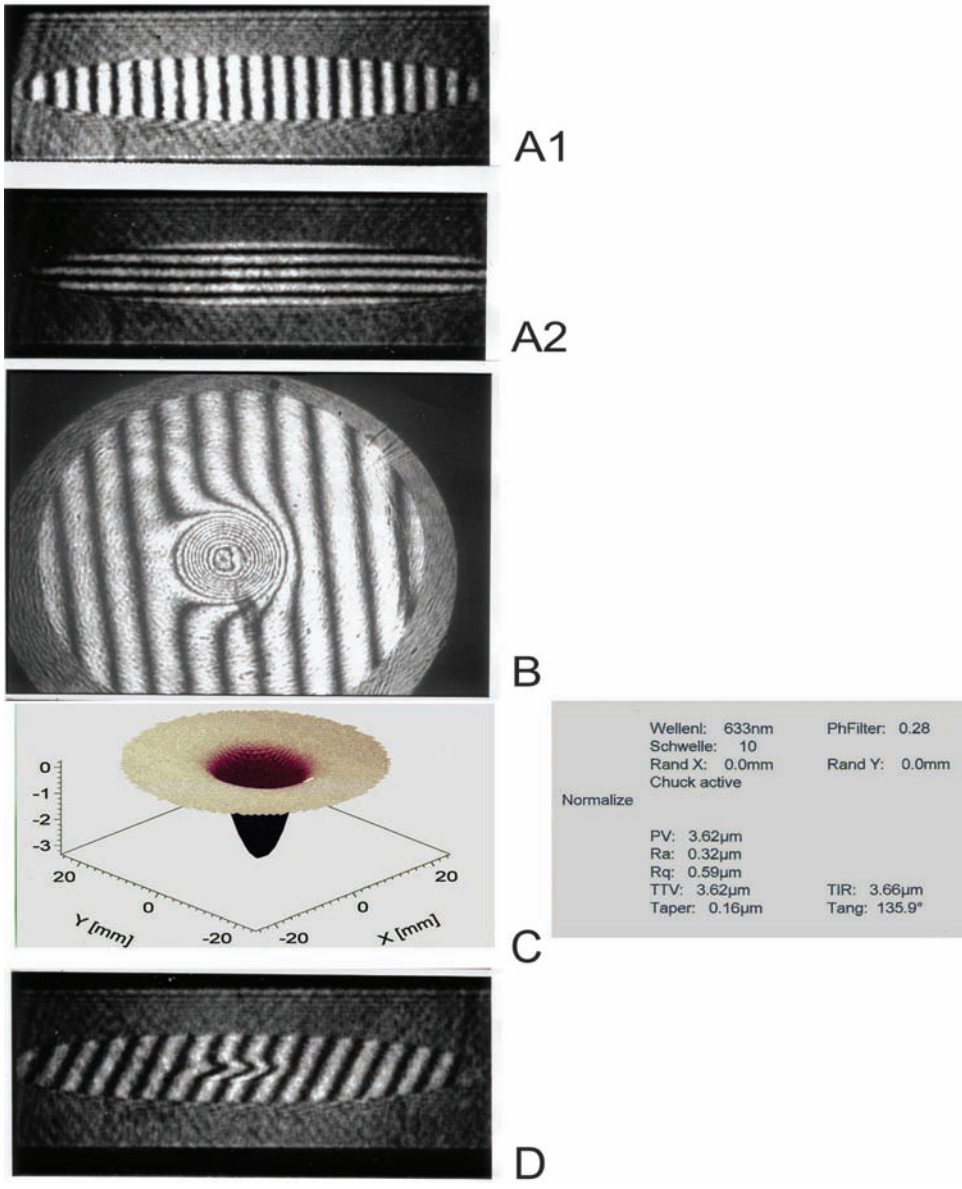

Figure 1.15 Generating a calibration master. A1 and A2 show the blank for the calibration master in oblique incidence, with fringes aligned vertically and horizontally, respectively; the angle of incidence is set for a 5-μm fringe equivalent. The spherical dish polished into the 50-mm-diameter flat is shown in B with $\lambda/2$ fringes (HeNe laser). C shows the result of an automatic phase-shift evaluation in a Michelson interferometer, using the ISTRA software generated by the Institute for Technical Optics, Univ. of Stuttgart.[19] D is the original sample placed back into its position when obtaining A1 and A2.

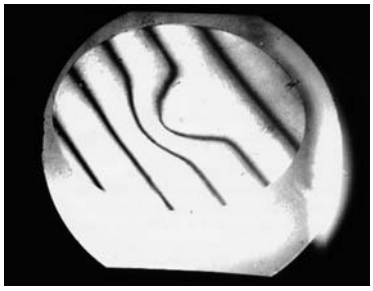

Figure 1.16 Normal calibration for 3-μm fringes as seen in a prism interferometer. Note that in the 90-deg prism interferometer, the angle of incidence cannot be derived from the perspective of foreshortening, seen in the image of a circular sample.

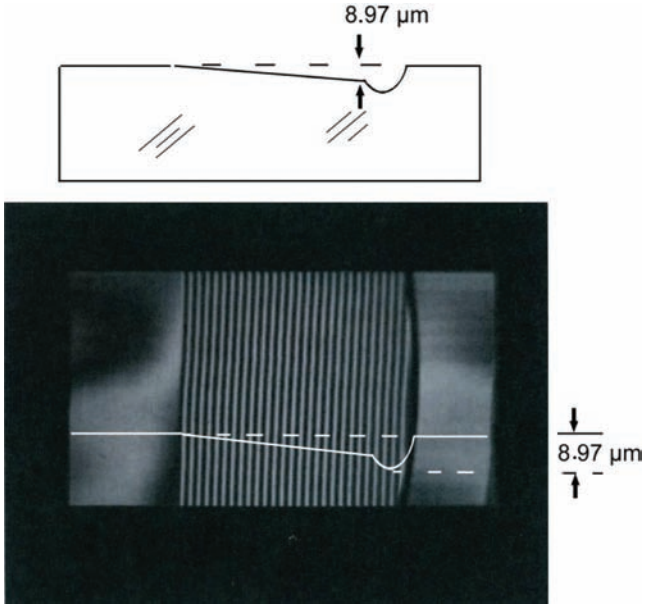

Figure 1.17(a) Michelson interferogram of a calibration master micromachined on a brass substrate. A wedge machined by diamond fly cutting feeds and infeeds simultaneously into the flat mirror. The interferogram shows the residual coplanar mirror flanks and the wedge, ending with a small groove (tool removed).The groove shows the circular fly-cutting path and indicates that the deepest part of the wedge below the planar reference is 8.97 μm.

1.6.3 Are 5-μm fringes meaningful?

The rapid development of 5-in. wafers and of magnetic storage substrates and their production control had a tremendous impact on the advancement of optical metrology instrumentation. The unsuitable quality of lapped,

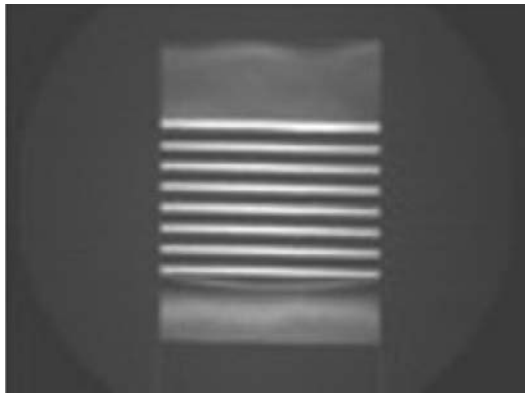

Figure 1.17(b) Calibration master as in Fig. 1.17(a) for aligning the 1-μm fringe equivalent in a prism interferometer.

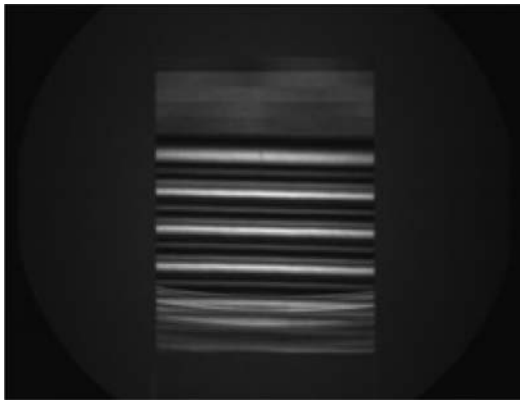

Figure 1.17(c) Like Fig. 1.17(b), except now for a 2-μm fringe equivalent.

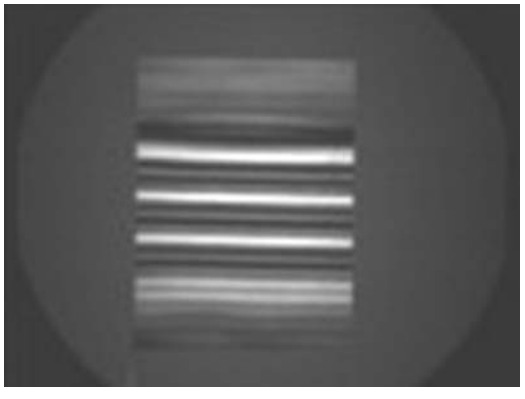

Figure 1.17(d) Like Figs. 1.17(b) and (c), except now for a 3-μm fringe equivalent.

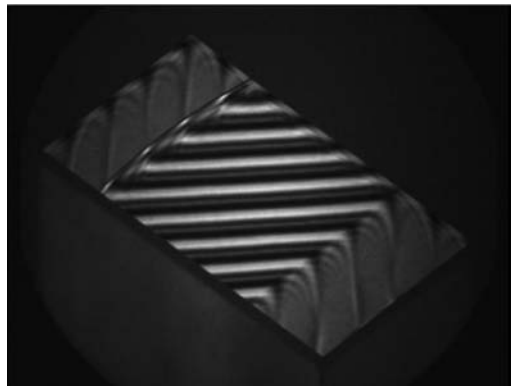

Figure 1.17(e) Calibration master turned 45 deg. Fringe equivalent set for 2-μm fringes, recognized by 8.5 fringes on the flat zone. This case corresponds to the case shown in Fig. 1.12(b).

diamond-sawed substrates [examples in Figs. 8.2(a) and (b)] in the early production phases prompted the desire to have contactless, 5-μm fringe-equivalent instruments with 125-mm diameter and λ/20 accuracy. Inconsistent results and differences between instruments from the same and from different suppliers were related to poor reference surface, collimation errors, and the distance between the sample and the prism's hypotenuse. Scrutiny was also focused on the calibration of the fringe equivalent ascribed to an instrument.

The wedge calibrating master has an inherent problem: The light leaving the prism in grazing excidence strikes the sample's surface under a different angle, depending on the wedge's direction relative to the direction of view. Figures 1.17(f) and (g) represent the same calibration master seen from opposite directions.

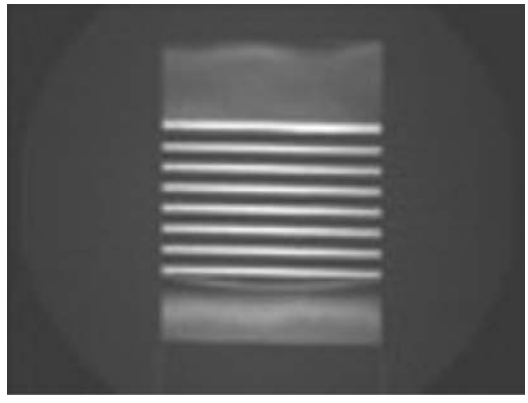

Figure 1.17(f) 1-μm fringes with beam walkoff into the open wedge (8 fringes).

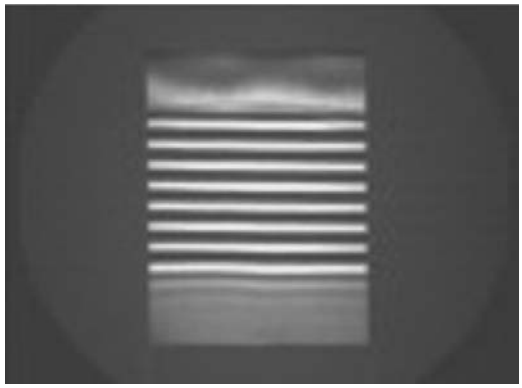

Figure 1.17(g) 1-μm fringes with beam walkoff into the closed wedge (9 fringes).

Rotating a sample under an interferometer in orthogonal incidence will not change the appearance of the interferogram in the case where the axis of rotation is orthogonal to the sample and coincident with the optical axis of the interferometer. The interferogram will be quite different with oblique incidence, as is illustrated by comparing Fig. 1.17(e) with the other parts of Fig. 1.17.

Another source of inconsistencies is the lack of collimation. This disturbance occurs in a 4- to 7-μm fringe-equivalent range and steers the light path within the prism close to the angle of total internal reflection. Details on this subject are discussed in Section 4.3.4.

1.6.4 Two-beam and multiple-beam walkoff

The user will soon recognize the wide range of roughness that allows one to obtain a flatness interferogram on all substrate materials, from float-glass samples to steel lapped with 360-grain and saw-cut silicon wafers to precision-ground, diamond-machined ductile metals. The fringe profile, however, varies between the typical two-beam and the aesthetically pleasing multiple-beam profile—at the same fringe pattern. Furthermore, the user will find that both the fringe profile and the fringe pattern depend on the clearance between the sample and the reference. Some dependence of the effective fringe equivalent on changes in the sample's inclination can be predicted, be it by inclining a sample to obtain a more desirable fringe pattern, or by local departures from nominal flatness.

The dependence of the fringe equivalent on minor angular changes of the entire sample or of parts of its surface can be seen experimentally when minutely changing the asymmetry between the calibration master and the sample around an axis parallel to the direction of view. Some one-sided squeezing might break the no-contact rule.

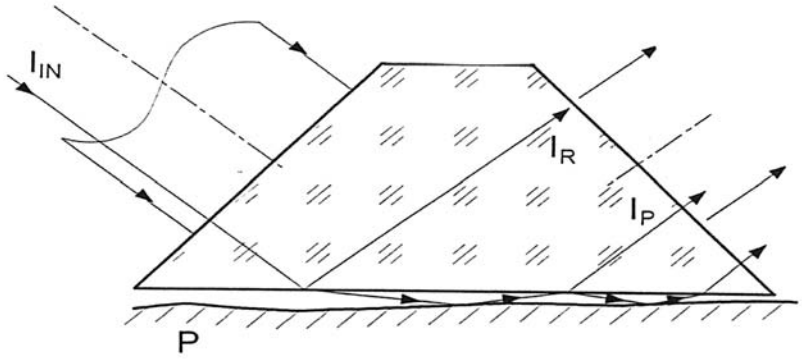

Figure 1.18(a) The 90-deg prism interferometer and the walkoff of beams successively reflected on a sample. The truncated top of the prism, with a precision optical finish, had been used for proximity control during rapid sample feeding, applying a laser triangulation method developed in a variety of experimental setups, both at the Institute for Technical Optics[19] and in the author's lab. The prism allows for observation of both the oblique incidence interference patterns on the nonspecular surface in the outgoing beam and, simultaneously, stray light from zones of constructive interference atop the sample's surface, seen through the truncated surface.

Figure 1.18(a) explains the answer: Successive reflections within the cavity collect increasingly longer optical path lengths upon each further reflection, modifying both the fringe profiles and the fringe spacings. The influence of this so-called walkoff on the fringe profile and even on the fringe's amplitude peak position is illustrated by the vector diagrams in Figs. 3.5(a) and (b). In case the sample is given some inclination (for instance, in order to obtain more fringes), the beam's walkoff is less if the apex of the wedge lies in the same direction as the walkoff, and vice versa. Rough sample surfaces with (most likely) only one or two reflections contributing to the image formation produce two beam-like interference patterns without making the walkoff become noticeable. Due to the walkoff, the accumulated optical path difference very obviously increases with increasing depth t of the cavity. A reduced-walkoff instrumental solution is described in Section 10.2.

1.6.5 Stray light need not be annoying

No technical surface that is meant to be (or to become) an optical component is free of some scattered light that can be seen from every direction, at reduced brightness, of course. The experiment shown in Fig. 1.18(b) would not be possible without stray light. Although the path of collimated light is shone in a grazing fashion along the surface, and the cross section of the image is necessarily rather oblong, one can observe the constructive (bright) zones of interference in a 1:1 nonuniaxially compressed fashion on the sample.

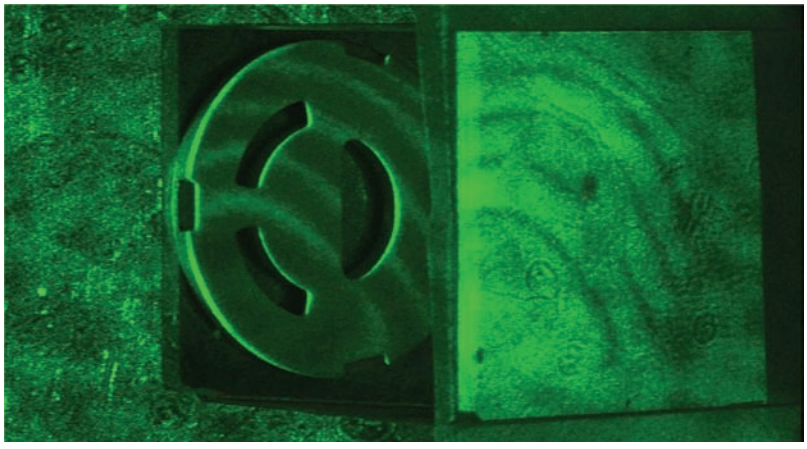

Figure 1.18(b) Collimated green laser light shone through the 90-deg prism, as in Fig. 1.14(c), producing 2-μm fringes of a flat lapped ceramic sample (left). The dark flatness fringes are seen on a transparent drafting paper screen (right). At least two consecutive, quasi-specular reflections on the sample are required in order to produce the bright interference bands that generate the scattered light. The sample is a mass-produced ceramic seal of standard water faucets; less than 2¢ per piece is allowed for continuous process quality control.

When adjusting the angle of incidence to the prism, the practitioner will instantly recognize the light scattered off of constructive multiple-reflection interference paths, striking the sample within the narrow cavity. The bright zones can be observed at any angle through either of the two cathedes of the prism. The 90-deg prism can be truncated to become a Dove prism [Fig. 1.18(a)], allowing convenient, instant orthogonal observation of the surface under the hypotenuse, without the impractical, perspective, uniaxial compression in the exiting beam. Figure 1.18(b) is an example of these scattered-light fringes.

While discussing the occasional good use of stray light, let us mention a side effect from Chapter 9. Refer to Fig. 9.6(a), which shows a large sample to be inspected by a grazing-incidence Fizeau interferometer. Two mirrors, T (the semitransparent Fizeau reference) and M (the flat reference), are located with symmetric angles relative to the large semifinished flat sample, in order to obtain a long-path grazing-incidence Fizeau configuration. Let us select an angle of incidence to the sample from Fig. 1.12 that is 80 deg (approximately a 2-μm fringe equivalent). In this Fizeau configuration, the beam passes the sample twice (back and forth), resulting in an effective fringe equivalent of 1 μm.

Figure 1.18(c) shows scattered-light fringes on the nearly finished 400-mm [outside diameter (OD)] flat mirror. The sample was spray coated with silver.[20] The thickness variation of this spray silver coating was measured to

Figure 1.18(c) Due to the double reflection at the mirror and the preset 80 deg of incidence, the Fizeau scatter interference levels represent a mutual distance, as viewed orthogonally on the mirror, with 1 fringe equivalent = 0.913 μm at the HeNe laser wavelength.

be less than 30 nm. The record was taken in dim ambient light. The expenses for the low-cost laboratory components are substantially less than for a full-sized interferometer; needless to emphasize is the profitable use of an air-bearing slide or of a rotary table for complete lateral scanning [Fig. 9.3(b)].

1.6.6 The scatter flat test

Global reflectance, characteristic of a technical surface such as the finest lapped ceramic wafer carrier or a glass mirror shortly before being a 100% mirror, offers intriguing opportunities for metrology. An expanded collimated laser beam, directed obliquely onto the cleaned surface, produces scattered light that can be observed on the surface as a zone of some brightness from nearly any direction. In addition, the reflection characteristically shows a lobe of quasi-specular reflection, much like in Fig. 1.14(a). The specular component might even be strong enough to allow at least one back and forth reflection, thus establishing a long-path Fizeau interferometer. On a sample (being much larger in diameter than the available collimated beam), one can recognize the light path on the dull surface orthogonal to the scattering mirror surface. The experimental setup is reproduced in Fig. 1.18(c), showing a 400-mm OD sample mirror, the front Fizeau mirror T, and part of the rear mirror M. In the defocusing plane one can see the bright focal image produced by T and, depending on the grazing angle chosen, at least one or even more foci. The next focal image represents two passages of the beam over the sample (back and forth); the first two foci

are brought to coincidence, as in the normal Fizeau technique. One can see the Fizeau fringes in any plane along the light beam; however, they are viewed in a rather foreshortened, unsharp quasi-image. The view onto the sample mirror (in sufficiently dark ambient light) is reproduced in Fig. 1.15 part D. At least the first two back-and-forth reflections are needed to generate constructive and destructive interference zones; from the dark zones there will be no stray light. The straightness of the scattered fringes provides a quick and easy determination of flatness. Arrangement of the sample on an air-bearing rotating table is an obvious option for inspection of the entire sample surface. Calibration of fringe equivalent with respect to the angle of incidence is achieved by alternating the autocollimation by reflecting the illuminating beam off of the backside mirror M, once directly and once including the reflection by the sample.

Compared to other oblique-incidence methods, one observes an image that is not perspectively foreshortened. The fringes are seen with the arranged fringe equivalent. Fringe orientation is adjusted by the terminal Fizeau mirror M. Observation is possible only in dim ambiance. The application of this quite unusual method is limited to surfaces that allow at least two successive reflections (forward and backward) for establishing standing interference levels.

References

1. D. Malacara, A. Cornejo, and M. V. R. K. Murty, "Bibliography of various optical testing methods," *Applied Optics* **14**(5), 1065 (1975).
2. Originator is not known, but most likely the figure is from IBM in Sindelfingen, Germany.
3. J. M. Bennett and L. Mattsson, *Introduction to Surface Roughness and Scattering*, Optical Society of America, Washington, D.C. (1989).
4. J. A. Slater and D. A. Cox "Scratches: At what price quality," *Proc. SPIE* **654**, 68–75 (1986) [doi: 10.1117/12.938270].
5. Bulbtronics Co., 45 Banfi Plaza N., Farmingdale, NY 11735, USA and Epigap Optoelectronic GmbH, Köpenickerstr. 325b, Berlin, 12555, Germany.
6. R. Schulze "Optische Messmethoden" in *Handbuch der Physik* **29**, *Optische Instrumente,* S. Flügge, Ed., Springer-Verlag, Berlin (1967).
7. D. Malacara, *Optical Shop Testing*, John Wiley & Sons, New York (1978).
8. B. S. Fritz, "Absolute calibration of an optical flat," *Proc. SPIE* **433**, 123 (1983) [doi: 10.1117/12.936799].
9. H. Teller Trading Agency, Drachendorf, 07551 Jena, Germany, Borofloat glass, selected sections, water-beam cuts.

10. H. Mykura, "Interference microscopy at high wedge angles," *Proc. Physical Soc.* **67**(4), p. 281 (1954).
11. P. Langenbeck, *Wirtschaftliche Mikrobearbeitung: Wege zur Perfektion mit Luftlagertechnik und optischer Messtechnik*, Carl Hanser Verlag, Munich, Vienna (2009).
12. S. Tolansky, *Multiple-Beam Interferometry of Surfaces and Films*, Clarendon Press, Oxford (1948).
13. R. Haberland, M. Böffgen, and W. Klein, "Neue Verschleißerscheinungen an mono-kristallinen Diamantwerkzeugen," Industrie-Diamanten-Rundschau (1996).
14. P. Langenbeck, "Roof edge test (RET) for micro-roughness," *Proc. SPIE* **802**, 89–93 (1987) [doi: 10.1117/12.967106].
15. R. W. Pohl, *Optik und Atomphysik*, Springer-Verlag, Berlin, Chapter 12 (1958).
16. J. Flügge, G. Hartwig, and W. Weiershausen, *Studienbuch zur Technischen Optik*, Vandenhoek & Ruprecht, Göttingen (1976).
17. Supplier of thin Mylar® film: Du Pont de Nemours (Germany) GmbH, Du Pont str.1, D-61343 Bad Homburg.
18. H. Weber, "Der Laser als Mess-Instrument, Seminar on Micro-machining," ETH Zürich (1972).
19. Source for Istra software and laser triangulation: Institut für Technische Optik (ITO), University of Stuttgart, Pfaffenwaldring 9, D-70569 Stuttgart.
20. Peacock Laboratories, Inc., Philadelphia, PA 19143 USA: Spray silver chemical solutions.

Chapter 2
From Extended Light Source to Collimated Illumination

2.1 Introduction

The collimation obtained in the manner shown in Fig. 1.10(b) uses a suitable projection lens with diameter-to-focal-length ratios (d/F) that are limited to about 1:10 and do not yet require spherical correction. Many low-cost monochromats are available for optical components having large diameters.[1] Optical component diameters must be compatible with the work they are expected to perform. A 10-cm diameter needs a 1-m-long mechanical structure. Z folding makes the structure more compact. Antireflection coating of surfaces that are not involved in interference formation is required.

A simple modification to the Newton testplating setup that is operated with collimated light is shown in Figs. 2.1(a) and (b). Figure 2.1(a) shows a SiC wafer under a reference at 0.25-mm distance under collimated oblique incidence. The collimator is indicated only in Fig. 2.1(a). The sample and the adjusting feet of the reference rest on the same base. The base is a granite plate, a glass plate, or a chuck. The adjustment to the sample distance uses a removable lens-cleaning tissue, a cigarette paper, or a nylon string, which is removed as the distance is increased.

Angle u can be derived from the reference holders [diameter d_1 (crossing the viewing direction) and d_2 (in the viewing direction)], using

$$\cos\left(\frac{d_1}{d_2}\right) = \cos u, \tag{2.1}$$

if it is not known prior to recording.

Any collimator can be used interchangeably with the contactless Newton method as in Fig. 2.1(a), or with a flatness prism as in Figs. 1.4(b) and 2.1(c). A collimator arranged at 80-deg incidence to the operating base (a granite tool room plate) will permit the use of the contactless Newton method on all samples that could otherwise be testplated.

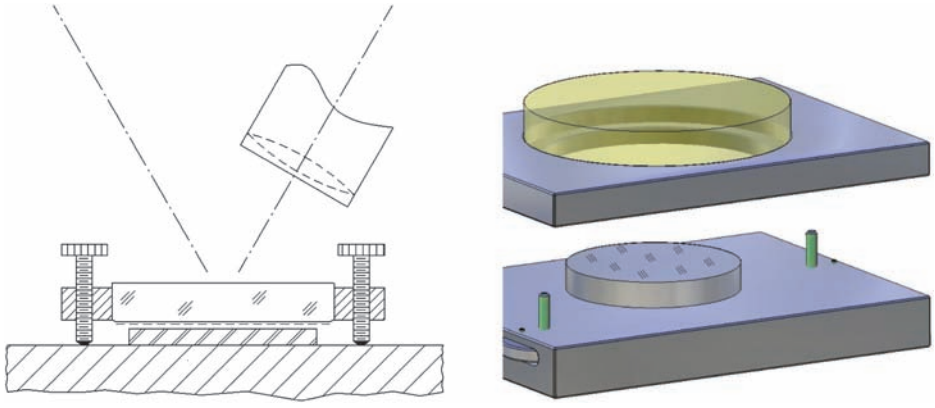

Figure 2.1(a) The contactless Newton method generates information equivalent to that generated by the Fizeau method but in a more effective manner.

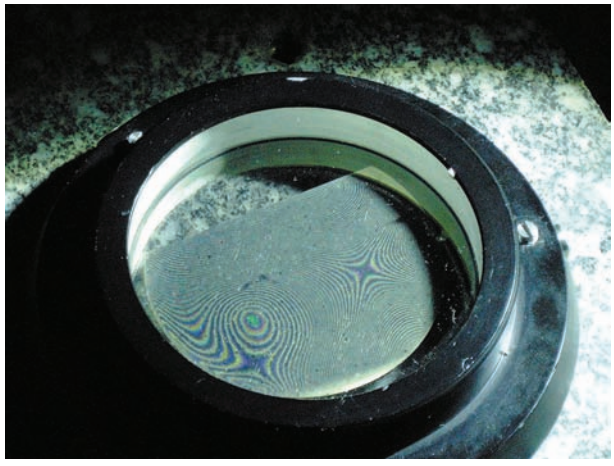

Figure 2.1(b) A SiC wafer of diameter 50 mm under a mercury spectral lamp without a filter. The gap is approximately 0.2 mm, recorded from the setup in Fig. 2.1(a).

For use on prism interferometer devices, the same collimator needs a dedicated direction. Finding and fixing the direction of the axis of collimated light toward the cathede of the 90-deg prism requires some preparation. The process starts with the preferred orientation and height of the prism parallel to and above the operating base. Application of calibration masters follows, as described in Chapter 1. The angle of excidence from the prism's hypotenuse is the angle of incidence to the sample arranged parallel to the hypotenuse, at some safe distance that is on the order of less than 1 mm. This angle must become known, as it determines

the fringe equivalent; it can be arranged for between 1 and 5 μm by selecting and fixing the collimator's direction.

Figures 2.1(c) and (d) [and Fig. 1.14(b)] show simple, low-cost surface testing with the prism used as a loose component in direct contact. A calibration master automatically fulfills the parallel condition; three tiny tape spacers can be beneficial. An inexpensive, handy, small, 90-deg prism may be used for quick in-production visual inspection of technical surfaces. The interference image will be seen on a transparent paper as shown in Fig. 2.1(d), using collimated light as in Fig. 1.14(b).

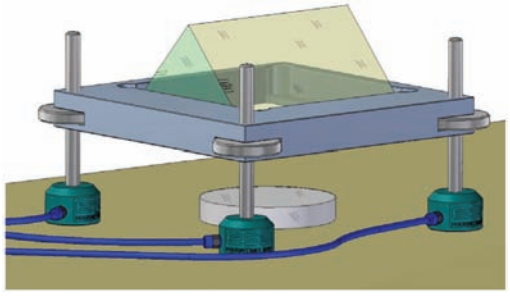

Figure 2.1(c) The flatness 90-deg prism used with the same collimator as in contactless Fizeau testplating in Fig. 1.14(c). The angle of incidence is marked by a thin fiducial line on the edge of the first cathede, coinciding with calibrated marks on the second cathede. The hypotenuse protrudes approximately 0.3 mm outside of the frame, which is designed to be asymmetric for weight balance. This is a very handy device for general optical shop utility. The three air-bearing feet allow for lateral scanning, for instance, on a granite surface plate. The three support rods serve in fringe alignment.

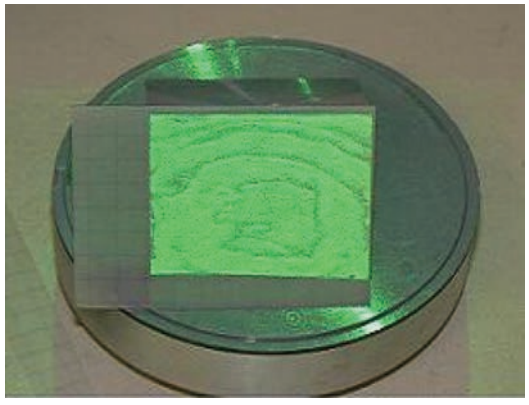

Figure 2.1(d) Inexpensive optical inspection of lapped technical samples. Here, an air-bearing foot was just molded. Fringes delineate a pocket in the bearing surface, supposed to be a spherical depression, about 4-μm deep. Fringes were recorded with a fringe equivalent of 2 μm.

Results of this procedure include:

- The contact Newton method can be replaced by the contactless Fizeau method.
- The method allows for noncritical sample handling and adjustment for suitable beam inclination.
- The procedure allows for a convenient selection of angles u of incidence.
- Use of lasers and laser diodes requires limitation of their power to comply with eye-protection regulations.
- On an air-bearing slide and after suitable alignment, a large sample can be transported laterally and, thus, can be tested by scanning.
- The procedure is useful for quality control and machine alignment; a bar of aluminum, micromachined to, e.g., 50×450 mm, indicates both perfect flatness and alignment in the rare case where fringes maintain both their initial spacing and their orientation at any other location (without walking during motion).

2.2 Technical Relevance of Oblique Incidence

A surprisingly large number of mass-produced products are specified to be *flat to their edge*, with a majority of these in the category of several centimeters in diameter. 100% quality assurance to about 1-μm departure from planarity is common. The fringe equivalent is selected to allow fast, simple interpretation of the permitted tolerance, e.g., 1 μm per fringe. This number is conveniently readable for untrained workshop personnel.

Most products to be tested require, time and again, quick and easy placement of the sample at the proper distance from the reference, without the need for subsequent alignment. A key problem here is often the lack of parallelism in the sample; the bottom surface to be tested might be so far off of any commensurate clamping zone that sample alignment hardware becomes necessary. Instant sample alignment involves simply placing the sample onto the hypotenuse of the prism, now facing upwards, after interlaying some stretched nylon wires [Fig. 2.2(a)], or cementing watch ruby stones (pellets of about 1 mm diameter and 1 mm thickness with a concave dip that serve as very low-friction axial and radial shaft bearings in watches and electricity-consumption counters) into the reference surface and polishing them to the desired height [Fig. 2.2(b)].

The temptation to place objects directly onto the bare hypotenuse [as in Fig. 2.2(c)] is understandable; however, eventually, the reference surface will become scratched. A low-cost repair solution uses immersion oil and a flat reference glass [Fig. 2.2(d)]. Such a plate can be a precision-polished quartz plate or a selected cut from low-cost float glass[2] (available at 10- to 25-mm thickness). For the refractive indices of oils see Section 7.7.1 and Ref. 3. For less-than-strict requirements, water white or universal oil suffices.

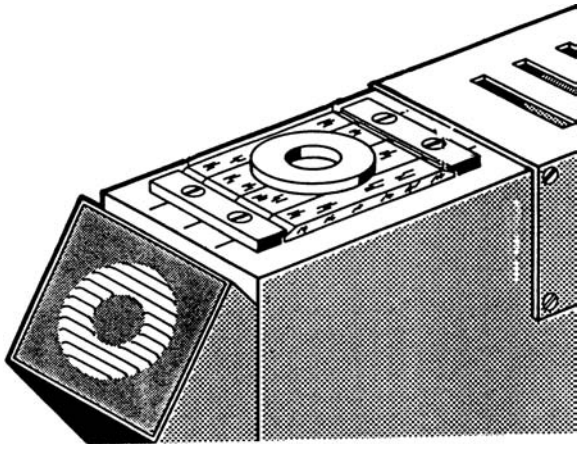

Figure 2.2(a) Nylon wires permit a "sloppy" placement of the sample onto the reference surface (the hypotenuse of the prism), aligned and without contact.

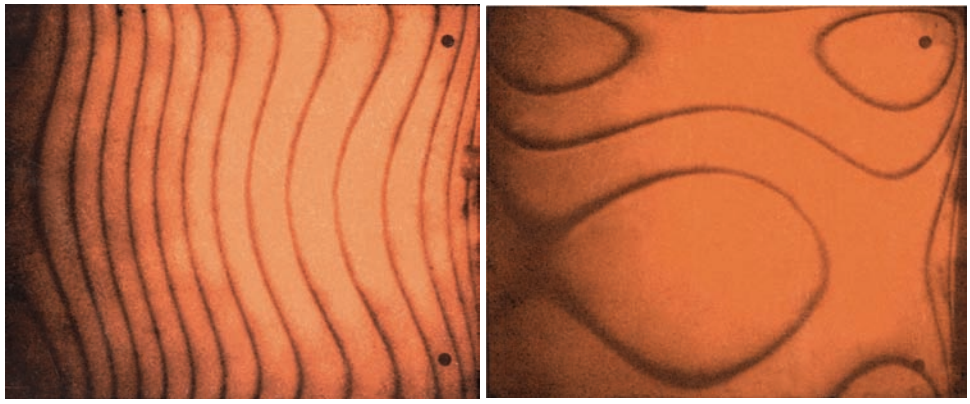

Figure 2.2(b) Watch ruby stones (three pieces) cemented into the reference plane and polished to suit the fringe alignment on large samples, resting on the stones. This setup allows rapid placement of samples (as shown here with photolithographic mask blanks at two different settings). The fringe equivalent is 2 μm.

Extensive use of oblique-incidence instruments became essential with wafer production. Quality control of mass-produced, not-yet polished, lapped substrates (wafers) prompted many new developments combining a preset angle of incidence, no contact to sample surface, and automatic sample feeding without the need to interfere with the preset alignment for repeatable fringe pattern evaluation. One possible rugged instrumental solution to these requirements is given in Fig. 2.3.

The essential difference between the oblique-incidence interferometer and the flatness prism is that the number of reflections on the sample surface is

Figure 2.2(c) and (d) (c) A very practical example of what *not* to do: samples are resting directly on the reference surface (the hypotenuse of the interferometer). (d) If a reference becomes scratched, it can be repaired by oiling on a protective, interchangeable flat plate made from either quartz glass or low-cost selected cuts of float glass.

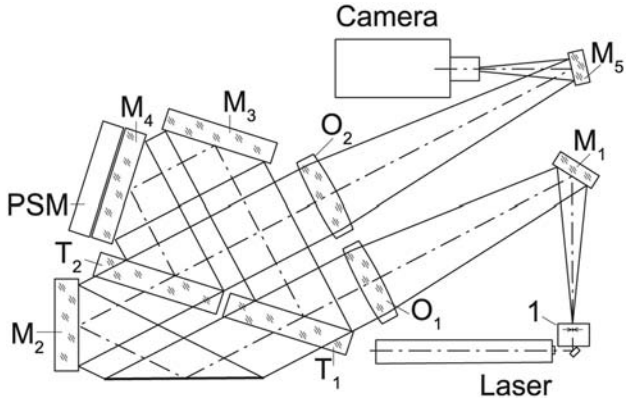

Figure 2.3 A two-beam oblique-incidence interferometer. The bottom bold line shows the nominal surface of samples to be fed in a pre-aligned condition. PSM is phase-shift mechanism (or motor).

reduced to one compared to multiple reflections under the prism. The interferogram obtained by the prism interferometer depends on the roughness and fringe equivalent, which itself depends on walkoff. Consequently, there is no fringe shaping from multiple reflections and from bothersome walkoff when using the oblique-incidence interferometer.

In the interferometer design shown in Fig. 2.3, the interference will always be two beam, which is a prerequisite for automatic fringe evaluation using the phase-shift method. Two objectives, O_1 for collimation and O_2 for imaging, are selected in order to obtain good-quality collimation and good-quality sample imaging. Figure 2.3 does not show two of the oblique-incidence interferometer's practical handling features:

1. External sample loading, adjustment, and unloading by rapid, repeatable sample feeding at the location marked by the bold horizontal line in Fig. 2.3; and lateral translation such that feeding becomes equivalent to scanning. (The author's laboratory concentrated on air-bearing motion systems, whose linear and rotary axes are interchangeable with optical axes.)
2. Measurement of thickness variation, curvature (bow), and wedge (taper) of thin substrates such as wafers. Thus, the sample holder (the chuck) has at least one extended zone for reference. This zone has the same flatness as the main chucking pattern [see Figs. 9.10(a) and 9.12(b)].

Optimizing the angle of incidence, adjusting the work holder to the sample thickness, and other sample handlings facilitated remotely from the instrument are described in the following section.

2.3 Fast Adjustment of Tilt and Height

2.3.1 Autoleveling with mechanical truing

The need to avoid contact between the sample and reference has led to a variety of technical solutions for obtaining parallel, or at least near-parallel, sample alignment at practical, small distances from the now-virtual sample location, without a lengthy search for alignment. Figure 2.4(a) illustrates an air-bearing-based autolevel; the "flat" sample is placed on an airborne tilt table that is carried by an air-bearing piston for height control. Both movements—tilt and height—become clamped upon reduction of air pressure at the moment of alignment.

The alignment procedure needs a flat truing plate, which pushes the sample down and simultaneously tilts the sample with its carrier. The carrier rests on a truncated, spherical air bearing. The final position is reached when the truing plate, being of sufficient width, comes to a stop on three adjustable peripheral anvils. The relief of air pressure from partial bearing zones causes instant clamping. Because the truing plate does not come into contact with the sample, it has an air-bearing function as well. The truing plate is made from a porous graphite material (Purbone[4]). A small amount of air pressure fed to the rear side of this plate forms a uniform air cushion when the plate is pushed toward the sample. This function addresses any slight, otherwise unavoidable, lateral motion of the sample during leveling.

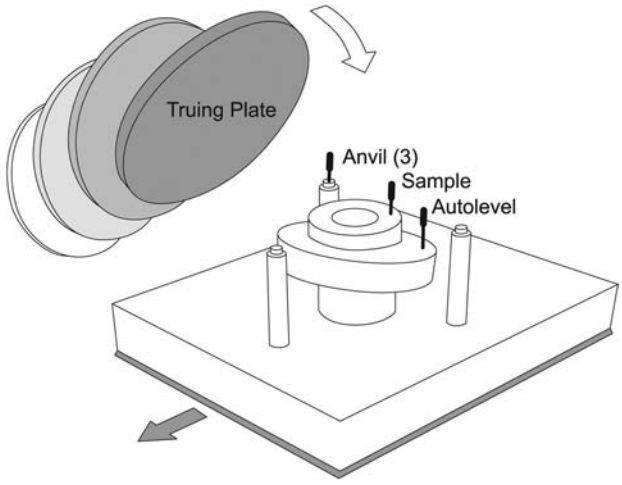

Figure 2.4(a) Air-bearing-based contactless height and tilt alignment using a truing plate [see Fig. 9.14(d)]. The truing plate is made of a micromachined porous material as used for air bearings in order to avoid hard contact with the sample. A nominal clearance between the sample and the reference is maintained.

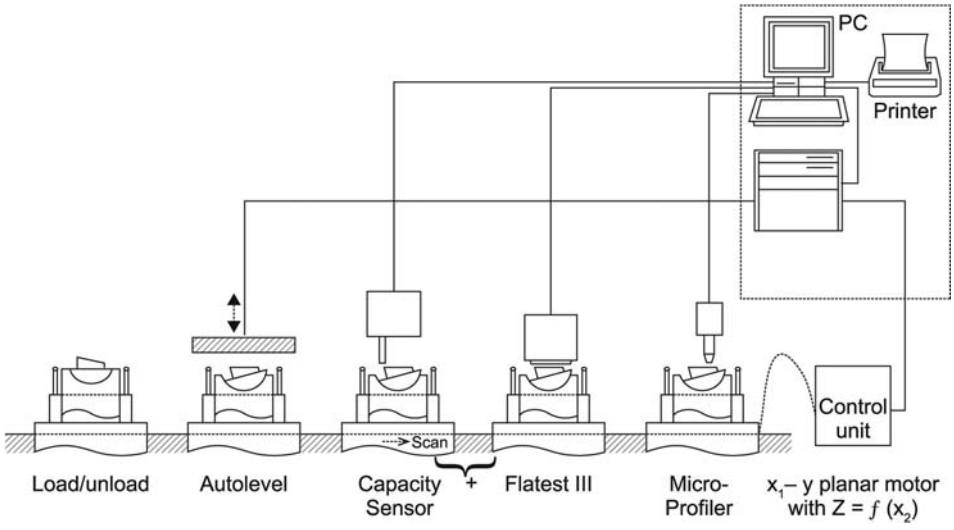

Figure 2.4(b) Promotional illustration of autoleveling based on air bearings. The sample stage rests on a spherical bearing that is lifted by cylindrical bearings or a piston; alignment takes place with a truing plate that briefly pushes the sample into a plane defined by the anvils. The sample is locked in place by reducing the air pressure on selected zones of the lift/level mechanism.

The sample stage can be equipped with a vacuum chuck; an exemplary chuck in a retainer is shown in Fig. 2.4(b). As is also shown in this figure, the entire autolevel apparatus can slide with a planar air bearing on a surface plate to reach different metrology stations, including loading and unloading areas, without losing alignment. Simple linear and planar stepping motors,

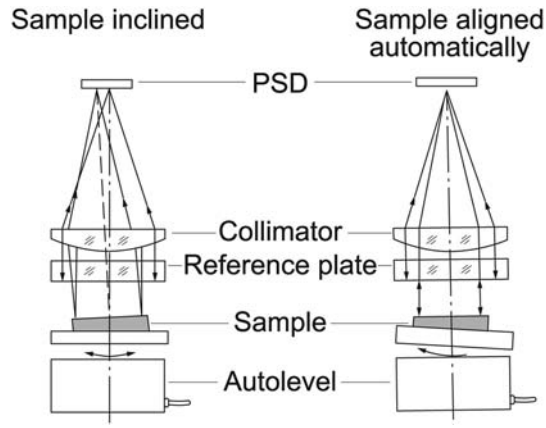

Figure 2.4(c) The electro-optical version of autoleveling needs no height control for the long distance between the Fizeau reference and the sample (this is different from the prism interferometer).

themselves being airborne, make the autolevel a useful device for rapid automatic quality control.

2.3.2 Autoleveling with optical position sensing

The autolevel can be operated with electro-optical position detectors and electronic control devices introduced into the system. The detector system may be integrated into the interferometer, as briefly illustrated in Fig. 2.4(c). Samples larger than, for instance, 200 mm OD might present handling problems. Additionally, the high cost of sample handling calls for alternative scanning methods.

Lateral scanning interferometry might provide an answer: it combines large-scale linear and rotating air-bearing tables with smaller-scale precise optics. The optical axis of the latter allows precise mechanical scanning motions enabled by air-bearing aggregates. The ultimate outgrowth of this type of metrology is the stationary interferogram recorded off of a rotating disk or off of a linear sliding substrate that has been diamond machined on an air-bearing aggregate, prior to un-chucking, of course. These scanning methods will be covered in detail in Chapter 9, which also covers instrumental solutions for oblique-incidence testing of larger technical surfaces.

2.4 Variable-Angle *u* on Samples with Strong Slopes

The closer a sample surface approximates a flat surface, the less relevant (in terms of fringe displacement representing the true surface deformation) is the beam walkoff. Most frequently the criterion *flat* or *not flat* suffices, and rejects

are judged qualitatively for correcting the production process. The more wavy the sample's surface, the less uniform and less well defined are both the actual preset fringe equivalent and the relation between the actual error location on the sample's surface and the fringe position.

The culpable beam walkoff can be reduced experimentally on flat samples; the collimated bundle shone toward the apex of the wedge sample/reference will walk off less than if shone outside of the wedge. In slightly off-normal incidence, this might even let a multiply reflected beam find autoreflection at some higher order of reflection [Fig. 10.3(a)]. The unavoidable beam walkoff of multiple reflected beams will modify the fringe profile to show side bands [see the vectorial illustration in Figs. 3.5(a) and (b) (upper right record), and Fig. 3.6(b).] Additionally, the contrast will be reduced. Finally, and most importantly, differences in the amount of walkoff will reduce the amplitude's peak as well as shift the fringe location.

2.5 Interference Contrast

The location of dark fringes in an interferogram, as seen on a screen, is not a function of source brightness. Overexposure onto any recording medium, be it film or electronic camera, will let the brighter zones grow wider, thus modifying the profile of the dark fringes. The effect is even stronger in interferometer collimation with its nonuniform brightness. This photometric effect can be seen in Fig. 2.5(a) by the varying width of the dark fringes.

Spurious reflections from component surfaces that are not part of the cavity can become a severe disturbance to fringe evaluation. A case in which these reflections are coherent with the main beam is shown in Fig. 2.5(b), where the final fringe location is a physical effect. The vector diagram in Fig. 3.2(c) illustrates this with an uncertainty circle atop the otherwise smooth amplitude curve.

Let us look at that with which we are already acquainted: the two bare glass plates in the Newton testplating configuration (Fig. 1.1). There will be four reflections, one at each surface; only those two reflections at the surfaces confining the small gap t between the plates are of metrologic relevance. Each plate, therefore, is given a wedge angle large enough to make an interference pattern in its two reflected beams narrow enough to not be further resolved. We may then consider the interference only between the closely neighboring surfaces. The first surface is known to reflect about 4% of the 100% incident intensity. Of the transmitted 96%, again 4% is reflected at the second surface. The brightness ratio between the two reflected interfering beams is 4%: 3.8%, close to 1. The result will be contrasts as seen in Fig. 2.5(a).

Any recording medium can become overexposed, resulting in such details being lost if their relief height is less than about 50% of the fringe equivalent. [Compare this to Figs. 3.7(a) and (c), where loss of detail in information is physical, not photometric.]

Figure 2.5(a) was generated for a perfect 90-deg prism in a Michelson two-beam interferometer that produces two beams of nearly equal brightness distribution. One can recognize the decreasing brightness from center to periphery. The interferometer's field shows a rectangular sample, the 90-deg angle prism with fringes alternating between less exposure brightness and more exposure brightness. This variation cannot possibly represent surface errors; in fact, it is related to the sensitivity of the recording medium and to the variable product $I \bullet time$, where I is the exposure.

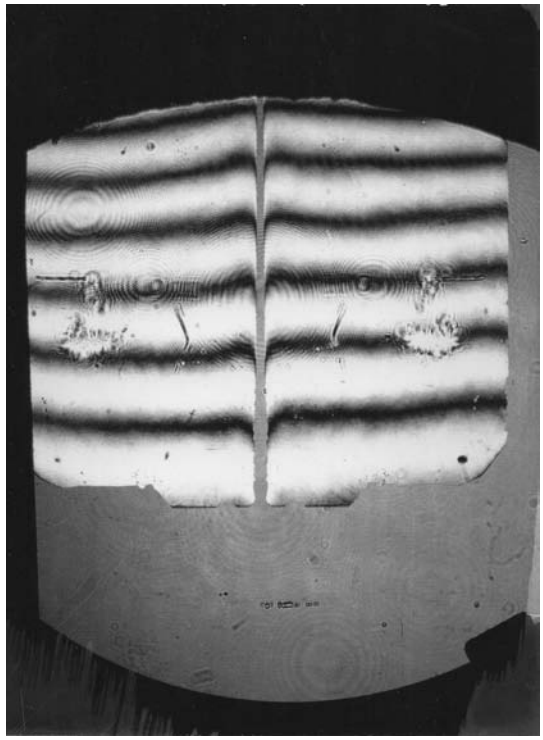

Figure 2.5(a) A 90-deg prism in a Michelson two-beam interferometer. The record shows near-perfect contrast in the central area, falling off toward the periphery. The spacing of dark fringes diminishes approximately 10%. The 90-deg angle as seen along the first two bright fringes is acceptable, as is the edge roll down. The fringes in the outer section indicate a mild curvature, which could be cylindrical (axis orthogonal to the prism's edge) and have some spherical contribution, plus an edge roll down on either one or on both facets of the prism.

Figure 2.5(b) Spurious coherent reflections and stray light deteriorate the fringe definition. [See the vector diagram uncertainty circle in Fig. 3.2(c).]

Figure 2.5(b) presents the multitude of possible errors on the sample that are still to be analyzed. The curvature of these fringes could also be due to lack of collimation. Chapter 5 will address these possibilities in a more quantitative manner. The 90-deg angle is not constant along the edge; are the fringes curved due to collimation error on one or both flanks of the prism, or on the entry surface of the prism? Is the minor edge roll off on one or both flanks? These questions will be addressed later in the book. The relevant reflectances are 85% at the reference mirror (aluminum coating on glass) and near 95% at the 90-deg prism due to internal total reflection (a nonpolarized light source).

A useful criterion for correct contrast of fringes is based on interference generation by addition of amplitudes and the resulting ratio of brightness generation by the square of summed amplitudes being closely approximated by

amplitude = 1, and brightness = 1, within an empty interferometer field;
amplitude = 1 – 1 = 0, and brightness = 0, within dark zones of the sample;
amplitude = 1 + 1 = 2, and brightness = 4, within bright zones of the sample.

2.5.1 Contrast of Fizeau fringes determined by reflectances

The interference setups for Figs. 1.2 and 1.5 used glass with nearly the same reflectances on both surfaces. Contrast, defined as $(I_{max} - I_{min}) / (I_{max} + I_{min})$, becomes 1. Substrates from metal or silicon need some higher-reflectance beamsplitting coating on the reference plate in order to produce well-recognized

contrasting fringes. With that beamsplitting coating we now turn to the common Fizeau or Tolansky interference setup, drawn schematically in Fig. 3.1. This setup differs from the Newton setup in that it allows a greater gap t and different reflectances.

As an experiment, we deposit different coatings onto the two glasses as follows: mirror M acquires a coating of a "homemade" chemical silver, known to have reflectance $R_1 = 0.6$.[5] This value is generally representative of many metals and of silicon. The front mirror T in Fig. 3.1 is coated with a beamsplitter, either after Tolansky or using a dielectric coating available at coating facilities. That coating is to be specified for a normal-incidence HeNe laser or another nonpolarizing light source with $R_0 = 0.2$ and transmittance $T_0 = 0.7$. For any layer, there is also some absorption A. The sum of $A + R + T$ must be 1. This leaves $A = 0.1$, which is nearly negligible for experimental purposes.

Looking at the coherent amplitude addition, one must consider that $t_0 = \sqrt{T_0}$ can be the same in both directions; $r_1 = \sqrt{R_1}$ refers to target mirror M; and $\rho = \sqrt{R}$. R and T are easy-to-measure quantities. The intensity-related values of reflectance and transmittance are also found in physical tables. Here we chose $R_1 = 0.2$, $R_2 = 0.6$, and $T = 0.7$.

The amplitudes E_0 and E_1 of the two beams are governed by $r_1 \cdot t'$ and r_2 as follows:

$$E_0(r_0) = r_0^2 = R_0 = 0.2, \text{ and } r_0 = 0.44;$$
$$T = 0.7, \text{ and } t = 0.83;$$
$$E_1 = t'\ r_1\ t';$$
$$R_1 = 0.6, \text{ and } r_1 = 0.77; \text{ and}$$
$$E_1 = 0.54.$$

With these amplitudes, the vectorial addition uses $E_0 = 0.44$ and $E_1 = 0.54$. For constructive interference, $E_1 + E_0 = 0.98$, and for destructive interference, $E_1 - E_0 = 0.1$. Two-beam modulation with a contrast of $(0.96 - 0.01) / (0.96 + 0.01) = 0.98$ is highly detectable. It is remarkable that this is nearly the same contrast (not brightness) as had been seen with bare glasses.

There will be residual, repeated reflections in the cavity; however, these reflections will be much weaker, as shown in Figs. 3.2(a) and (b). The third beam, E_2 in the same figures, is characterized by $t' \cdot r_1 \cdot t' \cdot r_2 \cdot r_1 \cdot t' = 0.19$ and intensity 0.04. E_2 will barely influence the course of interference in the first two beams. In short, the amplitudes of successive beams decrease rapidly.

The number of contributing back-and-forward reflections can be controlled (to some degree by coatings) to vary between near negligible (as in two-beam-like Fizeau interference) and many reflections (as in the multiple-beam Fizeau case). In the Fabry–Pérot case, the wedge angle is 0. The vector

addition can be presented graphically, using the subsequent qualitative vector representation in polar coordinates.

2.6 Notes on Recording Fringes

The values of R and T can be selected for dominant function of the first two beams or for multiple successive interfering beams. The recorded brightness distribution depends on the sensitivity, a characteristic of the recording medium. With outdated photographic media, the nonlinearity of the γ curve demanded much care for proper exposure. CCD devices are less demanding and have extended the range of linear sensitivity, but overexposure can occur with them as well. HeNe lasers used for optical shop testing usually involve wasting light by filters or by polarization arrangements.

CCD cameras are so inexpensive today that both the image and the focal plane of an instrument have their own camera. Image brightness admitted to each camera must be quite different for focal plane observation and for (simultaneous) image plane observation, as illustrated in Fig. 4.1(b).

The distribution of contrast and, therefore, the detected pattern of fringes can grossly and misleadingly be altered by superimposed, coherent, residual reflections (e.g., at surfaces that are not antireflection coated) and by artifacts from outside of the interference cavity. The seasoned observer might subjectively remove the artifacts in his mind; objectively, artifacts that do not originate in the interference cavity itself are not considered in automatic electronic phase-shifting evaluation.

The uncertainty of fringe positions and, therefore, of topographic information due to coherent artifacts, from wherever they might originate, are represented in summary by an uncertainty circle in the vector diagram shown in Fig. 3.2(c). For the interference fringe localization, this is equivalent to $\Delta P/P$, limiting the system's accuracy. The quantitative value of such uncertainty can be assessed by a series of repetitive measurements of the same sample, using different fringe settings. Values of 0.05 are not unusual. Any artifact from within the cavity will migrate with the fringes as a function of "pushing."

Notes for the practitioner

1. An optimized choice of reflectance and, consequently, coatings is recognized by dark fringes that are darker than in the "empty" field and bright fringes that are substantially brighter than the environing empty field, as shown in Fig. 2.5(b). Upon minutely pushing either component, the artifact seen in Fig. 2.5(b) will either (1) grossly modify the fringe profile when located on one of the interference components or (2) have no influence on the fringe profile, being simply a useless obstruction.

2. The low-contrast, superimposed fringe undulation in Fig. 2.5(b) originates from inside the cavity and moves with the desired fringes when one component is moved. The artifact would remain stationary if it were on a lens surface.

References

1. Sill Optics, PB 1127, 90523 Wendelstein, Germany.
2. H. Teller Trading Agency, Drachendorf, 07551 Jena, Germany: Borofloat glass, selected sections, water-beam cuts.
3. Cargille-Sacher Laboratories Inc., Cedar Grove, NJ 07009 USA: Cargille™ immersion oils and refractive index fluids.
4. Purbone: Trade-name of a porous graphite material: Shanghai Gongtao Ceramics Co, Ltd., Shanghai, China.
5. Peacock Laboratories, Inc., 1901 S. 54th St. Philadelphia, PA 19143, USA: silver spray chemical solutions.

Chapter 3
Interference Visualized by Vector Diagrams

3.1 Vectorial Representation of Dual- and Multiple-Beam Interference

Analysis of the optical interaction in two- and multiple-beam Fizeau interferometers can be presented graphically using a qualitative vector representation in polar coordinates. Consider the interferometer operated in reflection, shown in Fig. 3.1, which provides the geometrical and physical constants of the interferometer.

Perfectly flat surfaces and a perfectly plane wavefront entering the interferometer are assumed. A series of multiply reflected wavefronts is obtained from this interferometer in the usual manner. Let these wavefronts be represented by vectors $\mathbf{E}_0$, $\mathbf{E}_1$, $\mathbf{E}_2$,...$\mathbf{E}_n$. Vector $\mathbf{E}_0$ refers to the wave reflected at the transmission surface. Vectors $\mathbf{E}_1$ and $\mathbf{E}_2$ represent the waves reflected by the interferometer cavity. With vector $\mathbf{E}_0$ and $\Sigma_n \mathbf{E}_n$, one observes reflection fringes; with $\Sigma_n \mathbf{E}_n$ alone, one observes transmission-like fringes. Both sets of fringes are topographically equivalent and differ only in contrast.

Using the notation from Fig. 3.1, the first two vectors are

$$\begin{aligned} \mathbf{E}_1 &= t^2 \rho \exp\{[i(2ß + \psi) + \varphi]\}, \\ \mathbf{E}_2 &= t^2 \rho(\rho r) \exp\{[i(2ß + \psi) + (\psi + \alpha) + 2\varphi]\}, \end{aligned} \tag{3.1}$$

where i is the distance between mirror M and the transmission flat at the narrowest position, and φ is the phase change due to a single pass inside the interferometer cavity:

$$\varphi = \frac{4\pi t}{\lambda}. \tag{3.2}$$

Vectors $\mathbf{E}_1$ and $\mathbf{E}_2$ establish a two-beam Fizeau interferogram of low contrast; the interferogram will be modified by the subsequent waves. All

topographic information about the combined two interferometer surfaces is already contained in the two-beam interferogram. Figure 3.2(a) is a vector diagram showing $\mathbf{E}_1$ and $\mathbf{E}_2$. Due to a reflection at the two mirror surfaces, the phase $\psi + \alpha$ is, in most practical cases, $\psi + \alpha = 2\pi$. The phase $2ß + \psi$ represents a constant rotation and, therefore, is not shown in the diagram. Note that phase φ is the only variable related to the zero phase of the incoming beam. A complete 2π cycle of φ is equivalent to passing one order of interference (moving from one fringe to the next in the interferogram).

Because vector $\mathbf{E}_1$ describes a phase φ, vector $\mathbf{E}_2$ rotates through 2φ, as is indicated in Fig. 3.2(a). When the resultant of $\mathbf{E}_1$ and $\mathbf{E}_2$ is plotted versus φ in polar coordinates, the graph in Fig. 3.2(b) is obtained. The amplitudes in the diagram are normalized by $t^2\rho = 1$; thus, $\mathbf{E}_1 = 1$. For constructing the qualitative diagrams, a value of $\rho r = 0.85$ is assumed.

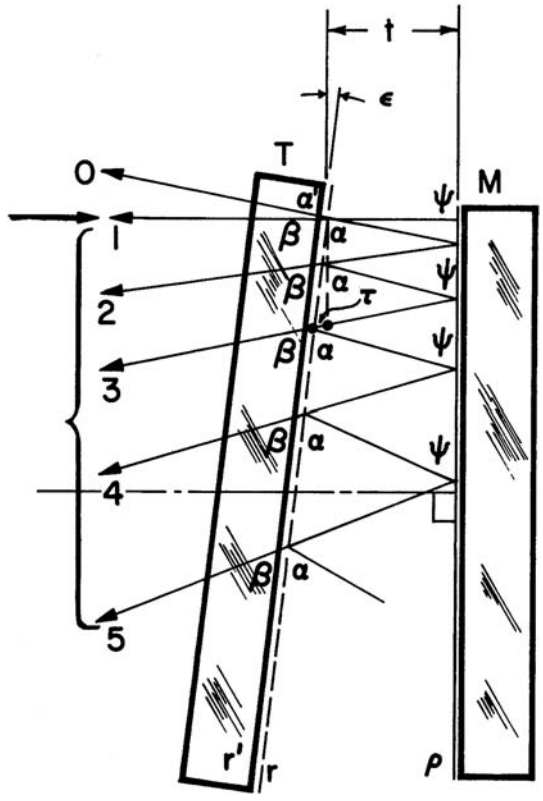

Figure 3.1 Fizeau multiple-beam interferometer. Reflectivity of M is ρ, of T on the air side is r, and on the glass side is r'. Phase change in reflection at M is ψ, at T on the air side is α, on the glass side is α', and in transmission is β.

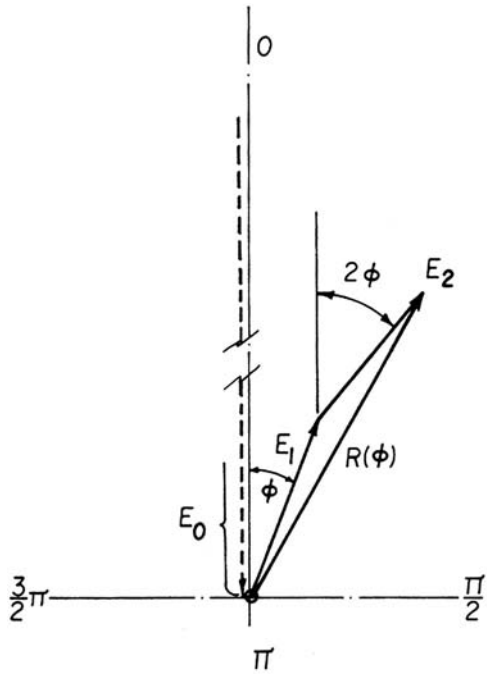

Figure 3.2(a) Vector diagram representing the first two vectors $\mathbf{E}_1$ and $\mathbf{E}_2$ from a multiple-beam series. The lengths are proportional to the amplitude. As $\mathbf{E}_1$ rotates by φ, $\mathbf{E}_2$ will rotate by 2φ.

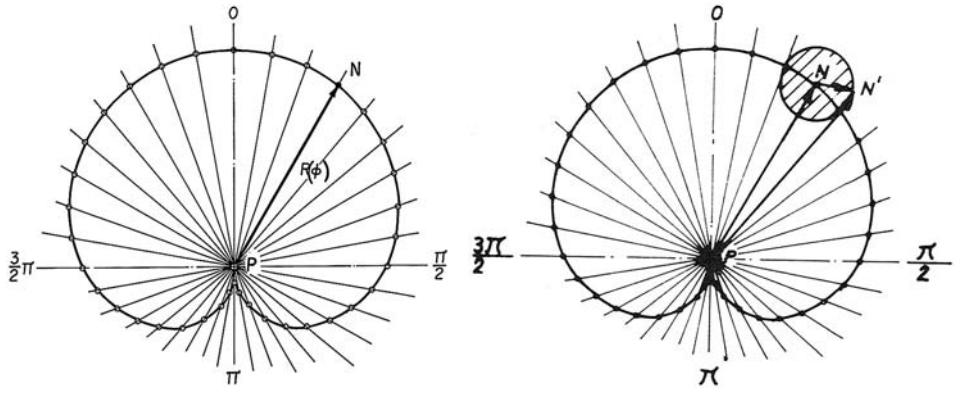

Figure 3.2(b) (left) Amplitudes $\mathbf{E}_1$ and $\mathbf{E}_2$ plotted in a polar diagram. (right) Stray light and spurious reflections off of uncoated surfaces contribute small vectors that can be represented by an uncertainty circle.

3.2 The Airy Case: Zero Wedge Angle

The addition of the subsequent vectors to the first two is shown in the vector diagram of Fig. 3.3(a). Each vector spins around one more time than its respective predecessor and n times as often as the first vector $\mathbf{E}_1$.

The phase law is therefore $\pi n = n\varphi$ (the Airy case). Only in the immediate neighborhood of 0 (or 2π) is the relative phase φ small enough that the individual vectors add up in more or less the same direction. In the zero direction, the amplitudes add up in a line to form a geometric progression and make up a maximum resultant. In the opposite direction π, the geometric progression becomes an alternating one, leading to a minimum resultant. In the neighborhood of π, the vectors as functions of φ rotate so fast that, at almost any angle, the individual vectors tend to partially cancel each other. Figure 3.3(b) shows the resultant in polar coordinates for 2, 4, 6, and 14 beams. An increasingly sharper peak develops atop the location of the initial maximum as more vectors make up the sum. The high peak of the curve represents bright fringes on a dark ground (transmission-like fringes). Only a few vectors have been drawn for this qualitative representation; however, as more and more vectors are added, the dashed curve in Fig. 3.3(b) will result. The closer the product $r\rho$ approaches unity, the narrower this curve will become. This fact is illustrated by the dependence of the sharpness of multiple-beam interference fringes on the reflectance of the two mirrors in the interferometer.

3.3 The Fizeau Case

In practical Fizeau interferometry, the phase law $\varphi_n = n\varphi$ is often only a sufficiently good approximation of the real phase law. After Tolansky[1] (and Brossel cited therein), the real phase law is more precisely approximated by

$$\varphi_n = \left(\frac{2\pi}{\lambda}\right) tn \cos\theta \left[1 - n\varepsilon \tan\theta - \left(\frac{2n^2+1}{3}\right)\varepsilon^2\right], \tag{3.3}$$

where θ is the angle of incidence of the incoming beam to the rear mirror, and ε is the angle between M and T (see Fig. 3.1) . The phase law reduces to a still simpler form if θ is zero:

$$\varphi_n = \left(\frac{2\pi}{\lambda}\right) tn - \left(\frac{2\pi}{\lambda}\right) t\left[\left(\frac{2}{3}\right) n^2\varepsilon^2\right] = n - \varphi - \tau_n. \tag{3.4}$$

Equation (3.4) does not immediately show the influence of the phase-defect factor $(2\pi/\lambda)tn$ because this influence is relatively small compared to the value of $(2\pi/\lambda)tn$. The effect of the phase-defect factor, however, *is* evidenced when considering the periodicity of $(2\pi/\lambda)tn$. The n^{th} vector

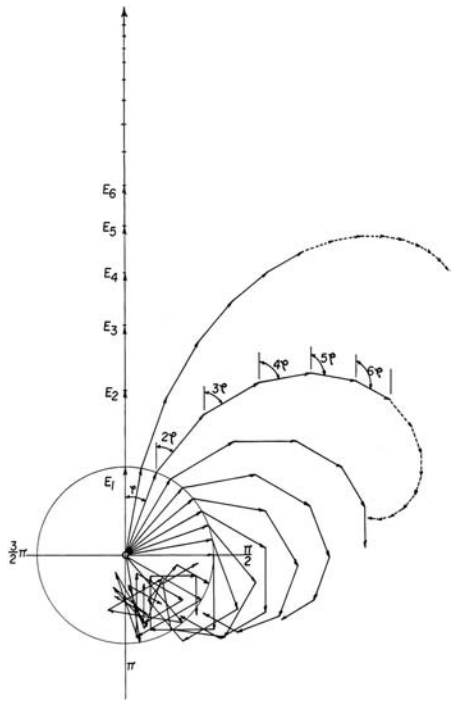

Figure 3.3(a) Airy distribution displayed in a vector diagram representing the first six vectors from a multiple-beam series. As the first vector $\mathbf{E}_1$ has a phase φ, the n^{th} vector has a phase $n\varphi$.

spins around n times, while φ describes only one cycle. The vector sum is not affected by the number of cycles the vector $\mathbf{E}_n$ has already completed; rather, it is affected by the surplus angle over the last completed cycle. Therefore, the phase-defect factor must be considered in competition with 2π, whereby it gains tremendously in weight. The n^{th} vector might be shifted to be completely out of phase with its position, as determined by the Airy case.

For any given geometrical dimension, the more important the contribution of the n^{th} vector is to the vector sum, the more evident the effect will be (that is, in the case of high reflectance on both mirrors). In order to demonstrate this qualitatively in a diagram similar to Fig. 3.3(b), fictive dimensions have been chosen so that fewer vectors need to be drawn. Such a diagram shows the principle but does not impede the generality. The influence of the phase defect will be more clearly seen in the near neighborhood of zero (or 2π) than in the neighborhood of π. This is because, in the neighborhood of π, the vectors have already completed so many cycles that the average value of the vector sum is not further influenced by individual vectors [Fig. 3.3(a)]. The vector diagram in

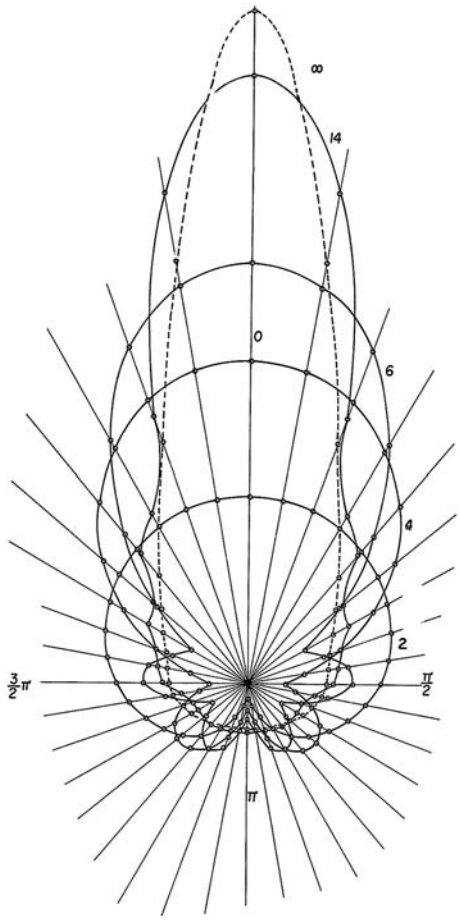

Figure 3.3(b) Resultant of the first 2, 4, 6, and 14 vectors represented in polar coordinates. The curve, obtained by an infinite number of vectors, takes on approximately the shape shown in the dashed line (the Airy case).

Fig. 3.5(a) is composed like that in Fig. 3.3(a), using the first six vectors; however, in this case the following equation is used as the phase law:

$$\varphi_n = n\varphi - \left(\frac{1}{3}\right)\left(\frac{\pi\lambda}{\rho^2}\right)n^3\tau_0. \tag{3.5}$$

3.4 The Function of the Zeroth-Order Beam E_0

Curves such as those in Figs. 3.2(b) and 3.3(b) are shown without the participation of vector $\mathbf{E}_0$, representing the reflection on the glass/air interface of the front mirror (or better, reference mirror) carrying the beamsplitter coating. The beam represented by $\mathbf{E}_0$ is not separable and is an essential part

of the interferometer. Its constant phase usually equals or nears zero, and its amplitude is greater than the sum $\Sigma\mathbf{E}_n$, due to the small absorption in the beamsplitter and mirror coatings. In the interferogram, $\mathbf{E}_0$ has two effects: (1) reversal of contrast (bright fringes on dark ground become dark on bright ground) and (2) the fringe contour becomes further slimmed.

Experimental evidence using this setup is given in Fig. 3.4(a). Figure 3.4 (b) was produced by combining the multiple-beam interferometer (based on Fig. 3.1) with a Michelson two-beam configuration. Mirror M_2 can be aligned to produce two-beam interference with the front mirror T of the multiple-beam interferometer. This mirror was partially covered by two screens, thus presenting the interferometer combination in the central section of the image in Fig. 3.4(b); whereas, the pure reflection interferogram ($\mathbf{E}_0 + \Sigma\mathbf{E}_n$) is seen on both sides. Contrast reversal and fringe sharpening become evident; where

$$\varepsilon = \frac{\lambda}{2P}, \lambda = 6.3 \times 10^{-5}\text{cm}, \; P = 0.1\,\text{cm}, \text{ and } t_0 = 2\,\text{cm},$$

$$\varphi_n = n\varphi - 0.031n^3. \tag{3.6}$$

Superposition as in Fig. 3.4(a) renders additional fringe sharpening and contrast reversal. A minute juxtaposition of the Fizeau fringe centers is related to the longitudinal position of mirror M_2 or some deviation of its surface from flatness. (Air turbulence might interfere as well.) Both 1 and 3 jointly determine the reference for the Fizeau part 2. In the center of Fig. 3.4(b), one recognizes significant enhancement of finesse and contrast reversal.

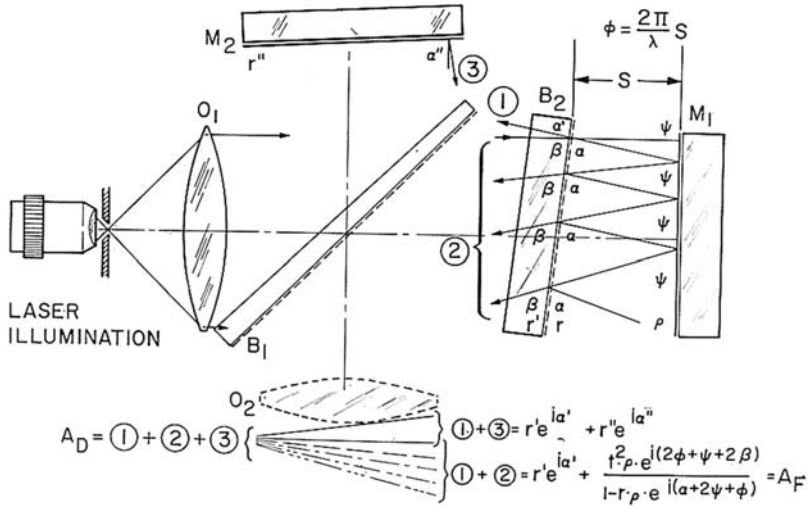

Figure 3.4(a) The multiple-beam interferometer (Fig. 3.1.) combined with a Michelson two-beam configuration demonstrates the addition of vector 3 in phase with 1. [See corresponding vector diagram in Fig. 3.4(c).]

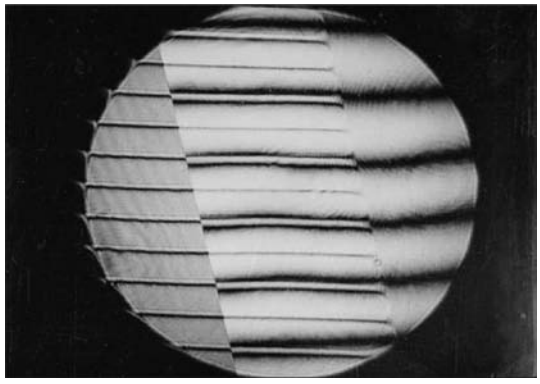

Figure 3.4(b) Vector addition of the Fizeau and Michelson configurations demonstrates the role of the zeroth order: 1; left sector: 1 and 2; right sector: 1 and 3; center: 1, 2, and 3.

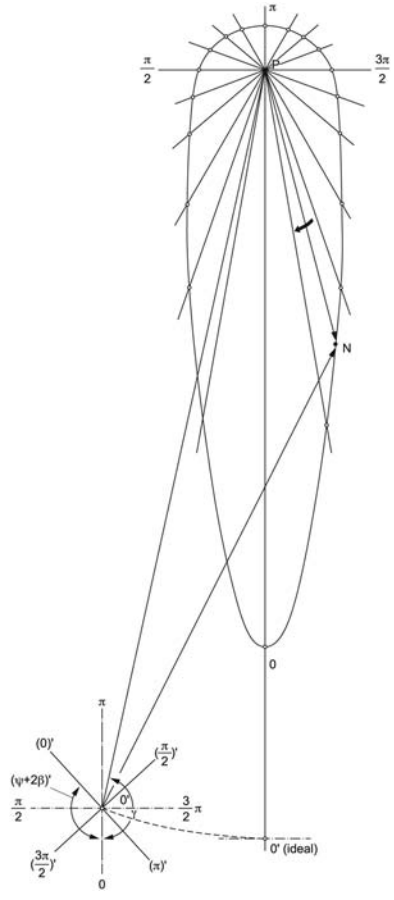

Figure 3.4(c) Vector diagram describing a path across the center of Fig. 3.4(b), parallel to the field stops. The diagram demonstrates the effect of phase and amplitude of the zeroth-order Fizeau beam added to the multiple-reflection Fizeau sum shown in Fig. 3.3(b): contrast reversal (no technical use known) and fringe sharpening (improved finesse). A local juxtaposition of a reflection Fizeau fringe can be effected by any coherent reflex external to the B_2/M_2 cavity, e.g., a retroreflection off of the well-aligned pinhole stop or a lens surface that is not antireflection coated.

Parameters of a fictive interferometer were chosen to compose the vector diagrams with a few vectors but still be representative. These parameters, provided in Fig. 3.2(a), are grossly exaggerated in order to demonstrate with only a few vectors the tendency of the wedge interference to slightly shift the amplitude's maximum away from the position of the maximum, with only two beams contributing. The phase defect increases with the increasing distance of the Fizeau mirrors—a convenience made possible by a single-frequency, single-mode laser.

Comparing Fig. 3.5(a) to Fig. 3.3(a), one recognizes the general influence of the phase defect on the phase relation between vectors. The higher the order n of reflection, the more evident becomes a retrorotation of the higher-order vectors. This retrorotation causes some marked modulation of the vector sum, building up on the side of increasing phases, as shown in Fig. 3.5(b). One also learns from Fig. 3.5(b) that the maximum resultant in the Fizeau case is shorter, broader, and shifted compared to the Airy case shown in Fig. 3.3(b). The curve for six beams in Fig. 3.3(b) is repeated in Fig. 3.5(b) (see the thin line).

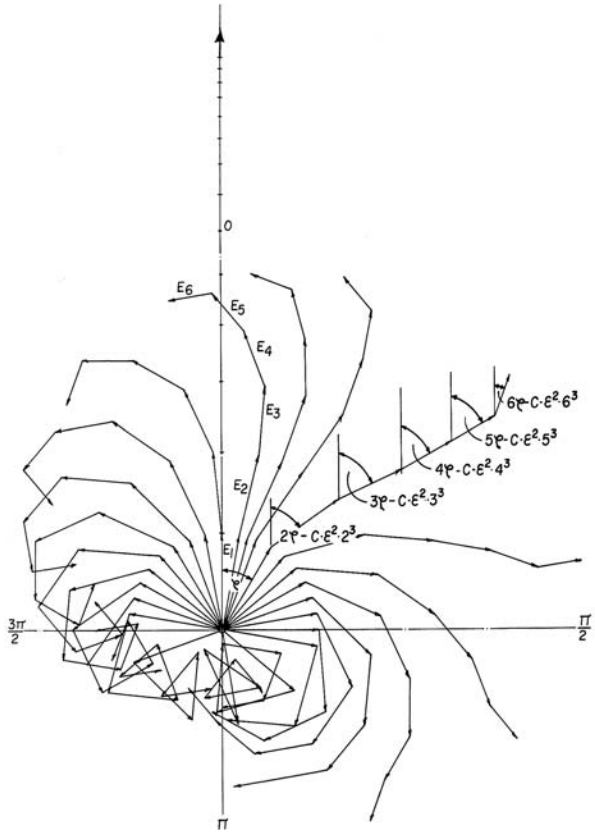

Figure 3.5(a) Vector diagram representing the first six vectors in a Fizeau distribution and showing the influence of the accumulating phase defect.

The diagram in Fig. 3.3(b) represents the sum of vectors, building up a peak at zero and a broad minimum around π. Many more vectors will produce the dashed curve—the Airy distribution [Fig. 3.3(b)]. These curves, after squaring the amplitudes, represent bright fringes on a dark ground [transmission fringes, as in Fig. 3.4(b)]. Given a minute transmission on the rear surface, one will see these bright fringes on a dark ground. The vector $\mathbf{E}_0$, representing reflection at the first surface, is not yet part of the diagram. Only after addition of $\mathbf{E}_0$, starting on the π line (due to phase jump), will the diagrams show the customary dark fringes on a bright ground (reflection fringes).

Experimental evidence was obtained by artificial addition of vector $\mathbf{E}_0$ in an interference setup based on Fig. 3.4(a). The interference is represented by the consecutive beams in series 1; the 2 series is shown in Fig. 3.4(a) in the two outer segmented areas. The two segments are obtained by inserting two

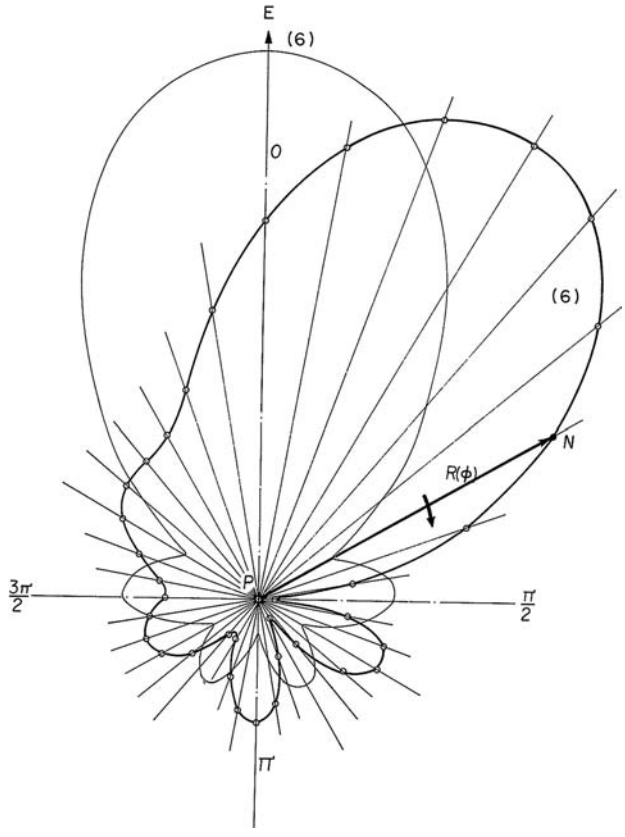

Figure 3.5(b) Resultant of the first six vectors shown in Fig. 3.5(a) in polar coordinates. The diagram shows the generation of side bands and the decrease and shift of maximum amplitude as a function of phase defect. An illustrative example of this is in Fig. 4.4(c).

screens, partially covering mirror M_2. M_2 was adjusted to reflect beam 3 onto the interference field such that both contrast reversal and enhancement of finesse could be demonstrated.

A small phase change $\Delta\varphi$ is followed by quite different changes in the vectorial summation. Phase φ may change substantially without appreciable influence on the sum around π, hence, also without change in image brightness. Conversely, the summed amplitude reacts very sensitively on both sides of 0 (with respect to 2π) to such changes of φ on the sample, as well as to the additional phase defect caused by beam walkoff, shown schematically in Fig. 10.3(b). This effect can become a substantial source of misinterpretation in large-cavity configurations (e.g., corner-cube testing). Countermeasure off-axis illumination is described in Section 5.2.2.2.

3.5 Advantages and Disadvantages of Using Multiple-Beam Interferometry

The obvious advantage of Fizeau multiple-beam techniques is that they are economical, making the Fizeau the most frequently used instrument for macroscopic metrology of reflecting surfaces (including all applications presented in this book). For microscopic applications, the author prefers the multiple-beam Tolansky method.[1]

Large-scale production of ultraprecise cubes and corner-cube prisms has brought about the need for fast measurement of surface flatness, 90-deg angles, and error separation of surface and angle, as well as the influences of the material's interaction with its homogeneity. Production of polygon mirror wheels by micromachining on air-bearing fixtures prompted another need for precise, angular measurement on surfaces that often are too small to derive their angular position by fringe spacing measurement.

3.6 An Application: Evaluating the Task of Nulling

Measuring the uniform dark tint (also called the null field) in multiple-beam interferometry is a sensitive method for detecting both sub-$\lambda/10$ surface departures from flatness and minute angular displacement between two flat surfaces.[1] We will assume an absence of the first and consider only the angular sensitivity. As the sample size decreases, the angular sensitivity also decreases. This desirable null-field metrology feature requires higher reflectances, beamsplitting (vacuum coating, with constant thickness tacitly assumed), and an easily removable metal coating on glass samples undergoing repeated corrective polishing (Strong[2] and Tolansky[1]).

The accuracy of null-angle alignment (pointing) can be increased by incorporating calibration microsteps in the reference flat. These steps can be in relief or elevated with an approximately 25-nm height difference for each

step. The final coating includes either a beamsplitting layer (microsteps in relief) or a reflection coating (microsteps elevated). The chosen microsteps were approximately λ/20 high and of concentric geometry [Fig. 3.6(b)]. The stepped surface provides at least one part of the total surface and satisfies the uniform-dark-tint condition, while each next-order dark fringe is outside of the sample diameter. A setting accuracy of 0.01 arcsec was achieved[1] using small-diameter optics. The actual width of the momentary dark fringe will still be unknown, but zero is approximated more closely than in other methods.

Although photoelectric means could improve upon this accuracy, for production convenience, visual methods were preferred by the author. One typical application of this kind of pointing interferometry occurs with the micromachining of polygon mirrors.

Figure 3.6(a) is a schematic representation of the brightness profile across two fringes between the two near-parallel-reflection Fizeau interferometer mirrors. Angular information is lost as soon as the fringe spacing exceeds the sample diameter (meaning that parallelism is improving). The probability of obtaining the wide, bright area between two dark fringes is much higher than the probability of adjusting both the distance and the angle between the two surfaces such that the most-sensitive dark tint is obtained. The latter case is desired because the uniformity of a dark tint is easier to determine with higher accuracy than the uniformity of a bright tint. Knowing from an *a priori* measurement the ratio of the dark-fringe width to the fringe spacing P and the finesse $F = W/P$ in Fig. 3.6(a), one can estimate the fringe spacing from the width of the uniform dark field and, thus, the angle between the surfaces. In order to achieve the dark-tint condition, one might need to move the surface longitudinally as well, adjusting t. Technically, this is time consuming and impractical because of the small size of the required displacement (~λ/20).

A stepped mirror surface, such as the one reproduced on top of the experimental sequence shown in Fig. 3.7(a), provides at least one area that will meet the uniform-dark-tint condition when the interferometer mirrors are parallel. The steps, each of λ/20 height, are arranged in a symmetrical fashion.

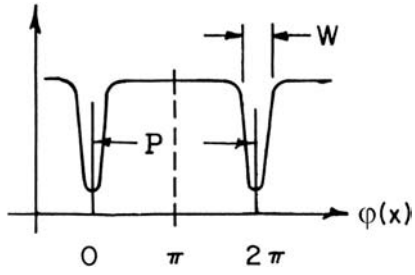

Figure 3.6(a) Brightness profile of the reflection Fizeau interference between two flat mirrors T and M.

The dark fringe on a flat mirror will be at least as wide as the outer diameter of one of the uniformly dark rings.

3.6.1 An artifact for nulling (autocollimation) and scanning

A sample test surface was approximated for the design in Fig. 3.6(b). Some of the recorded interferograms are shown in Figs. 3.7(a)–(c). Figure 3.7(a) is a reflection Fizeau interferogram of that test surface and represents the three annuli, piled on top each other. The test surface was used as the rear mirror of a Fizeau reflection interferometer, and the distance between the mirrors was on the order of 1 cm. A HeNe laser was used for illumination.

From Fig. 3.7(b), we see some lack of the intended parallelism between the two surfaces T and M, the angle being determined by the fringe spacing to be $\alpha = \lambda/2P$. If the mirror diameters were smaller than the

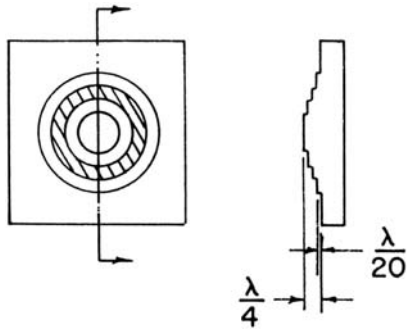

Figure 3.6(b) Artificial topography of a flat mirror. Annular structure is achieved by vacuum coating antireflection material and overcoating the complete sample with a beamsplitting layer for use in a multiple-beam Fizeau interferometer. Note: diamond turning the complete mirror to achieve the annular structure is the ideal production method for this and for relief profiles.

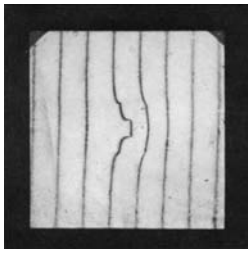

Figure 3.7(a) Reflection Fizeau interferogram with a stepped test surface (reference mirror of a Fizeau interferometer, 5-cm diameter). This calibrates the ratio of the dark fringe width to the spacing (a ratio known as finesse).

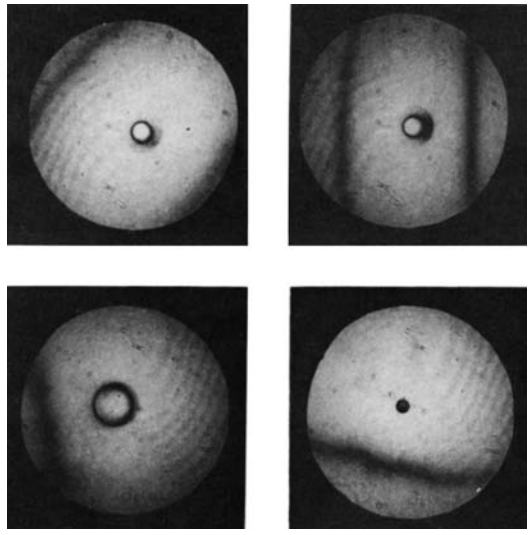

Figure 3.7(b) Reflection Fizeau interferograms showing poor parallel alignment between the stepped test surface and the transmission mirror. The departure from parallelism is identified by the existence of a fringe. On a smaller surface, this fringe cannot be seen at all, while asymmetry of the ring is still detected.

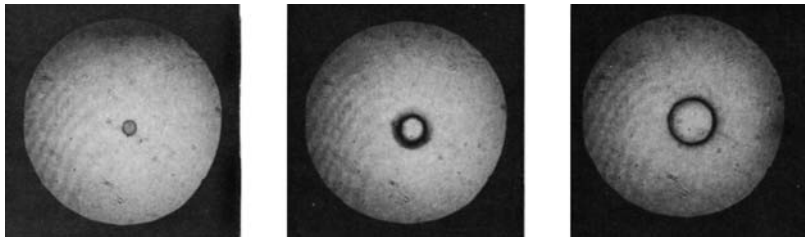

Figure 3.7(c) Reflection Fizeau interferograms showing $<$ 0.05-arcsec parallel alignment between the stepped test surface and the transmission mirror. Parallelism is indicated by the uniformity of one of the three circular steps.

fringe spacing and the surface had no relief, this angle could not be detected by any practical interferometric means. However, when relief is present, the asymmetry of the dark zone indicates that the mirrors are not parallel.

Opposed to these misalignments are some nearly perfect alignments, shown in Fig. 3.7(c). The differences between the interferograms shown in Fig. 3.7(b) result from the varying distances between the two mirrors. The lack of parallelism, i.e., the angle between the mirrors, can be estimated from the second of the three interferograms in Fig. 3.7(c). First, one determines

from Fig. 3.7(a) that $F = 1/15$; the width of the dark fringe is as wide as or even wider than the dark-ring diameter $d = 2.25$ cm. Hence,

$$\alpha \sim \frac{\lambda}{2 \cdot 15 \cdot d} = 6.3 \cdot 10^{-5}/67.5\,\text{rad}, \tag{3.7}$$

$$\alpha \sim 0.02\,\text{arcsec}.$$

If d were only 1 cm, then $\Delta\alpha$ would be 0.04 arcsec. This accuracy could never be achieved with the simple uniform-tint method, unless an extremely sensitive longitudinal adjustment of one mirror is made that would position the two surfaces for a uniform dark tint in the entire field.

The conclusions drawn from this experiment are as follows:

- The stepped-mirror artifact is a useful accessory in interference autocollimation for angular nulling with respect to pointing measurements.
- The stepped-mirror artifact is a useful accessory for detecting/measuring longitudinal distance changes on the order of 0.01 fringe upon lateral scanning.
- The question "Why should one use the multiple-beam Fizeau technique for surface testing at all?" is raised. The information lost between the dark sharp fringes can be recovered only by longitudinal scanning, in that case, however, with 10–100× better fringe resolution. The hardware of a Fizeau-type interferometer is both substantially less expensive than that of two-beam instrumentation and much more convenient to use. (A quasi two-beam profile on the fringes is obtained through the choice of Fizeau beamsplitter.)
- Interferometric angular setting, i.e., parallelism between M and T, is not possible with fringe spacing exceeding the diameter of the optical components, unless the sensitive dark field and its uniformity are adjusted. In the present experiment, this has a 1 in 15 chance of occurring, if the dark/bright ratio (the finesse) is 15. That alignment requires substantial patience of the operator or expensive control equipment. The chances of finding the null angle without the annular artifact on the mirror, independent of very minute changes of distance t, are enhanced with such an artificial profile.
- The stepped reference mirror found a very practical application in the testing of air-bearing spindles. The absence of axial and angular error motions can be expediently verified down to 10 nm with the stepped reference mirror adjustably mounted on its axis and using an interference autocollimator. In a similar fashion, the reference mirror may be spherical (Fig. 1.4) for testing radial error motions of a spherical zone of aluminum that has been diamond turned on the spindle. Because of the pumping annular interference pattern in the case of error motions, this test was named "the blinking bull's-eye test."

Notes for the practitioner

1. Diamond turning is a good inexpensive method for producing a metal mirror (copper or aluminum) with three or more annular steps, with increasing depths of the profile.
2. A typical application of this profiled mirror is the measurement of nutational error motions and of differential axial lifts of an air-bearing spindle rotor (or rotary table). (See Section 7.1 on centration.)

3.7 Other Forms of Pointing Interferometry with Respect to Nulling

Kollmorgen Corp.[3] designed and distributed an attachment to their classic autocollimator using white-light interference obtained by the Köster beamsplitting prism. The Köster prism is the key component in length-measuring comparator interferometry [Fig. 3.8(a)]. In the case of perfect autocollimation, the white-light interference pattern with a centrally located dark fringe [almost identical to that in Fig. 1.7(a)] is obtained with the exiting beam reflected at a flat mirror positioned at a deliberate distance. The dark fringe in the center reproduces a zero null setting with 0.02-arcsec accuracy.

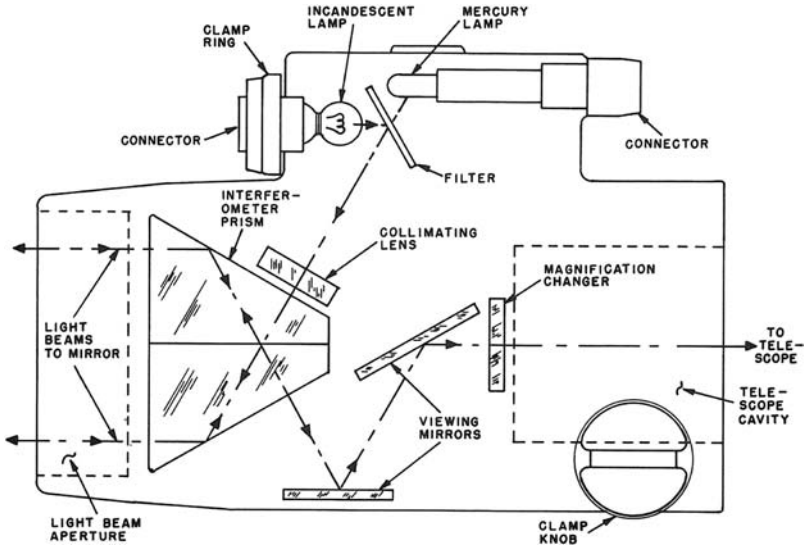

Figure 3.8(a) The Köster pointing interferometer defining the perfect line of symmetry: white-light interference fringes are obtained from a flat mirror, reflecting the two partial beams back into the prism. The null field (dark) occurs only upon reflection on axis. (Reprinted from the Kollmorgen Corp. user's manual.)

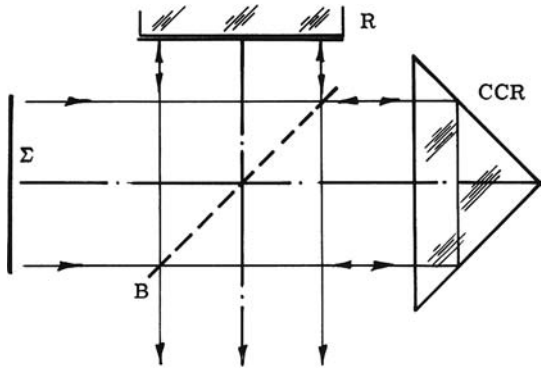

Figure 3.8(b) Front surface of a coated CCR beamsplitter autocollimating interferometer that acts as a shearing inverting interferometer. This is a useful metrology device in cases where the front surface of the CCR is perfectly orthogonal to the spatial diagonal of the equally perfect CCR. Details are provided in Sections 5.2.1.7 and 5.2.2.2.

Less sensitive to air turbulence (which is inevitable around air bearings) is an inverting shear autocollimating interference reflector for pointing, developed in the author's laboratory[4] and shown in Fig. 3.8(b). A description of the use of this device and its interferograms will follow the discussion of corner-cube retroreflectors (CCRs) in Section 5.2.

3.8 Fizeau Interferometers with Large Cavities

Discussion of the beneficial and detrimental features of Fizeau multiple-beam interferometry requires awareness of walkoff. The extreme coherence length of the laser enables simple and inexpensive interferometric test setups using Fizeau multiple-beam interference with the distance t between mirror M and mirror T being rather large. Summation of the errors collected by the back-and-forth reflection, which is wanted in the longitudinal direction, will be accompanied by lateral integration of errors, which are unwanted but unavoidable. This walkoff follows the path orthogonal to, and away from, the apex of the wedge of the interferometer cavity (Fig. 3.1).

Illuminating the interferometer slightly off axis, as in Figs. 10.3(a) and (b), allows one to experimentally find an angle that allows the beam to be first reflected toward the apex, to a point where the angle of incidence is zero, then returned away from the apex from there on. With the number of reflections being limited by the choice of reflectance for the beamsplitter coating, one may reduce the amplitude of successive beams and, thus, make the contribution of walkoff to the fringe profile (and to its actual location) less recognizable. Multipass interferometry will benefit from this type of alignment [see Figs. 5.22 (a)–(c)].

3.9 Stringent Requirements for Collimation

Collimation was introduced with projection of the secondary light source to infinity [Fig. 1.10(a)]. What do we know about quality of collimation—collimation being more than just illumination? The rudimentary method to test collimation is to walk along the beam, observing its diameter on a piece of paper and adjusting the distance of the light source to the collimation objective. This allows one to adjust the focal length (e.g., 700 mm) to some +/–5% of the nominal value, zero being somewhere between the two values. Refocusing the beam with a flat mirror onto the light-source plane (i.e., autocollimating) lets one adjust forward/backward about +/–1.5% by visually judging the dimension of the light source image, re-imaged onto the light-source plane.

Expanding a brilliant laser beam (from a HeNe single-mode, single-frequency laser) into a diameter of, for instance, 10 cm calls for a converging optical element. It suffices to use a single biconvex antireflection-coated lens with a short focal length, for instance, 4 mm. For a more practical do-it-yourself handling of a microscope objective, most lasers have a standard thread on their housing, the beam being centered therein.

The focal light distribution to be expected is governed by normal spherical aberrations. Figure 3.9(a) shows the caustic surface (the focal zone) obtained by a microlens or objective. The diverged beam, for all practical purposes, should fill a 1:7 to 1:10 cone. The brightness profile along the beam will have its central peak and, invariably, some closely surrounding cloudy irregularities as well.

A common practice for cleaning the beam involves insertion of a pinhole stop into the caustic (the focus). One navigates in the same manner in the XY plane for best brightness transmission and for rotary symmetry, then searches and optimizes along the optical axis Z. The travel range in X,Y,Z will be up to 2 mm, with 2-μm resolution and holding/clamping positions without backlash. The pinhole diameter should be large enough to transmit a practical amount of light and small enough to produce clean zeroth-order

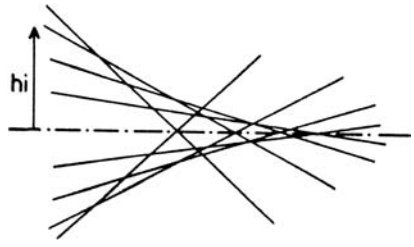

Figure 3.9(a) Micro-objective producing a focal zone [see also Fig. 3.9(b)]. Rays around the focal zone of a single lens will be stopped by a pinhole.

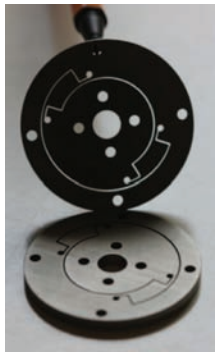

Figure 3.9(b) Homemade XYZ pinhole alignment fixture with fine Z motion by the sleeve gliding on a micro-optics housing with a differential thread.

diffraction: 5 μm and 10 μm is a good start. The brightness distribution beyond the pinhole should extend uniformly from the center to the first annular dark zone. The depth of the pinhole should be as small as possible. Its carrier metal foil can be obtained in a thickness of a few micrometers (mechanical shims). Commercial pinhole stops are available with diameters of 5–20 μm on a metal foil of approximately 8-mm diameter. At any laser institute, one will find help for shooting pinholes into the metal foil. The foil is best glued to a carrier ring for centration and later assembly.

One might find that the mechanical axis of the hardware does not coincide with the direction of the well-cleaned beam. Since the latter has priority, the instrumental hardware should be equipped with some means for nutating the complete diverging unit (thereby, not affecting the alignment between the laser, objective, and pinhole).

Navigating the pinhole stop within the focal zone is accomplished with commercially available XYZ micrometer tables. The author prefers a homemade unit, briefly described here and shown in Fig. 3.9(b): Two identical circular flexure disks that have been wire-discharge machined are stacked together at 90 deg, providing separate fine controls for X and Y. Each disk has fine push/pull screws for making adjustments. One flexure disk carries the pinhole foil, preferably precentered on an insert. The second disk is connected to a threaded sleeve, which is able to glide in the Z direction on the housing of a microscope objective.

Z adjustment is affected by a differential thread with a typical pitch difference of 0.2 mm. A threaded ring is permanently glued to the objective housing. The sleeve allows for fine Z motion. The Z sleeve is greased with high-viscosity grease (Lesonal™[5]). Once the coarse dimensions are established, one may provide some Z preload by an O-ring squeezed into the vacant annular distance between threaded parts. From thereon, happy navigation! A practical and low-cost aid to collimation setting is the shearing

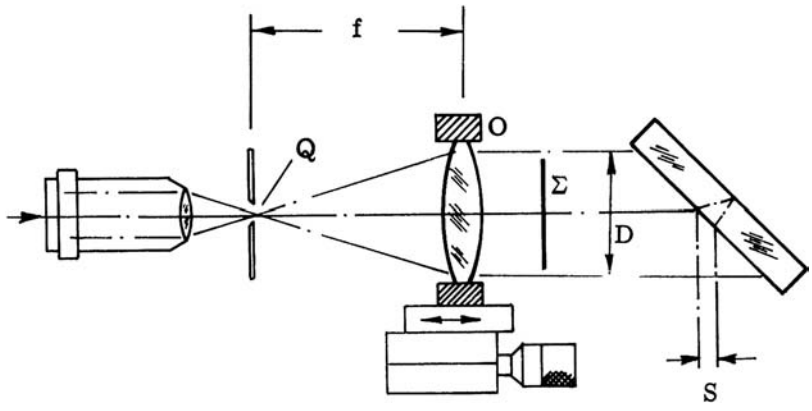

Figure 3.9(c) Setup for collimation and testing with Murty's shearing interferometer.

interferometer test after Murty [Fig. 3.9(c)], a detailed description of which is given in Section 4.3.

3.10 Acceptable Uniformity of Illumination

The smaller the quasi-point source, the more monotone will be the brightness distribution in the central light cone. There is no inexpensive way to avoid the normal Gaussian brightness falloff from the center to the first dark ring. Preferably, the diameter of the collimator's retainer coincides with the first dark diffraction ring. For a larger beam diameter and for the focal-length-to-diameter ratio (*F*/*d*) to be maintained on the order of (7 to 10):1, it might be necessary to Z fold the diverging beam.

Notes for the practitioner

1. Pinholes may be preliminarily improvised by pushing a needle into a stack of aluminum foils, clamped tightly between two flat metal flanges. One of the, perhaps, 30 foils will have the suitable pinhole diameter. One will observe the irregularity of the holes by the inhomogeneity of the transmitted brightness; however, this method suffices as a start.
2. A good clean beam was found in the reflection of a plain laser beam off of an aluminized spherical cap melted to the end of a glass rod [Fig. 3.9 (d)]. No well-polished surface of regular optics is as a smooth as the hardened cap of molten glass. There will be no "diffraction elephants" in the beam reflected by a molten, quasi-spherical glass cap. The technical price one must pay is the central obstruction in the field.

Figure 3.9(d) Molten-glass rod cap for diverging a plain laser beam.

References

1. S. Tolansky, *Multiple-Beam Interferometry of Surfaces and Films*, Clarendon Press, Oxford (1948).
2. J. Strong, *Procedures in Applied Optics*, Marcel Dekker, New York (1989).
3. Kollmorgen Corp., Electro-Optical Div., Northampton, MA 01060
4. P. Langenbeck, "Improving the accuracy of visual interferometric angle measurements," *Applied Optics* **8**(10), 2029–2029 (1969).
5. Trade-name Losoid by Losimol GmbH, Hannover, Germany.

Chapter 4
Optical Laboratory Equipment

4.1 Experimenting with Collimation: Autocollimation

Proper collimation by an objective is obtained as soon as the light leaving the secondary light source can be retroreflected through the pinhole into the source. Retroreflection by an adjustable flat mirror that is slightly off axis lets one observe and judge the size of the return focus on the pinhole stop. The size of the return focus is then minimized by adjusting Z, the distance between the pinhole and the objective. The principle of autocollimation is represented in Fig. 4.1(a). Note that this test cannot be performed using a CCR.

With the introduction of autocollimators, the pinhole stop [label c in Fig. 4.1(a)] is replaced by a reticle, which is more convenient for visual inspection of the coincidence of this reticle's image with another reticle. An initial test of any collimating unit includes holding a flat mirror against the objective's retainer ring in order to obtain a first impression of the angular position of the objective. There is no *a priori* assurance that the axial surface of the retainer for the collimating objective will be orthogonal to the optical axis of the objective, or that the cylinder axis will be parallel to the optical axis. The objective's axial Z position is controlled by a fine thread on its retainer. The orientation of the collimation objective with no identical curvatures on its outer surfaces should minimize diffraction angles; a plano-convex lens will have its planar side facing the light source. An achromat will be mounted with the side having larger curvature facing the light source.

For the applications described in this book, an autocollimator like the one shown in Fig. 4.1(b) comes close to the preferred setup. The source unit and the return beam observation unit are assembled separately and ruggedly affixed to the housing, thus allowing some later retrofitting to the returned beam observation unit without affecting the collimation, once the assembly is completed. The retroreflected beam will be viewed through a 50/50 beamsplitter. The latter can be a commercially available thin pellicle.[1] These expensive beamsplitters are sensitive to vibrations and attempts to clean off dust.

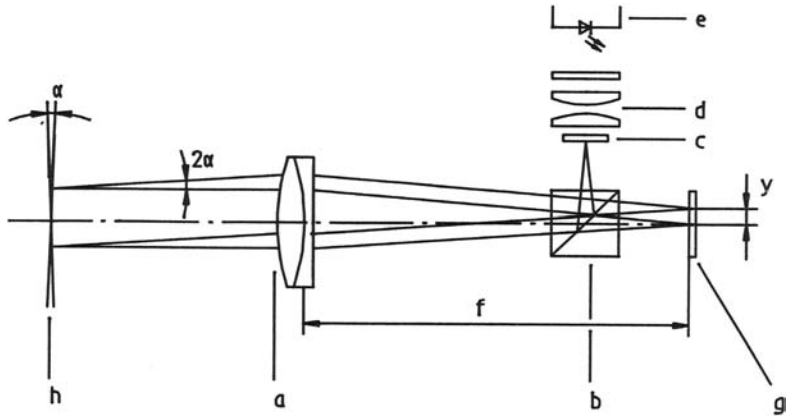

Figure 4.1(a) The principles of autocollimation. Labels a–g indicate the following parts: a is the collimating objective, an achromat or, a monochromatic plano-convex lens; b is the beamsplitter cube or a thin glass membrane with 50/50 beamsplitting and antireflection coating; c is a reticle; d is the condenser unit; e is an LED; f is the focal length of a; and g is a CCD matrix.

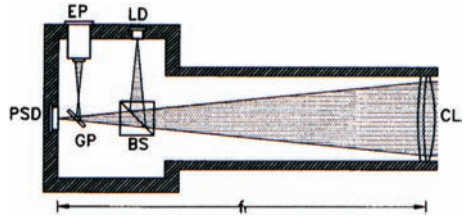

Figure 4.1(b) Schematic representation of the components of an autocollimator with a CCD camera for separate observation of the image plane and of the position-sensitive detector (PSD) for the return focus.[3] LD is the location of either a laser diode or of the light-source unit; EP is the eyepiece; BS is the beamsplitter; GP is the glass plate; and CL is the collimation lens. (Reprinted from Ref. 5 with permission from AIP.)

Thin glass plates—substrate cover plates used in microscopy—are less expensive and more stable than pellicles, and their coatings (beamsplitter and antireflection) are much less expensive. They can be sorted in a transmission Fizeau for flatness and homogeneity. Beamsplitter coatings can be applied by professional coating services. Specifications to the supplier include the beamsplitting ratio of reflection to transmission (R/T), antireflection on the rear side; wavelength to be used (polarizing or nonpolarizing), and the angle of incidence (such as 45 deg). The beamsplitters made from thin cover plates are ideal for interference microscopy. Tolansky,[2] a

senior maestro of Fizeau techniques in microscopy and crystallography, started using split mica chips with a self-made semitransparent chemical silver coating (as in thermos bottles) as a Fizeau beamsplitter, simply placed carefully on microspecimens.

A second beamsplitter divides the brightness of the return beam into about 5% for the focal plane and 95% for the image plane. Instruments such as that shown in Fig. 4.1(b) are used for both current and outdated applications of deflectometry.[3] The collimator needed for interferometric measurement needs a refined review. Note that visual observation of decollimated laser light by an eyepiece should be avoided.

Figures 4.1(a) and (b) show a beamsplitter cube in the diverging path acting as a thick plate that introduces unwanted aberrations not correctable by the user. An exception to the foregoing is the interferometer unit after Shack.[4] The Shack monoblock universal interferometer illumination and observation unit has the pinhole foil cemented to a beamsplitter cube, carrying an antireflection-coated plano-convex lens on the opposite side. The radius of the lens surface coincides with the pinhole. The return beam also passes through the plano-convex lens cemented onto the cube.

4.1.1 Autocollimation: The key to any interferometer

There is abundant literature on autocollimation; for generations the autocollimator has been the key metrology instrument in optical production and laboratories. The clarity of some autocollimators' promotional literature often exceeds that of textbooks. We limit description of the classic autocollimator to the advantages in metrology it provides [Fig. 4.2(a)] and to what it does not provide [Fig. 4.2(b)]:

The autocollimator provides:

- changes in angular orientation of a flat mirror [Fig. 4.2(a)],
- nutation around zero in two axes, 0.25-arcsec visual, 0.01-arcsec electronic [Figs. 2.4(a) and (b)],
- distance changes with a retroreflector,
- goniometric applications (Section 4.1.2).

The autocollimator *does* not provide:

- changes in lateral position of the reference mirror (cross motion),
- longitudinal zero,
- roll around the autocollimation's axis,
- definition of best-fit direction of view in linearity measurement (problem of pyramidal line).

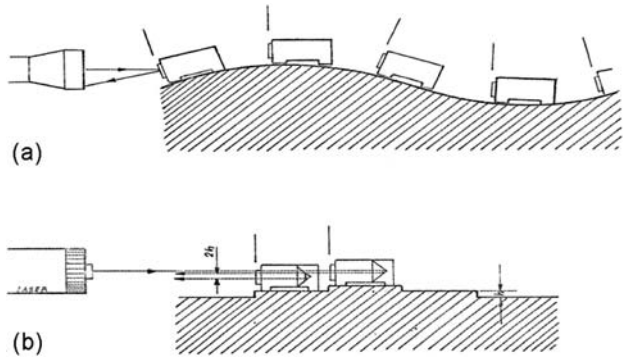

Figure 4.2(a) and (b) (a) The classic autocollimator provides measurement of changes in angular nutation of a flat mirror, away from zero and within a limited range (commercial 0.25–0.01 arcsec). (b) Direct lateral displacement, a most useful measurement, cannot be obtained with the classical autocollimator, nor can roll be measured. An alternative linometric method will be discussed in Section 5.2.1.3.

4.1.2 The autocollimator

The traditional autocollimator is used for measuring angular alignment changes of a flat mirror as the mirror is moved along the axis of the autocollimator. The measurable angular deviation of a flat mirror, moved for distance l on the supposedly linear or flat guide, is multiplied by the measured differential angle α_1, yielding a height $\Delta h = \Delta\alpha l$. The mirror holder usually has its "anti-abrasion feet" at a distance of $l = 200$ mm. The path, therefore, is divided into n sections of distance l. If the displacement is from l_1 to l_2, then $\Delta\alpha_{½} = (h_2 - h_1)/(l_2 - l_1)$. With $l = 200$ mm and $\alpha = 1$ arcsec, $\Delta h = 1$ μm.

1-arcsec changes in direction of the returned optical axis will translate into 3-μm lateral displacement of the return focal image, if the collimating objective has a focal length of 600 mm. This presents the opportunity to utilize interferometric means for detection of the angular change, as in, for instance, the interference autocollimator by Kollmorgen[6] or the null-setting Fizeau technique described in Section 3.5.1.

At this point, in turning from pure collimation testing to interferometric autocollimation testing, one faces the problem of separating departures from flatness of the sample from angular misalignments of the same (Section 5.2.6). Verification of the wavefront planeness of the collimated beam is a major task in interferometry.

4.2 Fizeau Interference and Autocollimation

4.2.1 Common applications of autocollimation

A typical application of an autocollimator in precision engineering combines electronic fast 2D leveling of a sample on a tilt table [Fig. 2.4(c)] with

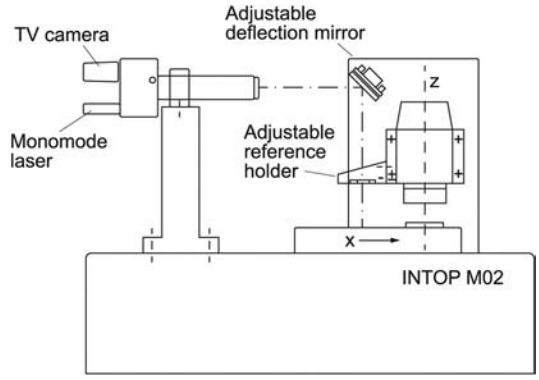

Figure 4.2(c) The Fizeau reference plate may be assembled near the sample, far from the autocollimator. The benefits of this placement are reduced walkoff and reduced air turbulence. The downside of this setup is the extra imaging objective or zoom objective. This setup had proven to be very instrumental in diamond fly cutting and turning.

subsequent view/evaluation of the sample surface by the Fizeau interferometer reference. The latter is attached to the front of the autocollimator in a fixed autocollimating position. Adjustment "to suit" of the interferogram of the preleveled sample will be by inclination of the entire instrument. In order to avoid walkoff and air turbulence within the interference cavity, one may remove the Fizeau reference plate from the autocollimator and mount it far from the autocollimator, close to the sample, as is very practical in micromachining [Fig. 4.2(c)].

In interferometers, the view of the defoci in the focal plane [a typical example is shown in Fig. 10.1(b)] will help to ascertain the returned light beams that will become coincident in order for the interference fringes to be observable in the image plane. Finding the reflected beam upon initial preparation of measurements requires diligence and patience. A small, low-cost, mounted pointing laser on the autocollimator housing can be helpful. For ascertainment of collimation, see Section 5.2.3.

PSDs or photomatrix detectors are used for measuring lateral focus displacements in $x(\alpha)$ and $y(\beta)$ and arrive at an accuracy of 0.25 arcsec (standard). Certain promotional materials claim the ability to measure 0.01-arcsec nutation. Often the nutations of a mirror mounted on a moving slide (intuitively orthogonal to the axis of travel) are referred to as pitch and yaw. The measurement of roll, the angular motion around the optical axis Z, cannot be realized without an additional reference. Measurement of roll, or angular error motion, is an important task in the assembly of ultraprecise machining and measuring machines. Generally, precise orientation with respect to gravity is required. Because there is no optical solution that does not depend on the orientation to gravity, electronic spirit levels are used.

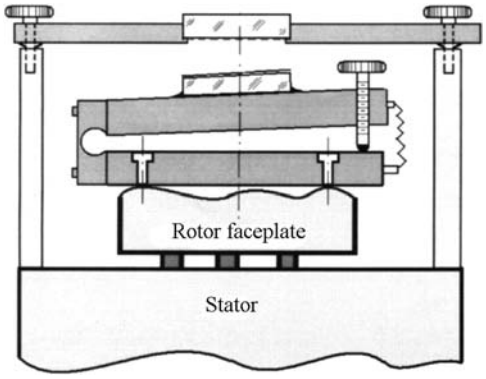

Figure 4.2(d) Tilt motion of an air-bearing spindle analyzed with a Fizeau reference flat mounted to the spindle's stator and a sample. The mirror is either aligned on the rotor following a sequence [as in Fig. 4.2(e)] or machined onto the spindle's rotor. The sample is flat-disk machined and not removed from the spindle. Note that one will obtain the best-fit axis to the irregular tilt, whereas the amount of uniform residual tilt remains unknown.

A significant application of autocollimation is the measurement of polygon angles on the machining equipment. With reference angles defined either by an angular encoder on the dividing head or by a master polygon, the freshly cut surface will be driven under the interferometric autocollimation (IAC) reference [Fig. 4.2(d)], undergoing no angular change, and will present an instant interferogram. The resulting interferogram permits one to qualify the flatness obtained and, simultaneously, to assess divisional and pyramidal deviation of the newly machined facet. For verification of a constant IAC viewing direction between successive null positions, one may place a CCR on the slide, next to the dividing head, in order to register the CCR interferogram and confirm a stable zero condition. Details can be found in Chapter 6.

Another significant application of the autocollimator is the alignment of two flat mirrors for measurement of angular error motion (tilt) that is expected upon rotation of one of the two mirrors [Fig. 4.2(d)]. Once both mirrors are aligned orthogonally to the axis of rotation given by the sample spindle [illustrated schematically in Fig. 4.2(e), which provides a view of the defocus plane of the autocollimator], one may switch from autocollimator function to interference function. Now the implementation of a mirror, as described in Section 3.5.2, will be very instrumental.

4.2.2 Orthogonality of two spindle axes

The enhanced sensitivity to angular errors of a 90-deg angle arranged between two flat reference mirrors finds useful application in the measurement of angular error motion of air-bearing spindles and of turntables, or combinations thereof [e.g., the goniometer shown in Fig. 4.3(a)].

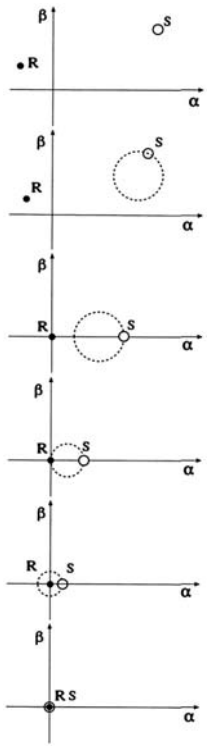

Figure 4.2(e) Schematic view of the defocus plane of the autocollimator/interferometer. After completing the iterative alignment of the stationary and rotating mirrors [shown in Fig. 4.2(d)], one may begin interferometric refining alignment to the no-observable-motion state.

For this task, the sample spindle carries a flat F_2 on its nose, free of wobble and with superfine 2D adjustment features. A second flat F_3 is brought up from the center of the turntable [as shown in Fig. 4.3(b)], wobble free as well. The 90-deg angle F_3/F_2 is now observed by the autocollimator or, better, by the interference autocollimator. Alternating first one spindle then the other spindle will gradually get both F_3 and F_2 to represent residual or no-angular-error motion. In that process, orthogonality of both rotary axes is obtained without extra effort. Now the spindle's angular motion errors can be attributed by equating them to 90-deg angular errors, divided by four. Choosing an alignment of fringes according to Fig. 5.5(b) or (c) is practical. A third flat F_1 based on the ground and adjustable in two axes collinear with the two spindle axes completes a CCR. In setting both angles of F_1 to also be 90 deg, one obtains an almost perfect CCR. We now proceed to the last step and apply the interferometer configuration, as in Fig. 5.20(a). Residual wobble (angular error motion) will be seen magnified 10× in the interferogram compared to reality.

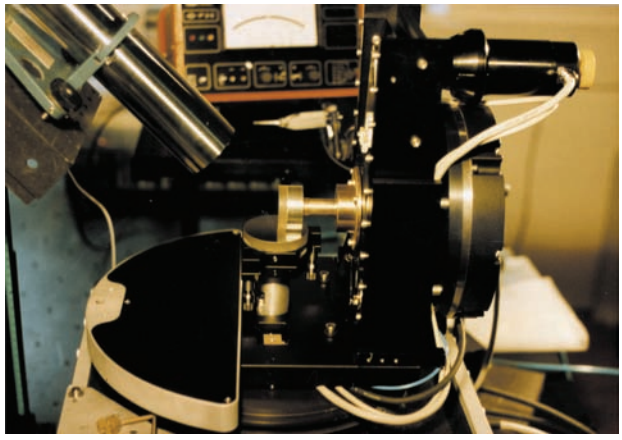

Figure 4.3(a) Measuring angular error motion in an air-bearing goniometer.

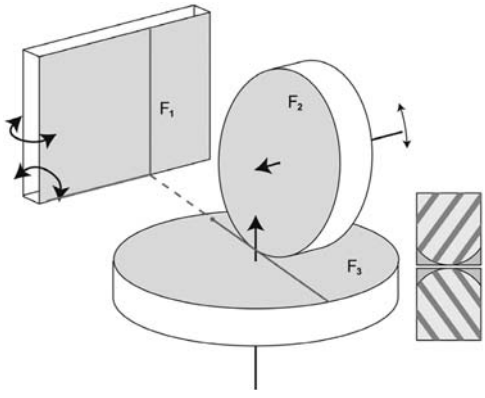

Figure 4.3(b) Mirrors F_1 and F_2 represent the two spindle axes. Mirror F_3 is mounted to the base (not shown), and, there, is given fine control for both inclinations, thus completing a CCR. The spatial diagonal of the CCR is the viewing direction of the interferometer.

4.2.3 Price-worthy Fizeau instrumentation

A not-quite-correct collimation uses plano-convex lenses instead of corrected achromats, with the convex side pointing toward the light source. With its aperture in the category of 1:10, the spherical aberration is still under limits, perceptible in the interference between the planar side (the reference) and the nearby reference flat sample to be tested for flatness. The convex side is antireflection coated. The planar side has a general-utility beamsplitter coating, customary in Fizeau interferometers. In Fig. 4.4(a), the collimating lens is shown in an orientation that limits the use of collimation to a ratio of

focal length to useful diameter: $F/d > 8$. This is still sufficiently accurate for collimation. The degree of *sufficient accuracy* can be tested beforehand and is described in the next section.

The technical price for this simple solution is a long focal length at the required diameter. Practically, it calls for Z folding the beam into a suitable compact housing. Mechanical provisions for a range of focal length adjustments of $\pm 3\%$ will suffice. Additionally, the Fizeau reference surface is a fixed part of the collimator, whereas in standard Fizeau interferometers the reference is adjustable. Large plano-convex lenses are used with large ($\geq$250-mm diameter) profile projectors.[7–9]

4.2.3.1 Two typical applications of plano-convex collimating lenses

Figure 4.4(a) is an open-front-surface Fizeau interferometer, designed for testing flatness of high quality, quantity-produced flat works prior to removing the works from their polishing carrier. The instrument is placed

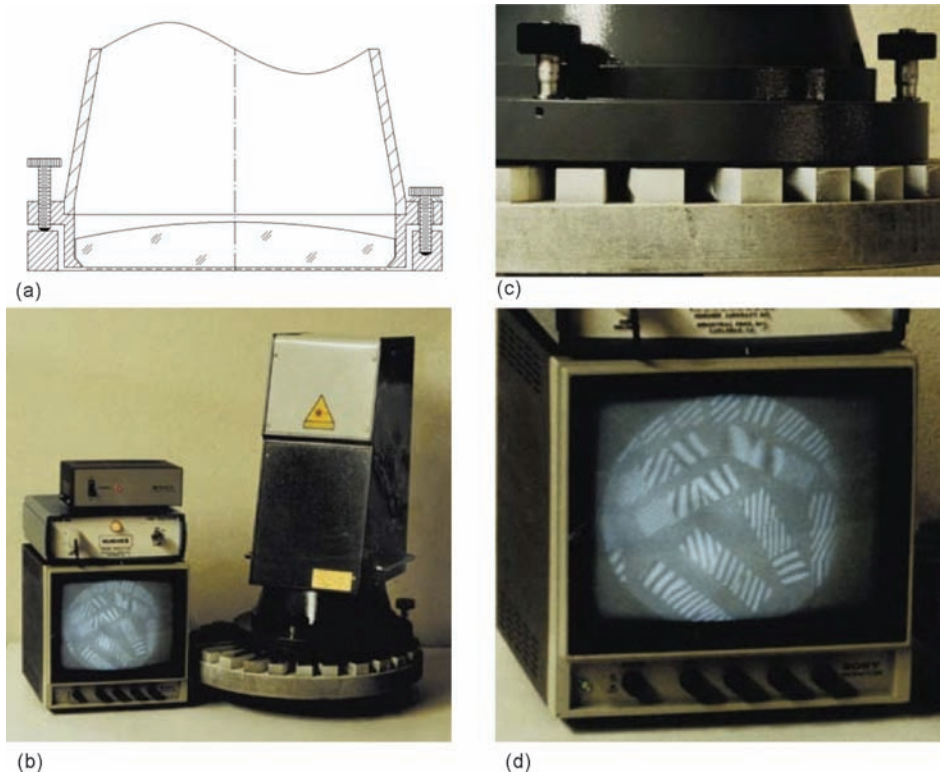

Figure 4.4 (a) Fizeau interferometer for in-process quality control on a planar polishing machine. The flat face collimating the monochromat serves as the planar reference. (b) The completed instrument. (c) The instrument resting on the work, interfaced by a Teflon® ring, prevents hard contact of the set screws. (d) An abnormal interferogram, as explained in the text.

onto the carrier with a Teflon® ring supporting the leveling screws [Fig. 4.4(c)]. The view of Fig. 4.4(b) might reveal an acceptable flatness of each work but also shows severe faults (due to the difference in work orientation), which are impossible to polish.

The surprising interferogram in Fig. 4.4(d) needs explanation. The individual prisms were fixed to the carrier by waxing and, in the final phase of polishing, were tested by the interferometer. The instantly satisfying result was straight unidirectional fringes and good edge sharpness. The carrier rested, ready for work removal, over a long, cold weekend. A temperature difference might have led to the speculative assumption that some workpieces had lost their bonding by optical wax to the carrier disk; yet, the parts could not be lifted off manually until warmth was applied from below.

Figure 7.9(a) shows another application for this type of Fizeau interferometer: testing 400-mm-diameter blanks for inhomogeneities. Obviously, sufficiently large components are rather expensive. Cost saving is possible with the design in Fig. 4.4(a), compared to a design with a separate collimator plus a reference flat.

The test shown in Fig. 7.10(b) is also an example of long-cavity Fizeau interferometry. The beam walkoff and resulting influence on the fringe profile [after Fig. 3.5(b)] is clearly seen in the interferogram, delineating inhomogeneities within the material.

4.3 Testing the Collimation of an Expanded Laser Beam

4.3.1 Murty's parallel shearing plate

Referring to Fig. 4.5(a), the collimated beam is viewed in reflection interferograms obtainable in different angular orientations of the Murty shearing plate.[10] Alternatively, a pair of flat-glass plates (selected cuts from float glass) may be used.[11,12] Such plates are mounted in a frame, holding them at a distance of, typically, 10 mm. Thickness and refractive index need not be specified in both cases. Flatness and parallelism are to be assumed.

A good Murty plate is a useful laboratory tool for, e.g., interferometric angle measurement, taking into consideration the must-read article by D. Malacara and O. Harris[13] of a plane wavefront off of the two opposing plane surfaces with fringe spacing $P = \infty$. By plausibility, one expects a uniform interference tint from reflection off of a plane-parallel plate. Brightness will vary between bright and dark, depending on the optical path difference upon reflection of a plate's thickness, with respect to the two reflecting surfaces' mutual separation.

Inclining the plate around an axis orthogonal to the optical axis will laterally offset (with respect to shear) the two reflected beams, and the image contour will become oblong. Because the included angle between the beams

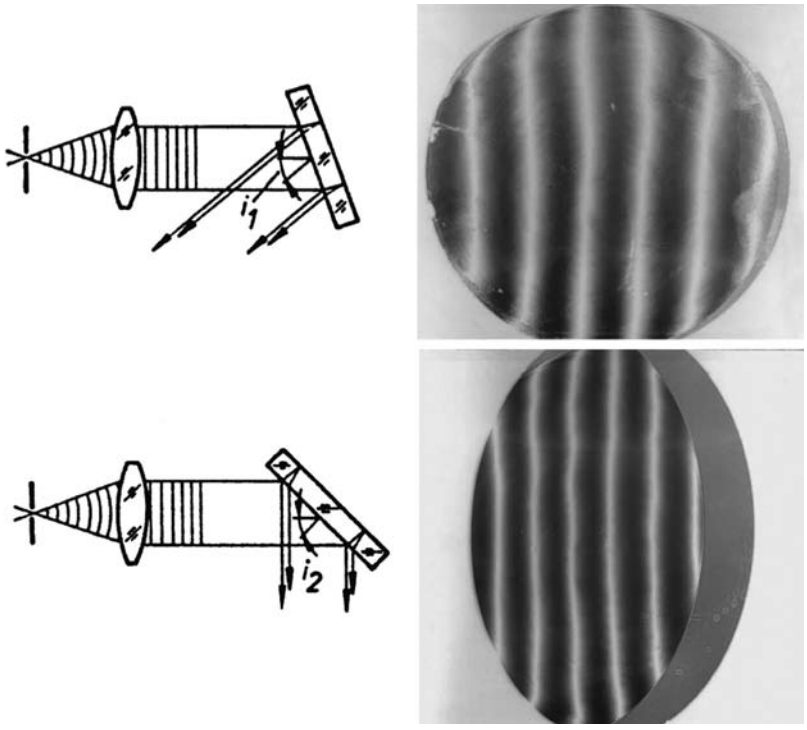

Figure 4.5(a) (left) Collimation test according to Murty[9] performed with one solid plane-parallel plate. (right) Two interferograms with different angles of incidence *i*. Both the internal path length and the lateral shear are greater with the larger angle of incidence; therefore, this second setting (i_2, bottom row) is more sensitive in rendering departures from collimation. Note that the optical flat must be free of any flatness departures on both of its surfaces, and free of inhomogeneities, as well.

remains stable upon tilting the plate, one would expect an initially uniform-tint interferogram from a collimated beam, with respect to the flat wavefront. The interferogram will show fringes if the entering wavefront is not flat. During rotation of the plate, the fringes will pass rapidly.

The criterion for good collimation is as follows: As the optical path within the plane-parallel plate increases with incident angle upon rotation of the plate, the tint of the interferogram will alternate between uniform dark and uniform bright. A note for the curious reader: In earlier "white-light" days, this plane-parallel glass plate had the function of compensating for optical path differences in classical two-beam interferometers. More recently, Malacara and Harris[13] used the rotation of the plane-parallel glass plate to obtain a highly resolved angular measurement by counting fringes. Measurement of the homogeneity of indices of refraction in thin glass plates by counting fringes in a multipass interferometer was introduced by the author of this book in 1968.[14]

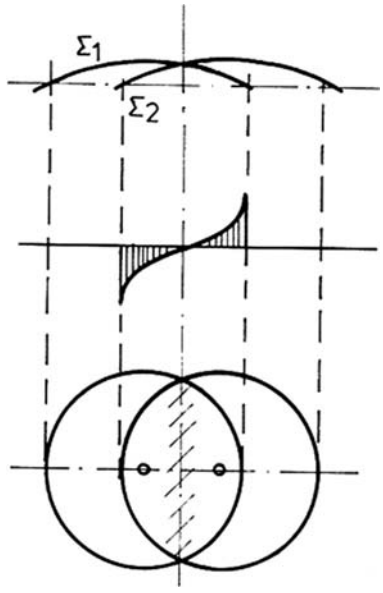

Figure 4.5(b) Lateral offset (parallel shear) of two equal and coherent wavefronts (be they convex or concave) shows a straight line of intersection orthogonal to the direction of shear. Shear starts from zero, and the next pair of λ fringes appears as shear progresses. These fringes are parallel to each other as long as the two wavefronts retain their sphericity. The Murty plane-parallel plate produces this shear as a function of the angle of incidence. For understanding a shear interferogram, one might look at only one-half of the image.

If the plate has a wedge (set parallel to the axis of inclination and, thence, orthogonal to the optical axis), upright fringes will "walk by" (passing through the FOV) as the plate becomes inclined. Often such a wedge is preferred because fringe changes are assessed more conveniently than are changes in uniformity of tint in the brief moments of starting and stopping the rotation.

In the case of collimation as well as resulting from spherical geometry, two laterally sheared spherical wavefronts will produce straight lines (fringes) of intersection that are close to acceptable but of convex or concave spherical shape. Upon shifting the light source along the axis for plus and minus (for example 1%) relative to the best "zero" position and maintaining constant the angle of the plate to the axis (for instance, at 30 deg), one will observe two possible outcomes:

1. When surfaces T and M are parallel, performing the above procedure, one will see many fringes, then fewer, then no fringe in the desired position, meaning that that is the collimation set. Leaving the best-focus position, one will see a few fringes, followed again by many fringes.

2. With wedge α parallel to the inclination apex, initially, one will see many narrow fringes, followed by wider ones, arriving at a fringe assessed to be the widest (the sought-after position for angle α, where collimation is as good as can be judged), followed by narrower fringes again.

The widest fringe spacing P would be $P = 2\,(d - S)$, where S is the shear, and d is the collimator diameter. At $S =$ zero (meaning orthogonal incidence to the parallel plate), one will have normal optical path difference: $2nt$, where n is the refractive index, and t is the distance (neither n nor t is measurable).

The on- or near-optical-axis reflected beams will be observable through the pellicle beamsplitter [see Fig. 4.1(b)]. The fringe spacing, observed with a given wedge and with inclination of the plate set for $S = d/2$, allows one to estimate the smallest angle of divergence that is detectable on the wavefront. Changing the focal distance light source or collimating objective from + to − stops that displacement as soon as the fringe spacing is maximized as follows:

$P = d/2 = S$, and estimating $\delta_{\min} = \lambda/d$ rad,
with $\lambda = 6 \cdot 10^{-5}$ cm, and d in cm, $\delta_{\min} = 10/d$ arcsec.

4.3.2 Variable shear: two parallel plates

P. Hariharan[11] added sensitivity control to the Murty collimation test by replacing the one bulk glass plate with two glass plates arranged at a fixed 45-deg angle to the optical axis. The plates are arranged parallel to each other with the distance between them being controllable, and always maintaining parallelism. The inner surfaces remain bare. The reflexes from the outer surfaces are reduced in their intensity by an antireflection coating and, in addition, the reflexes are deviated by some wedge on the plates. Both plates are mounted on a mechanical linear slide (with one plate stationary) and can be adjusted to a distance to suit the desired amount of lateral shear between the two reflected parallel beams. Thus, the shear can be set to simplify the interpretation of fringes, representing very small aberrations. The goal of this experimental solution is to visualize wavefronts having a mild spherical curvature, representing a lack of collimation. Plane wavefronts will produce straight fringes at any spacing of the two plates. The varying spacing allows one to detect the zones in which departure from flatness begins. Each plate needs only one perfect surface to face that of the other plate. Section 8.2.1 gives an illustrative example of the difference between the common two-beam interferogram and a shearing interferogram.

4.3.3 Variable shear and tilt to suit

Simplification of collimation testing with the Murty concept was introduced by Weingärtner and Stenger in 1985,[12] when an additional controllable tilt angle α was introduced, as in Fig. 4.5(c). This modification applies best to larger

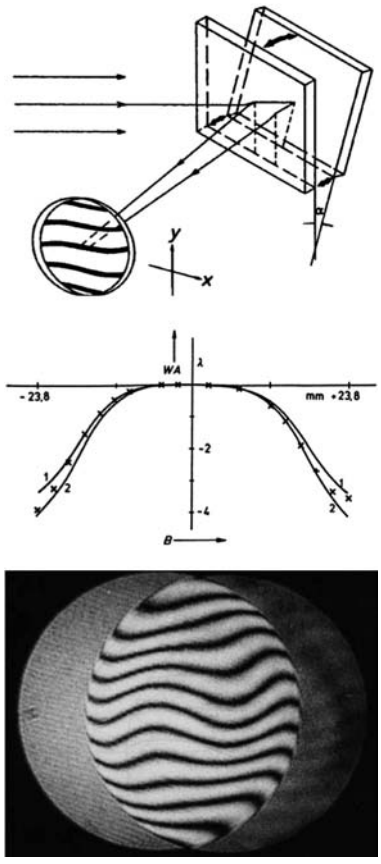

Figure 4.5(c) Weingärtner and Stenger's[12] modification of Murty's test. In addition to the shear producing two inner surfaces of the glass plates, a controllable wedge angle is introduced. This permits one to adjust the direction and amount of shear to the amount of departure from collimation. Control of the distance between the pinhole and the collimating objective will generate straight fringes, indicative of acceptable collimation. An advantage of this test is that shear may be first adjusted to find the gross departure from collimation, then it can be reset for detecting minute departures from collimation. Shear is produced by the distance and tilt of the plates.

departures from collimation, where it is not possible to control the alignment of the focal distance, and corrective polishing might be the only solution.

4.3.4 Double wedge plate shearing interferometer

An improvement in accuracy and operating convenience of Murty's testplate method was introduced by Sirohi and Mahendra,[15] who used two wedge plates instead of one. They observed the two plates simultneously, and, as usual in basic metrology, found the differential measurement to be more accurate and convenient to operate than a single measurement.

4.3.5 Variable shear and tilt: enhanced sensitivity

The author's version of Murty's collimation test operates with the prism interferometer. The beam to be collimated is sheared, as in Fig. 4.6(a). Here, the rear beam is burdened with some additional optical path length $\Delta L = \Delta m\lambda$, where m is the number of wavelengths that fit into a geometric length and depends on changes of the angle of refraction into the cavity, $n \bullet \sin e = \sin\alpha$. Near the angle of total internal reflection, the angle of refraction is highly dependent on minor changes $\Delta\varepsilon$ from the incident-angle-collimated direction of ε on the glass side. Such minute angular changes can be equated to nonflat wavefronts. Furthermore, additional path length within the cavity originates from the gap H between the flat reference (the prism's hypotenuse) and the flat sample. At the same time, the lateral offset is increased compared to the walkoff, as long as the beam does not go near the site of total internal reflection. The discussed effect occurs within an angular range of 0.5 deg, coming nearer to the angle of total internal reflection.

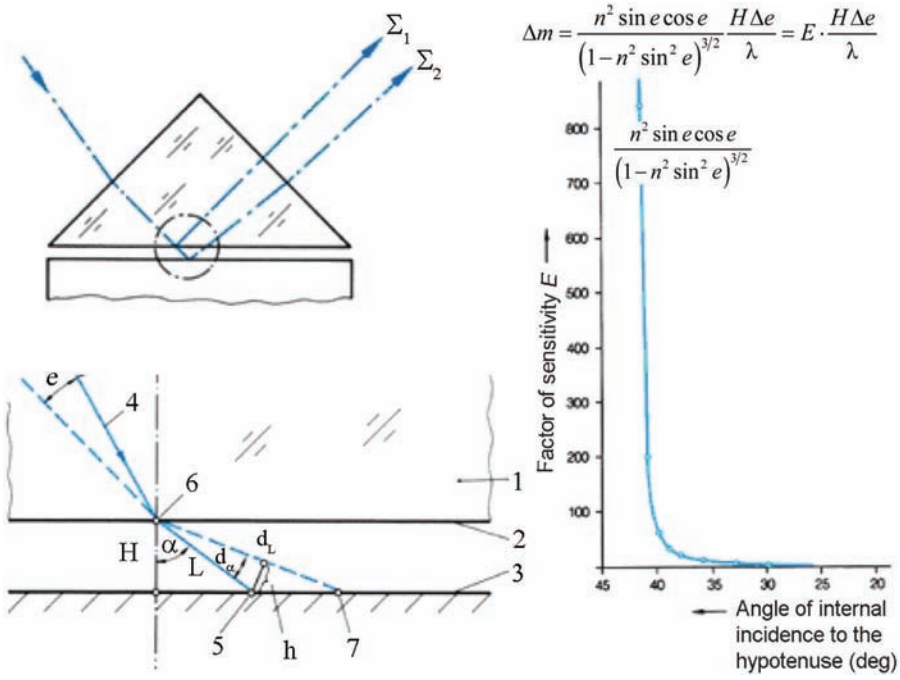

Figure 4.6(a) (left) The prism interferometer produces grazing incidence to samples parallel to the hypotenuse at a distance that is variable between 5 and 200 μm. Considerable walkoff produces side bands to the main fringe. (right) The factor of enhancement (sensitivity) E of small deformations of a flat wavefront as a function of the internal angle e of incidence to the flat beamsplitting reference (the hypotenuse of the prism). (Figure adapted from Ref. 16.)

Table 4.1 Computed factor E as a function of angle e of incidence.

e	20 deg	30 deg	33 deg	36 deg	38 deg	39 deg	41 deg	41.5 deg
E	1.14	3.37	5.36	10.18	19.34	30.62	59.39	836.6

E is the sensitivity factor and is computed using $n = 1.458$ for quartz glass. Table 4.1 provides the factor of deformation of a nominal flat wavefront as a function of the selected values of angle e of incidence to the glass/air interface in a prism interferometer.

The dependence of focal adjustment on the observable quantity $\Delta m = L(\Delta P/P)$, the local change in fringe spacing, indicates a transition from good to poor collimation. The interferograms in Figs. 4.6(b)–(e) demonstrate this unusually sensitive criterion for acceptable collimation.

The experimental setup for producing grazing incidence used an autolevel stage, as shown in Fig. 2.4(a) and an interferometer as in Fig. 1.14(b). A frame,

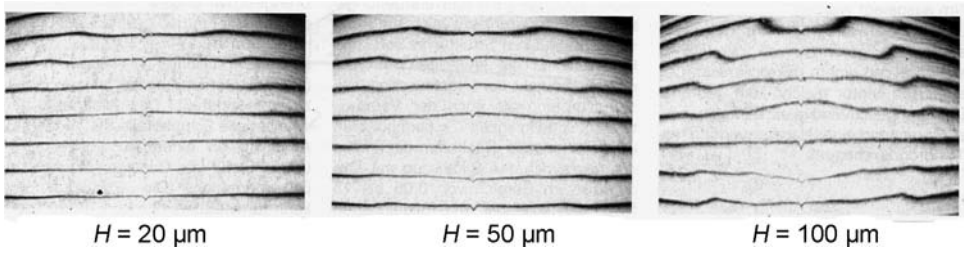

Figure 4.6(b) Interferograms of a flat glass plate with 5-μm fringe equivalent. The nose on the fringes point toward the zeroth order. The plate is arranged at distances H. The fringe equivalent is 5 μm, set with the aid of a calibration master [see Fig. 1.7(a)].

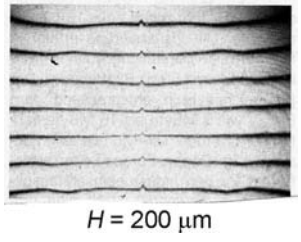

Figure 4.6(c) All of the interferograms in Figs. 4.6(a)–(e) except this one had their wedge aligned in the direction where multiple reflections led toward the apex, thereby enhancing the deviations from a perfect wavefront entering the prism—the intention of this test. The wedge alignment, here, in the opposite direction, reduces the amount of walkoff to the point where the departures from collimation are not evident. The sample distance to the hypotenuse H could be increased to 200 μm before the interferogram began to show a defect on the Illuminating wavefront.

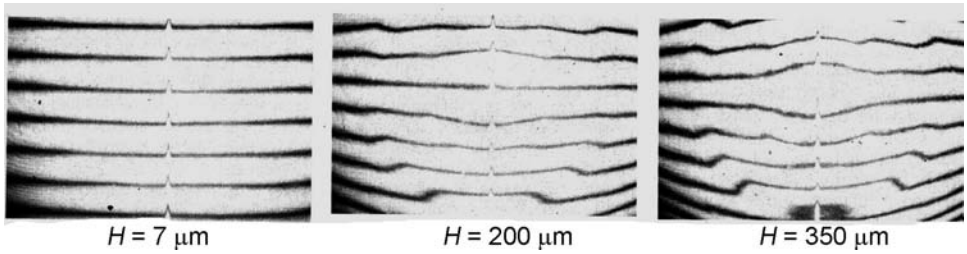

Figure 4.6(d) Like Figs. 4.6(c) and (d) but with a fringe equivalent of 1 μm.

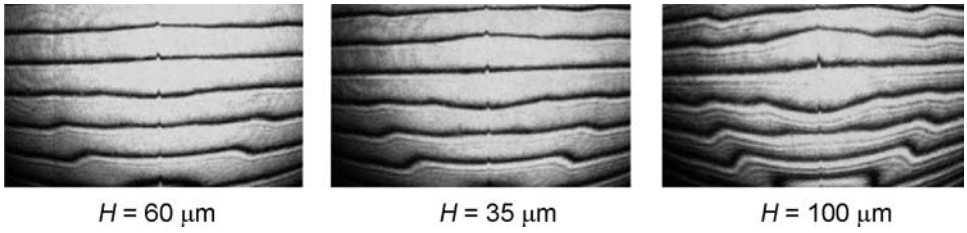

Figure 4.6(e) Like Figs. 4.6(b) and (c) but with the instrument realigned to produce 2-μm fringe equivalent and with the collimator defocused by 1% of its focal length.

as in Fig. 2.1(c), carrying a 100-mm flatness prism found its reference position atop the three anvils surrounding the sample holder. This test is very practical as a null-setting criterion for collimation, but no quantitative evaluation is seen to be reasonable.

A 100 mm × 100 mm prism interferometer was used in the experimental setup. The glass plate used for all exposures could be aligned to locate the sample at a distance H. The first fringe equivalent chosen was preset to be 3 μm. The small nose on the fringes points toward the apex (against the direction of walkoff), as seen in Fig. 4.6(e).

4.3.6 A useful, robust interferometer

Figures 4.6(b)–(e) present the combination of a 90-deg prism with a perfect flat, much like the combination in the 'flat test' used for checking technical flatness. This combination, however, if rigidly packed with constant gap H, will allow no further adjustments. The device may serve to analyze a nominally collimated beam, carrying a wavefront deformation impressed on it by, for instance, reflection at a target acting as a fold mirror. (In the author's laboratory, diamond-turned substrates for memory disks were the target.) The nominally flat wavefront might be

deformed by poor collimation as well. The abovementioned term *rigidly packed* means that the flat is mounted to the 90-deg prism at a distance of $H = 0.1$–0.2 mm with an inclination such as to produce fringes parallel to the longer side of the hypotenuse, with fringe equivalent of 5–7 μm.

This device can be used like a hairline ruler for a quick qualitative visual check of wavefront flatness by holding it into the beam in question for inspection. The only delicate manipulation needed will be a manual inclination for a search of the angular range that is near total internal reflection. Not far from this position, one will obtain the sensitive fringes [reducing angle *e* shown in Figs. 4.6(b)–(e)]. Qualitatively, when testing the flatness of a mirror, this would occur at approximately 5- to 8-μm fringe equivalent. This interferometer device is insensitive to vibration, as it is simply handheld into the beam at a distance from the work, with no contact to the sample. Note: like a hairline ruler, this device offers a highly sensitive, but only a qualitative, quick test.

One application of this device was the collimation test described in the preceding section [see Figs. 4.6(b)–(e)]. Another application is illustrated by the reflections of flat disks being micromachined [Fig. 4.7]. The central figure, compared to the one on top, shows better overall flatness of the sample but also deeper tool marks. The upper figure shows poorer flatness but not such deep marks. The bottom figure shows a totally useless condition. The only possible quantitative statement from these results is: a perfectly flat sample will produce perfectly straight fringes. Fringe deformation begins to be recognizable when the device inclined for approaching approximately 5-μm fringe equivalent (Fig. 4.8) cannot be related to the target.

The assembly in Fig. 4.9 shows the prism from BK-7 glass with the hypotenuse specified for λ/20. The red bands are identical spacers of approximately 100 μm. The brass reference plate is micromachined to λ/20 as well. The prism and base plate are fixed to each other at both side flanks by two sheets of aluminum. The prism, base plate, and side sheets are to be loaded while gluing. Gluing should take place at a temperature about 15 °C above room temperature. The spacers need not be glued.

This type of quick check originated as a byproduct of the process of adjusting the collimation of a flat-test interferometer when suddenly, while changing sensitivity (by changing angle *e*), the interferogram indicated departures from flatness that far exceeded the quality of the same components inspected with 2-μm fringe equivalent. We owe this detection to a persistent but patient customer with his probing queries.

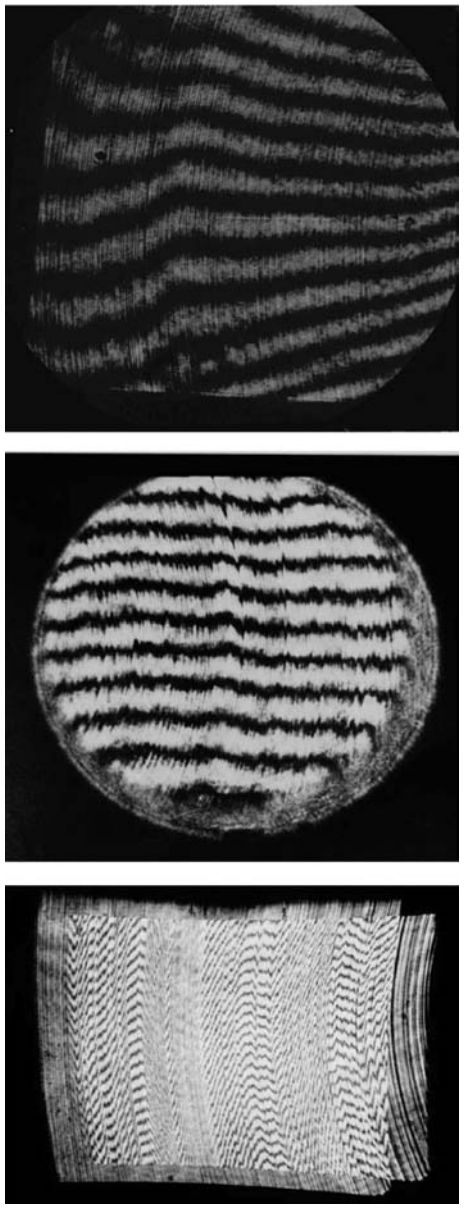

Figure 4.7 Samples of memory substrate disks in different phases of micromachining. The top and bottom disk are useless. The center disk approaches better flatness with irregular machining marks.

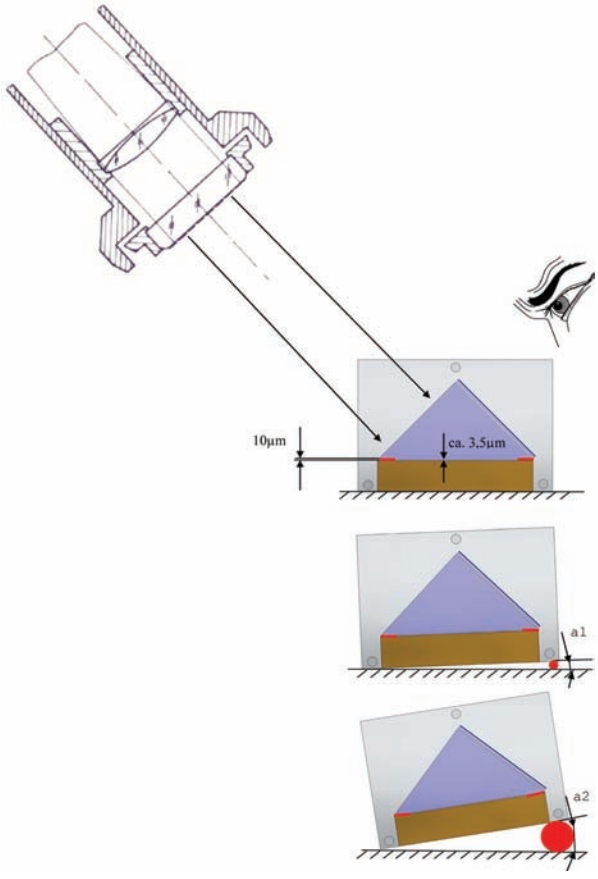

Figure 4.8 Diagram showing the use of the handheld interferometric hairline for collimation testing. Interference is observed on a screen of transparent paper placed on the second cathede.

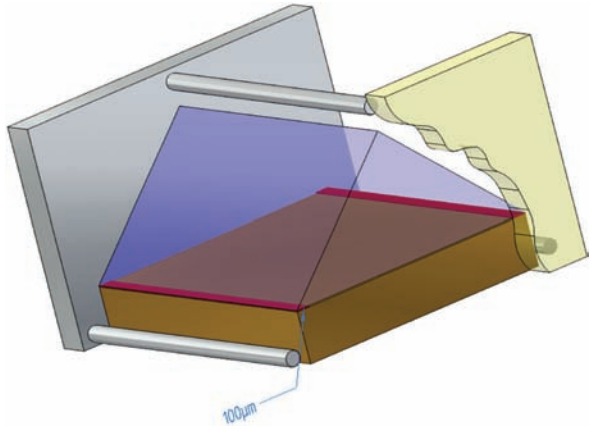

Figure 4.9 A rugged handheld shearing interferometer device for inspection of a light beam shown onto the upper cathede and observed on a screen (transparent paper) placed on the second cathede, as in Fig. 2.1(d).

References

1. National Photocolor Corp., 428 Waverly Ave, P.O. Box 586, Mamaroneck, NY 10543-0586, USA: source of pellicle beamsplitters.
2. S. Tolansky, *Multiple-Beam Interferometry of Surfaces and Films*, Clarendon Press, Oxford (1948).
3. C. Tuttle and R. Cartwright, "A method for the measurement of flatness of polished surfaces," *J. Optical Society of America* **30** (1940) (communication from Kodak Research Laboratory).
4. "TORC Original Shack Inteferometer," Tuscon Optical Research Corp., 210 Plumer Ave., Tucson, AZ 85710, USA.
5. Y. J. Sohn, J. H. Kwon, O. S. Choe, and T. B. Eom, "Portable autocollimators using the laser diode and the position sensitive detector," *Review of Scientific Instruments* **69**(2), 402–405 (1998).
6. Kollmorgen Corp., Electrooptics Div., Northampton, MA 01060, USA.
7. Edmund Optics, 101 E. Gloucester Pike, Barrington, NJ 08007-1380, USA.
8. Zygo Corp., Laurel Brook Road, Middlefield, CT 06455-1291, USA.
9. Jenoptik AG Carl-Zeiß-Straße 1,07743 Jena, Germany.
10. M. V. R. K Murty, "The use of a single plane parallel plate as a lateral shearing interferometer with a visible gas laser source," *Applied Optics* **3**(4), 531–534 (1964).
11. P. Hariharan, "Simple laser interferometer with variable shear and tilt," *Applied Optics* **14**(5), 1056–1507 (1975).
12. I. Weingärtner and H. Stenger, "A simple shear-tilt interferometer for measurement of wavefront aberrations," *Optik* **70**, 124 (1985).
13. D. Malacara and O. Harris, "Interferometric measurement of angles," *Applied Optics* **9**(7), 1630–1633 (1970).
14. P. Langenbeck, "Optical homogeneity measurement by a two-angle method," *Optik* **28**, 592–601 (1968).
15. R. S. Sirohi and P. K. Mahendra, "Double wedge plate shearing interferometer for collimation test," *Applied Optics* **26**(19), 4054–4056 (1987).
16. P. Langenbeck, "Wellenflächen im Shearing Interferometer prüfen," *Feinwerk und Messtechnik* **99**, 387–390 (1991).

Chapter 5
Straight Lines and Right Angles

5.1 Measuring 90-deg Roof Angles on Mirrors and Prisms

Referring back to Fig. 3.1, the mirror M opposing the transmission flat reference mirror T is now replaced by a 90-deg combination of two flat mirrors (Fig. 5.1). The two mirrors, mounted on a fixture as shown, can be adjusted to 90 deg while observing defoci in an interferometer. The 90-deg fixture stands on a tilt table, allowing alignment of the orthogonality of the α edge relative to the interferometer axis (not shown), angle β. The two mirrors M_1 and M_2 forming the 90-deg angle are flat all the way to the edge.

Obtaining an interferogram is made convenient by first observing the three focal-plane images produced by the interferometer's autocollimator, as shown in Fig. 5.1. On the axis is the focus T, representing the reference. Next to the focus T are the two foci, W_1 and W_2, of the two mirrors. The distance $W_1 - W_2$ is changed by controlling angle α; $W_1 = W_2$ only for $\alpha = 90$ deg ± 0. Nutating the stand (changing the angle β) allows T, W_1, and W_2 to be on a line, represented in the bottom of Fig. 5.1. Rotating the 90-deg fixture in the β direction will neither change distance $W_1 - W_2$ nor move these two foci closer together along the α axis. Before W_1 and W_2 fully coincide, one can already observe two partial interferograms with potentially confusing variations [Figs. 5.2(a) and (b)] that behave as though they are part of only one wavefront having a kink angle.

Varying the alignment of T by minute amounts and letting the 90-deg mirror assembly be close to 90 deg, one obtains three characteristically different but equivalent interferograms. These alignments can be selected for convenience of evaluation [see schematic diagrams in Figs. 5.2(a) and 5.5].

The actual interferograms look more like those in Fig. 5.2(b). These three interferograms represent 90-deg roof-angle mirrors micromachined on aluminum. [The reader might look at Figs. 5.12(a)–(d) and Fig. 2.3(c) representing the simultaneous assembly of three 90-deg angles]. The interferograms in Fig. 5.2(b) can be confusing and might need interpretation, as follows:

- Each half-beam is reflected under near 45 deg first at one mirror, for instance, M_1, then at M_2, and vice versa.
- The departure ε from 90 deg is picked up twice by each half-beam 2ε.

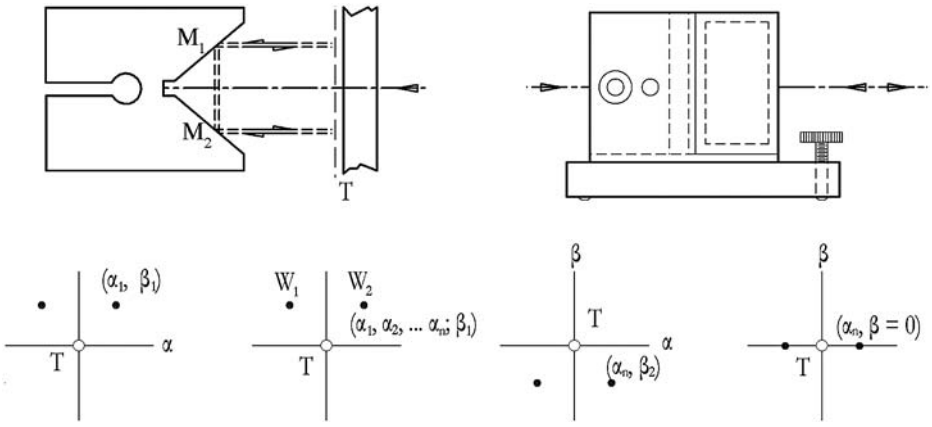

Figure 5.1 In an autocollimator one will see the two defoci, W_1 and W_2, of the roof mirror, representing the edge error. Adjusting the roof angle to 90 deg will make these two defoci coincident. The focus T relates to the transmission flat of the interferometer and does not necessarily equal the optical axis, as it should.

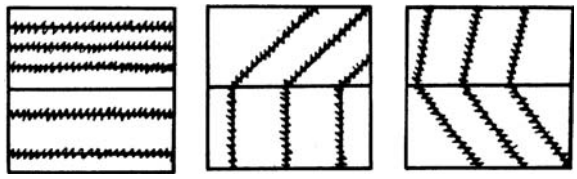

Figure 5.2(a) Typical fringe patterns representing the same 90-deg roof mirror with different fringe alignments by reference mirror: (left) with fringes parallel to the edge; (center) with one or the other set of fringes orthogonal to the edge; (right) with arbitrary fringe alignment.

- Total angular error between the two half-beams is therefore 4ε.
- The interferogram will show this angle to be 4ε in the case where M_1 and M_2 are flat.
- A departure from flatness present on only one mirror will be picked up by both half-beams and will become evident in the interferogram as being distributed symmetrically to the edge. The interferogram on the left in Fig. 5.2(b) represents 90-deg roof mirrors made of two halves, each micromachined and then screwed together (see Fig. 5.12). It shows one of three screws tightened too far, thus deforming the feeble structure. It is impossible to derive from the interferogram of a 90-deg roof angle whether the deformation is on M_1 or M_2, or both.
- Distinguishing between errors on either (or both) surfaces and angular errors is not possible.
- Surfaces must be viewed individually.

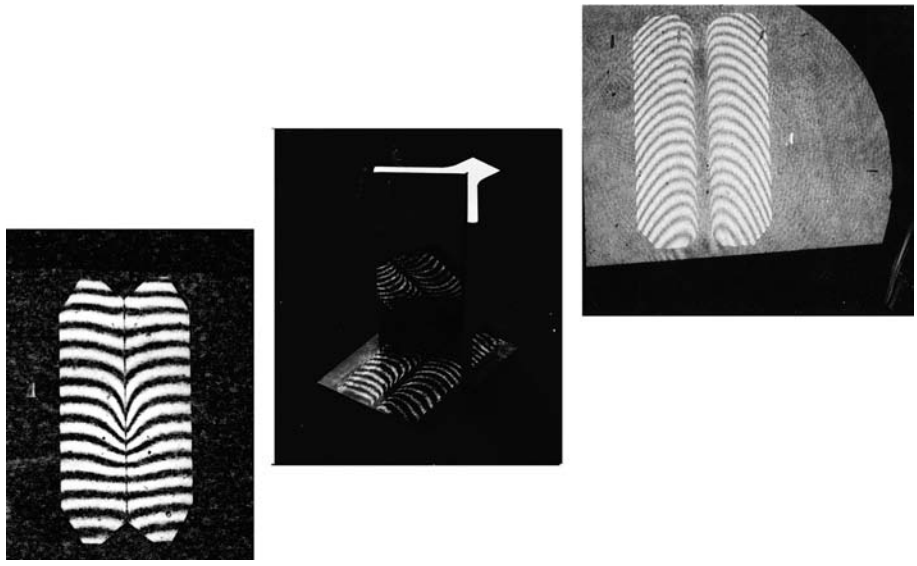

Figure 5.2(b) No distinction is visible between errors on one or both surfaces nor of angular departures from 90 deg: (left) 90-deg roof mirror composed of two diamond fly-cut flanks of the material Al 6061 individually machined and connected by three screws; one or both mating flanges are not coplanar when tightly contacted (compare to Fig. 5.12). Center and right side: The same to-be-mass-produced object with a premachined solid body, diamond fly cut close to the edge. Center: The roof mirror above the record of its interferogram.

- The wavefront entering the 90-deg mirrors becomes reverted with respect to the 90-deg edge. This reversion presents a severe problem in interferometric evaluation.
- In a technical use, M_1 is mounted separately on a device that introduces angular error motion upon rotation (like the angular error motion of an air-bearing spindle carrying M_1 on its axis of rotation) and will show the 90-deg edge error formed with a stationary mirror M_2, magnified by a factor of 4 (see Section 5.2.1.6).

5.1.1 Reversion of wavefronts

Reversion is explained schematically in Fig. 5.3 by comparing two interferometer cases: (a) shows T–M, and (b) shows T–(M_1/M_2). An error on the incoming wavefront is shown schematically with Σ_{in}. In the interferometer T–M (Fizeau), the location of the error retains its size and location and, therefore, may be tolerated, as it will not show up in the interferogram unless the wavefront undergoes a lateral offset (shear). A shear movement might be intentionally introduced for the detection of local defects. Shear will occur in any interferometer operating with a wedge between the sample and the reference. But the shear might not become resolved in the sharp image of the interference

cavity; as a matter of fact, the location of sample's image found along the optical axis of such an interferometer is identified by *no shear* being recognized. Instruments working with small cavities produce a lesser lateral walkoff, which might not become resolved in the image plane. Sheared wavefronts cannot be avoided when operating a dual-beam interferometer with different arm lengths.

The M_1/M_2 roof angle reverts the wavefront around the edge, and the entering error will be seen twice with the same sign: plus or minus on the wavefront Σ_T and on Σ M_1/M_2. Without additional information, one cannot judge from one interferogram whether an error seen is on M_1, on M_2, on both mirrors in some ratio, or on the collimating wavefront, the latter being one more reason for strict collimation testing.

A primitive experimental method for attributing an error seen in an interferogram of an M_1/M_2 assembly uses its lateral displacement: Within the image of the two half-mirrors, an error will be displayed symmetrically to the edge. The two images of the error will move apart or closer together, relative to the edge, in the case where the error is on the incoming wavefront; otherwise, an error on M_1 or on M_2 will retain its location relative to the edge with lateral sample displacement [see Fig. 2.5(a)].

A second reflection of the interferometric beam within the cavity will revert the wavefront one more time, but not necessarily canceling the effect of the first reversion. Instead, and depending on the transmittance of the beamsplitting mirror T, the second reflection through the assembly generates a second interferogram. The latter forms a moiré pattern with the first reflection. We will see this as a welcome convenience in lateral displacement testing in Section 7.5.2.

Collimated-wavefront errors are not nearly as distinct as those chosen for clarity (see Fig. 5.3). There will be mild departures from flat, but these departures

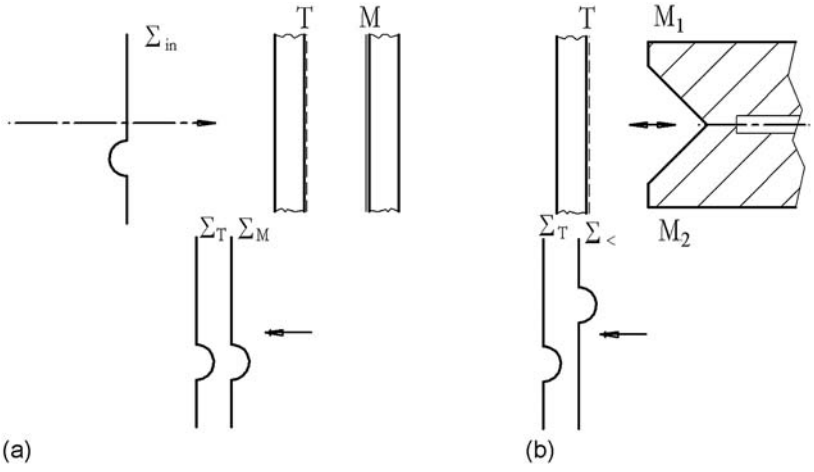

Figure 5.3 The effect of an error on a wavefront entering a flat mirror in (a) a Fizeau assembly and (b) a roof-mirror assembly [compare with Figs. 5.17(a)–(c)].

will be the cause for hidden inaccuracies. Inaccuracies due to wavefront reversion are typically noticed in asymmetric two-beam configurations. Therefore, in Fig. 9.8, the reference beam is reverted in the same manner as the sample beam. See Section 5.2.6 for more information on the measurement of 90-deg angles.

5.1.2 Measuring small angles with straight fringes

Let us assume a flat mirror, having a small prismatic kink ε, positioned orthogonal to a collimated beam. A plane wavefront will propagate after reflection on that mirror, carrying a kink angle of $\delta = 2\varepsilon$. In the case of a 90-deg roof mirror and kink angle equaling the edge error off of 90 deg, one obtains $\delta = 4\varepsilon$, which is the reflection at orthogonal incidence to the edge.

In Fig. 5.4 the normals to the mirror sections N_1 and N_2 include the angle γ. In the plane of decollimation one will see the corresponding two foci next to that of reference T_1: N_0. The three normals to the wavefronts are drawn in Fig. 5.4(a). Their traces, N_1 and N_2, in a location orthogonal to N_0, are shown in Fig. 5.4(b). The interference fringes will be oriented orthogonally to the traces of the wavefront normals. The solid angles between the normals are: the kink angle δ on the wavefront to be measured, α_1 between N_0 and N_1, and α_2 between N_0 and N_2. Angle γ in Fig. 5.4(a) will show up as the angle between interference fringes in the recorded image.

The cosine relation of spherical trigonometry connects these four angles:

$$\delta = [\alpha_1^2 + \alpha_2^2 - (2\alpha_1\alpha_2 \cos(\gamma))]^{1/2}. \tag{5.1}$$

In the interferogram, one measures $\alpha_{1,2} = \lambda/P_{1,2}$ and γ. The values of P must always consider magnification M. Angles α may be chosen by control of the direction of N_0 (the alignment of mirror T) to suit the convenience of fringe evaluation. Three of these choices are illustrated in Fig. 5.5.

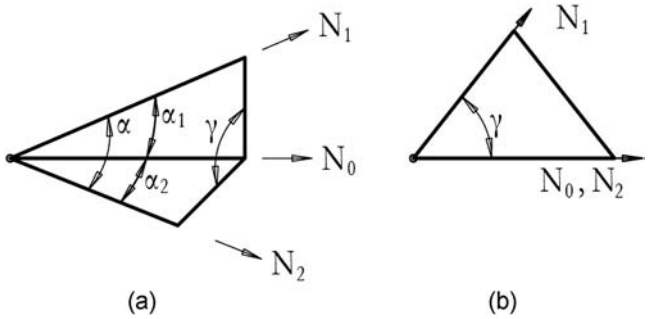

Figure 5.4 The normals (a) N_1 and N_2 to the mirror sections and (b) N_0 to the reference, their traces being in the image plane.

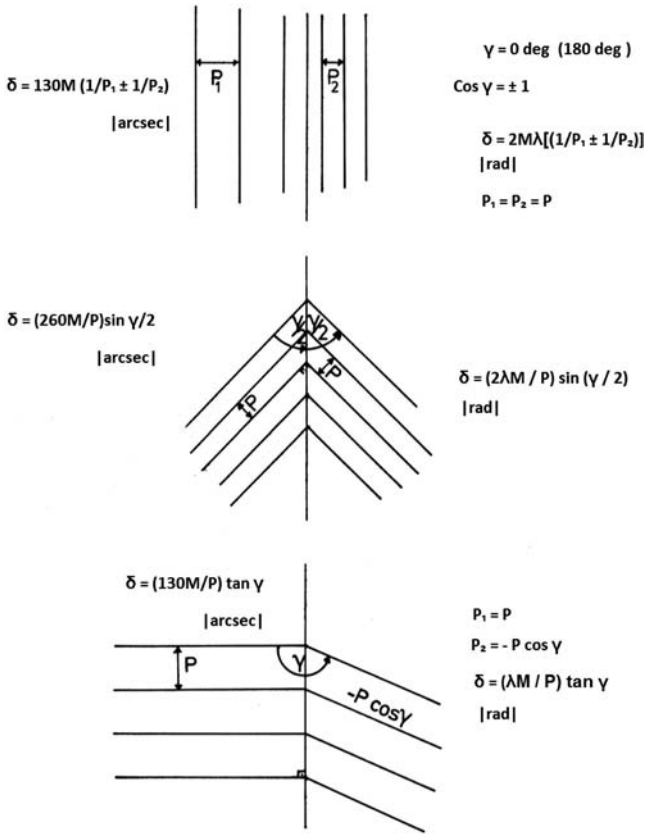

Figure 5.5 Three sets of instructions for measuring small angles on wavefronts by deliberately aligning fringes P_1 and P_2 to suit the equations given for each case. Shown in the center column are the three corresponding interferogram alignments that are convenient for measuring the fringe pattern that represents the kink angle δ on the wavefront.

5.1.3 Enhanced sensitivity for 90-deg-roof-angle quality assurance

Roof-angle reflectors are mass produced with very narrow tolerances on their 90-deg angle and their edge sharpness. Such mirrors and prisms, shown in Fig. 5.6, permit a double (back and forth) pass of an interferometer beam. The configuration is a long-path Fizeau interferometer. Possible error contribution by the prism's front surfaces and homogeneity of the glass are negligible. The wavefront reversion, as discussed in Fig. 5.3, will be cancelled due to double reflection.

Some typical autocollimated foci, arrived at by aligning transmission mirror T, are schematically presented in Fig. 5.6. The alignments in (d) and (e) represent a null field in one-half of the interferogram and fringes P in the other half, making interpretation quite convenient. The angle of incidence *u* to the

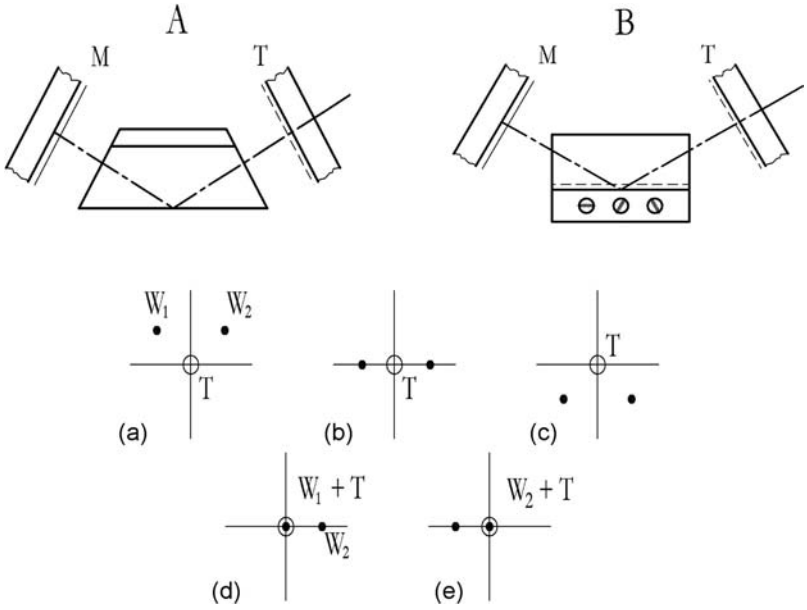

Figure 5.6 Schematic showing measurement of 90-deg angle errors of roof mirrors (right side, B) and prisms (left side, A) in a long-path Fizeau interferometer. The associated defocus dots for different alignments are sketched in the lower part of figures (a) and (c), and correlate with V-type fringes, one up, the other down. (b) Relates to two sets of parallel equispaced fringes; (d) and (e) relate to a null field in one half-image and straight fringes parallel to the edge in the other half-image.

edge of both the roof prism and the roof mirror must be taken into account so that the 90-deg edge error ε converts into wavefront angle δ:

$$\delta = \varepsilon\, 8\cos(u) \text{ for the roof mirror (B in Fig. 5.6);}$$

$$\delta = \varepsilon\, n 8\cos(u) \text{ for the roof prism (A in Fig. 5.6).}$$

The factor of 8 results from double reflection at the 90-deg mirrors (double pass with n = refractive index and, u = angle of incidence to the edge). The departure ε from 90 deg for the roof mirror assembly is

$$\varepsilon = \frac{\lambda}{8\cos(u)}\left[\left(\frac{1}{P_1}\right)^2 + \left(\frac{1}{P_2}\right)^2 - \left(\frac{2\cos(\gamma)}{P_1 P_2}\right)\right]^{1/2}. \tag{5.2}$$

With $u = 45$ deg and with the interferogram alignment as recommended in the bottom of Fig. 5.5 and assuming a fringe reading accuracy of $(\Delta P/P) = 0.1$, one obtains the smallest, thus measurable, error on the wavefront as follows: $2\,\delta \sim 1$ arcsec and $\varepsilon < [1 \text{ arcsec}/8\cos(u)] = 0.15$ arcsec on the roof mirror, and 0.1 arcsec on the roof prism. Both are valid for visual interferogram interpretation. Utilization of this enhanced extreme angular sensitivity obviously depends on the flatness of each of the facets.

5.1.4 Plus or minus angular error? High or low on surfaces?

Knowledge of $+\varepsilon$ or $-\varepsilon$ is essential for corrective measures. Neither the autocollimation foci nor the associated interferogram will reveal the sign. Figures 5.1 and 5.2(b) will not reveal the sign without additional information.

Let us look at a low-cost auxiliary means of determining the sign of the kink angle. In the schematic Fig. 5.7, T stands for transmission, and M stands for the rear mirror. Shown on the left side is a negative kink and on the right side a positive kink. A minute axial (parallel) displacement of the mirror M toward T (narrowing the cavity) causes fringes leaving the wedge to seek a zone where they maintain their order n of interference. Fringes move away from the apex (zeroth order). A small groove polished into a reference mirror will show up as a nose on the fringes. This nose traces the groove and, therefore, points away from the zeroth order and away from the apex of the wedge. Fig. 5.8(a) shows an example of the nose pointing to the wider part of the cavity.

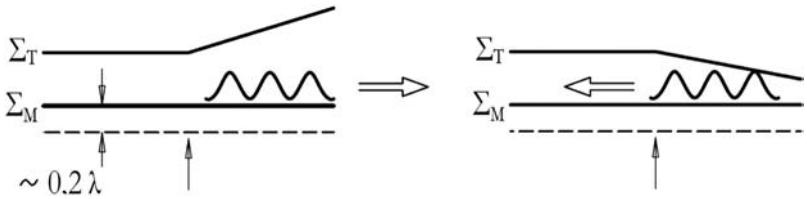

Figure 5.7 Determining the sign of the kink angle by knowing the direction of zeroth-order interference. The dashed line represents the mirror position prior to pushing the mirror.

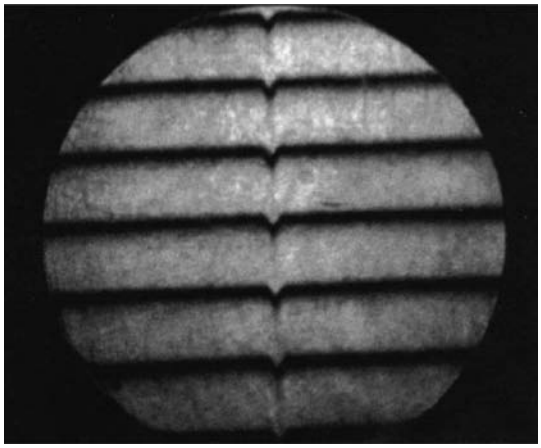

Figure 5.8(a) A reference mirror with nose polished into the surface. The nose points away from the zeroth order. Upon parallel reduction of the gap T/M, fringes move in a direction opposite to the nose, and vice versa upon reversing the orientation of the wedge.

A note for the practitioner

At the beginning of serial testing (the "set and fix" phase), keep the zeroth-order direction constant by pre-aligning the reference. Alternatively, a marking trace can be vacuum deposited on any mirror; the nose, now "up," will point toward the open side of a wedge and away from the zeroth order.

The edge error on prisms needs attention. Typically, the surfaces forming the 90-deg prisms fall off along the edge about 0.5 μm deep and extend about 0.5- to 1-mm across the edge into the surface. This *a priori* information is useful in the error evaluation of angles tested from inside prisms. For internal reflection, these edges "stand up" and, like the positive trace, the nose on the fringes [Fig. 5.8(b)] points toward the closer side of any wedge formed between the partial wavefronts, reflected by, e.g., a 90-deg prism. The example of a roof prism in Fig. 5.9(b) shows such a residual nose pointing away from the wider end of the wedge formed between the wavefronts. The optician will conclude that either one or both flanks of the 90-deg angle are "rolled off" to the degree of effecting a 0.2λ error on the doubly reflected beam (in the Fizeau setup per Fig. 5.6). The qualitative reason for testing prisms by internal reflection is that a convex deformation measured on the wavefront (an "up-nose") represents a concave deformation on the prism flanks because the internal reflection sees the sign of deformation opposite to the way the external reflection sees the sign of deformation.

A situation that is confusing to any interferometry novice occurs when testing 90-deg angles in two-beam interferometers (Michelson, Twyman–Green). In a given alignment, one observes fringes moving in one direction

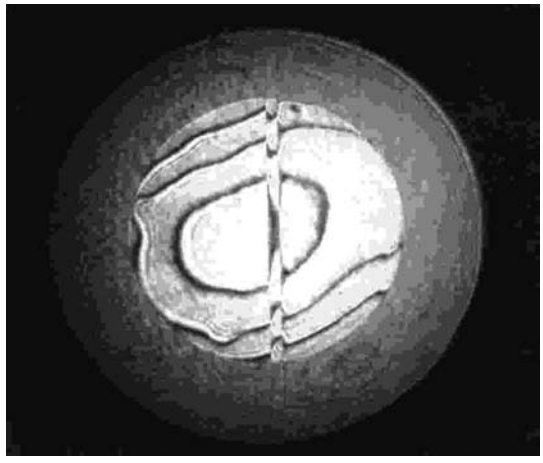

Figure 5.8(b) Marking the direction of zeroth order by an elevated trace on the reference: the nose points toward zeroth order.

when pushing the reference mirror in the opposite direction. When pushing the prism, reversion of the wavefront in the 90-deg angle or inversion in the trihedral prism is the cause for this effect. After reflection of the reference beam by a flat and of the sample beam by the reverting or inverting sample reflector, the optical axis of the latter has changed its sign from plus to minus.

A note for the practitioner

The extension and depth of the nose along the edge of the two 90-deg facets provide useful information for the final polishing. The hardness of the polishing pitch, viscosity of the polishing slurry, and specific load of the sample together with careful timing and control of temperature govern the last polish of the surface without losing surface orientation within the trihedral prism.

5.1.5 Polarization

The illumination's direction of polarization will have a dramatic influence on the fringe profile (finesse, sharpness) and contrast. The direction of polarization is predetermined by the laser (it is marked on the housing); the direction can be chosen by either rotating the housing or by a rotatable $\lambda/2$ plate (transparent mica).

Due to successive reflections at dielectric surfaces (glass/air) within prisms at oblique incidence, the state of polarization in the final image will be different from the incoming state. Beamsplitters (45-deg) in two-beam interferometers and other beamsplitters for observation of images produce this effect as well. The state of polarization will be harmless in normal-incidence Fizeau and in two-beam interferometers.

Different states of polarization will be present in different image sections, as is typical with testing dihedral or trihedral prisms that are not metal coated. This is evidenced experimentally in Figs. 5.9(a) and (b), which show the same prism as being bare, without metal coating and with metal coating, respectively. The do-it-yourself features of chemical silvering fascinated well-known interferometry researchers, such as S. Tolansky[1] and J. Strong.[2] Today, chemical solutions are commercially available. The reader will find an analysis by E. R. Peck[3] of kaleidoscopic polarization effects within CCRs.

Figures 5.9(a) and (b) compare a 90-deg roof prism in a setup with (a) bare glass surfaces and (b) a metal coating of silver spray that can be washed off.[4] Due to the successive internal reflections at oblique incidence in the bare prism, the initially linearly polarized light becomes elliptically polarized, each partial wavefront having a different state of ellipticity. Since this corresponds to two components each being linearly polarized at 90 deg, one will observe two distinct interference systems through an analyzer, selectable by its angular orientation. With the $\lambda/2$ plate, the plane of polarization can be oriented symmetrically to the edge so that one part of the reflected beam appears in

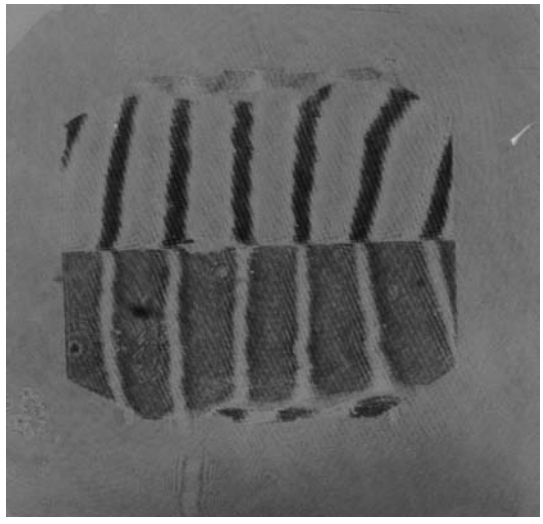

Figure 5.9(a) A roof prism with a bare surface (uncoated), tested with an interferometer, as in Fig. 5.6(a). The direction of polarization of the incoming beam can be deliberately chosen for contrast reversal (as shown), and vice versa.

Figure 5.9(b) Same setup and sample as in Fig. 5.9(a), except that now the prism is sprayed with a temporary metal flash (chemical silver[4]), eliminating phase jumps upon internal glass/metal reflection.

p polarization and the other in s polarization. This has no effect whatsoever on angular evaluation.

A note for the practitioner

In testing a roof edge prism as just described, one can easily find the angle of incidence, at which the angle of total internal reflection will be reached and metal coating will become superfluous. However, the coating will be needed

for comparing internal and external measurements, checking for possible inhomogeneity or front-surface errors.

An analyzer film in the image plane will be helpful, as it transmits in only one direction of polarization and will show no influence on the rotational position of the fringes obtained from a metal-coated prism. In the case of a bare, noncoated prism, upon rotation of the analyzer, fringes will vary in contrast between two extremes, as shown in Fig. 5.9(a).

In transitional positions of the analyzer, fringes of non–metal-coated prisms show a mutual offset [Figs. 5.10(a)–(d)] that is very deceiving. The

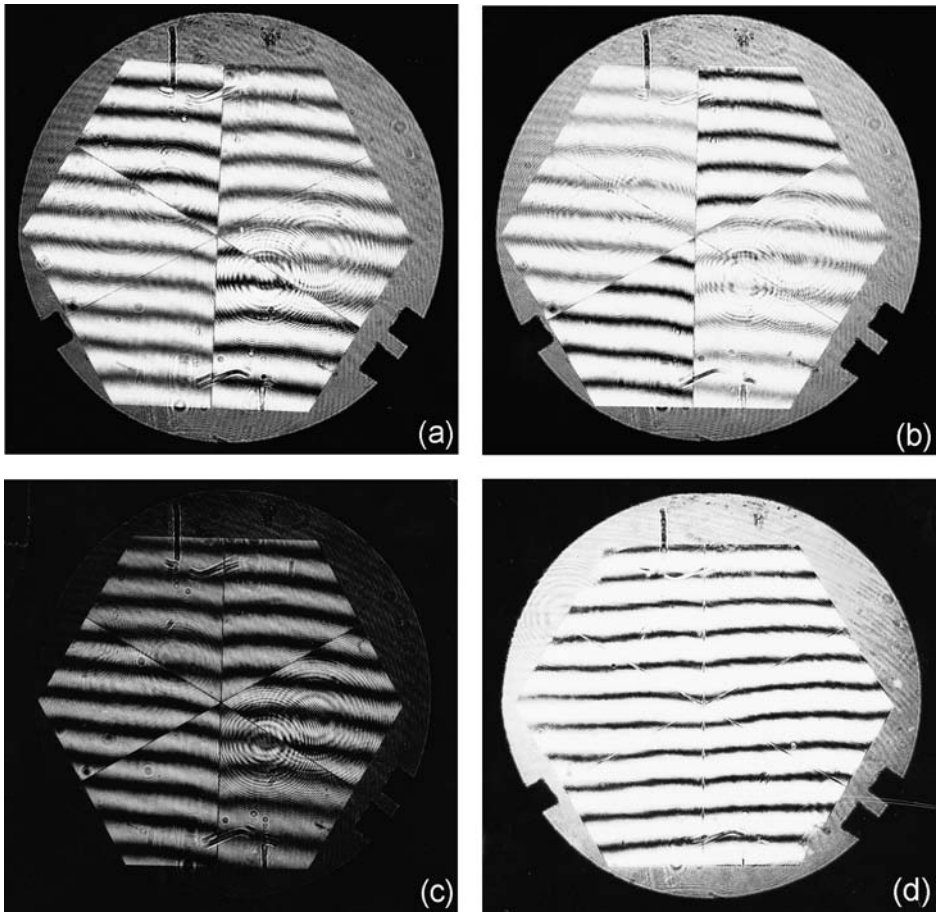

Figure 5.10 (a)–(c) Interferograms from non–metal-coated CCRs with a few deliberate changes in the settings of the incoming direction of the polarization and analyzer. (d) The same CCR, now metal coated, shows no phase jumps on the glass/metal interface, and the neighboring facets show fringes continuing across the edge. The wavefront reflected by the CCR looks like that reflected off of a plane mirror.

metal-coated prism shows no influence from the analyzer and thereby proves that there are no phase jumps at the reflecting surfaces [see Figs. 5.9(b) and 5.10(a)–(d)]. However, the analyzer will allow only the amplitude components of each beam to pass; therefore, the fringe profile will be less sharp, as can be seen when comparing the fringes in Figs. 5.9(a) and 5.9(b). In the vector diagram of Fig. 3.3(b), the successive vectors are all foreshortened, and the resulting sharpness (finesse) is reduced. In Chapter 10, we will see that this is an effective means of controlling the amplitude in multipass configurations.

The phase jumps upon three successive reflections at oblique incidence at the glass/air interface (as in the CCR), and the relation of the oblique incidence to the direction of polarization of the incoming beam entrains a kaleidoscopic variety of fringe offsets at the facet edges as well as a change of contrast between neighboring facets. Fringe spacing and inclination remain constant as the analyzer and/or polarizer are turned; Figs. 5.10(a)–(c) show an arbitrary selection of the direction of polarization, with the common property of no metal coating on any surface of the CCR. The metal coating (spray chemical silver[4]) creates a large difference, as seen in Fig. 5.10(d). The thickness of the silver coating has no influence on the internal glass/metal interface reflection.

Fascinating but technically useless, Figs. 5.10(a)–(c) are interferograms taken of an uncoated corner cube prism, showing both the phase mismatch between the facets of the trihedral prism and variable brightness, depending on the direction of incoming polarization. The analyzer might balance the contrast to be equal in some sectors, but phase jumps between facets remain. Only a silver metal coating [Fig. 5.10(d)] makes a significant difference.

Unlike the dihedral roof prism in Figs 5.9(a) and (b) that permits symmetrizing the polarization, the trihedral corner cube prism does not permit simultaneous adjustment of the direction of incoming polarization and the associated phase jumps to suit all three facets and their mirror image.

5.2 Function of the Trihedral Prism: the Corner Cube Prism (or CCR)

The CCR is the single most frequently used component in optical metrology when the angular errors are smaller than 1, or less than 0.2 arcsec. A typical set of specifications for commercially available CCRs is reproduced in Table 5.1. For the angular specifications shown in the table, the surface flatness of facets must be on the order of $\lambda/20$.

A CCR built from flat mirrors will autocollimate a collimated light bundle or a part of the light bundle from any longitudinal and/or lateral position, even allowing angular misplacements (where the spatial diagonal of the CCR is not parallel to the optical axis). The mathematics of this fascinating feature has found many descriptions in textbooks on instrumental optics[5] and in other publications.[6]

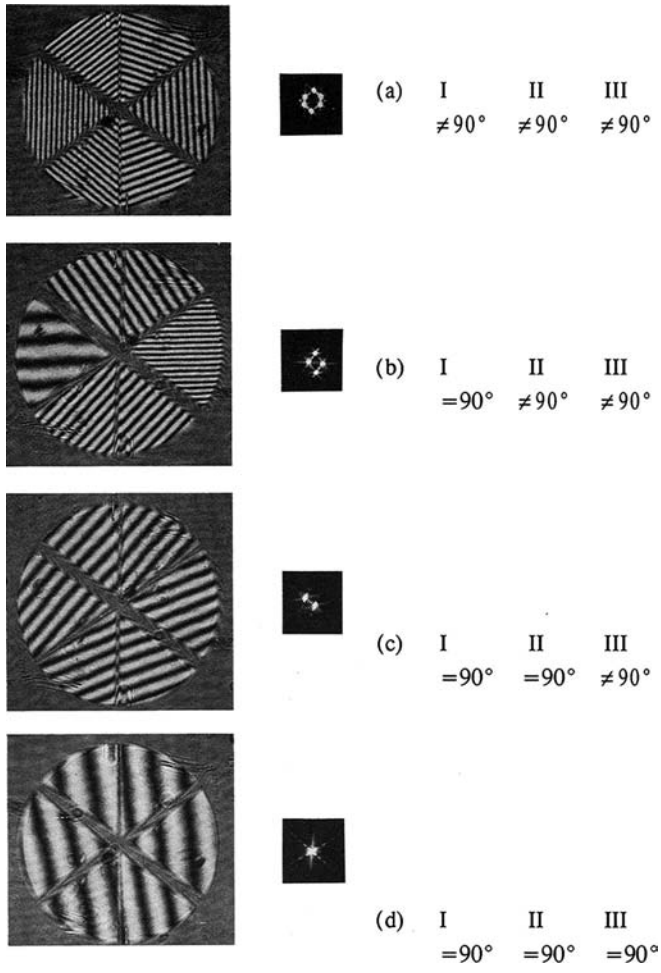

Figure 5.11 Interferograms of an adjustable trihedral mirror (or CCR) composed of three individually adjustable flat mirrors, each having an edge departure from 90 deg to the adjacent mirror on the order of 5–10 arcsec on (a) three edges, (b) two edges, (c) one edge, and (d) with no edge error. In (d), the interferogram now resembles that of a good, flat mirror. Interferograms are shown on the left, and the foci in the decollimation plane are shown in the middle column. The focus of a flat reference mirror is not shown.

Here we discuss the geometric features and angular tolerances of a trihedral mirror (or CCR) (see Fig. 5.11). A CCR is arranged by three perfectly flat mirrors, individually adjustable to form a 90-deg angle with each of the two neighboring mirrors. This arrangement is viewed in a two-beam Michelson interferometer [Fig. 5.19(a)]. Each dihedral edge is initially set for 90 deg, less about 20 arcsec, and acts a roof mirror with the neighboring facets. Edge error and signs are adjusted to be nearly equal. A circular stop is placed in front of the image for cosmetic purposes. Each roof edge and its

image, mirrored by the third facet, produce two foci in the decollimation plane. After some patient tweaking, one will see the six foci in the decollimation plane [Fig. 5.11(a)], which is what is seen in an autocollimator.

The reference mirror's focus (in Fig. 5.20) will be adjusted to the center of the six foci (its focus is not shown in the figures). Adjusting for some symmetry will create an interferogram as shown in Fig. 5.11(a). Each edge is seen twice in the image due to the dihedral geometry between the edge and its image on the opposite facet, acting as a fold mirror. Typical specifications for a trihedral prism (or CCR) are shown in Table 5.1.

Figure 5.11 shows the successive reduction to zero of each edge's error and the associated decollimated foci after retroreflection. The final interferogram [Fig. 5.11(d)] is obtained with the associated "one focus" and is the true retroreflection. The interference image of this latter corner cube mirror looks

Table 5.1 CCR specifications (PV is peak to valley). (Reprinted with permission from Prisms India.)

Standard No.	Parameter	Specification (Type-1) Refer to Drawing No. R1ASN-75-04-1-A4-CCRR-7001/Type-1
1	Glass material	Fused silica (Suprasil® from Hereaus, Germany)
2	Clear aperture	≥40 mm
3	Outer diameter – D1	40.4 mm +0.00/–0.02
4	Outer diameter – D2	42.8 mm +0.00/–0.02
5	Outer diameter – D3	40.4 mm +0.00/–0.02
6	Length/depth	30.264 mm +0.1/–0.0
7	Chamfering on surface S4	0.2 mm × 45 deg
8	Perpendicularity of the ground edge with respect to the entrance surface	<18 arcsec
9	Concentricity of ground edge with respect to the vertex	<0.02 mm
10	Circularity	<0.02 mm
11	Parallelism	<18 arcsec
12	Dihedral angle	90 deg ±0.5 arcsec. Dihedral angle error should be measured using an interferometer. The respective interferogram and angle error values should be provided along with the inspection report for each corner cube.
13	Surface figure (PV) on S1, S2, S3, and S4 surfaces	λ/10 @ λ = 633 nm. Surface figure should be measured using an interferometer. The respective interferogram and PV error values should be provided for each corner cube along with the inspection report.
14	Surface quality on S1, S2, S3, and S4 surfaces	40:20 scratch and dig
15	Surface roughness on S1, S2, S3, and S4 surfaces	≤1 nm
16	Homogeneity of refractive index	2×10^{-6} Supplier provides a fused-silica material certificate from Hereaus, Germany with the following test data: homogeneity of refractive index and melt data for the procured batch of material.

like that of an optical flat, as will the focus if there were not diffraction at the three edges. A separate record of the six foci in Fig. 5.11(a), but now including the central focus of the reference beam, is reproduced in Fig. 5.21. An overwhelming, otherwise intolerable, influence of diffraction at the three wide edges is recognized.

The trihedral mirror arrangement and corner cube prism reflector likewise exhibit remarkable features:

- The law of reflection (the angle of incidence equals the angle of reflection) is not valid for the assembly. The assembly can be inclined and shifted longitudinally and laterally, without changing the location of the focus in the defocusing plane, and even without changing the interferogram.
- The entering wavefront becomes inverted around the center. Only a rotation of the assembly around the beam's axis (with the edges rotating 1:1) can be noticed in the image.
- The three angular errors can be reduced to zero, so a perfectly collimated beam becomes autocollimated as it would from a flat mirror. Within the interferometer, the light is returned to the source, through the pinhole, into the laser. The laser begins pumping if multiple reflections occur between the interferometer and the laser's front mirror. This occurs in an enhanced fashion at certain distances where the distance between the fixture and the light source is a multiple of the length of the laser tube.
- A beam's axis (represented by a plain, nonexpanded laser beam) that becomes parallel displaced by an amount S will be retroreflected with $2S$ and will always be inverted around the center of the CCR. Some intriguing technical applications result from this feature (see Section 7.5.3). A ray entering the front surface of a CCR will be mirrored at the center of its place of exit (Fig. 5.13).
- In a large autocollimation setup, any beam section caught by a much smaller CCR is always returned to the focus. Pure lateral displacement (where the optical axis is the same as the motion that is orthogonal to the optical axis) will not change the optical path length from the CCR to the light source. This is recognizable in the interferogram by a "no fringe count" [Fig. 5.23(c)]. Only longitudinal displacement, on axis and skewed, results in fringes walking. Counting fringes is the basis for distance/change measurement.
- There is a distinct difference between a CCR mirror and a CCR prism. Rotating a CCR mirror around the optical axis of an interferometer will *not* alter the interferogram set by the interferometer's reference mirror (see Fig. 5.18). Rotating a CCR prism in the same way *will* alter the interferogram, except in the rare case where the spatial diagonal of the CCR is orthogonal to the prism's flat front surface.

5.2.1 Retroreflectors in practice

5.2.1.1 Illustrative micromachined retroreflectors

Although 99% of CCRs are manufactured from glass, we begin our detailing of CCR generation with a description of an assembly of three metal (aluminum) mirrors, micromachined and screwed together. An application of metal micromachined CCRs is in an IR cryogenic space spectrometer. The entrance aperture of the spectrometer is 140 mm, and its weight is minimized and qualified for liquid helium. No retrofitting is allowed[7] in this device from Max Planck Institute/Kaiser & Threde. The base of the CCR is shown in detail with edges as sharp as possible and λ/10 surfaces (where relaxation is λ NIR). The three components of the CCR include a tapered base, which carries two side flanks, as seen in Fig. 5.12(a). The reflecting surfaces were fly cut to λ/10, ($\lambda = 632$ nm, orthogonal incidence) and have through-holes for fixing the flanks. The flanks carry relief feet that are screwed on to protrude less than 0.1 mm out of the base of the side flanks. They were micromachined on an angular dividing head to be orthogonal to the flank. Two 45-deg flanks forming the one 90-deg angle extend to the rear. These are also micromachined and connected by screws. Relief-like annular zones surround the holes for screw-on connection of the flanks.

The steps of the trial-and-error assembly of this CCR are reproduced in Figs. 5.12(a)–(d). The trial-and-error phase was substantially reduced by first diamond machining the feet of the mirror component in order to make their small surfaces coplanar (requiring no wedging and subsequent squeezing or deformation). Then, the component was mounted on a dividing head such that the feet (mirror finished) can be observed by an interferometer for nulling and for 90-deg setting. The reader might observe the much-reduced gap at the three edges in Fig. 5.12(d), compared to the same gaps in (b) and (c).

5.2.1.2 Calibration of distance change: predominant application

Autocollimation by a CCR has become the basis of optical measurement of changes in distance to the collimating focus by fringe counting. Zero calibration using white light, combined with fringe counting (gauge block comparator), was well established long before the benevolent laser became the undebatable light source. Nevertheless, one might enjoy the encompassing descriptions in *Handbook of Physics*.[8] A summary of length calibration through 1994 is found in Ref. 9 or in the equipment user manuals by such well-known laser gauge suppliers as Hewlett-Packard or Zygo.

5.2.1.3 Using the CCR's lateral displacement in linometry

The optical axis of a (laser) beam retroreflected by a CCR will be offset by an amount of $2S$ if the CCR becomes laterally displaced for S. The direction of offset is the inversion line, which connects the point of entry on the front face

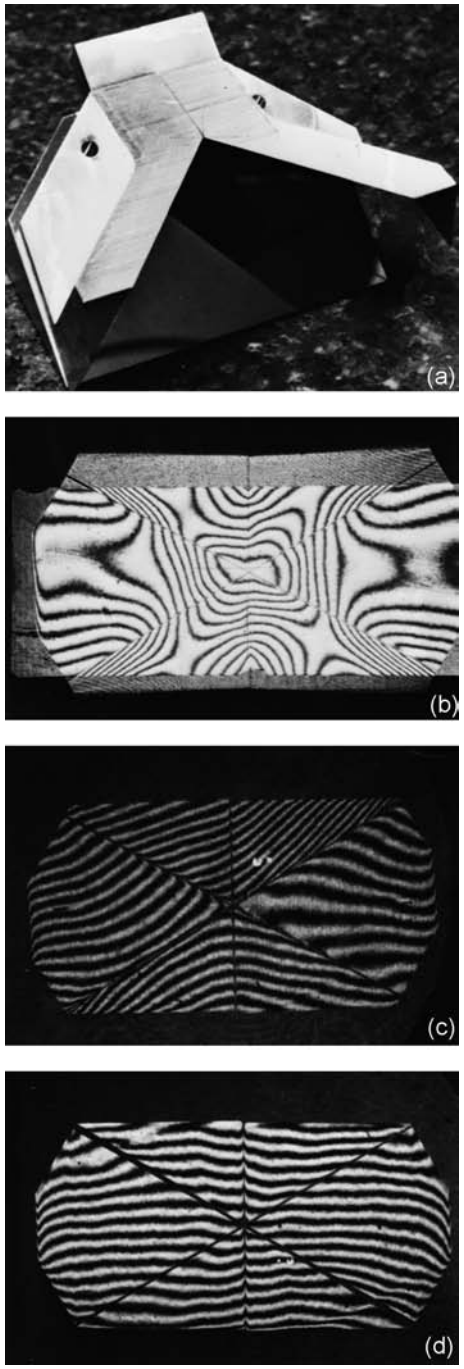

Figure 5.12(a)–(d) Three phases of trial and error in the assembly of a CCR from AlMn 4, micromachined from three diamond fly-cut components. In (d) one recognizes the material deformation by the tapped blind holes on the rear side of the mirror component. No changes are reported upon repeated cooling to liquid helium.

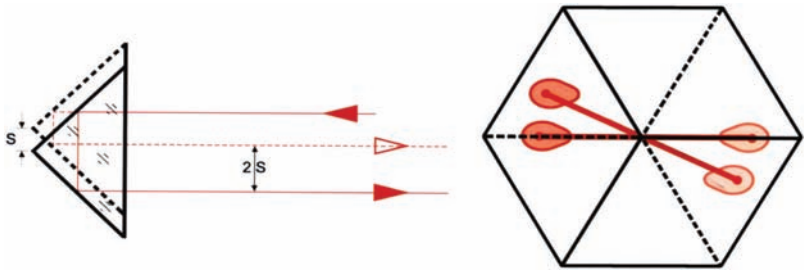

Figure 5.13 The front view of a CCR with entry locations of a laser beam and the inverted locations of exit, after three internal reflections each. An asymmetric profile of the laser beam becomes inverted as well. Diffraction will occur at the three edges, however sharp they might be. The relative brightness of the diffraction might not be negligible with applications of a non-expanded laser beam crossing an edge. Figure 5.21 shows the record of a diffraction pattern obtained with a laser beam expanded to about 20 mm in diameter directed to the center of a 40-mm wide CCR.

of the CCR with the axis (the spatial diagonal of the CCR). A possible asymmetric shape of the incoming laser beam will be inverted around the CCR's axis as well, as shown in Fig. 5.13.

The relevance of this rather trivial feature lies in technical applications; Fig. 5.13 shows the beam reflected by a CCR or by any 90-deg roof angle being laterally displaced by $2S(x,y)$ if the CCR is laterally displaced for $S(-x,-y)$ only—independent of z. Immediately, one thinks of detecting the cross motion of a slide whose linear travel z is measured with a distance interferometer using a CCR. For all practical purposes, we look at $S(x)$ only. Common values of the ultraprecision linear slide's cross motion range from below 0.2 μm (acceptable) to 5 μm (catastrophic). The lines drawn in Fig. 5.13 represent the plain laser beam carrying said lateral displacement signal.

The two empty arrows are a constant calibration factor determined by the more or less arbitrary initial setup of the stationary and moving parts of the metrology system. The measurement of the beam's lateral position changes was found quite easily with the ready-to-use CCD Laser Micrometer, VG Series supplied by Keyence.[10]

5.2.1.4 Comments on CCR displacement applications

The task of measuring a straight line in space has prompted many solutions applicable to metrology and to machine tools. Most of these solutions are based on the use of quadrant photodetectors moved along a laser beam. A resolution of 0.001 mm has gained widespread acceptance as the best possible economic lateral resolution. An instrumental solution for the integration of cross-motion detection into the distance-change-measuring interferometer has not yet been found today.

Conversion of an *absolute* lateral beam position measurement (by a PSD) into a much-preferred *differential* measurement is illustrated in Fig. 5.14(a). A small reverting prism device (a two-beam reverting transmission interferometer) duplicates the entering beam to create two parallel beams that change their lateral separation in proportion to 4*S*. The beam profile (Fig. 5.13) is inverted as well.

Further enhancement of the sensitivity to lateral displacement (by a factor of 8) is demonstrated in Fig. 5.14(b). Two CCRs mounted (wrung) to a common base together with two auxiliary mirrors (90-deg roof edge) allow a lateral displacement *S* of the twin CCRs to become a differential of 8*S*. The preference of a CCR over a roof prism, which will perform the conversion on one cross axis, is based on the CCR's insensitivity to inclinations. This feature is not a characteristic of the much simpler and less-expensive roof prism.

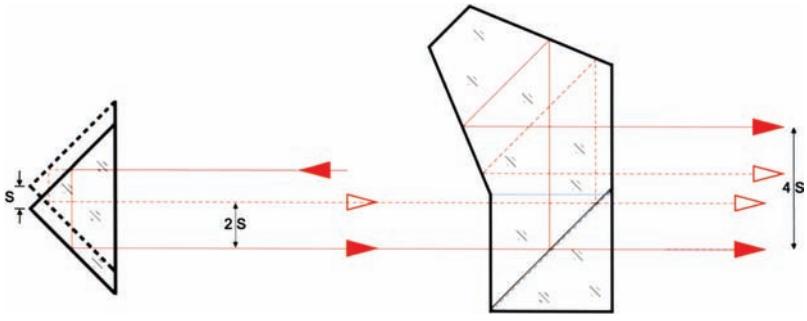

Figure 5.14(a) A CCR that is laterally displaced across an optical axis by an amount *S* will reflect the incoming beam in a laterally displaced manner, parallel to itself by 2*S*. 1 μm translates into 2 μm. A compact transmission-reverting interferometer transmits two beams with an initial lateral separation C, which is a constant given by the initial alignment (the two empty arrowheads). A lateral movement of the CCR causes the lateral separation of the two transmitted beams to become increased or decreased by an amount of 4*S*.

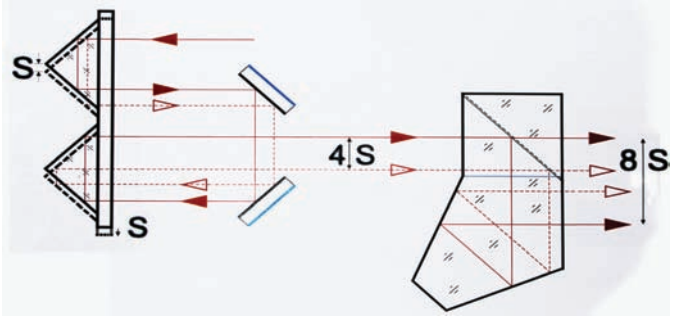

Figure 5.14(b) A configuration that doubles the sensitivity to cross motion by making the laser beam traverse two CCRs. Two 90-deg prisms or retroreflectors contacted to a glass basis, together with two flat mirrors as shown, will produce two beams with a differential beam separation of 8*S*.

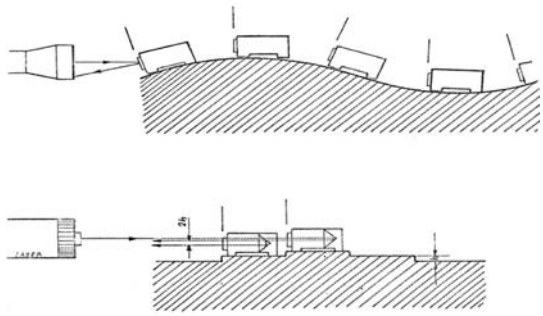

Figure 5.15(a) Schematic comparison of an autocollimator (top) versus a linometer (bottom).

Numerous applications of the linometer method exist in industry. Some examples are briefly described here. The sketch in Fig. 5.15(a) illustrates the much desired feature of autocollimator-compatible equipment: the ability to measure the cross motions of the linear slide. No such ready-to-use equipment is known to the author to be on the market. However, the lateral beam differential displacement method has two dedicated applications: The linometer[11] is used to measure the centration of bearing bores for crank shafts in large (8-m) diesel engines. The CCR, mounted in a hydraulic expansion mandril, is successively inserted into the different bores, and the return beam's position is measured. *X*/*Y* data result from rotating the emitter/sensor head 90 deg. The second application involves measurement of the straightness of a cylinder line of large diameter, as in 4-m-long glazing rollers or calendar drums. The CCR housing rides with an airborne slide atop the crest of the drum. The air bearing is molded off of a good section of the drum. Departure from a virtual line (stretched between flange positions and chosen as the reference at the two ends of the drum) became measurable on the order of 0.001 m using the cross-motion detector on top of the slide.

A note on the literature

The problem of measuring and establishing a straight line has prompted a wealth of experimental solutions. Among these solutions are van Heel's optical diffraction methods[12] (developed in pre-laser times), which are fascinating due to their accuracy with low cost (slits and gratings) and simplicity. A more recent solution to the straight line problem, outlined by R. F. Schenz, L. V. Griffith, and G. E. Sommargren,[13] uses the diffraction pattern formed behind an opaque sphere, illuminated by a plane wave. The diffraction pattern includes a central spot that can be followed over a long distance, the Poisson line. Finally, H. D. Betz describes an unusual method that uses intensity asymmetries and does not require high-resolution optics.[14]

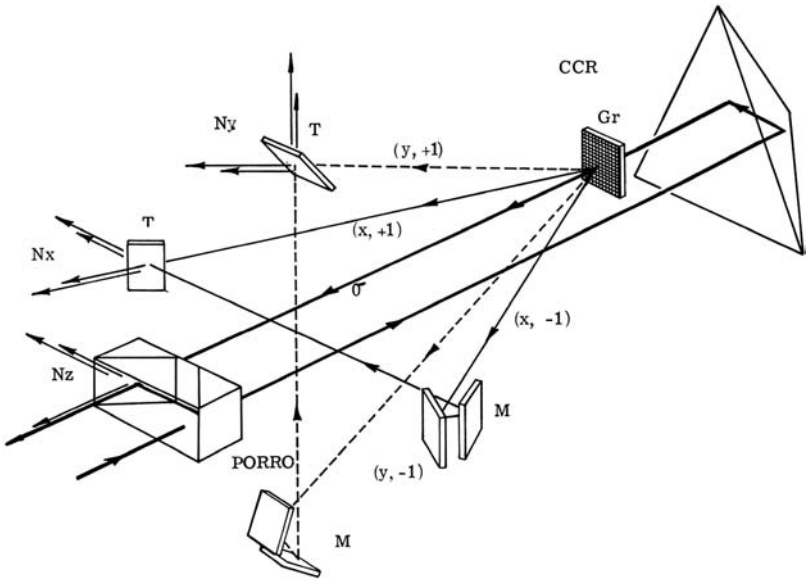

Figure 5.15(b) Promotional concept of a 3D measurement using a CCR that moves along the optical axis and a stationary diffraction transmission grating that acts as a beamsplitter grating.

5.2.1.5 3D metrology with a CCR

Long-standing tasks in precision engineering are the combination of laser distance change measurement using the CCR with simultaneous measurement of small lateral error motions along the work axis and of small roll angles. Some imagination might be permitted and required.

Breadboard experiments confirmed the conceptual approach on a 2D basis, as well. An example experiment is shown in the setup in Fig. 5.15(b). A 50-line-per-mm small moiré/Ronchi grating and the Porro detector assembly are fixed on a base and adjusted for first-order recombination, as is common practice in diffraction glass scale reading. A sinusoidal fringe movement is obtained upon lateral CCR x displacement ($2x$ on the outgoing beam). As is customary, the zeroth-order beam is used for distance change.

5.2.1.6 Model of an adjustable CCR for machine tool alignment

Section 5.2 presented the assembly of three individual flat mirrors to form a perfect CCR. This procedure becomes a routine exercise in precision engineering: Three linear axes are aligned to be orthogonal to each other; or, two spindle axes intersect in a common point, and the second spindle axis is made parallel to the face mirror of the first spindle. Upon in-feeding or nutating the second spindle within the plane orthogonal to the first spindle's

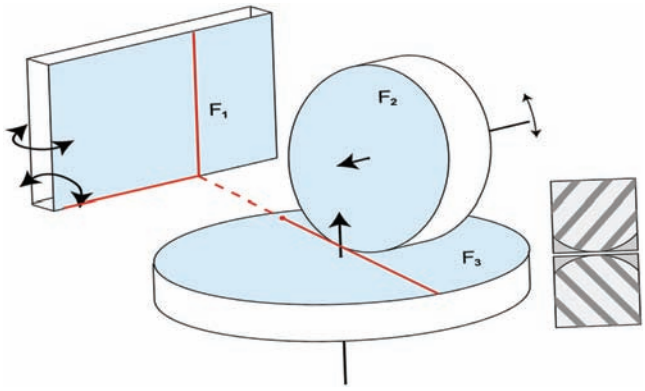

Figure 5.16(a) Schematic representation of the orthogonality alignment procedure. Mirrors F_2 and F_3 represent the two spindle axes. Mirror F_1 represents the orthogonal to the base for later completion of a corner cube.

axis, the point of intersection of the axes will not be lost. Such tasks occur during the assembly of goniometers [Fig. 5.16(a)] or of aspherical generators.

In carrying out that alignment task, it is instrumental to verify the orthogonality of the two individual spindle axes by the orthogonality of one mirror adjusted on each axis of rotation (like a turn table and a grinding spindle). Both of these mirrors must be able to be aligned; in the last phases of the iterative approach to zero, the spindle's tilt motion should be on the order of 0.1 arcsec. Thereafter, the task is to make the angle between the two flats be 90 deg.

Figure 5.16(a) shows two spindles, one with a rotary encoder mounted onto a 400-mm ultra-precision turntable. Each spindle carries its precision-alignable flat mirror, the two forming the abovementioned nominal 90-deg angle. These two representative mirrors F_2 and F_3 are shown schematically in the right side of Fig. 5.16(b), together with a typical interferogram obtained in the process of successively reducing the departures from 90 deg. The third mirror F_1 can be aligned by nutation and rotation of the F_3 component on the granite base for each angle between F_1 and the two components F_2 and F_3 to form a 90-deg angle. Both 90-deg angles can be tested separately, as illustrated in Fig. 5.16(c), employing the evaluation instructions given in Fig. 5.5 [center and bottom]. Hub motion and tilt can be tested in the same manner.

The turning of only one component (of F_2 and F_3) permits the measurement of tilt errors of the turning device. A linear axis that is parallel to the base and orthogonal to the spindle mirror can thus be arranged to run parallel to the base and spindle axis with less than 1-arcsec deviation. The three components form the perfect corner cube, once the mirror block has been moved closer to center [compare the left side to the right side of Fig. 5.16(b)]. All angles are measured by an interferometer, as in the CCR metrology described above. This could be a helpful calibration instrument and procedure for measuring and machining equipment.

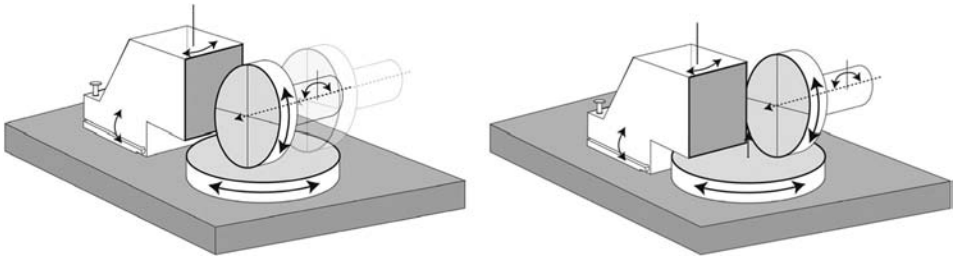

Figure 5.16(b) (left) Virtual components on a granite base plate form an experimental trihedron (CCR). The rugged block (darker-gray flat, square mirror) has a tilt provision to make its normal parallel to a precision granite base. The granite base also serves as the air-bearing planar reference of a turntable (the lighter-gray round surface) with its surface precision finished *in situ* to operate without measurable axial error. The second lighter-gray round flat mirror surface represents the reference face plane of an air-bearing work spindle. (right) The latter can be nutated such that its axis is parallel to the base, and the spindle can be protruded, maintaining its axis parallel to the base. The axis of the rotating disk is always orthogonal to the base.

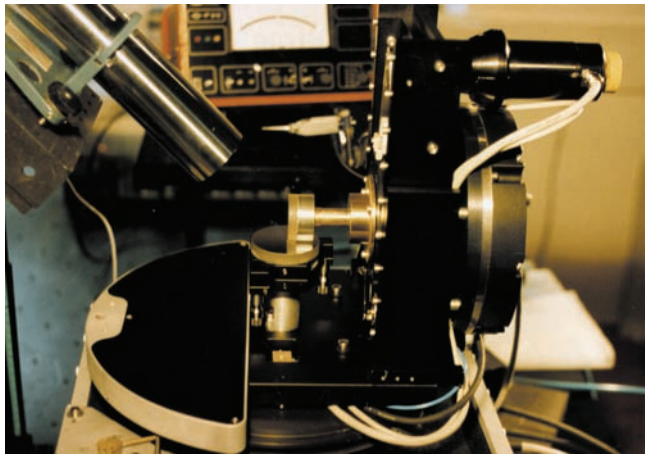

Figure 5.16(c) Autocollimator used for 90-deg pre-alignment. The interferometer measures angular errors less than 2 arcsec, as described in Section 5.1.3, by measuring angular error motions of two air-bearing spindles assembled to become a precision goniometer with less than 2-arcsec specified departure from the orthogonality of the axes.

5.2.1.7 Measuring tilt motion of one adjustable mirror

The enhanced sensitivity to angular errors of 90-deg angles, arranged with an adjustable flat reference mirror, finds useful application to the measurement of angular error motions of air-bearing spindles and of turntables, or combinations thereof. The actual goniometer, shown in Fig. 5.16(c), requires the axis of an air-bearing spindle to be precisely orthogonal to the axis of the likewise air-bearing table, which carries said spindle. For this task, the sample

spindle carries a flat F_2 on its nose, free of wobble and with the finest 2D adjustment features. A second flat F_3 is brought up from the center of the turntable, wobble free, as well. Figure 5.16(a) schematically illustrates this combination of mirrors and also shows an interferogram like one that will be seen in the process of iteratively arriving at 90 deg. Angle orthogonality is indicated by a fringe pattern looking like one of a good flat. This pattern must remain stable upon rotation of one or both together.

The 90-deg angle created by F_2 and F_3 is now observed by an autocollimator or, better, an interference autocollimator. Turning the first spindle, then the second spindle, in an alternating fashion will gradually allow both mirrors to represent residual (or no) angular error motion. During that process, the orthogonality of both rotary axes is obtained with tolerable effort. Now, the spindle's angular motion errors can be attributed by equating them to 90-deg angular errors, divided by 4. Choosing an alignment of fringes per Fig. 5.5 [parts (b) or (c)] is practical.

A third flat F_1 affixed to the ground will be adjustable in order to make the normal to F_1 be parallel to both F_2 and F_3 in two axes. These two axes, being collinear with the two spindle axes, complete the CCR. We now take the last step and apply the interferometer configuration seen in Fig. 5.20(a). Residual wobble (angular error motion) will be seen magnified $10\times$ in the interferogram compared to a measurement with only one reflection at 0-deg angle of incidence.

The assembly of a CCR from individual mirrors finds an attractive metrologic application in autocollimation metrology for small angular motion. Interferograms such as those in Fig. 5.11(b) will be obtained by inclination of one of the three mirrors, actuating only one of the two possible angles, without altering the second one. A solid body bending flexure makes this possible.

This modified CCR will return a collimated beam to the autocollimator, independent of its lateral and angular position. The uniaxial inclinations of the one mirror around one edge only (1 of 6) will be derived from changes in its interferogram, as in Fig. 5.11(b). This angular change is measured with an enhanced sensitivity compared to common autocollimation off of a flat mirror inclined to the same degree: $\varepsilon = (0.3)\,\delta$, where δ is measured from an interferogram in arcsec.

5.2.1.8 CCR solid-block inverting shear interferometer (ISI)

The Michelson interferometer, shown in Fig. 5.18(a), can be compacted into one solid block by placing a beamsplitter coating onto the CCR's front surface [Fig. 5.17(a)]. To avoid irritating polarization effects, one may metal coat the trihedral surfaces. With reflectance of the CCR near 100%, the beamsplitter's reflectance is recommended to be around 35%. This will allow suppression of the brightness of successive internal reflections and will give a two-beam-like profile to the fringes.

Given a perfect plane wavefront, the fringes will be straight, and the CCR's orientation will be indicated by the spacing and the direction (orthogonal to

fringes) relative to the optical axis. Due to inversion upon internal reflection, the device reacts very sensitively upon the wavefront's departure from flatness, as is illustrated qualitatively in Figs. 5.17(b) and (c).

An ISI permits one to simultaneously observe autocollimation and departure from perfect collimation. Its optimal use is with an interference

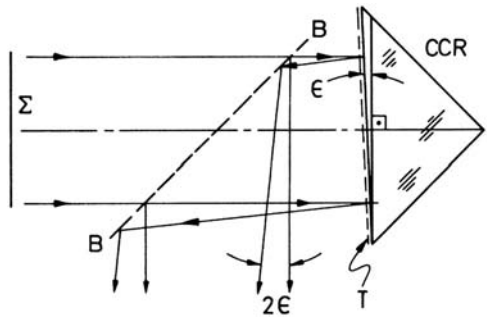

Figure 5.17(a) An autocollimating solid-block inverting shear interferometer (ISI).

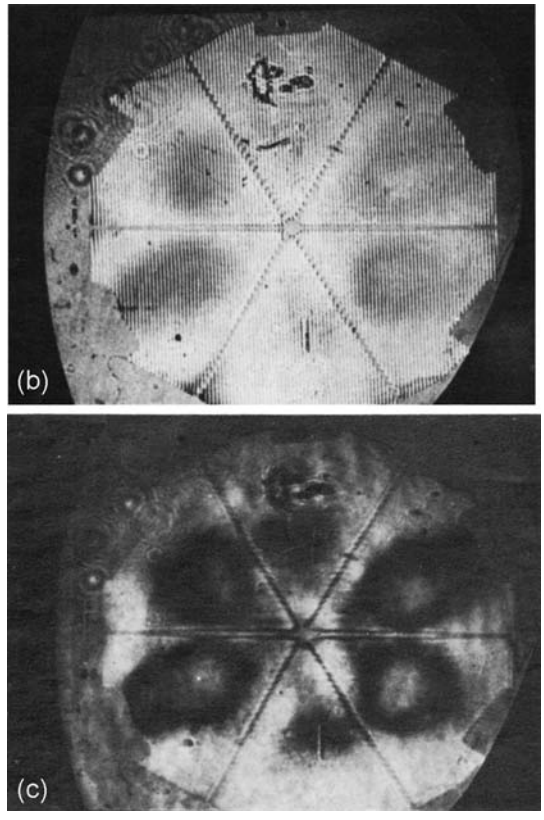

Figure 5.17(b) and (c) Interference autocollimation by the reflector according to Fig. 5.17(a). Uniform tint in the six sectors indicates a flat wavefront entering the CCR in precise orthogonality to the front surface of the CCR, or, in another case, parallel to the spatial diagonal of that CCR.

autocollimator with both defocus plane and image plane display on a monitor. Another useful application is the metrology of air-bearing spindles. An ISI placed centrally on top of an air-bearing turntable allows for simultaneous detection of hub and tilt motions upon rotation of the turntable. More details about cross motion will be presented in Section 5.2.3.1.

5.2.1.9 Application of a CCR in centration measurement

An interesting CCR application results from the knowledge gained in Section 5.2.3. A CCR placed (a) onto the center of an air-bearing rotary table with the assembly observed under a large-diameter Fizeau interferometer will show a straight fringe pattern, as in Fig. 5.18(b), indicating good collimation. In the case of no axial lift (no error motion), fringes remain stationary upon rotation of the air-bearing table. Otherwise, one will derive an error representing both an axial and a tilt component of angular error motion. In that latter case (b), the CCR will be placed at the periphery of the table. Regardless of its seat (even on a rough, unfinished surface) and in case of good collimation, one will obtain the same fringe pattern as in (a). Upon rotation of the table, this pattern will begin to "pump." The tilt motion will be derived from the number of fringes walking by the CCR. The fringe count between minimum at 0 deg and maximum at 180 deg presents the angular tilt motion and is independent of the actual collinearity of the axes of the spindle/turntable and of the

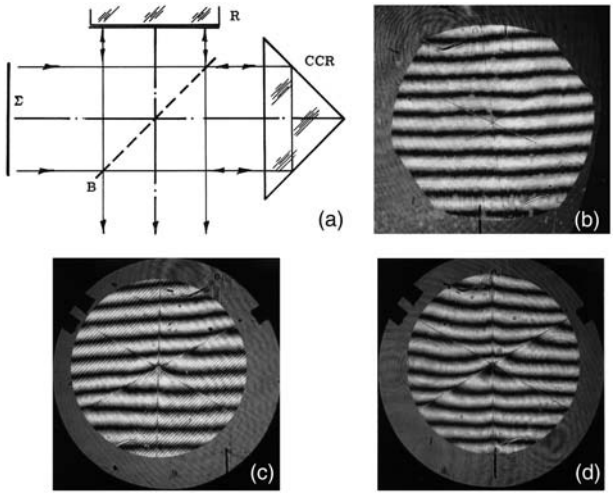

Figure 5.18 Testing a CCR in a Michelson two-beam interferometer: (a) Schematic interferometer; note the wavefront inversion by the CCR. (b) A near-perfect CCR, similar to a λ/10 flat mirror. (c) The limit of acceptability. (d) Not acceptable: edge error (rolled-off edges) and two angular errors.

interferometer. The only prerequisite validating this test is the perfect collimation of the interferometer (see Section 5.2.3).

5.2.2 Quality assurance of the CCR

Corner cube prisms need a glass with refractive index inhomogeneities of $\Delta n < 10^{-5}$. This specification must be met in lateral X and Y extensions and in the Z direction as well. The reason for this requirement is as follows: The light beam will travel within the CCR in directions both orthogonal to the front face and parallel to same. Therefore, the raw material needs to be tested in three directions. In Section 7.6, the reader will find information on homogeneity measurement, and in Section 5.2.6 information on separating surface errors from angular errors on cubes.

To prepare the CCR, the manufacturing process starts with production of cubes with angles as near as possible to 90 deg and surfaces flat to λ/20. The cubes will serve in the homogeneity metrology. A subsequent cut through the spatial diagonal of the cube will provide two CCR prism blanks. The blanks will undergo a grinding of the outer dimensions to customers' requirements.

The preferred internal interferometric measurement of angular errors might be done in a two-beam Michelson interferometer [Fig. 5.18(a)]. A prerequisite to internal testing is finishing of the front surface, again to λ/20 flatness. The angular orientation of the front surface, orthogonal to the spatial diagonal of cube, is quite demanding. Mounting the finished CCR on an air-bearing spindle and turning it under an interferometer allows detection of a small wedge between the front surface and the retroreflected wavefront. The spindle itself must rotate with less than 0.1-arcsec wobble.

Three interferograms of typical CCRs are reproduced in Fig. 5.18 [parts (b)–(d)]. An interferometric technique for separating edge error from flatness errors is treated in Section 5.2.6. The fringes of a CCR in the two-beam interferometer may be aligned to be opportune for evaluation, e.g., orthogonal to one edge and with respect to its image (method C in Fig. 5.5). Within the two other pairs of the six image sectors, the fringes at the beginning of the corrective work will then be oriented in an unpredictable, less favorable way. Fiducial marks on the prism and in the interferometer field are helpful for repetitive alignment and for edge/image correlation. Typical examples are shown in Fig. 5.10.

The departure from 90 deg or edge error ε relates to the ridge on the wavefront δ by

$$\varepsilon = \frac{\delta}{4n\cos\alpha} = \frac{\delta}{4.9} \sim \delta \cdot 0.2, \tag{5.3}$$

where n is the refractive index of the glass used (1.5 for estimating); α is the angle of incidence to the edge within the CCR (35 deg), and $\cos\alpha \sim 0.82$; δ is

the ridge angle on the wavefront measured in the interferogram, using method C in Fig. 5.5(c); and ε is the departure from 90 deg of an edge ($\varepsilon \sim 0.2\delta$).

Using a common polishing technique, one may expect an accuracy of 0.2 arcsec with an experimental resolution in the interferogram reading equal to 1 arcsec. Because of wavefront inversion, one might expect errors on the incoming wavefront to be confused with wavefronts on the prism's front face or inside. The distinction can be made by laterally shifting the CCR within the interferometer field [Fig. 5.22(b)]. A temporary chemical silver spray coating[4] applied to the front surface for testing the same will allow detection of the front surface's departures from flatness.

One-half of the retroreflected beam may be returned for a second internal reflection by an external flat mirror M, as shown in Fig. 5.19(a). This is comparable to testing roof angle prisms (Section 5.1.3.) Together with a beamsplitter T in Fig. 5.19(a), a multiple-beam Fizeau interferometer with a very long cavity is accomplished. When unfolded, this configuration is equivalent to that in Fig. 5.6.

The coatings on T and M might be on the same flat, but the use of two separate mirrors, as in Fig. 5.19(a), was found to be more practical for tests prior to final finishing. The gain in sensitivity by this double-pass Fizeau configuration is a factor of 2, compared to the one edge viewed. Allowing a fringe reading accuracy $\Delta P/P$ of 0.1 and with $n \approx 1.5$, one obtains $\varepsilon \approx (0.15/n) \cdot \delta = 0.1\delta$, where δ is the angle determined on the wavefront, and ε is the angular error on the part.

Evidently, compared to the single-pass technique [as in the Michelson interferometer [Fig. 5.18(a)], this double-pass technique makes sense only with "perfect" surfaces on the facets of the CCR. Additionally, the wavefront reversion occurring several times (7/1) in the single-pass configuration will be cancelled in the double-pass long-path Fizeau configuration.

The interferogram in Fig. 5.19(b) shows good flatness of facets, as well as of T, and an excellent sharp edge, but an angular error of 2 arcsec. This is not a regular occurrence, as compared to Fig. 5.19(c), which shows the more

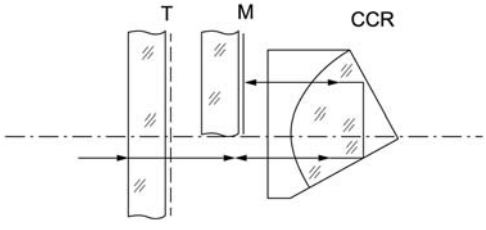

Figure 5.19(a) Schematic of the Fizeau technique used on a CCR. The double-pass (long-path Fizeau) mirror M returns the beam a second time across one edge. T is the Fizeau reference, which is wide enough to observe parallelism between T and M. The CCR is not metallized. Compared to a single-pass Michelson, the sensitivity is doubled to $\varepsilon \sim 0.1\ \delta$.

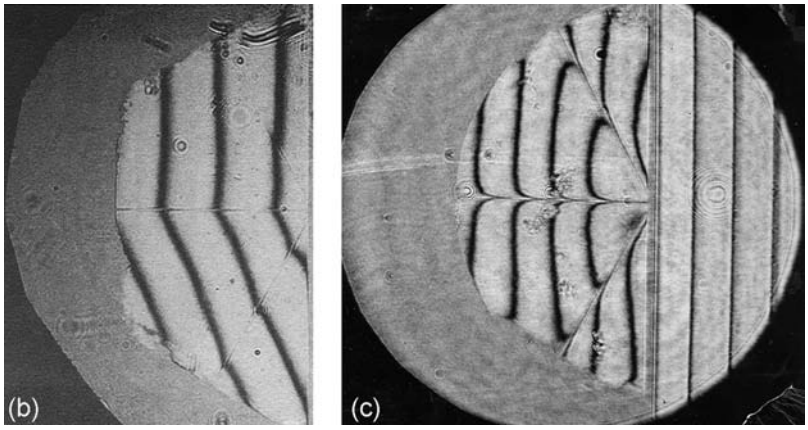

Figure 5.19(b) and (c) Both samples are not acceptable. (a) Facets include a 2-arcsec departure from 90 deg: a perfect edge without roll off. (b) Rolled-off edge and flatness departure; no uniform edge angle can be determined due to the relatively large area occupied by the roll off.

common case. From Fig. 5.19(c) one may visually interpret poor edge quality (roll off is approximately one-half of a fringe, with 0.06 μm on either of only one facet, or 0.03 μm on each of the two facets). Likewise, one may interpret poor facet flatness near the prism's center (again, on both or only one facet) and edge angle ε in the better zone of $\varepsilon \leq 0.1$ arcsec.

The right half of Fig. 5.19(c) shows the straight Fizeau fringes between T and M. These fringes are parallel to those adjusted to be orthogonal to the edge, within the prism, and nearly equally spaced. The fringes of the two interlaced Fizeau signals correct autocollimation from the doubly passed CCR. The fringe equivalent in the CCR's half-field is $S = \lambda/(2 \bullet 2 \bullet \cos u) = 0.125$ μm. The amount Δt of roll off is therefore $\Delta t = S \bullet (\Delta P/P) \sim 0.06$ μm; again, ~0.06 μm on only one of two facets, or ~0.03 μm on each facet. The aspect of Fig. 5.19(d) calls for some interpretation. The single-pass interferogram, as seen in a Michelson setup, shows the edge between two facets and its image, mirrored by the third facet, the latter acting as a flat fold mirror having no influence on the image of the edge. It cannot be concluded from this interferogram which one of the two facets carries the roll off. This question can be answered only by an external interferogram, as in Fig. 5.26(a). The rolled-down zone acts as a small, cylindrical convex lens stripe, blending asymptotically into the flat substance. Removing the roll off means, therefore, removing material from the larger part of the "delinquent" facet that is parallel to itself.

Notes of reiteration

1. The symmetric distribution of errors seen on the reflected wavefront requires separation using methods to be described in Section 5.2.6. Additionally, in Fig. 5.20, one must still ascertain that there is no hidden

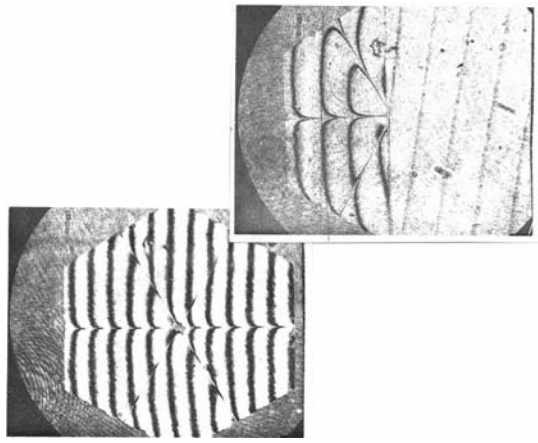

Figure 5.19(d) Comparison of a single-path with a double-path configuration. The rolled-down edges as seen in the interferograms insinuate that this roll off occurs on both facets forming that edge. The rolls on the fringes (rolled down), although unwanted and annoying, provide valuable information for the continued polishing of the final substance. The fringe equivalent for double pass is $S = 0.125$ μm. The cube test [Figs. 5.26(a)–(c)] will show the two facets of one 90-deg roof separated but in a common interferogram record.

error due to wavefront reversion. Both prisms displayed in Figs. 5.19(b) and (c) are failures.

2. Edges and their mirror images produce diffractions, as does any minute scratch in a surface, no matter how small. Edges that are still noticeable in a qualitative manner will produce a diffraction pattern around the focus of the decollimated beam (Fig. 5.20).

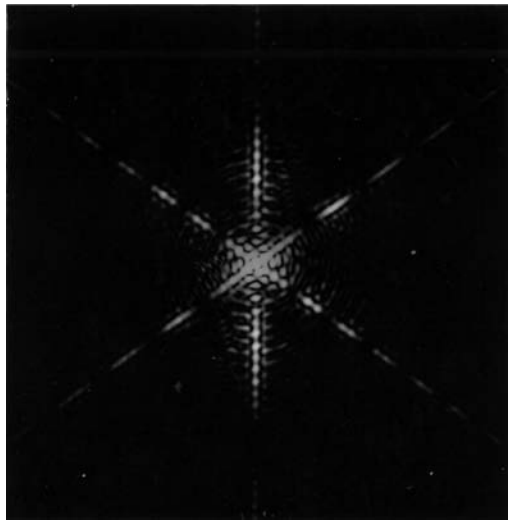

Figure 5.20 The defocus produced by a CRR with nonsharp, beveled edges.

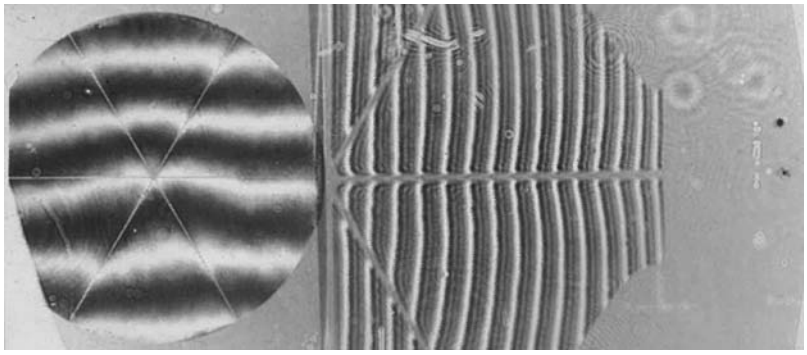

Figure 5.21(a) CCR in on-axis illumination indicates that alpha equals zero.

5.2.2.1 Summary of sensitivity enhancement by double pass

Due to the large distance T/M, the walkoff can grow large, despite both flat reference mirrors being used at normal incidence. The "to be flat" mirror M in Fig. 5.19(a) will reflect the beam $2n$ times (n is the order of reflection), and any residual curvature will generate walkoff. If M and T are technically perfectly flat, the fringe deformation $\Delta P/P$ will relate to F only. In case a higher order of reflection n is used, the walkoff on F can be reduced experimentally by off-axis illumination; in most practical situations the off-axis angle will be less than 1 arcmin [see Figs. 10.3(a) and (b)]. Departure from 90 deg ε of the roof mirror edge in Fig. 5.21(a) will give: $\varepsilon = \delta/(\cos\alpha)$ (mirror) and $\varepsilon = \delta/(8n\cos\alpha)$ (prism), where n is the index of refraction. Angle α on the edge of a CCR is 35 deg; therefore, edge error ε is 0.1δ, as measured from the interferogram. This holds for normal incidence to the front surface.

5.2.2.2 Fringe sharpening?

The reader might note the fine crisp fringes in all of the records shown so far; these are obtained by arranging a small off-axis illumination [Fig. 5.21(a)]. Figures 5.21(b) and (c) demonstrate the difference between *strictly on axis* and

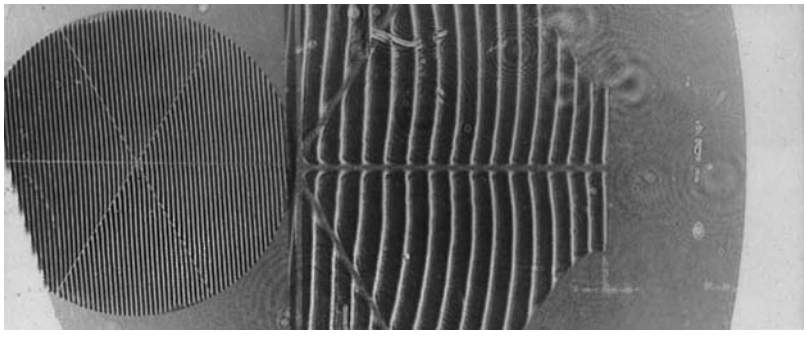

Figure 5.21(b) CCR in off-axis illumination by the reference CCR.

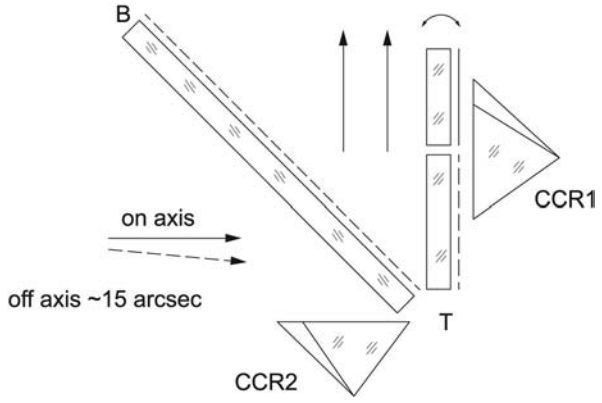

Figure 5.21(c) An interferometer configuration with transmission mirror T and CCR1 is routinely used for double-pass testing of the CCR1. Here, T is chosen to be extra large in order to serve as the reference in a second interferometer T/B/CCR2, for the sole purpose of defining and recording the direction of the optical axis with respect to the orthogonal to T. Beamsplitter mirror B is sufficiently large to observe both interferometers simultaneously. This permits the introduction of a controllable and recordable mild off-axis illumination, which will cause a reduction in the beam walkoff and will enhance fringe sharpness (finesse) (see Section 10.2).

about 15 arcsec *off axis*. For this comparison, an extra CCR was added to the test configuration, as in Fig. 5.21(a), and observed through an additional Michelson interferometer. The setup is made up of this auxiliary CCR, which determines the optical axis, a large beamsplitter plate as shown in Fig. 5.21(c), and the transmission flat T, extended for this experiment. T is also an essential part of the double-pass CCR configuration. Inclining the optical axis to 15 arcsec off axis [Fig. 5.21(c)] will alter the fringe profile without interacting with spacing and curvature of the fringes belonging to CCR1.

5.2.3 Improving collimation

The enhanced sensitivity obtained by multiple passes of a beam through an interferometric configuration with long distance between mirrors (large cavity) calls for further refinement and documentation of the process involved in ascertaining collimation. Inversion might introduce errors in the final interferogram that do not relate to the sample. The following test has been developed.[15]

A perfect and sufficiently large CCR in a two-beam Michelson [Fig. 5.18 (a)] presents a wavefront inversion around the apex of the CCR. This inversion will, at least, reveal asymmetric errors on the incoming wavefront (Fig. 5.3). Mild spherical wavefronts might not be detected by an interferometer such as the one in Fig. 5.18(a). Several small CCRs placed as drawn in Fig. 5.22(a) enable one to analyze an incoming beam/wavefront that is assumed to be flat.

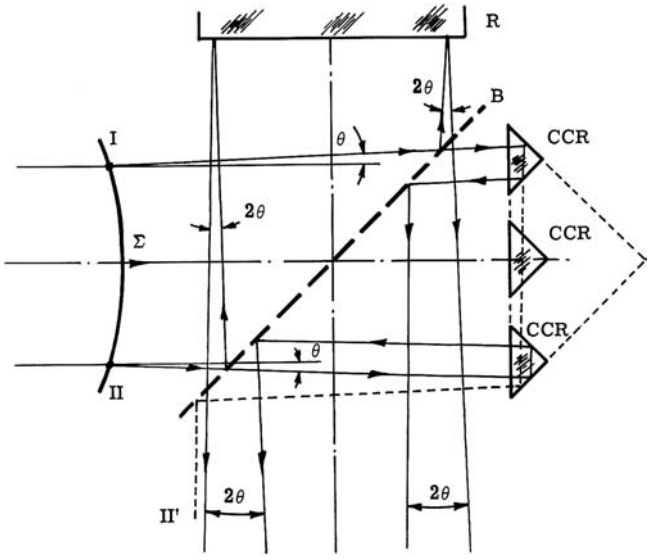

Figure 5.22(a) Schematic showing an interferometric collimation test.

Consider the two diverging external bundles I and II. The flat mirror R deviates each partial beam into a left (–) and a right (+) direction δ, δ representing normals to the incoming wavefront Σ. The same bundles I and II will be autocollimated by the small CCRs in the control beam: into directions $+\delta_I$ and $-\delta_{II}$. At the interferometer's exit there will be two pairs of partial bundles, each showing interference representative of ±2δ. In the case where incoming bundles I and II are parallel, representing a plane wavefront, there will be no angular differences measurable between the two interferograms of the small CCRs. Straight, equally spaced, and parallel fringes with no difference between the two (or more) will signal good collimation. The direction and spacing of the fringes may be selected by the orientation of reference mirror A to optimize the convenience of the evaluation. A slight defocusing of the collimator in either direction will render such changes in the interferograms [Fig. 5.22(b)].

With P_1 and γ_1 *before* a small change in collimation, and P_2 and γ_2 *after* a small change in collimation, the angular change δ is computed in Section 5.1.3 as

$$2\delta = \lambda\left[\left(\frac{1}{P_2}\right)^2 + \left(\frac{1}{P_1}\right)^2 - \frac{2\cos(\gamma_2 - \gamma_1)}{P_1 P_2}\right]^{1/2}. \tag{5.4}$$

With rotary symmetry of the incoming wavefront, one may expect an angular difference of 2δ between the two bundles I and II to show up as 4δ. Among the

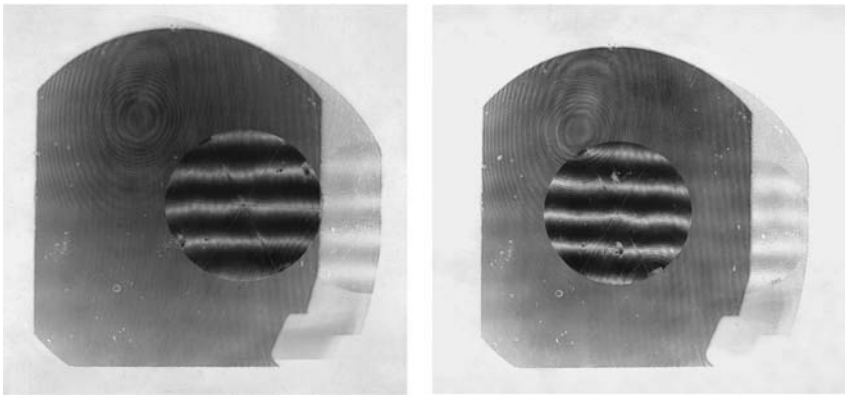

Figure 5.22(b) A CCR moved from the side toward the center of the interferometer field. Here, the stationary fringes, as shown, signal rather good but not yet perfect collimation (or, a very small inclination of fringes). During this movement, fringes will not walk at, except the in case where the CCR's lateral movement is strictly orthogonal to the optical axis of the collimated beam.

possible alignments of mirror R for the interferogram, one will find the following to be opportune:

- As much as possible, $P_1 = P_2$, with the direction of P_1, P_2 symmetrical to the line connecting the apexes of the CCRs.
- $\delta = (\lambda/4P)$ sin γ [in rad] $= (3/P)$ sin γ [in arcsec], with P in cm and $\lambda = 0.6$ μm.
- $P = 1$ cm and $\gamma = 3$ deg. With sin $\gamma = 0.05$, the departure from collimation will be $\delta = 0.15$ arcsec. Ideally, $P_1 = P_2$, $\gamma = 0$, and $\delta = 0$.

The accuracy of the fringe reading ($\Delta P/P$) determines the smallest detectable lack of collimation. With only a visual setting, this collimation test provides a focusing precision that is (according to this author) more precise and easier to apply to any Fizeau-type interferometer on the market than other known collimation tests. CCR diameters may be "as available" but at least in the proportion shown in Fig. 5.22(c).

Instead of simultaneously comparing two or three CCRs for optimizing collimation, one may also operate with only one CCR by shifting the CCR from one side of the collimated field to the other, not worrying about movement of the base of the CCR housing. One will observe no change in the interfergram of that CCR in any position of the field. Fringe spacing and orientation are controllable only by the entire Fizeau interferometer—between the null field and any fringe pattern—under only one condition: that the CCR remains stationary.

In the case where a null field becomes aligned, the following statement is applicable: The optical axis of the Fizeau interferometer is collinear with the

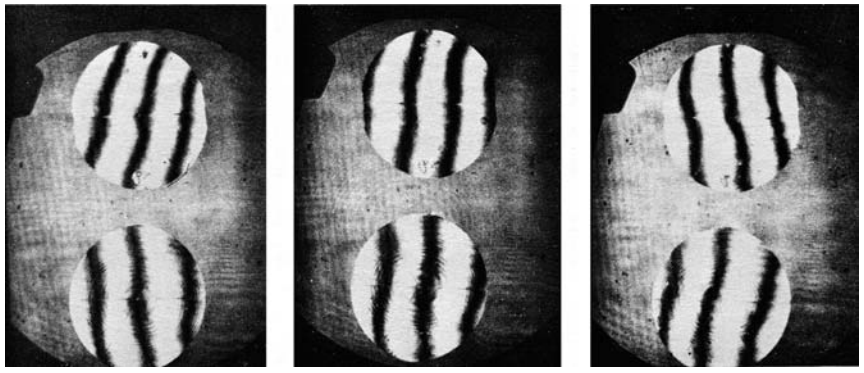

Figure 5.22(c) Collimation test with two CCRs in a 125-mm-diameter interferometer field. The collimator has a focal length of 625 mm. Left: 0.075 mm in front of best focus; right side 0.075 mm behind best focus; middle is therefore concluded to be the best focal setting.

spatial diagonal of the CCR but is *not* necessarily coaxial. Inclination of the CCR from one to another angular position, even by many degrees, will not alter the initial fringe pattern (see Fig. 5.23), with one exception: Rotation of the CCR [for instance, being placed on an air-bearing table as in Fig. 5.22(d)] will result in the fringes moving parallel to themselves, indicating an axial lift during said rotation and, again, with one further exception: The front surface of the CCR is orthogonal to the geometric spatial diagonal of the CCR. In this author's experience, that condition is rarely fulfilled. A so-called hollow CCR made only of mirrors will not exhibit any such error. These features of a CCR led to this author's development of an interferometric tilt measurement of ultraprecise turntables and spindles, using the front flat surface of a Fizeau interferometer as the tiltless reference.

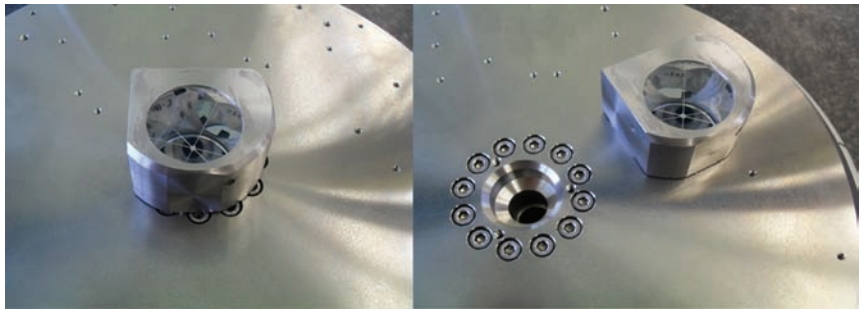

Figure 5.22(d) Corner cube used to measure axial error motion of an air-bearing spindle. Fringes will remain stationary upon rotation. Likewise, the CCR shifted to the periphery will also show the same fringe pattern as the one in the center [the lower interferogram in Fig. 5.22(b)]. The fringe patterns on both CCRs, being identical, will change in the following manner: CCR1 remains stationary in the next fixed angular position. CCR2 will show a different fringe pattern because of the tilt between the spindle axis and the interferometer axis.

Alternative, less costly collimation tests based on differential moiré were developed by Sirohi,[16] using a double wedge shearing plate in the interferometer, and by Mehta,[17] using a differential moiré technique.

A note for practical use when setting up collimation, starting with an unknown gross decollimation: Lateral shifting of a single CCR within a not-well-collimated beam will cause the image of the point source (visible in the pinhole plane) to laterally migrate; it will remain stationary as soon as collimation is achieved, after which, the interferometric procedure may begin. There is no requirement on the quality of either the lateral or longitudinal displacements of the CCR; the interferograms are typical inspected when stationary, as in Fig. 5.22(b). Even tilting the CCR [as in Figs. 5.23(b)–(d)] will not alter the fringe pattern upon completed collimation.

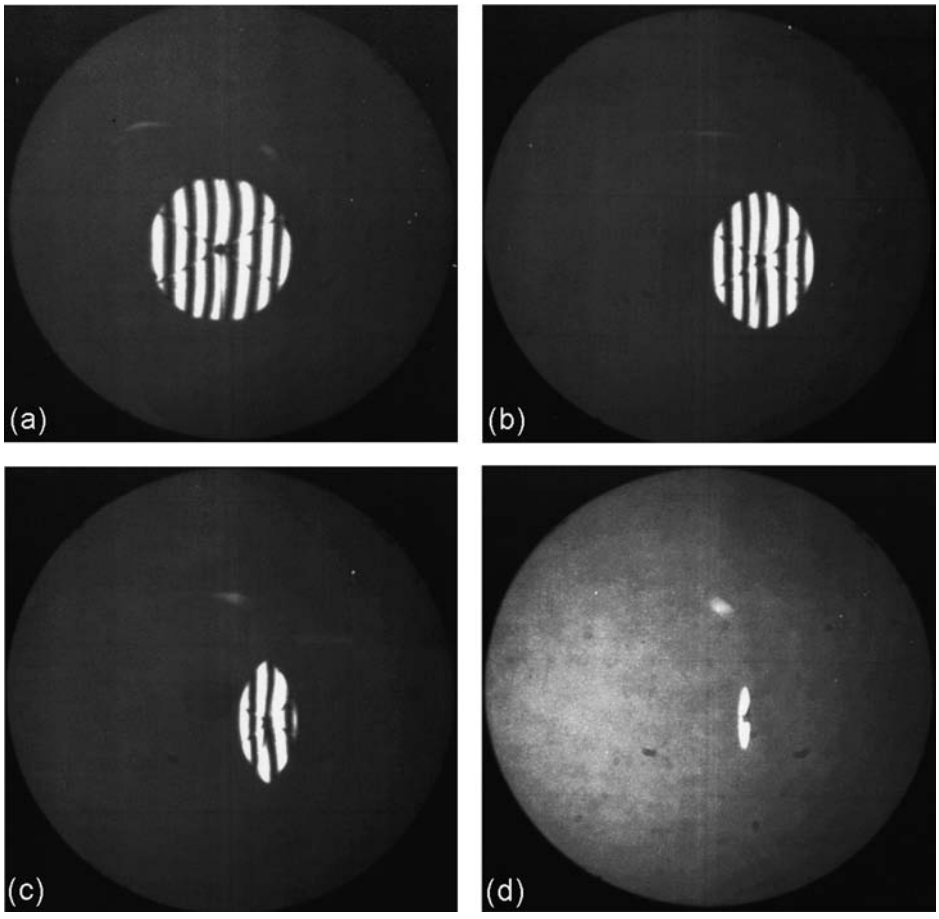

Figure 5.23 A CCR in collimtion testing mode: (a) The optical axis of collimation is the spatial diagonal of the CCR. (b) The CCR in (a) is now tilted 15 deg. (c) The CCR in (a) is now tilted 30 deg. (d) The CCR in (a) is now tilted 45 deg.

During motion, one will observe that fringes walk parallel to themselves; however, no fringe walking will be observed in the case where the CCR's lateral movement occurs strictly orthogonal to the optical axis. From this is derived a very useful piece of laboratory equipment for finding the orthogonal to a collimated beam: the CCR mounted on a "perfect" slide for linear, lateral travel.

The work with collimation testing revealed other useful features of a CCR: The CCR need not be oriented with its front face orthogonal to the optical axis or with its spatial diagonal parallel to the optical axis of the collimator. Figures 5.23(a)–(d) show the identical CCR at 0 deg (the common case), 15 deg, 30 deg, and 45 deg, all in the same interferometer alignment. A residual retroreflection at the 45-deg setting follows from the sufficiently large angle between the spatial diagonal and each of the three facets (not so with only one 90-deg roof angle).

Lateral motions of the CCR may be measured by a separate second interferometer, looking independently at the CCR along an inclined axis; however, the 30-deg line will show a reduced fringe equivalent of $P'/\sin(30\ \text{deg})$.

5.2.3.1 A useful "fringe" benefit

3D navigation of a CCR within a collimated beam of a diameter a few times that of the CCR is briefly outlined here for the interested reader. Starting with any commercially available interferometer such as one that produces Fig. 5.23(c), we mount the CCR (with a diameter smaller than the field diameter) on an X'–Y' slide and arrange this X'–Y' slide with axes, for instance, 30 deg to the optical axis, this being the Y' axis. The interferogram will have an oblong shape, as in Figs. 5.23(b)–(d). Moving the CCR in the X and Y directions simultaneously in such way as to let the CCR travel along the optical axis of the interferometer in either direction will produce the fringes that walk parallel to themselves—the customary distance change measurement. A separate interferometer looking along Y' will measure that CCR's cross motion to the collimator's optical axis.

5.2.3.2 CCR rotation

Rotation of a CCR around its spatial diagonal will have no effect on the interferogram set initially, regardless of its actual lateral position (see planarity test of air-bearing spindles). In the case where the lateral shift is orthogonal to the optical axis, the fringes will remain stationary and will not walk parallel to themselves. An additional collimated beam from another interferometer shone onto the CCR under, for instance, 30 deg, will produce an interferogram as shown in Fig. 5.7(a). This additional beam will allow measurement of said lateral shift by usual fringe counting, but now the interferogram will have a fringe equivalent of $\lambda/\sin\alpha$.

5.2.4 An alternative to the CCR: the ball reflector or "cat's eye"

The ball lens is a retroreflective device that is an alternative to the CCR. Representative rays from a ball lens are shown in Fig. 5.2(a). The ball or sphere must be made of glass with a refractive index $n' = 2$ for attainment of retroreflection.

A spherical interface between air with $n = 1$ and glass with n' is exposed to collimated light, characterized by angular direction $u = 0$. A flat mirror approaching (moving in the n' medium) the focus produced by the spherical interface will be in an autocollimating position, as shown in Fig. 5.24(a), at a distance of $x = 2R$. The same will be true if the flat mirror is replaced by a spherical mirror having the same radius R as the first refracting interface. The distance h/u' equals $2R$, and $u' = h/2R$. Additional relations between parameters are as follows:

$$
\begin{aligned}
&nu - n'u' = (h/R)(n' - n), \text{ with } u = 0;\\
&-n'u'R = n'h - h;\\
&-n'u' = n'(h/R) - n(h/R);\\
&-n'u' = (h/R)(u' + h/R) = h/(Ru' + h);\\
&+n'(u'R - h) = +h; \text{ and}\\
&n' = h/(h/2) = 2.
\end{aligned}
$$

Glasses with $n' = 2$ are LaSF9 or LaSF39 from Schott.[18]

The retroreflective ball with $n' = 2$ has become known as a cat's-eye spherical retroreflector (SRR). In the 1990s, a widespread marketing effort in the precision engineering community for this very low-cost handy interferometer was initiated by K. Wehrle.[19] In 1992, the mere coating of one side of the SRR with gold became patented[20] [Fig. 5.24(b)].

Balls of rare glasses LaSF9 and LaSF39, with refractive index $n = 2$, are commercially available in diameters of 2 and 4 mm. Their primary use is in small interferometers for measuring distance changes.[21] The SRR's advantage over a CRR is its relative insensitivity to lateral displacement within a not

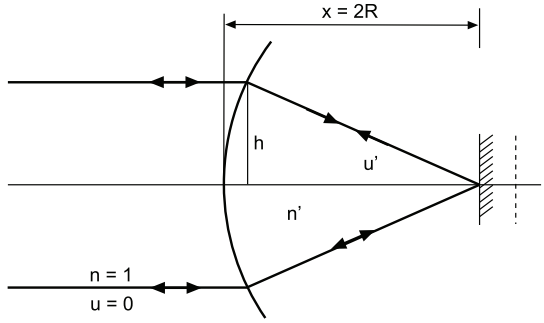

Figure 5.24(a) Deriving the condition for retroreflection by a ball lens with index of refraction $n = 2$.

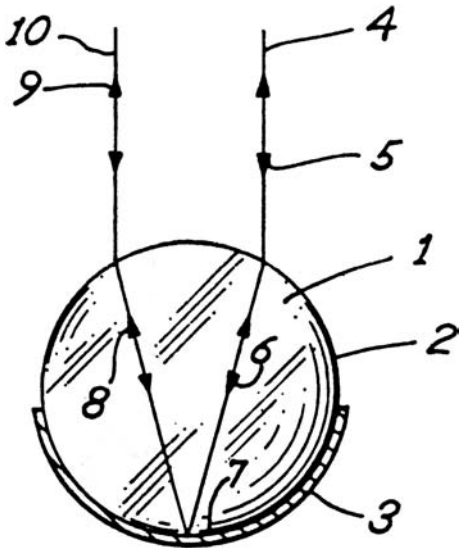

Figure 5.24(b) Spherical retroreflector made of glass with refractive index $n = 2$.

necessarily well-collimated laser beam. Illumination may be intentionally uncollimated. Applications are ultraprecise microscopic air-bearing X/Y tables and axial feed or growth of air-bearing grinding spindles.

Due to low market prices, the production of this attractive device has been abandoned. Ball lenses for collimation and decollimation are found in fiber optics, in read/write heads of a DVD/DVR apparatus, and in endoscopic devices. In probing surfaces with a diamond stylus for roughness, the ball reflector is found on the back of the microflexures, carrying the diamond stylus [Fig. 5.24(c)].

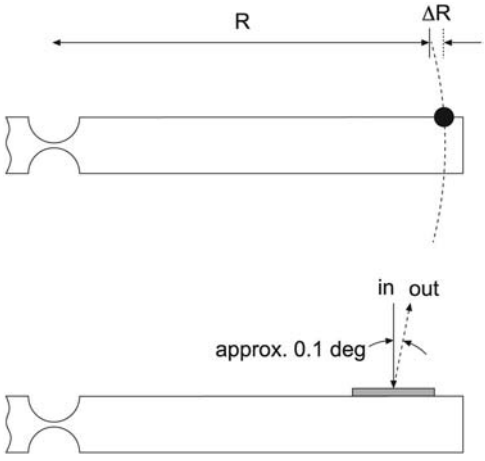

Figure 5.24(c) Spherical retroreflector for interferometric measurement of displacement of a probing stylus. Error due to lateral displacement is negligible. A flat mirror cannot be used for this detection.

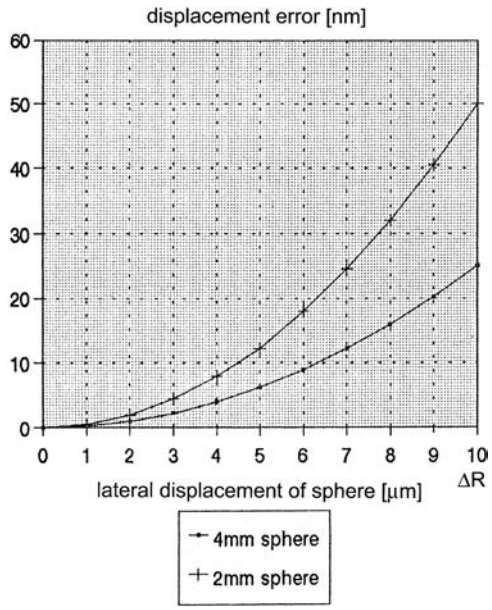

Figure 5.24(d) Longitudinal displacement error in nanometers as a function of lateral SRR displacement on the order of a few micrometers.

Still in the experimental phase is the embodiment of a 2-mm SRR inside the rotor of a mini grinding spindle, for sensitive nanometric in-feed of the journal rotor. An SRR mounted near the back of a grinding or polishing pellet is part of the concentric distance-measuring laser interferometer.

Centration of the SRR must be within the tolerances shown in Fig. 5.24(d). In-feed, work contact, chatter, and material removal can be measured in process. Measurement is not disturbed by the rotation of the reflector, as is the case with the diffraction pattern produced by an equally small CRR.

5.2.4.1 Applications of the SSR

The convenience of working with a not necessarily collimated beam permits an interferometric change of distance measurement within a few 100 mm. Example applications of the SSR are the linear *X*/*Y* air-bearing tables for microscopic measurement and linear variable differential transformer (LVDT) pinoles. Air-bearing pinholes with an integrated axial in-feed motion (of the rotor, not the rotor's housing) used in the process of ultraprecision grinding with interferometric in-feed benefit from the CCR being replaced by a ball reflector.

5.2.4.2 Integrated-optic distance-measuring interferometer

In the early 2000s, CSEM[22] began promoting an extraordinarily small, rugged, application-friendly distance-measuring interferometer with an integrated auxiliary interferometer for refractive index of air compensation (air pressure

and temperature). This instrument was designed for ultra-precision applications and was able to operate with a small, lightweight flat mirror as the reflector. The further fate of the instrument is unfortunately unknown to the author.

5.2.5 Autocollimation test for equality of radii of curvature

Mass-produced lenses and balls need a fast quality inspection, which traditionally has been performed by contact spherometry or by contactless spherical interferometry. A fast test for equality of radii of curvature was developed in the author's laboratory, a setup of which is shown in Fig. 5.25. Essentially, this test may be understood as a form of the collimation test presented in Section 5.2.3. It offers a fast, differential, comparative assessment of equality of samples placed successively on a Teflon® platform. The platform only needs a one-time alignment to suit the dimension and calibration.

Unlike the mechanical contacting spherometer, the optical method is contactless. This method serves relative, comparative metrology, not absolute curvature measurement. There are, however, useful implications to this method: With more than two (for instance, four) CCRs placed in the plane of CCR1, the sample stage may be translated (without rotating the sample) for observing centration of the spherical surface (lens) to the optical axis given by the hardware in Fig. 5.12.

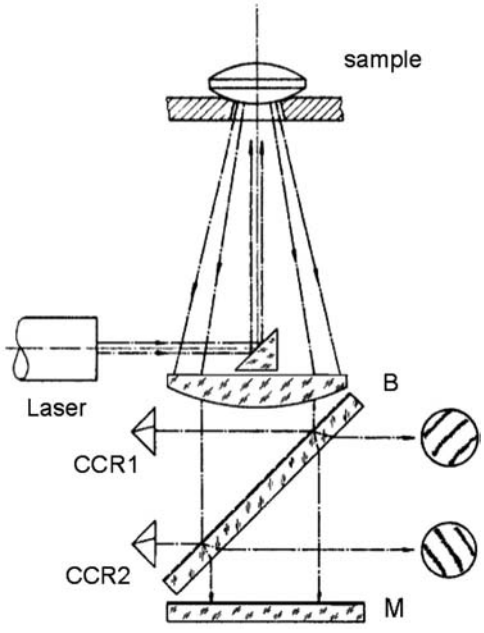

Figure 5.25 Quality control method for serial checking the equality of the radii of curvature.

5.2.6 Separating angular errors from flatness errors on cubes and 90-deg prisms

Roof angle interferograms do not allow separation of angular errors from flatness errors. Figure 5.26(a) illustrates an interferometric setup that provides simultaneous flatness of one (cube) surface and flatness of a second neighboring surface, plus departure from 90 deg from these two adjacent surfaces of the problem part. This setup is similar to that in common autocollimation, where the cube rests on a flat reference plate but does not produce (interferometric) surface information of both the sample and the base.

The components include a beamsplitter B1 (50/50) for the Michelson-type arrangement. B2 is a reference plate with a double function. One cube surface has a beamsplitter coating of auxiliary silver[4] for the Fizeau technique. The second half of B2 has a reflective coating and serves as reference for the right angle between it and the cube. In addition, the plate of B2 is plane parallel (for convenience of fringe alignment) and partially reflective coated, as shown. The mirror coating on the otherwise uncoated surface of B2 serves as a reference for the 90-deg roof angle between B2 and the cube.

Parallelism between B2 and the cube's surface is observed by way of the Fizeau fringes [Fig. 5.26(b)]. Both interferograms are imaged simultaneously, as shown in Fig. 5.26(a). The Fizeau fringes will show the edge falloff and possible surface defects. The two beam fringes will allow measurement of the departure from 90 deg, as discussed in Section 5.1. The sequence might start by setting the cube parallel to B2 using the Fizeau technique and reading the departure from 90 deg from the two beam interferograms. Or, the sequence can start by setting the 90-deg angle first and reading the angular error from the Fizeau interferogram.

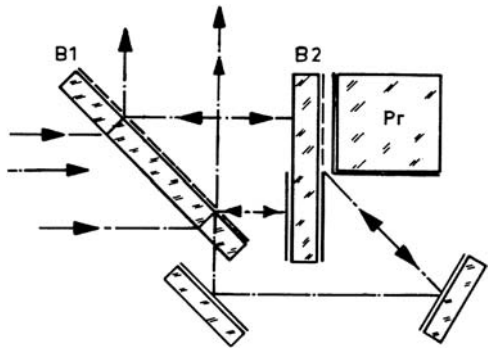

Figure 5.26(a) Schematic showing the dual function of B2. The first half of the glass plate of the Fizeau beamsplitter is coated and provides the best-fit flatness and the angular zero for one facet of the sample cube. The second half of B2, 100% mirror coated, forms a nominal 90-deg angle with a neighboring second cube facet, providing both edge error (off 90 deg) and departure from flatness of facet 2 (B2 being "perfect"). A temporary coating of silver spray is necessary.[4] Dimensions are set to suit cube size.

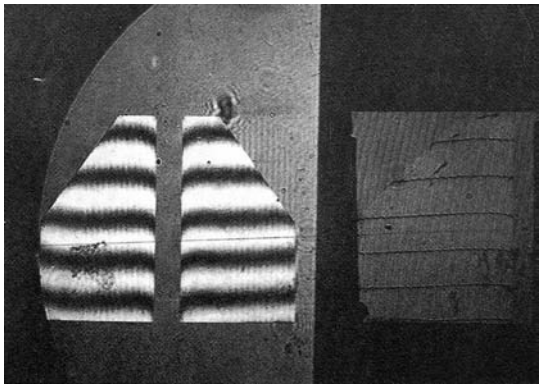

Figure 5.26(b) Both interferograms are recorded simultaneously. Two-beam interferograms represent a 90-deg angle plus one facet's flatness. The second surface is a flat reference. The Fizeau and two-beam fringes are aligned for nearly the same pyramidal angle (a safe measure, but not necessary). See also Fig. 5.26(c).

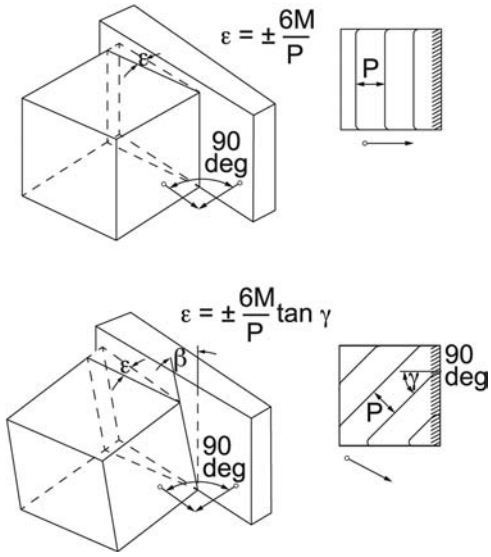

Figure 5.26(c) After setting the external angle B2/cube to be 90 deg (straight, continuing fringes), one observes Fizeau fringes and measures the departure ε from 90 deg by the equations noted in the schematic. This is the interferometric method that can be used instead of the traditional method of contacting the cube (or prism) to a testplate and applying the autocollimator reading to the external 90-deg angle.

The two-beam 90-deg angle interferogram represents one only surface of the cube because B2 is a flat reference. The fringe equivalent is $\lambda/2\cos\alpha$, with $\alpha = 45$-deg fringe equivalent on the one surface ($\alpha = \lambda/1.4$).

The following question arises: Can angles on uncoated cubes be measured more easily than angles on coated cubes? The answer is yes, as shown in Fig. 5.27,

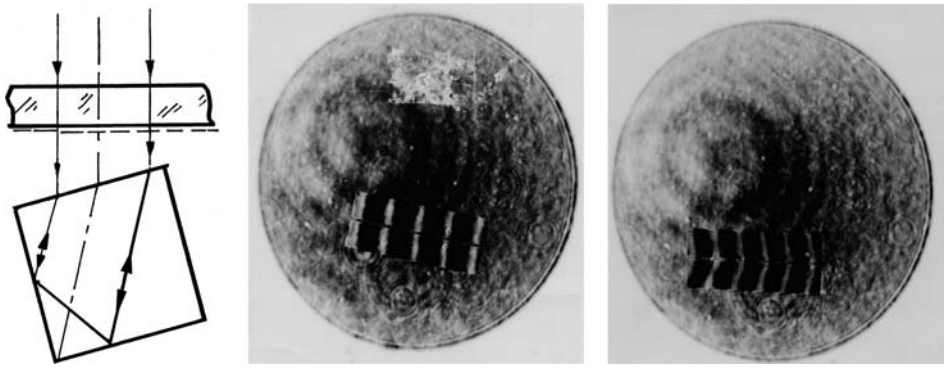

Figure 5.27 Internal 90-deg measurement on uncoated glass cubes with "flat" facets. The measurement shown integrates potential inhomogeneities and the facet's flatness.

by internal testing of the roof angle between two "flat" facets of a cube. The advantages of using uncoated cubes are that the measurement is fast and no auxiliary coating is necessary. A simple Fizeau setup is possible with a beamsplitter coating for reducing the intensity of multiple reflections (Section 2.2.1). The disadvantage of using uncoated cubes is that the interferogram shows the sum of all errors, including flatness departures and inhomogeneity, the latter being anticipated long the optical path in two directions. Two typical interferograms are shown in Fig. 5.27. An advantage of this method for fast acceptance control is the ability to perform successive testing of the four 90-deg angles on a rotary table.

For the polishing of sharp 90-deg corners, excluding rolled-down edges, one needs to know whether only one surface or both surfaces of the 90-deg corner are rolled down. Both of these neighboring surfaces are seen in the interferometer in Fig. 5.26(a) but not in Fig. 5.27. In the attempted situation of "no roll off," one does not have the sign as an indicator of a possible angular error between the facets. Pushing the sample as was recommended for less sensitive cases (Fig. 5.7) is not opportune because the Fizeau–cube alignment might cease to exist. Pushing the fold mirror in the two-beam part of the setup and watching the fringes walk toward the zeroth order is an improvised solution. A classical compensator plate placed between the two beamsplitters might do the job. Figure 5.28 summarizes the procedures for determination of the sign of edge-errors, as measured in the interferometer setup as in Fig. 5.26(a).

A note for the practitioner

The presence of either reversion or inversion in an interferometric breadboard setup is recognized from the sign of a locally confined error: the same sign means no reversion or canceled reversion has occurred. The reference beam and sample beam have an odd number of reflections. An odd number of reflections will cause reversion or inversion.

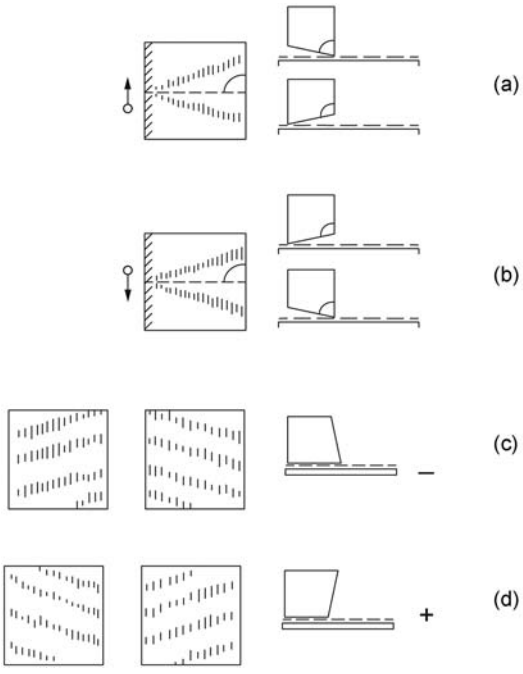

Figure 5.28 (a) and (b) Determination of the sign of angular errors of the 90-deg angle using Twyman–Green interferograms. (c) and (d) Determination of the sign of the angular error of the 90-deg angle using Fizeau interferograms. In all cases, the zeroth-order direction must be known.

5.2.7 Measuring the parallelism of transparent laser rods

When measuring the parallelism of transparent laser rods, a first attempt will measure the Fizeau interference between a front and rear surface. A small angle between the surfaces will be seen as $2\alpha = n \bullet (\lambda/2) \bullet (N - 1)$, where n is the refractive index and N is the number of fringes. All possible error sources contribute here: surfaces not being flat, material not being homogeneous, and angular errors.

A pure angular measurement without said "volume effects" and without auxiliary coating on the faces becomes possible by letting the rod become part of a retroreflector at each side [Fig. 5.29(a)]. The two flanks of a perfect mirror 90-deg angle, tested after Fig. 5.3, suspend the rod such as to form a retroreflective assembly on each side. To this setup the corner cube evaluation applies. Of particular interest is the applicable fringe equivalent of $S = 0.25$ μm, which is helpful in the sample's flatness evaluation. Here, the fringe departure from straightness is $\Delta P/P = 2$, indicating a 0.5-μm bow on the rod's surface. The question of whether it is convex or concave is answered by slightly reducing the path length of the reference arm of the dual-beam interferometer (pushing the reference mirror or tilting a flat glass plate). The

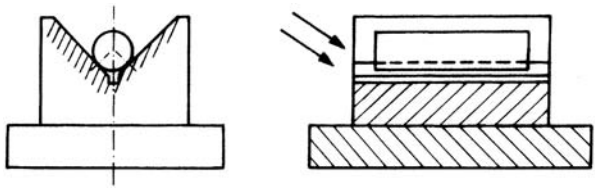

Figure 5.29(a) Laser rod resting in a perfect 90-deg mirror prism forms two retroreflective configurations that permit evaluation of the flatness of the rod's surfaces.

viewing direction of the interferometer is close to the spatial diagonal of the trihedron formed by the 90-deg prism and the rod. The relatively wide trace in the two interferograms is caused by the groove in the prism; these two facets of the interferogram represent the rod's surface to which the above flatness evaluation applies. Only after corrective polishing for acceptable flatness of both rod surfaces can their parallelism be measured and corrected.

Figure 5.29(b) is equivalent to Fig. 5.13, also with only one angle of the three being perfect. Obviously, the rod's surface is not flat but convex for about two fringes, with a fringe equivalent of 0.25 μm. For the fringe

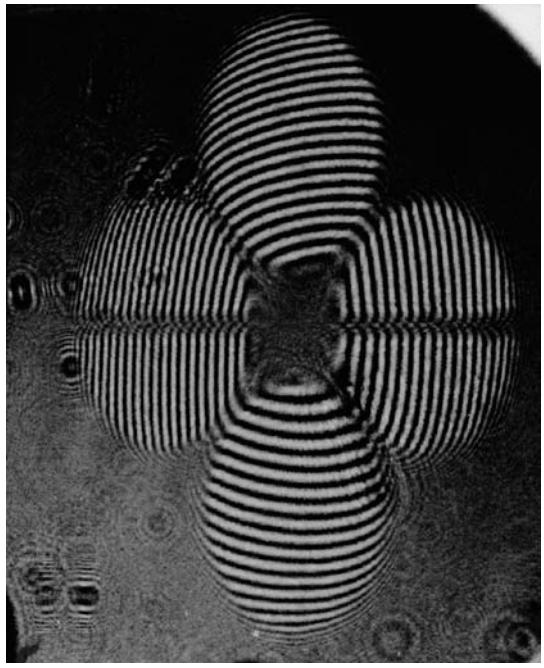

Figure 5.29(b) Interferogram from an 8-mm-diameter ruby rod resting in a 90-deg mirror prism. Evaluation of α_1 and α_2 as well as α_3 (known to be 90 deg) follows from the procedure discussed for corner cubes, as does evaluation for β_1, β_2, β_3. Vectoral subtraction yields departure from facet parallelism, independent of the rod's cylindricity and homogeneity, as long as the fringes are straight enough to allow first intuitive determination of their direction and spacing.

equivalent to be valid, the interferometer's optical axis must coincide with the spatial diagonal of the corner cube, as is prearranged by the angle at which the interferometer beam is shone into the assembly.

5.2.8 90-deg angular calibration cubes

Angular calibration cubes are 10- to 30-mm cubes with 6 facets and 8 precise 90-deg angles, mirror coated. Their primary use is in alignment of large machines, antennas, and communication systems.

For its QC, the Al-coated quartz cube rests on a turntable platform, to which it is preloaded by a spring with a Q-tip (seen as shadow in the first interferogram in Fig. 5.30); the cube sample thus is arranged in front of a

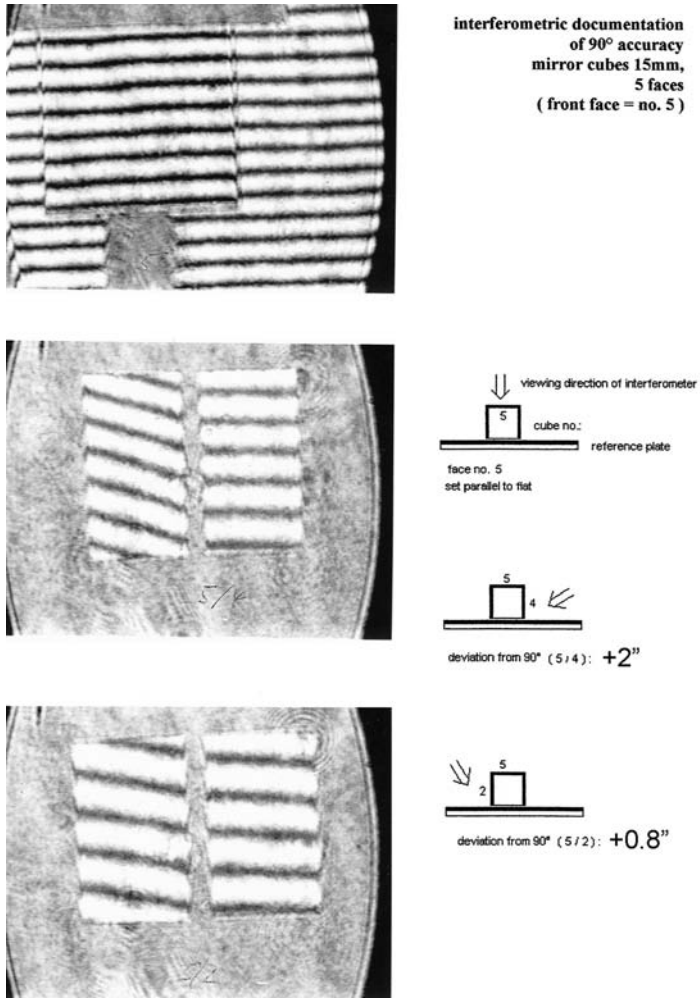

Figure 5.30 Simultaneous calibration of angular and facet flatness errors of reference cubes. The arrows indicate the viewing direction of the interferometer.

larger flat reference, close but not touching. The assembly is placed in a two-beam Michelson interferometer. A front view allows adjustment of the parallelism between the front face of the cube and the rear reference (the first interferogram in Fig. 5.30, shown upside down). The fringes almost line up, indicating facet five (indicated on the schematic) to be parallel to the base, within tolerance. The complete cube fixture can be swung with an air-bearing table for ±45 deg, allowing the collimated beam to be retroreflected. Fringes become aligned by the external Michelson reference to suit evaluation [Fig. 5.5(c)]. Shown in Fig. 5.30 are angles 5/4 and 5/2. For angles 5/1 and 5/3 the cube is turned with its stud and realigned parallel to the reference. Four protocols are needed to cover all eight angles and the flatness of the six facets.

References

1. J. Strong, *Procedures in Applied Optics*, Marcel Dekker, New York (1989).
2. S. Tolansky, *Multiple-Beam Interferometry of Surfaces and Films*, Clarendon Press, Oxford (1948).
3. E. R. Peck, "Polarization properties of corner reflectors and cavities," *J. Optical Society of America* **52**(3), 253 (1962).
4. Peacock Laboratories, Inc., 1901 S. 54th St. Philadelphia, PA 19143, USA: silver spray chemical solutions.
5. J. Flügge, *Leitfaden der geometrischen Optik und des Optikrechnens*, Verlag Vandenhoek und Ruprecht, Göttingen, Germany (1956); J. Flügge, Studienbuch zur Technischen Optik, UTB Vandenhoeck, Germany (1975).
6. P. R.Yoder, Jr., "Study of light deviation errors in triple mirrors and tetrahedral prisms," *J. Optical Society of America* **48**(7), 496–498 (1958).
7. Kayser & Threde, Inc., Würmtalstr. 2, D-8000 München: "Definitions Study: Liquid Helium IR-Spectrometer," report commissioned by the BMFT, Bonn, Germany (1988).
8. "Grundlagen der Optik," in *Handbuch der Physik*, S. Flügge, Ed.,Vol. XXIV (1956).
9. G. Sparrer, "Messanordnungen zur Kalibrierung kompletter Laser Interferometer, "*Microtechnik* **3**, 27 (1994).
10. Keyence Corp., 50 Tice Blvd., Woodcliff Lake, NJ 07675, USA.
11. P. Langenbeck, "Linometer, "*Feinwerk und Messtechnik* **85**, 4 (1977).
12. A. C. S. van Heel, "High precision measurements with simple equipment," *J. Optical Society of America* **40**(12), 809–814 (1950).
13. R. F. Schenz, L. V. Griffith, and G. R. Sommargren, "Development of an extended straightness measurement reference," in *Proc. Third Annual Precision Engineering Conf.*, Atlanta, GA (1988).

14. H. D. Betz, "An asymmetry method for high precision alignment with laser light," *Applied Optics* **8**(5), 1007–1013 (1969).
15. P. Langenbeck, "Improved collimation test," *Applied Optics* **9**, 2590–2593 (1970).
16. R. S. Sirohi and M. P. Kothiyal, "Double wedge plate shearing interferometer for collimation test," *Applied Optics* **26(**19), 4054–4056 (1987).
17. D. S. Mehta and H. C. Kandpal, "A simple method for testing collimation," *Optics & Laser Technology* **29**(8), 469–473 (1997).
18. Schott Glass AG, Hattenbergstrasse 10, 55122 Mainz, Germany.
19. K. Wehrle, "Miniaturisiertes Laserinterferometer," Kontrolle II und Microtecnic, page numbers unknown (1994).
20. G. Ulbers, "Optical retro-reflector," U.S. Patent No. 5,126,879 (1992).
21. P. Langenbeck, "Optical homogeneity measurement by a two-angle method," *Optik* **28**, 592–601 (1968).
22. CSEM, Centre Suisse d'Electronique et de Microtechnique S.A., Maladière 71, CH-2007, Neuchâtel, Switzerland.

Chapter 6
Polygons

6.1 Polygon Mirror Wheels

The specifications of polygon mirror wheels (Fig. 6.1) can be met by micromachining and are verified best by interferometry, both on the machine at the multiple clampings and unclampings on a dividing head and after final dechucking. Facet angles, facet flatness, absolute and relative pyramidal angular errors, the axial base surface and, for some applications, the front surface are all subject to interferometric quality control. The planar base, a granite surface plate, will permit the component to become part of an ultraprecise scanning system; the polygon's base can usefully serve as an axial air bearing of a spindle with an integrated drive (Fig. 6.2).

An imbalance of the drive system may impair the finest relative pyramidal quality of the polygon scanner, as will skewed assembly of the polygon on the bearing axis. Dynamic deviations from accuracy are minimized in designs, making the polygon component part of the spindle, as shown in Fig. 6.2. A complete set of specifications for mass-produced polygons is provided in Table 6.1.

Designing the polygon wheel to be an integral part of an air-bearing spindle is the ultimate precision solution for a scanner. The unit goes through various production and assembly stages that involve interferometric testing. Adherence to the specifications in Table 6.1 requires a sequence of delicate operations. The following is a summary of the essential work steps involved in the production of an air-bearing polygon scanner:[1,2]

1. Prepare and verify the axial surface of the polygon.
2. Diamond machine and verify facet flatness and angles.
3. Measure relative pyramidal error.
4. Attach polygon to spindle bearing (the polygon is the spindle face plate) and ascertain that no deformation of the component by the air-film pressure has occurred. The polygon body must withstand the mechanical force exerted onto its base by the air pressure needed for the air-bearing operation.
5. Ascertain that the drive of the spindle with an integrated motor is error free.

Figure 6.1 Polygon mirror wheels (from the Siemens Hell laser scanner) produced for known serial products. The bottom polygon has a diameter of 180 mm.

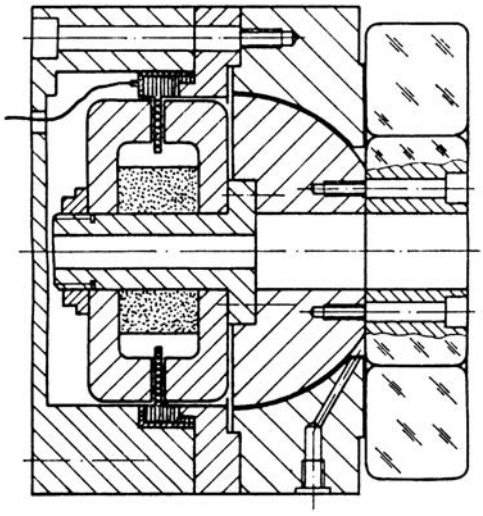

Figure 6.2 The polygon wheel, whose planar base is an integral part of the air-bearing's rotor, and the rotor of the electromotor, being an integral component of the same rotor, together make up the design of one of the most rugged scan units (reprinted from Ref. 2).

Table 6.1 Specifications of a polygon disk.

1. Diameter over facets	180 mm ±0.2 mm
2. Polygon thickness	48.8 mm ±0.3 mm
3. Number of facets	8
4. Material for polygon	brass 63 Cu or 70 Cu
5. Temperature range	
• Operation	10 to 40 °C
• Stock	–20 to 50 °C
6. Humidity	
• Operation	20 to 80%
• Stock, no condensation	10 to 80%
7. Temperature change	
• Operation	max: 6.7 K/h
• Stock	max: 30.0 K/h
8. Speed range	All parameters are specified for a speed range of 2000 to 4000 rpm.
9. Position of rotation axis	Vertical, polygon upside
10. Lifetime	5-year min.
11. Facet-to-facet angle in rotational direction	135 deg ±7.5 arcsec
12. Absolute pyramidal error	max: ±60 arcsec measured between the rotational axis and one specified polygon facet.
13. Relative pyramidal error	max: ±3 arcsec across all facets. Pyramidal error between adjacent facets must be under 3 arcsec absolute. The pyramidal error will be measured dynamically.
14. Coating of mirror surfaces	
• Uniformity of the protective coating	±15 nm
• Surface persistency	According to DIN 58197, minimal requirement for antireflection layers and mirror layers
• Surface quality	50/1 × 0.63; G 3 × 0.4; C 3 × 0.4; DIN 3140, Part 10. Dimensions and tolerances for optical parts, defects of surface coatings or 60-40 Mil-Standard 0-13830-A.
• Adhesivity of the layer	Slow pulling down of Tesa strip 552 (width 19 mm) may not damage the coating.
• Reflectivity of all surfaces at arbitrary polarization	At input angle 25.5 deg and wavelength 830 nm, the reflectivity is higher than 93%. Reflectivity of all facets at the same input angle differs less than 1%.
• Changes in reflectivity	For the input angle range of 13 to 38 deg, a maximum change in reflectivity of 1% is allowed. The input angle is the angle between the input beam and surface normal.
• Uniformity of reflection	Change in reflectivity across the facet at a constant input angle is less than ±2% (measured with a 5-mm-diameter light beam).
15. Surface flatness	λ/10 at 830 nm in a circle of 42-mm diameter.
16. Scatter (total integrated scatter)	<2%. The scatter will be measured using the following setup: A laser beam with a diameter of 40 mm, intensity L_0, and specified wavelength reflects at a specified input angle on the polygon mirror. The reflected beam is focused on a black stop of diameter 250 μm using a *f*/14 lens. Scatter light intensity around the stop in aperture 480 × 10 mm symmetrical to the scan direction is measured as L_1. The same measurement is repeated with a well-polished mirror; the corresponding light scatter intensity is L_2. Then, $$TIS = \frac{L_1 - L_2}{L_0} \times 100\ (\%).$$
17. Secondary maxima (fly-cut polygons only)	max. 0.1% if the distance to zeroth order is smaller than 15 mrad
18. Cutting direction (fly-cut polygons only)	parallel to the long axis on the facet
19. Cleaning of surfaces	The mirror surface can be cleaned of dust or other contaminants at least 10 times.

6. Verify the axis of rotation at operating speed.
7. Run dynamic test of unit.

The two mating axial planar surfaces (rotor/stator) seen in Fig. 6.2 make up the externally pressurized air film. They define the angular orientation of the bearing's axis by both their departure from flatness and bearing balance. The airborne hemisphere preloading the disk defines the radial position of the axis of rotation. Radial and axial motion errors of this spindle type are known to be less than 0.1 μm.

The polygon material must be able to be diamond machined (like ductile brass) for a mirror finish. Its dimensions must be chosen to resist deformation by air pressure. Severe deformation of the polygon body results from burrs around screw holes standing up into the plane of assembly (by drilling after lapping the face) or being rolled down by lapping. The elastic bending by screw-motion forces will be immediately evident in the interferometer.

6.1.1 Preparing and verifying axial surfaces of polygons

Polygons undergo successive assemblies; they are mounted and clamped to the production fixture with air on for setting the angles and, finally, with air off (clamped) while machining. There will be a series of frequent air on/off cycles before the completed polygon will be mounted on the operating bearing.

The axial surface serves as a reference for the axis of rotation as well as for the relative pyramidal orientation of facets. The primary quality of the axial surface must be rotary symmetry (it may be concave but never convex). Prohibited are machining processes that, by their nature, produce surface undulation such as axial loading, by lapping and manual corrective lapping attempts. Turning of the axial surface and then lapping is common but can lead to asymmetric surfaces.

Figures 6.3(a) and (b) show a polygon body resting on a Flatest [product name for instruments using oblique incidence, as in Fig. 1.14(c)] interferometer, displaying interference patterns of a 2-μm fringe equivalent; in Fig. 6.3(a), one recognizes an out-of-roundness of one 2-μm fringe at the peripheral zone, causing air-bearing coning, and the polygon's relative pyramidal error. In the same figure, some fringes around the screw holes indicate that zones rolled down about 4 μm. The axial clamping of such a polygon wheel to any mating component (the hemisphere in Fig. 6.2) generates deformations of the entire polygon body. Figure 6.3(b) shows an intact air-bearing surface.

The Flatest interferogram of the axial surface of the 180-mm-OD-lapped polygon mirror wheel (brass 65, hard chromium coated) shows 5-mm concave (2-mm) fringes. Zones around the through holes are rolled down by the lapping. Upon attaching to the hemisphere (Fig. 6.2), when tightening the screws, the polygon wheel will become deformed to the point of being useless. Manual, so-called corrective lapping was abandoned due to the results shown in Fig. 6.3(c).

Figure 6.3(a) Unacceptable base surface of a polygon mirror wheel. Connection to the complementary hemisphere of the air-bearing spindle will deform the entire polygon body (reprinted from Ref. 2).

Figure 6.3(b) Acceptable base surface, in which no out-of-plane deformation around the screw holes occurs and good rotary symmetry is achieved.

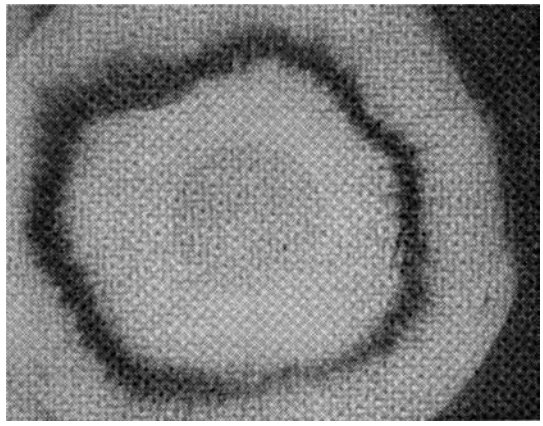

Figure. 6.3(c) Actual surface, precision-lapped, λ/2 Fizeau fringes (reprinted from Ref. 2).

Milling the axial bearing surface with its proneness to generate saddle-shaped surfaces (up to 0.5-μm sag) is even worse, for lack of rotary symmetry. Turning or grinding on a precision air-bearing lathe with less than 0.1-μm axial runout is the best option; one might compare the interferogram of a lapped surface with a precision-diamond-turned surface.

Departures from axial rotary symmetry, measurable by fringe irregularity, will cause an angular spindle wobble, with variable magnitude, depending on speed. The polygon surface, clamped without an air film to the machining chuck, might self-align with an air film to another, likewise, best-fit plane. Even with all facet normals of the polygon lying in one plane, tilt might occur between the machining plane and the operating plane after assembly. The tilt will then be recorded as a relative pyramidal error.

6.1.2 Verifying facet flatness and angles

The errors to be addressed in micromachining polygons are related to clamping, thermal material effects (upon spray cooling while machining), nonflatness-like cylindrical power due to machine misalignment, and vibration due to poor machine stability. Thus, continuous quality surveillance is required if one wants to produce λ/10 fringes over, for instance, a 50-mm diameter on each facet.

An interference autocollimator (IAC) is integrated in a convenient location on the machine with its separate reference mounted remotely and with adjustability next to the work [Fig. 6.3(d)]. The reference holder, therefore, is mounted ruggedly to the spindle housing, and the reference flat is aligned to represent the *x*-*y* machining plane. Thus, the IAC is used for both in-process inspection of flatness and for angular zero-pointing measurement of facets. Facets of both the reference polygon and the just-machined work polygon can be inspected on the machine prior to dechucking.

Coplanarity of the machine slide, the interferometer reference, and the cutting plane is a prerequisite for ultraprecision polygon work. Dividing

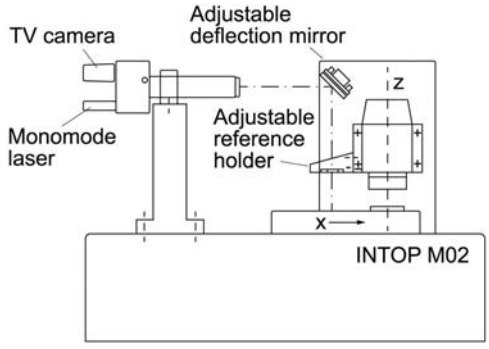

Figure 6.3(d) The Fizeau reference flat mounted on the machining spindle, near and parallel to the machining plate. This setup allows interferometric scanning of just-finished workpieces, coplanar to the *x-y* plane.

angles may be preset using a regular commercial encoder connected to the air-bearing dividing/chucking head. The locking accuracy of the chucking device is ascertained by interferometry and the master polygon. No creeping loss of the angular position is caused by tangential machining force. Safe clamping also means that no wear and no backlash occur in the dividing head.

Alternatively, angles between polygon facets can be calibrated against a "homemade" standard, as shown in Fig. 6.4; there, an angular standard (90 deg) is held near the reference mirror with one of its two surfaces parallel to the external Fizeau reference, parallelism being indicated by interference. The complete chucking device with the polygon is alternately located between the machining and the measuring position.

In the case shown in Fig. 6.4, collimated light (from the interferometer) that is transmitted by the reference mirror is reflected off of an already finished 45-deg surface. A typical interference pattern is depicted in the same figure; the pattern will indicate flatness of the facet that has just been machined and parallelism to the standard and the 45-deg angle (see Section 5.2.6).

The literature reports on much effort to verify a polygon's angle, mostly using autocollimators and encoders. One such effort is Intop's well-developed interferometric angle verification program, which, in some cases (90, 45, and 22.5 deg), is even autocalibrating. Other angles, such as 15, 30, and 60 deg, are derived from the geometry of a perfect corner cube reflector, which, in itself, can be verified by interferometry. Details can be found in Chapter 5.

The following is an interpretation of the records in Fig. 6.5 with regard to the numbered specifications in Table 6.1 that relate to the final machining, prior to the polygon's removal from the dividing head:

Specification 15. *Surface flatness* is just acceptable and could be better (an approximately 0.1-fringe local defect seen in a repeatable position relates to the slide).

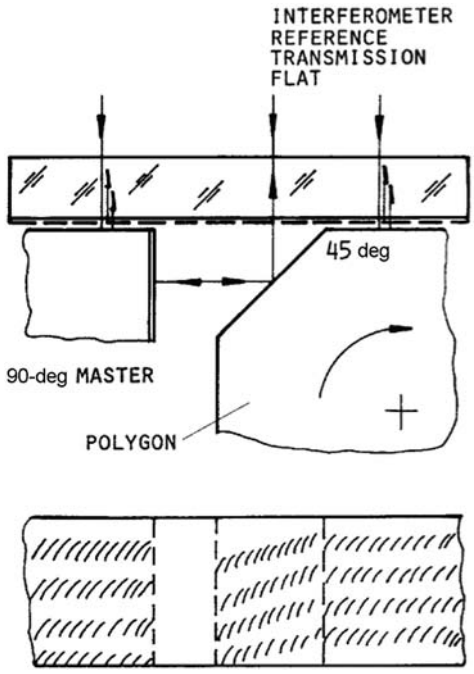

Figure 6.4 Interferometric 8-facet angular metrology using a 90-deg master fixed near the reference plate (transmission flat).

Specification 13. *Relative pyramidal error*: first inspection of this most relevant quantity indicates *acceptable*. A separate verification is necessary (see next section).

Specification 11. *Facet-to-facet angle of rotation*: Bringing any facet, e.g., facet 1, into a zero alignment (meaning straight fringes orthogonal to the axis), and thereafter rotating the polygon 180 deg, as indicated by the master, will show the angular error between facet 1 and 5 in terms of departure from the inclination of the fringes. The assumption is zero pyramidal angular error.

Specification 12. *Absolute pyramidal error*: The absolute pyramidal angle, or its error, depends solely on the initial alignment of the dividing head's axis being parallel to the *x*-*y* plane. This is verified by machining a 180-deg witness sample and applying interferometric measurement, as described above.

Specifications 5 through 10. These are satisfied by agreeing on laboratory conditions, excluding conditions prevalent at customer facilities.

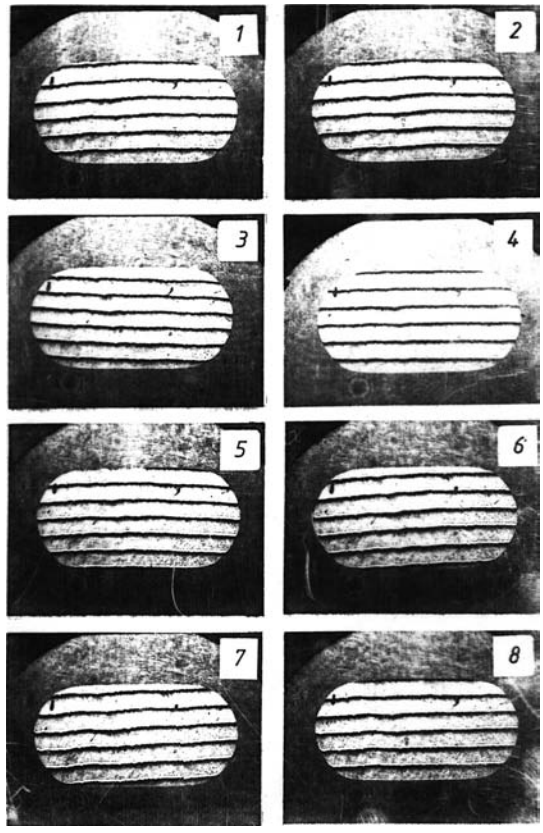

Figure 6.5 The eight facets of a polygon with a 180-mm diameter and a 40-mm height (same dimensions as the polygon at the bottom of Fig. 6.1). The flatness record of the polygon was taken prior to its removal from the dividing head.

6.1.3 Polygon rotation in 0.1-arcsec steps

The nanodrive provides to the air-bearing dividing head a stepwise rotation with a resolution of 0.1 arcsec. After fast driving near the desired angular position, switching to slow motion by nanodrive and observing the fringes with the machine-mounted interferometer [Fig. 6.3(d)], the parallel reference fringes become oriented orthogonal to the axis of rotation, as in Fig. 6.5. Finally, the desired position is locked. This locking is realized by changing the air-pressure supply to the dividing head in order to make the reference polygon preload the work polygon onto the stator of the dividing head.

6.1.4 Polygon's relative pyramidal error (static)

The polygon's relative pyramidal error is usually measured with an autocollimator, but it can also be effectively measured by interferometry.

The schematic on the left side of Fig. 6.6 shows a polygon resting on a flat reference mirror mounted on a turntable. The polygon's axial surface is checked to be parallel to this reference mirror by inspecting the interference between both (through a central passage in the turntable). The pyramidal angles (roof angles) formed between the facets and the reference mirror must all be identical, for instance, 90 deg. Without moving the polygon on the reference mirror, this assembly rotates in front of the interferometer such as to obtain an interferogram of each roof angle (same procedure as in Chapter 5).

This metrology method allows documentation of the pyramidal angles of the facets and, by the difference between them, of the relative pyramidal deviation. Figure 6.6 (right side) shows a typical interferogram of the 90-deg angle, with an evaluation as derived in Section 5.1.3. The hinge-like fringes of the 90-deg edge will be straight, in the case where the edge has zero departure from 90 deg. The angle on the reflected optical wavefront θ measured on the interferogram by fringe evaluation (spacing P) is 4 times the departure from 90 deg at the edge (roof angle). (See Sections 5.1.3 and 5.2.2.) This evaluation follows the formula: $\theta = 4\varepsilon = (130 \tan \gamma)/(PM)$, where M is magnification, P is in millimeters, γ is in degrees, and ε is in arcseconds. The flat reference mirror in the interferometer is usefully replaced by a roof mirror in order to avoid wavefront reversion. In that case, the roof reference must be calibrated to be precisely 90 deg prior to evaluation.

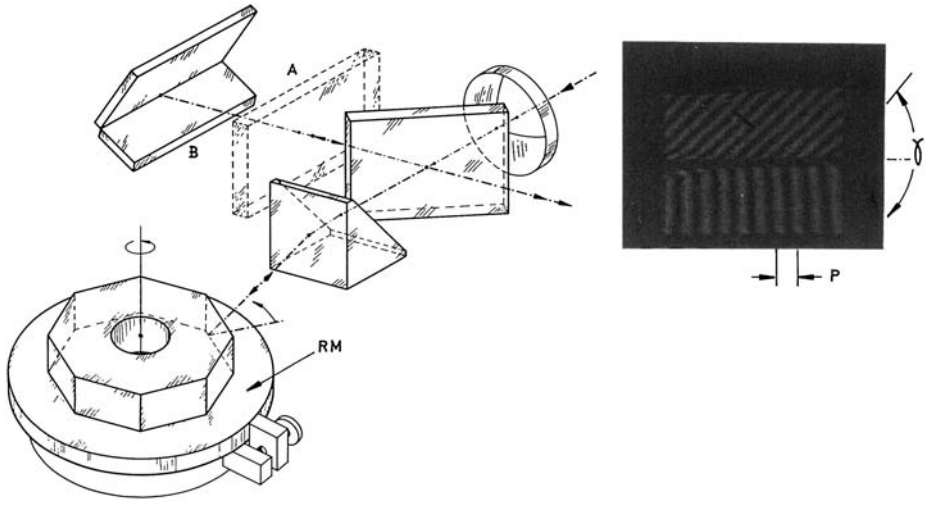

Figure 6.6 Interferometric measurement of the distribution of relative pyramidal errors of a polygon mirror wheel. The planar surface of the polygon (air-bearing flat) rests on a glass reference plate (RM). The parallelism between the air-bearing flat and the reference plate is ascertained and tested repeatability and separately from below (not shown in figure) (reprinted from Ref. 2).

6.2 Angular Standards Calibrated by Interferometry

It is almost unbelievable but true that many shops have a problem in defining 90- or 180-deg rotation to *some* precision. Fortunately, these two most frequently required angles can be tested to less than 1 arcsec by interferometry. Figure 6.7 summarizes angle interferometry for common angles (180, 90, and 45 deg) and for less-common angles (120, 60, and 30 deg).

The rugged 90-deg adjustable roof mirror was introduced in Fig. 5.1 for generation of 90 deg, controllable by interference fringes. Small departures from 90 deg can be measured to 0.1 arcsec. The adjustable 90-deg hollow angle can be replicated by a solid 90-deg prism. The metallic flexure block can

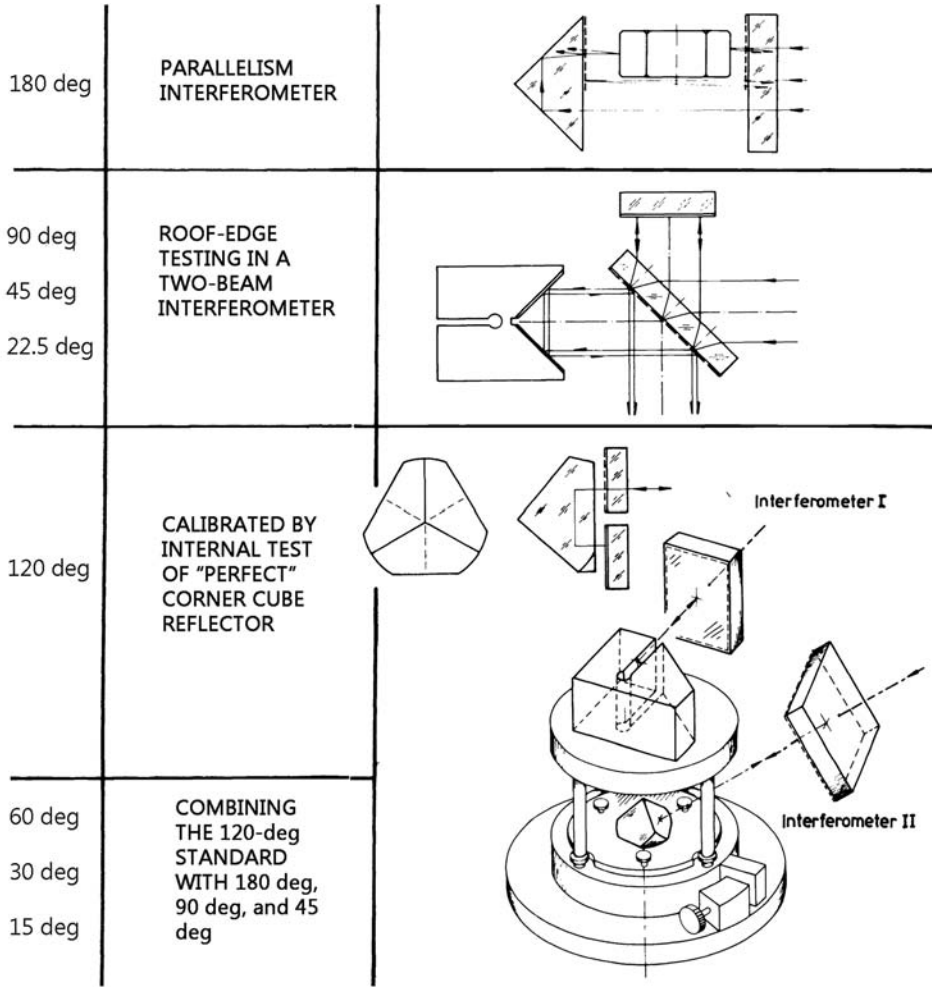

Figure 6.7 Generation of angular standards that can be controlled by interferometry (reprinted from Ref. 2).

be designed for 45 deg, often used for 90-deg beam deflection by a penta-prism. The flexure is adjusted until retroreflection occurs, when each partial beam hits a mirror at zero incidence. The fringe pattern only needs to be aligned from a V shape to straight fringes crossing the edge. The lateral width of the interferogram will be one-half of that obtained from the 90-deg angle.

Obviously, the very small (less than 10 mm) and very large (more than 10 cm) sizes are both rare and difficult to handle. Testing 180 deg is practical in a long-path Fizeau configuration, as in Fig. 6.7, top right. The cavity is built up by the transmission flat T and the 90-deg prism, with its hypotenuse beamsplitter coated on one half. The cavity is as long as is required by the 180-deg sample and is placed between the two reference surfaces, which are set to parallel at the onset. The parallel sample surfaces can be aligned to show identical interference patterns. The wavefronts will not be reverted. For good parallelism, there will be three identical partial interferograms: the sample/transmission flat, the sample/90-deg prism, and the prism/transmission flat. This 180-deg test became essential to aligning the chucking device used for polygon manufacturing. The purpose of the test in that application is to measure two opposing polygon facets. Using a corner cube instead of a 90-deg prism facilitates parallel alignment of the two references.

The perfect corner cube is the ideal embodiment of 120-deg angles. However, a potential fallacy must be considered: there might be a wedge between the spatial diagonal of the CCR and its front surface. Section 5.2 explains a method of detecting such a possible wedge. Nevertheless, the tilt table shown under the reference CCR will allows one to adjust the reference CCR for pyramidal equality of the three facets' inclinations, relative to the turntable's axis. Some patience is required in setting an interference autocollimator into the oblique orientation to meet all three facets successively at the same incidence. Once this is achieved, one has the chance to combine the measurement on a rotary table with the 45- or 90-deg standards, using a second interference autocollimator. This is illustrated in Fig. 6.7, in the lower right.

Following these procedures, one will end up with homemade angle standards for 180, 90, 120, 60, 45, and 30 deg. These standards can be cross-checked by a turntable and rotary encoder (e.g., the Heidenhain[3] ROD 800).

6.2.1 0.1-arcsec resolution within ±15 deg

A highly resolving interferometric measurement of angular motion was introduced by J. Rohlin[4] in 1963. A CCR is mounted on a cantilever of 300-mm length assembled onto an air-bearing rotary table (Fig. 6.8). This setup uses the linear comparator measurement applied to rotary motion. Note that the corner cube is used in oblique to normal incidence.

The mechanical driving system must be free from backlash and rocking, and it must be able to hold positions. Zero position and its repeatability need to be solved. A friction wheel drive, as provided by the rotary nanodrive, was not yet introduced at the time of Rohlin's publication but will be the optimal

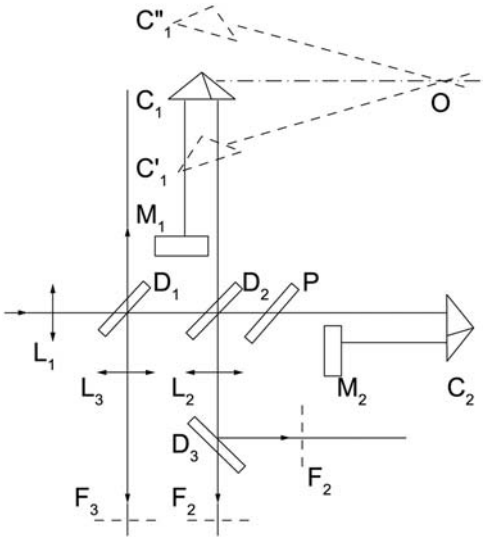

Figure 6.8 Highly sensitive angular measurement using length/distance change interferometry. Fringe counting provides 0.1 arcsec per fringe (applicable within ±15 deg) (redrawn from Ref. 4 with permission from OSA).

drive system. The Rohlin method combined with a nanodrive and a λ/100 nulling device (see Section 1.8.2) should be part of a metrology installation of the Rohlin encoder.

A more practical method for extended angular measurement using interferometric fringe counting in a setup of a rotating parallel glass plate was introduced by D. Malacara and O. Harris.[5] This method will be discussed in Section 7.6 on homogeneity. One application of both cited methods of angular metrology[4,5] is determination of refractive indices N based on the change in optical path in plates or cuvettes as a function of angle of incidence. Determination of ΔN to 10^{-6} at a practical optical thickness of 1–1.5 cm would require 0.1-arcsec resolution of the rotary motion.

6.2.2 Arcsecond rotation

The nanodrive transmission gear in air-bearing techniques reaches 1,000,000 revolutions per 1 revolution on an output shaft. The nanodrive features include freewheel capacity, clamping, no backlash, and high holding and driving torque.

References

1. D. Kessler and R. V. Shack, "Dynamic optical tests of a high-speed polygon," *Applied Optics* **20(**6), 1015–1019 (1981).
2. P. Langenbeck, "Compact air-bearing beam scanner: production and test," *Proc. SPIE* **396**, 73–79 (1983) [doi: 10.1117/12.935224].

3. HEIDENHAIN, 333 State Parkway, Schaumburg, IL 60173, USA, rotary encoders.
4. J. Rohlin, "An interferometer for precision angle measurements," *Applied Optics* **2**(7), 762–763 (1963).
5. D. Malacara and O. Harris, "Interferometric measurement of angles," *Applied Optics* **9**(7), 1630–1633 (1970).

Chapter 7
Optical Shop Daily Tasks

7.1 Centration in the Optical Shop

7.1.1 General-utility centering metrology

The task of centration for the *mechanical* engineer involves the following steps:

1. Place a calibration sphere (in fact, a hemisphere) on the spindle that needs to be certified for a special purchase order.
2. Provide a probe (e.g., TESA Technology) to measure the distance changes between the stationary probe and the equatorial zone of the calibration master.
3. Tap the master into the best achievable, centered position, as shown in Fig. 7.1. (All of these manipulations take place while the spindle rotates.)
4. Breathe deeply and push the button to obtain the numerical and graphical results shown in Fig. 7.2. The maximal radial error motion of the spindle axis (in this case, 0.02 μm) will be ascribed to that spindle, and the same will become certified.

7.2 Optical Work

The centering task for the *optical* engineer involves the following steps:

1. Take a fairly good spindle and make sure that the rim of the collet it carries shows no departures from flatness nor from roundness because these were to be machined on the spindle, as was the conical seat of the collet.
2. Select the most convenient sample for brevity: a plano-convex lens.
3. Place the sample with the flat side on the ring of the collet and secure its position by some internally supplied mild vacuum.
4. Have a convergent beam of light be either transmitted or reflected by the lens, and observe the focus of that beam arriving at a stationary

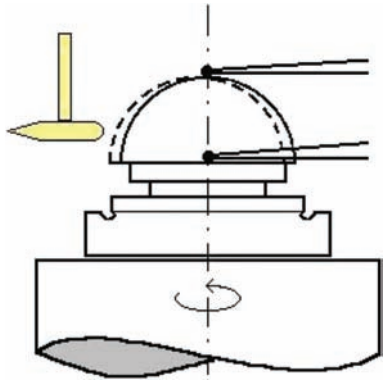

Figure 7.1 Traditional method for determining radial motion errors of a spindle to be used for centering work, which deals almost exclusively with polar cap surfaces.

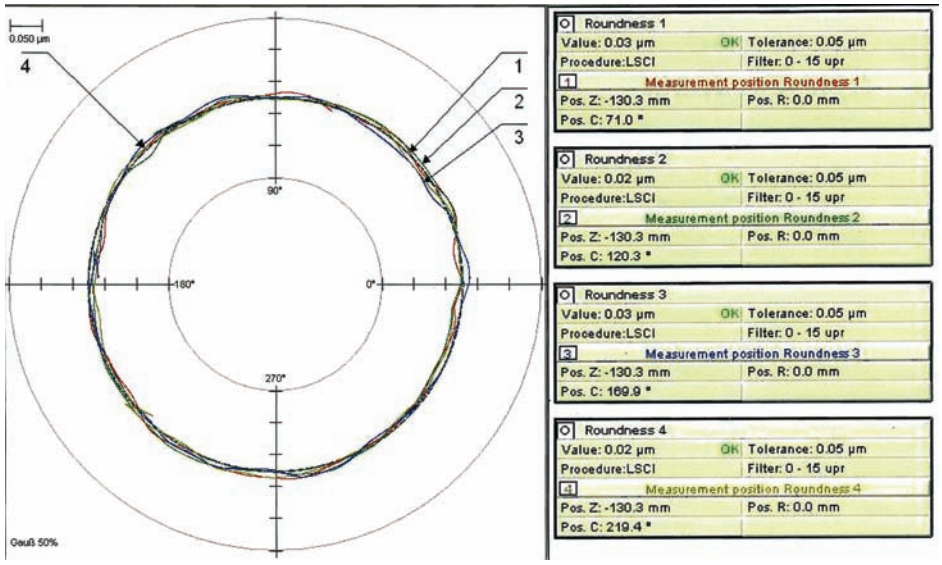

Figure 7.2 Metrology data registered for a general-utility air-bearing spindle with the probing setup shown in Fig. 7.1 (courtesy of Aditya Engineering, Pune, India).

position while the bearing is turned and the lens is tapped into its centered location.

5. Thereafter, increase the chucking vacuum, and bevel and center grind the periphery to the specified dimension on the spindle. This process defines the optical axis of the lens. Rightfully, one may assume that the optical axis of a single lens is (close to) identical to the mechanical axis of the work spindle.

7.3 Centering a Spherical Generator

Spindles with accuracies as shown in Fig. 7.2 are used in the diamond machining of parts for both ultraprecision mechanics (such as new air bearings) and optics. The majority of workpieces have flat or spherical surfaces that permit qualifying interferometry immediately after machining. Metal mirrors (Cu, Al) with convex or concave radii of curvature are produced by diamond machining in either turning or milling mode (fly cutting) (see Fig. 7.3). Any spherical generator needs only two spindles: one for the workpiece and one for the tool. Some tricky alignments are required here. The two axes must remain coplanar and intersect each other in the work's surface. The direction of infeed should be parallel to the axis of the work spindle. Nutation of the tool spindle α should be around an axis orthogonal to Z and X.

Any tool change or realignment necessitates a complete revision of the machining parameters. Let us assume exactly that situation. With the new tool being set and clamped, the machinist carefully infeeds toward a first touch,

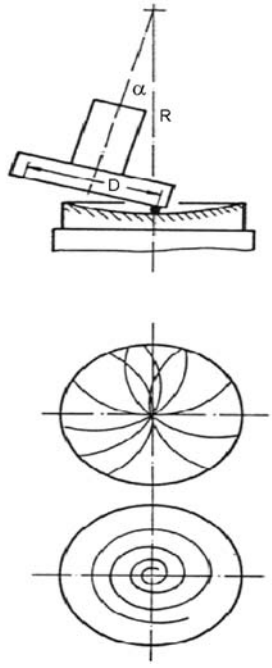

Figure 7.3 (top) Schematic showing the process of diamond machining spherical optical mirrors. The axes of the tool spindle and of the work spindle are coplanar. R is the work's radius of curvature; $D = 2r$ is the diameter of the circular path of the tool; and α is the angle between the coplanar spindle axes. α is set to zero for generating a flat work. The tool paths in the diagram represent the *milling* mode (center) and the *turning* mode (bottom).

which, ideally, would be an electrical signal. The machinist recognizes the correct infeed when "flakes" appear instead of the continuous, extremely long, uninterrupted chip. Only the crests of the previous roughness profile are removed. Then, the machinist overcuts by ~0.2 μm the surface that was machined before the tool change. One will see the old and the new surface intersecting and conclude by educated intuition a change of *one* coordinate only, e.g., 0.2 mm along *X*.

7.3.1 Finding the turning center experimentally

The challenge of setting and fixing a cutting tool to be driven exactly through the machining center is well known to any practitioner. There remains a tiny "wart" shown in Fig. 7.4(a): an unambiguous mark of the diamond-machining center (of the machine shown in Fig. 7.3), which serves no purpose.

The radial error motions of a spindle employed in micromachining were shown in Fig. 7.2. A new tool placed into the fly-cut spindle will, most likely, cut on a different radius *r* and, consequently, generate surfaces as shown in Fig. 7.4(b). The late Gordon James Watt named this *mechanical* interferometry because the amplification factor is 1:100,000. Normal interferometry has an amplification factor of 1:200,000, and the moiré technique, depending on the grating constant, has an amplification factor of ~1:5000.

By the 1970s, overcutting a good sample surface with a replaced new tool become an empirical method for relocating the turning center. Using a very low infeed of 1 to 2 μm, one can generate a new surface on top of the existing surface and judge—by experienced intuition—the necessary realignments of the tool.

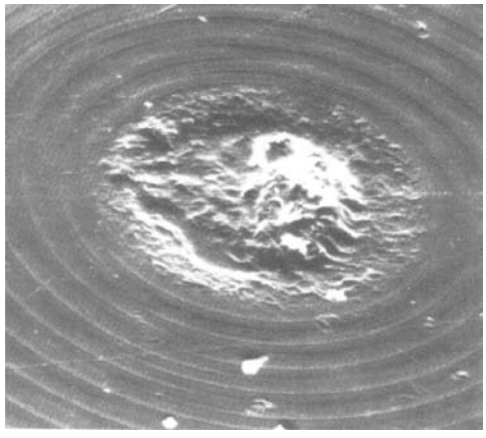

Figure 7.4(a) The typical turning "wart" at the turning center, where the cutting speed approaches zero, on a flat sample of diamond-turned copper. Cutting marks are at 1-μm feed per revolution. (Courtesy of Boley Co.,1988.)

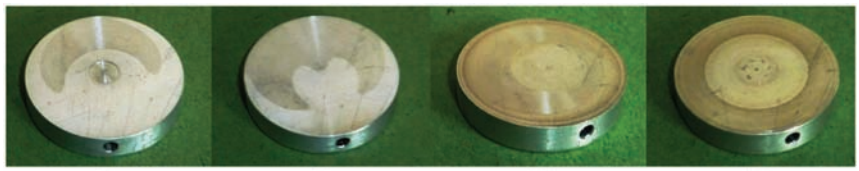

Figure 7.4(b) Example results of mechanical interferometry: refinding lost centration by repeatedly overcutting a surface with a minute infeed and resetting one coordinate by educated intuition. (i) and (ii) The tool path does not lead through the machining center, but in (i) it leads closer to center than in (ii). (The mirror surface would be a toroid.) (iii) One can see a closed circular zone of intersection, indicating the intersection of the two spherical surfaces that are being sheared (offset). (iv) The tool path leads through the machining center. A minute infeed changes only the diameter of the zone of intersection.

7.4 Attributes of Centering: State of the Art

The state of the art of centering prior to the advent of the laser and prior to the availability of precise and reliable air-bearing spindles is comprehensively described in Zschommler's *Precision Optical Glassworking*.[1] Some methods and hardware described therein are still operating today. Occasionally, one can find air-bearing spindles retrofitted to "good old" Boley or Schaublin lathes for ultraprecision machining of, e.g., the inner diameters of housings for optical microscope objectives having several lenses; their axes need to be coincident to themselves and to the inner diameters machined to tolerances as given in Fig. 7.2.

The theoretical and practical standards for the technologies of centering currently used were established by authors H. H. Hopkins and H. J. Tiziani.[2] The technology of optical centering applied today relies on methods described in this article. Interferometry for centration measurement is clearly prescribed therein and applies to both externally accessible surfaces (reflection) and to systems composed of more than one lens (transmission). The production of extremely fine resolving objectives made great advances in the 1960s through the analytical results summarized in Ref. 2.

Simultaneously, new air-bearing techniques began to emerge from various laboratories for calibration of ultraprecise spindles and machines. In his encyclopedia *Precision Spindle Metrology*, Second edition,[3] E. R. Marsh, describes today's state of the art of spindle quality assessment which, in essence, uses a calibrated reference sphere centered and fixed on the spindle nose (basically, as shown schematically in Fig. 7.1).

That approach is very similar to our subject of concern here: centering the plano-convex sample lens. Up to this point, the tasks of *centration of optical elements* and *spindle quality assessment* have seemed interchangeable. In both

cases, the sensor signals indicate the amount of, however minute, X/Y displacement that will be needed in order to obtain a substrate's centration on axis. However, there is one crucial difference between the two tasks. The optical surface is usually the bare (uncoated) small polar cap of a larger spherical surface covering a cylindrical substrate of a specified but not-yet-finished diameter. Any proximity sensor measurement of the distance to the rotating optical surface will be related to the so-called insensitive direction (the greatest uncertainty regarding centration if the sample surface is flat).

Thus, from here on, the tasks of *spindle certification* and *substrate centration* differ. The metrology reference sphere is gently tapped or otherwise moved into a state of centration and is removed after measurement is complete. The substrate, having a spherical surface, is placed onto a precision-finished collet and is fixed with temporary, dissolvable cement in order to withstand the subsequent operation of center grinding.

The centration task of the sample lens continues with the final machining of the substrate's cylindrical periphery. This final machining takes place on the collet in the same carrier spindle, or the collet can be transferred to another equivalent spindle. Only thereafter can the substrate be an individual optical element. Figures 7.5(a) and (b) are photographs of the two metrological setup possibilities.

7.5 Can the Centering Procedure Be Made Less Laborious?

Early low-cost optical tests for spindle rotational errors did not use spherical or cylindrical masters but were based on dupligrammetry (moiré).[4] (Dupligrammetry was a method preceding computer-generation of holograms used to measure spheres and centration.) Mass production of substrates for data disks by micromachining on air-bearing spindles relies on an interferometric test that was a thesis topic[5] at Univ. of Stuttgart, Institute for Technical Optics (ITO) in 1994. The schematic of this test is reproduced in Fig. 7.6.

7.5.1 Alternative solutions

Despite all of the the fine, fully developed and introduced methods of centering, the question arises time and again: How can centration be executed faster and in a less-expensive manner? At the author's laboratory, we looked at two different answers: (1) turning the optic on a stationary sample and (2) performing interferometry with increased sensitivity.

7.5.2 Rotating the optical beam instead of the sample

The conceptual drawing in Fig. 7.7 shows the usual seat of the collet; however, here the collet is being machined into the air-bearing stator of a Watt-Intop (product from author's lab) spindle. The seat for the collet thus represents the

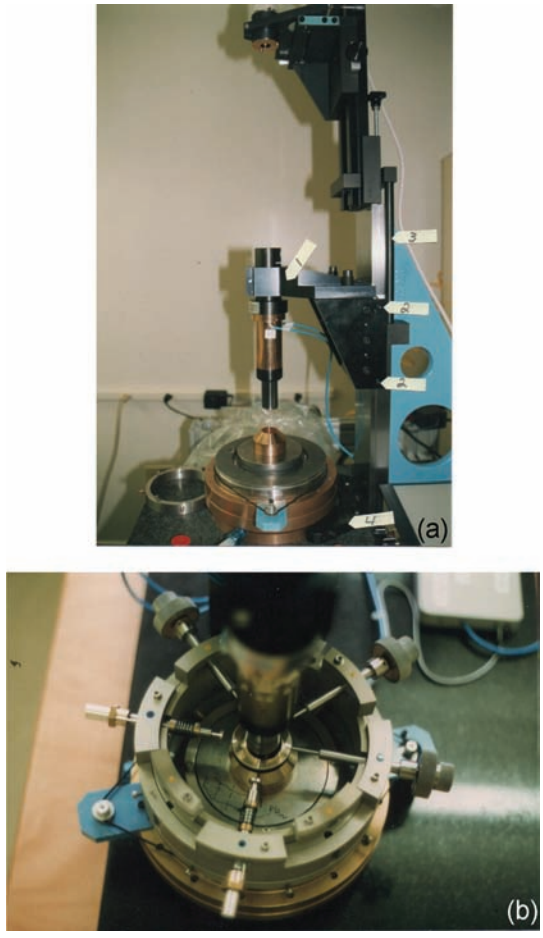

Figure 7.5 (a) Work station for centering and cementing of doublets. The air-bearing table represents the mechanical axis, and the collet, concentric to the axis, serves to hold the first lens. (b) The cage with pusher arranged on two levels. The first lens is held in position by the pushers in the lower level of the centering stage. The pushers on the upper level provide centration to the second lens. The stage has internal clearance throughout to admit a laser beam for transmission centration measurement. The focus will be detected in the appropriate place or by electronic PSD observation. The post holds two slides. The lower slide has a hollow pinhole for providing pneumatic preload on the cement layer between the lenses. The upper slide positions the detector for best service. The post can be removed for later positioning of an interferometer.

expected accuracy for the centering work. For the grinding operation, the function of the rotor/stator is reversed.

The laser line, as shown, is offset from the initial coaxial to a laterally displaced position by either a Dove prism or by an equivalent arrangement of two fold mirrors. Any low-cost laser has some asymmetries on its beam

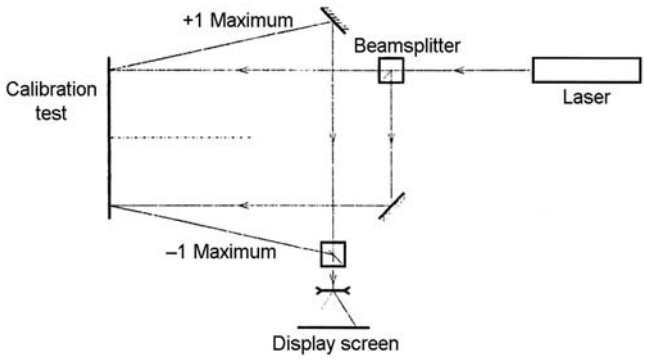

Figure 7.6 Interferometric test setup in which any CD can serve as a circular grating. Here, the CD to be tested is mounted on a spindle, and two parallel coherent laser beams are shone at positions 0 deg and 180 deg on the disk. Then, the diffraction orders are combined, as shown. This process is similar to the well-known diffraction-grating scale reading.[5]

profile. These asymmetries would not cause any harm but, upon rotation through the Dove prism, the profile is reverted. Briefly, the laser, as shown, is replaced by a small battery-driven laser pointer assembled in an adjustable fashion.

7.5.3 Centering interferometry

Let us consider Twyman–Green autocollimation applied to a single spherical surface [Fig. 7.8(a)]. Illumination is from a HeNe laser with $\lambda = 0.63$ μm. The Twyman–Green interferogram will simultaneously detect departures from sphericity and positional changes introduced when laterally displacing the lens. Axial position changes need not be accounted for when using an air-bearing work spindle. Likewise, we can assume radial errors of the work spindle to be negligible; any decent air-bearing spindle today has less than 30-nm radial error motion. In the Twyman–Green interferometer, the well-focused lens can be shifted laterally to produce interference, either as concentric rings or as a null field, or, alternatively, as straight fringes of spacing P, which is controlled at will with regard to direction and spacing.

Lateral displacement of a lens by the amount of s in the direction orthogonal to the fringes will result in $\Delta P = (P_1 - P_0)$; the corresponding focus displacement will be $2s$. The measurable parameters are the focal length f^1 in Fig. 7.8(a) and P_0 before and P_1 after the introduction of the lateral displacement s. Thus, angle α is defined as

$$\alpha = \frac{\lambda \cdot \Delta P}{P_0 P_1} = \frac{2s}{f}, \tag{7.1}$$

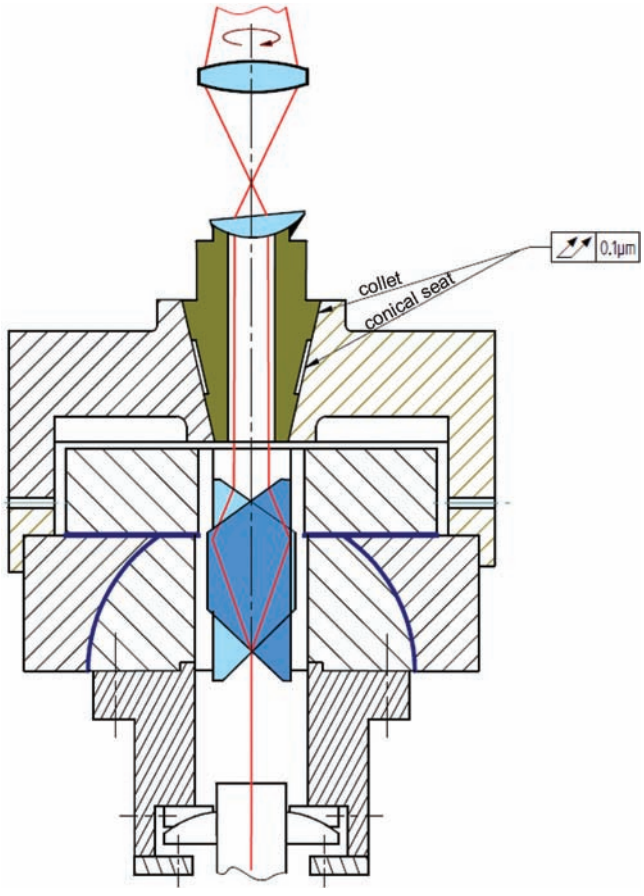

Figure 7.7 Centering station with the optic turning and the interchangeable collet stationary for convenience of the centering procedure, including temporarily cementing the optical element to the collet. The conical seat for the collett is ground on this spindle.

where s is the trial-and-error displacement:

$$s = \frac{f \cdot \lambda \cdot \Delta P}{2P_0 P_1}. \tag{7.2}$$

With a realistic value for $\Delta P/P_1 \approx 0.1$, and $P_0 = 1$ mm in the 1:1 image of P_r, $\lambda = 0.63\ \mu\text{m} \approx 6 \times 10^{-4}$ mm, and $f = 100$ mm, one obtains $s = 3 \times 10^{-3}$ mm = a 3-μm displacement to be measured. The angle α thus introduced is $\alpha \approx 6 \times 10^{-5} \approx 12$ arcsec. Both s and α are independent of the lens as long as $r << f'$. Some micrometer displacement then correlates with some arcsec beam deviation. Rotation of the work spindle will cause the focus to describe a circle in the focal plane and fringes to change their direction like the hands of a clock. The lens can be centered without rotation by adjusting for a null field

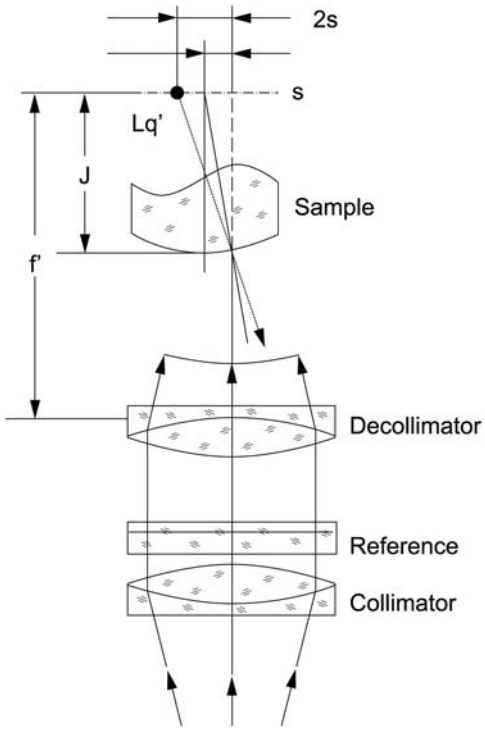

Figure 7.8(a) Centering in front of a spherical interferometer. Lq′ is the position of the light source after the sample is shifted by the amount *s*.

($P_0 = \infty$ and $s = 0$). This will not be sufficient with small lens diameters, due to the limited size of the image and P_r.

7.5.4 Enhanced sensitivity

Doubling of angular sensitivity is obtained with a reversion interferometer [Fig. 7.8(b)], in which the lens is now placed in front of an interferometer. The flat reference mirror in the customary Twyman–Green interferometer is replaced by a 90-deg roof mirror. In contrast to what occurs in regular Twyman–Green interferometry, the reflected reference light bundle will now behave as if reflected by a flat mirror in one direction only, parallel to the roof's edge. The angle of incidence equals the angle of excidence. However, in the direction orthogonal to the roof mirror, we observe a typical split into two partial bundles. In addition, the lens is arranged at the entry of the reversion interferometer and thus is associated with two foci [Fig. 7.8(b)].

The lens rests on a set screw, which represents the mechanical axis. The transmitted bundle enters the reversion interferometer at angle α to the optical axis of the interferometer. With a roof angle of 90 deg ± 0, the angular separation of the two foci in the reversion interferometer will be 2α,

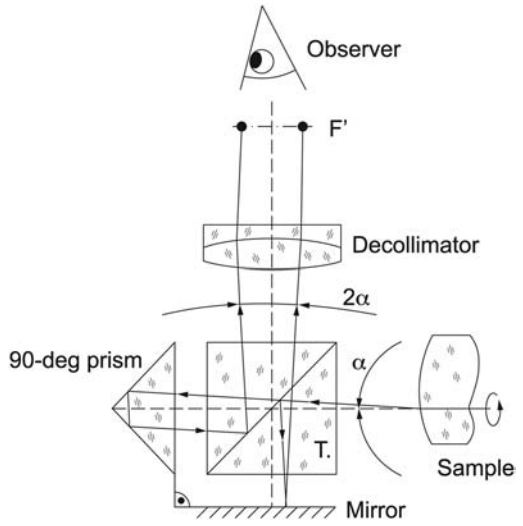

Figure 7.8(b) The reversion interferometer setup.

orthogonal to the roof edge of W, the preferred direction (W is defined in Section 7.5.6).

Rotating the still-decentered lens will, therefore, produce two circular paths of foci, as in Fig. 7.8(c), which also schematically shows the associated interferograms. The diameter of the circles reduces as centration improves. A null field ($P = \infty$) will occur twice per full sample rotation, defining the preferred direction (orthogonal to the roof edge). The amount of shift needed for obtaining centration follows from the fringe spacing in the direction orthogonal to the preferred direction [Eqs. (7.1) and (7.2)]:

$$4\alpha = \frac{\lambda \cdot \Delta P}{P_1 P_2} = \frac{4s}{f}. \tag{7.3}$$

$$s = \frac{f \cdot \lambda \cdot \Delta P}{4 P_1 P_2}. \tag{7.4}$$

Thus, sensitivity is enhanced by a factor of 2.

7.5.5 Fine control by the naked eye

The not-so-easy-to-assess null field as a criterion for centration [Fig. 7.8(c)] has an alternative. The reference mirror [in the inversion interferogram setup of Fig. 7.8(b)] is tilted by an amount γ, also within the preferred direction. The foci, thereafter, will describe two circles slightly offset, and null will be indicated by fringes representative of angle γ. This pattern will be identical for all phases of centration, and only at $\alpha = 0$ will the pattern remain stationary.

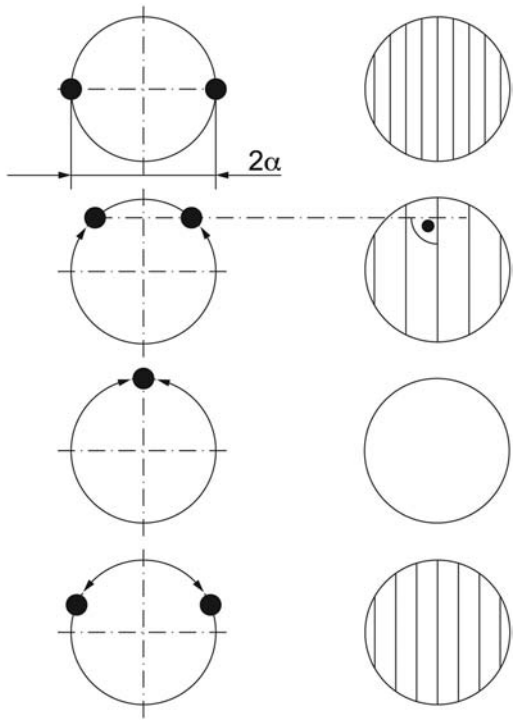

Figure 7.8(c) Foci and interferograms of the reversion interferometer as a function of sample P_r rotation.

One can ascertain by the naked eye that a final interference pattern, representing the $\alpha = 0$ position (where centration is achieved), cannot be further changed by the sample's rotation [Fig. 7.8(d)]. The fringes then correspond to 2γ. An additional minute tilt δ of the reference mirror, orthogonal to the preferred direction (parallel to W), will give a little kink to the fringes. This results in a wobble of the fringes while rotating the sample. Fringes that are aligned in this manner will always run nearly orthogonal to the preferred direction, superimposed by a slight wobble upon sample rotation. This *wobble* or *no wobble* criterion is a convenient means for visual centration control.

7.5.6 Further increasing centration sensitivity

In the case where the roof angle W departs by a small amount (5 to 10 arcsec) from 90 deg, one will observe two foci W_1 and W_2 next to R [from the reference mirror in Fig. 7.8(b)], shown schematically in Fig. 7.8(e). In the image plane, one can see two interferograms: W_1R and W_2R. Foci W_1 and W_2 are located symmetrically to the optical axis in angular positions of 2β for

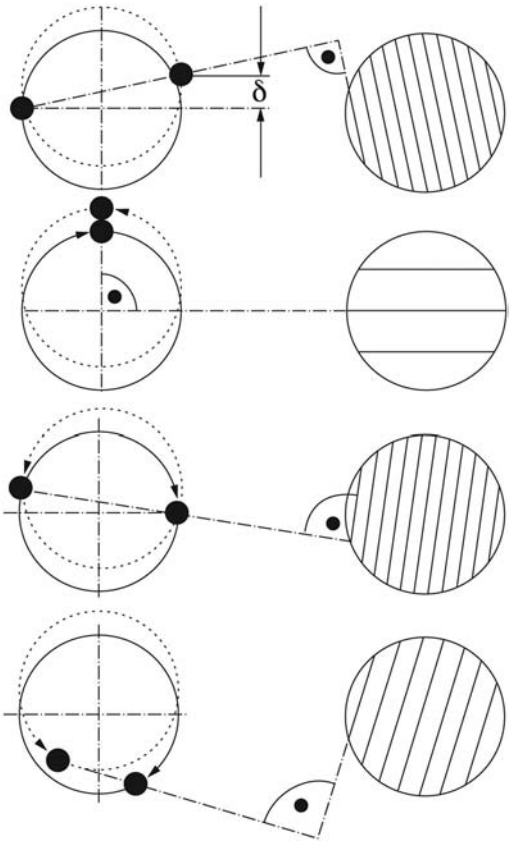

Figure 7.8(d) The effect of angle δ shown schematically. The centration criterion now has become the no-more-wobble fringe pattern upon sample rotation. The reference mirror in the reversion interferometer is now nutated by an angle δ (out of the drawing plane).

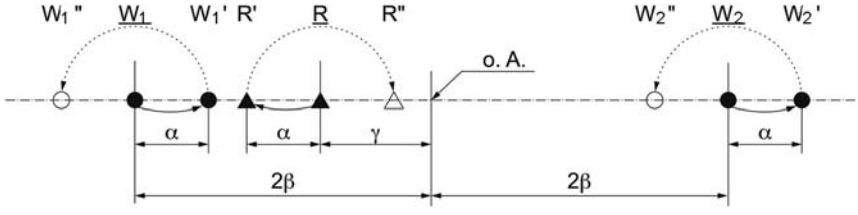

Figure 7.8(e) Positions of the foci in the reversion interferometer with the sample [in Fig. 7.8(a)] rotated from 0 to 180 deg (in the preferred direction) if the 90-deg angle of the reversion prism is modified to be 90-deg-β (β ~ 5–10 arcsec). Two simultaneous, identical interferograms W_1''/R'' and W''_2/R'' is the criterion for achieving centration.

each. Position R is determined by 2γ. The line connecting W_1 to W_2 is always orthogonal to the prism roof, defining the preferred direction. Fringes in both fields are parallel to each other and orthogonal to the preferred direction.

The beam deflected by α (the decentration of the sample) causes the foci to be in the following positions:

$$\begin{aligned} W_1' - R &= (2\beta - \alpha) - (2\gamma + \alpha) \\ &= 2\beta - 2\alpha - 2\gamma = \frac{\gamma}{P_1}. \end{aligned} \tag{7.5}$$

$$\begin{aligned} W_2' - R'' &= (2\beta + \alpha) + (2\gamma + \alpha) \\ &= 2\beta + 2\alpha + 2\gamma = \frac{\gamma}{P_2}. \end{aligned} \tag{7.6}$$

Subtracting Eq. (7.5) from Eq. (7.6), one obtains

$$4\beta + 4\gamma = \frac{\lambda \cdot \Delta P_{1,2}}{P_1 P_2}. \tag{7.7}$$

After turning the lens 180 deg, the new focal positions will be W_1, W_2, and R, yielding

$$4\alpha + 4\beta = \frac{\lambda \cdot \Delta P_{3,4}}{P_3 P_4}. \tag{7.8}$$

Finally, subtracting Eq. (7.7) from Eq. (7.8) results in

$$8\alpha = \lambda \left(\frac{\Delta P_{1,2}}{P_1 P_2} - \frac{\Delta P_{3,4}}{P_3 P_4} \right). \tag{7.9}$$

This is a sensitivity enhancement factor of 8, achieved still using the proven technique of adjusting for two identical interferograms. For the minimizing of α, one now needs to displace the lens along the preferred direction as far as needed to equalize the fringe pairs as closely as possible; Eq. (7.9) will then equal zero. Thus, the classic metrological practice of setting two neighboring interferograms to be identical provides the highest possible sensitivity.

With known values for λ, f, and P_2, and with $\Delta P/P_1 = 0.1$, one may use the pattern-equalizing technique to visually detect that $\alpha \approx 1.5$ arcsec. The conveniently controllable displacement should be 0.5 μm. The hardware consequences are as follows:

- The work spindle itself must have substantial out-of-roundness of under 0.5 μm, as shown in Fig. 7.2.
- Displacement and fixation of the lens must be possible in a range of at least $s = 0.5$ μm.

7.5.7 Conventional hardware for centration (air-bearing spindles)

Figure 7.8(f) illustrates an experimental setup for centration work.

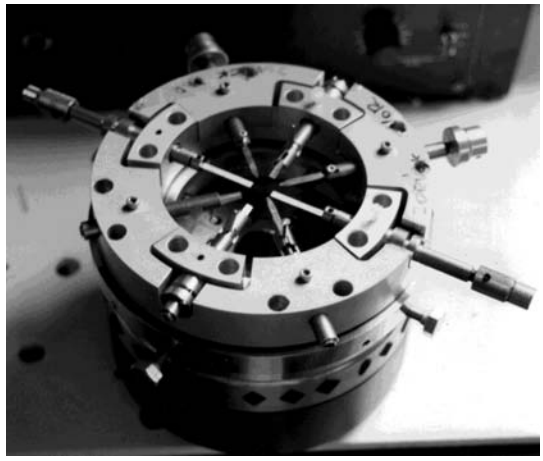

Figure 7.8(f) A conventional centering stand with an air-bearing spindle. The spindle carries a platform for doublet cementing, which requires two stages with a nanopusher.

7.5.8 Centration without rotating the lens

Achieving centration without the need to rotate the lens has proven to be a useful cost-reduction measure in the optical assembly. This possibility is realized by using a CCR instead of a roof prism. However, the three 90-deg edges of the CCR must each have the same edge error such that the resulting interferograms resemble the one in Fig. 5.11(a). The symmetric spider-web-like pattern, indicating good centration, will lose its easy-to-recognize symmetry immediately upon decentration of the lens. The partial interferograms are in no way representative of wavefront errors due to either transmission or reflection from the lens. Fringes that are not straight indicate a lack of collimation at the interferometer illumination.

The instrumental price for this kind of rotationless centration is a rugged design of the interferometer components that integrates lens-supporting hardware and nanopushers. This unusual detector system might be visualized by poking with a pointer into the center of a spider web. Pushing the pointer axially into the center will cause all of the "fringes" to move in or out simultaneously, and vice versa. Performing a circular motion on the web's center will instantly result in a pattern that is out of symmetry. Thus, the spider web is a good model for a 3D interferometer sensor.

The correlation between the optical and mechanical axes and tilt angles of surfaces relative to these axes, as well as in relation to refraction and absolute size, requires consideration of the German scratch-and-dig DIN 3140 standard, part 6, from which the ISO standard 10110 was derived. That, however, exceeds the scope and purpose of this experimental presentation.

The hardware consequences mentioned in Section 7.5.6 are realized with spindles having radial error motions as small as those shown in Fig. 7.2 and those of nanoscrews. Integrated into a common micrometer, the screw is a nonrotating anvil, coaxial with the micrometer. The anvil can be given a sinusoidal forward/backward motion of (plus/minus) some micrometers (e.g., 2 or 5 μm).

7.6 Homogeneity

Measurement of the homogeneity of refractive index n within a well-polished parallel glass plate becomes problematic because the transmitted beam's initial plane wavefront will be deformed by both inhomogeneities and out-of-flatness of one or both plate surfaces. Lack of parallelism is assumed to be within the flatness requirement. This situation becomes relevant if variations in n must be detected to better than $(\pm 1 \times 10^{-5})$/cm. In this case the measurement becomes more difficult, as the index gradient dn/dx is small, and the area of inhomogeneity is large. Common strioscopy and phase contrast can be applied to detect λ/200 local irregularities such as "orange peel" polishing defects. Our concern here is the λ/20–1λ slow-slope-index-induced variations, noticeable over some centimeters, that are impressed on a nominally plane wavefront. Any of the introduced interferometer methods jointly register these errors. The following section focuses on methods of separating form errors from inhomogeneity. Some methods require automatic interferogram evaluation.[7] Our interface will be the CCD camera.

7.6.1 Methods for error separation

Before spending much effort polishing a glass blank so that it is ready to be placed into a transmission interferometer, it is preferable to have a first impression about possible inhomogeneities. The classical method for this uses liquids having the same refractive index n as the glass. Such liquids are commercially available[8] or can be composed by mixing two liquids (n_1 low and n_2 high) in a ratio to yield $n_{\text{liquid}} \approx n_{\text{glass}}$. Reference 8 provides mixed white oils to match fused quartz to 0.00001.

Based on the availability of such index oils, three methods can be used for rendering pure inhomogeneity, independent of a sample's shape and roughness. Figure 7.9(a) represents these methods schematically in parts (i), (ii), and (iii). Parts (i) and (ii) illustrate the sample immersed in a tank filled with the index fluid (a drinking glass submerged in water can hardly be seen unless it has gross striations). Visualization of local $\Delta n/dx$ in the submerged sample may be either by strioscopy (Section 8.1.1) as shown in Fig. 7.9(a), or by interferometry, both methods using the same tank.

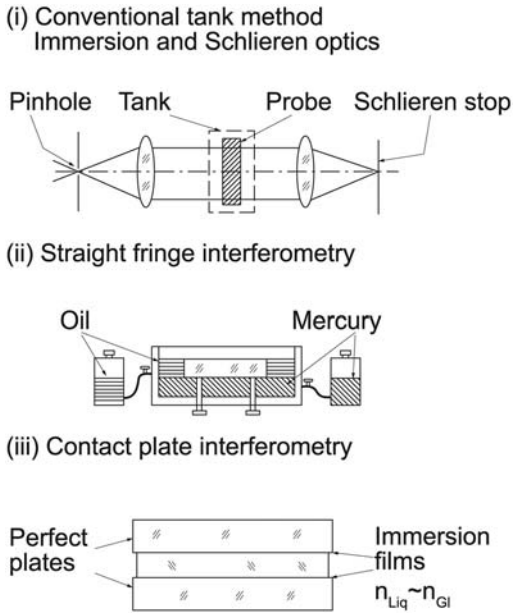

Figure 7.9(a) Homogeneity measurement of glass blanks requires separation of local thickness errors from variations of refractive index n, both having the same effect on optical path length changes. Immersion fluids matched to the average n and confined by perfect glass plates, windows on tanks, or oiled-on plates, will render Δn only, irrespective of the sample's thickness variation Δt. And, most importantly for cost savings, the immersion methods work on unfinished blanks.

Figure 7.9(b) shows a large tank for testing up to 500-mm-diameter blanks immersed in fluid. A 400-mm-diameter antireflection-coated front window closes the tank and takes up the hydrostatic fluid pressure. The Fizeau transmission flat is mounted on the wall, allowing it to be surrounded by fluid. An extended plate holder holds the rear mirror of the Fizeau interferometer at the same height as the transmission flat. The plate holder is supported by three feet standing on two air-bearing slides next to the tank. With this setup, the plate holder can be moved to reduce its distance to the transmission flat, while allowing the sample to hang in the cavity by a crane. The two angular fine controls needed for fringe alignment are integrated into the air-bearing feet. Collimation is by a 400-mm-diameter ($F = 4$ m) spherical mirror (not shown). The point source is a small, mirror-coated, convex lens and a laser beam, reflected by the spherical mirror.

The index fluid is a mixture of white oils with final index of $n = 1.456$ for quartz glass.[8] The distance t between the front Fizeau mirror and the rear reference mirror is represented in the relation $2t \bullet \Delta N = \lambda\ (\Delta P/P)$. The rear mirror can be moved to minimize $t_{\text{total}} - t_{\text{sample}}$. The reference mirror, hanging on a plate holder in the fluid, is moved on a three-legged frame, the feet of which are on air bearings [see Fig. 9.7(c)]. This method allows testing of

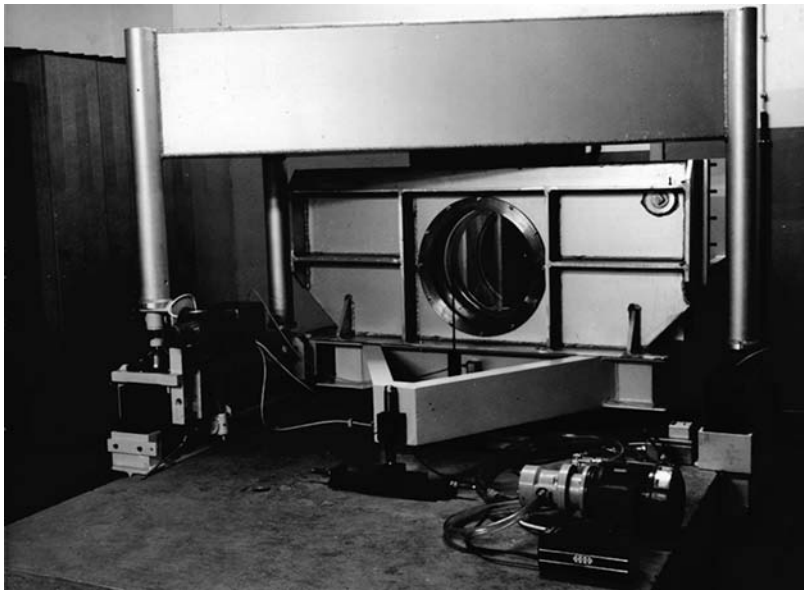

Figure 7.9(b) Homogeneity measurement according to Fig. 7.9(a) part (i): 400-mm Fizeau interferometer integrally combined with a tank filled with transparent index oil matched to quartz glass. A 400-mm-diameter glass window, verified to be sufficiently thick so as not to bend under the tank's fluid pressure, is a rigid part of the tank. A Fizeau transmission flat is mounted inside, next to the window. Large blanks, after having been finished to a bare minimum, are hung into the tank by a crane.

pre-ground quartz plates of ~10-cm thickness. The optical finishing of such plates for normal interferometric testing is substantially more expensive than immersing the blanks into an index-matching oil bath.

A few comments regarding temperature are warranted here. The general procedure (from mixture preparation to flooding the sample, and aligning the sample in the tank to final data recording) was performed in a nominally 18 °C environment. As every practitioner knows, maintaining a constant temperature is rarely possible, considering the effect of the body temperatures of people moving in and out of proximity of the setup. The mass of the fluid behaved adequately enough to show striations emerging over the longest distance t after some cure time had passed, since loading a large sample. A NO result meant that no fringe life was observed and no signal was recorded on a slow-moving differential thermocouple. Large parts must be moved slowly to allow for thermal balancing.

An alternative tank solution is shown Fig. 7.9(a) part (ii). The mercury mirrors shown therein were commonly used in the 1920s for "absolute" flatness determination.

A practical method for homogeneity testing involves a not-yet-polished sample between two "perfect" flats and a thin layer of index oil in the two interfaces [Fig. 7.9(a) part (iii)]. This assembly is a slippery fluid bearing that

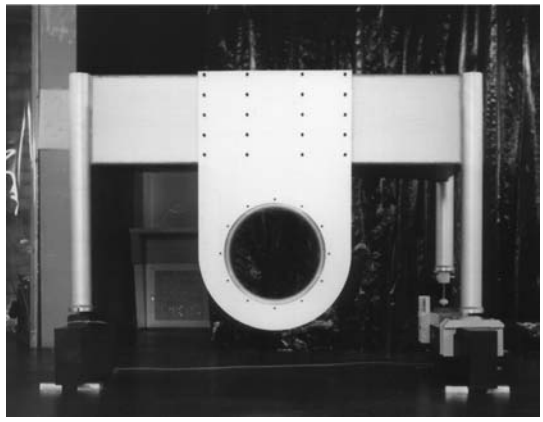

Figure 7.9(c) The rear mirror is hung into the tank on an extended plate holder. Angles α and β are adjustable by the three support pillars, which provide Z motion. Support pillars standing on air-bearing, Z-motion slides ride airborne on granite rails. This serves to reduce t_{total}.

requires some care in handling and avoidance of air blisters. One surface of the so-called contacting glass plates will be mirror coated so that the assembly can be used in a Fizeau setup. The specification for the contacting plates facing the sample is $\lambda/20$ across 200 mm.

The classical "dry" method for error separation after Twyman–Perry is illustrated in Fig. 7.10(a). Two types of interferograms of the same flat plate sample relate index errors Δn and thickness errors Δt, both shown in the figure. The reflection interferogram of the (well-polished) sample plate combines front and rear surface reflection; hence, it requires parallelism that is sufficiently close as to obtain about 7–15 fringes per diameter of collimator used. The optical path difference E in the reflection setup [shown in Fig. 7.10(a)] is

$$E_{\text{ref}} = 2(T\Delta N + N\Delta T). \tag{7.10}$$

The transmission interferogram needs an interferometer from which the fringe spacing can be aligned to be nearly identical to that obtained (without a chance for alignment) in the reflection interferogram:

$$E_{\text{trans}} = 2[t\Delta n + (n-1)\Delta t]. \tag{7.11}$$

Quantitative evaluation requires two X–Y matrices of complete field-of-view evaluations of $(\Delta P/P)_{\text{trans}}$ and $(\Delta P/P)_{\text{ref}}$. The two matrices will be $t(x,y)$ and $n(x,y)$. Subtracting the two matrices of Δn values obtained for each interferogram will yield a third matrix of Δn values:

$$\Delta n = \frac{\lambda}{2t}\left[n\left(\frac{\Delta P}{P}\right)_{\text{trans}} - (n-1)\left(\frac{\Delta P}{P}\right)_{\text{ref}}\right], \tag{7.12}$$

where $n = 1.456$ is the average index. With $\lambda = 0.6$ μm and $(\Delta P/P_0) =$ the fringe reading accuracy, one obtains $\Delta n_{\min} = 4.5 \times 10^{-5} \times (\Delta P/P)_{\min}/t$.

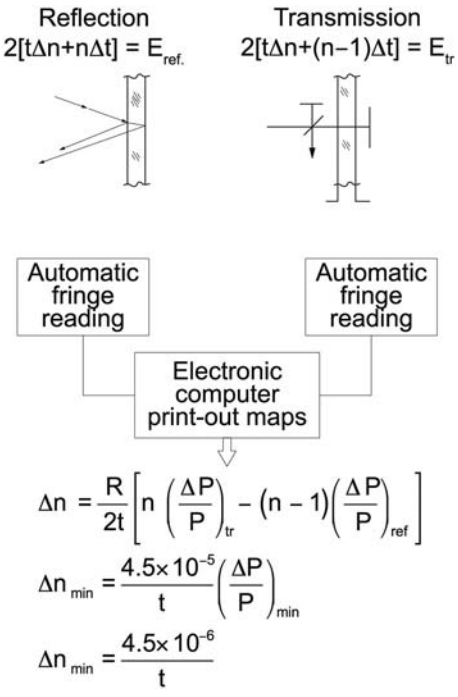

Figure 7.10(a) Schematic of the Twyman–Perry interferometric homogeneity evaluation, using the moiré technique. The requirements for the sample's wedge angle can be rather relaxed.

With $\Delta P/P = 0.1$, $\Delta n_{\min} = (4.5 \times 10^{-6})/t$, with the average t measured separately, in millimeters. The need for photoelectric fringe detection is evident. The method entails the need to polish both of the sample's surfaces and to hold a wedge angle α as well, α being on the order of λ/P, with P being a practical value (1 cm).

Mating the two interferograms for a qualitative assessment of their difference might work, if $(\Delta P/P)$ differences are smaller than 1. Disqualification of a sample follows if $(\Delta P/P)_{\text{trans}} >> (\Delta P/P)_{\text{ref}}$. This criterion allows practical handling of quantity samples. Equation (7.12) can be the basis for an inexpensive evaluation of inhomogeneities using the moiré technique.

The moiré technique offers an inexpensive, simple homogeneity check for cases where the sample has a wedge angle large enough to produce very narrowly spaced fringes in reflection. In a two-beam interferometer, as in Fig. 7.10(a), when producing straight fringes while the interferometer is empty, one can adjust the transmission fringes of a problem sample to be like the reflection fringes, in that the two sets of fringes are equally narrowly spaced. For optimal contrast of the moiré pattern resulting from the superposition of the two interfergrams, the reflectance of the two flat mirrors should be as low as that of uncoated glass. Figure 7.10(a) is the schematic interferometric setup for evaluation using Eq. (7.12), where n is a value given by the glass supplier.

Precision prism production requires homogeneity testing of samples in three directions. Cubes prepared for CCRs are turned 90 deg to obtain two

views in orthogonal directions. The suspicion of index variations is justified, as glass plates produced like pancakes might be striated parallel to the surfaces; such strias, being laterally uniform, are not recognized in normal transmission. A typical test is the 90-deg angle of a simple prism. The angular difference between a 90-deg angle that is measured externally versus being measured internally (assuming the hypotenuse surface to be perfect) will be caused by striation parallel to the hypotenuse.

For homogeneity measurement of extended large plates (e.g., 400 mm), the Twyman–Perry method can be applied according to the configuration shown in Fig. 7.10(b). A Fizeau interferometer such as that shown in Fig. 4.3 has, as the planar side of the collimating objective, a 1:12 to 1:15 monochromat beamsplitter, coated for multiple-beam interference. The sample will be mirror coated on both sides with chemical silver.[9] Interferograms are first recorded of the sample's top surface and, after wiping off the upper silver layer, of the bottom surface, which includes the sample's volume. The two X–Y matrices with $(\Delta P/P)_1$ and $(\Delta P/P)_2$ values subtracted will represent the reflection interferogram. After removal of the bottom silver layer, one obtains a third X–Y matrix $(\Delta P/P)_3$. As a double check, one may record a fourth set $(\Delta P/P)_4$ of the empty interferometer. The relation for evaluating Δn is given in Fig. 7.10(b).

The multiple-beam configuration can be operated as multipass for sensitivity enhancement (see Chapter 10). The sample will transmit the test

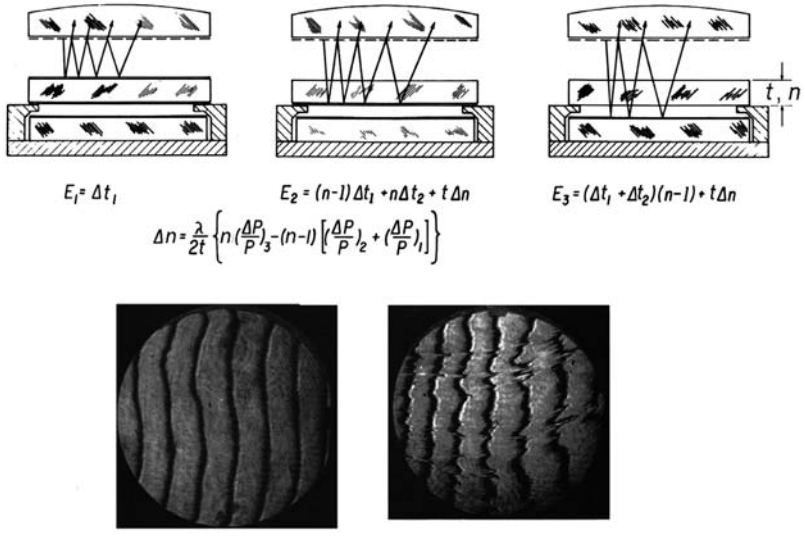

Figure 7.10(b) Homogeneity measurement in a Fizeau interferometer, realizing the Twyman–Perry method. The surfaces of the sample are given a flash polish and are chemical-silver coated. The two interferograms of 12 cm diameter, with a 6-cm-thick glass plate, relate to the sample's coated first surface and its departure from flatness (E_1 on the left) and to E_2 (on the right), after removal of the silver coating. E_2 represents the departure from flatness of the lower surfaces seen from the inside, plus inhomogeneities.

beam $2n$ times. The measurable inhomogeneity with a multipass technique is expressed as

$$\Delta n_{\min} = \frac{4.5 \times 10^{-5}}{T} \times \frac{\Delta P}{P}, \tag{7.13}$$

and

$$\Delta n_{\min}/n, \text{ with } n = 2, 3, 4.$$

Application of electronic fringe-evaluation phase shifting allows measurement of Δn on the order of $5 \times 10^{-7} x$ on 1-cm thick plates.

7.6.2 Fast qualitative assessment of homogeneity

The change of optical path length in a plane-parallel glass plate of a common thickness t, as a function of its angle of inclination relative to an optical axis, can be used for the detection of Δn, even using thin plates with polished or blank surfaces. A simple collimator suffices, as illustrated in Fig. 4.21(a). The change between two angles of incidence, i_1 and i_2, allows one to derive Δn from two reflection interferograms by evaluating the two local fringe deformations and by having previously determined t:

$$\Delta n = \left[\left(\frac{\lambda}{2}\right) t \times C_2\right] \left(\frac{\Delta P}{P}\right)_1 - \left(\frac{\Delta P}{P}\right)_2 \times C_1. \tag{7.14}$$

Detailed derivation of the constants C_1 and C_2 is given in Ref. 10.

The practical execution of this two-angle procedure is shown in Fig. 7.11. For a single back-and-forth pass, the two interferograms at angles i_1 and i_2 allow one to compute

$$\Delta n = \left(\frac{\lambda}{t} \cdot C_4\right) \left[\left(\frac{\Delta P}{P}\right)_1 - \left(\frac{\Delta P}{P}\right)_2 \cdot C_3\right]. \tag{7.15}$$

The constants $C_{1,2,3,4}$ containing the angles i are derived in both Refs. 10 and 11. The angles i_1 and i_2 need to be measured by an angular encoder with 2-arcsec resolution. Calibrated fixed hard stops will suffice.

The multipass technique (Chapter 10), as shown in Fig. 7.11, will enhance sensitivity n times; $n = 4$ is practical. Compared to Twyman–Perry, the two-angle method is $10\times$ less sensitive:

$$\Delta n_{\min \text{ trans}} = \frac{1.4 \times 10^{-4}}{t} \times \frac{\Delta P}{P_{\text{average}}}, \tag{7.16}$$

but it is fast and inexpensive. It relies on (1) the precise measurement of the angles i_1 and i_2 and (2) a rotary drive that is slow enough to pick up the two zeros on the two surfaces of a dedicated angular standard; speaking *pro domo*,

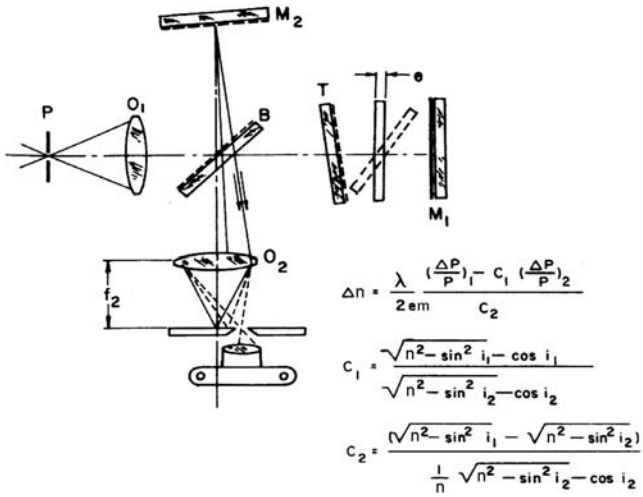

Figure 7.11 Homogeneity assessment by the interferometric two-angle method.[10] A flat plate sample is rotated through fixed angle $i_2 - i_1$ (± 1 arcsec), producing a change in optical path length. Local ($\Delta P/P$) differences between i_2 and i_1 relate to Δt and Δn. If either one of these two are somehow known to be zero, the other can be determined (m is the order of transmission). This schematic shows a multiple-pass interferometer for sensitivity enhancement.

an air-bearing table with an integrated nanodrive is a good choice for use with the two-angle method.

References

1. W. Zschommler, Editor, *Precision Optical Glassworking: Manual for Craftsmen and Designers*, *Proc. SPIE* **0472** (1984).
2. H. H. Hopkins and H. J. Tiziani, "A theoretical and experimental study of lens centring errors and their influence on optical image quality," *British J. of Applied Physics* **17**(1), 33–54 (1966).
3. E. R. Marsh, *Precision Spindle Metrology*, Second edition, DEStech Publications, Lancaster, PA (2010).
4. J. Camus, "Die Genauigkeit der Dupligramm-Methode," *Optik* **16**, page numbers unknown (1959).
5. M. Birkenmaier, "Entwicklung und Erprobung eines interferometrischen Messprinzips zur Überlagerung von Beugungsmaxima am Beispiel einer Drehspindel," Doctoral thesis, ITO, Univ. Stuttgart (1994).
6. P. Langenbeck and M. Bartelt, " Hochgenaue Zentrierung von Mikrolinsen," *F&M: Feinwerktechnik, Mikrotechnik, Mikroelektronic*," **106**(3), 160–163 (1998).

7. E. Roberts and P. Langenbeck, "Homogeneity evaluation of very large discs," *Applied Optics* **8**(11), 2311–2314 (1969).
8. Cargille-Sacher Laboratories Inc., Cedar Grove, NJ 07009 USA: Cargille™ immersion oils and refractive index fluids.
9. Peacock Laboratories, Inc., 1901 S. 54th St., Philadelphia, PA 19143, USA: silver spray chemical solutions.
10. P. Langenbeck, "Optical homogeneity measurement by a two-angle method," *Optik* **28**, 592–601 (1968).
11. H. J. Tiziani, "Prospects of testing aspheric surfaces with computer-generated holograms," *Proc. SPIE* **235**, 72–79 (1980) [doi: 10.1117/12.958964].

Chapter 8
Mass-Produced Specular Surfaces

8.1 Specular Surfaces That Are Grossly Unflat

The past few decades have seen an explosion of dedicated products with optical surface specifications that are flat with tight tolerances. For example, computer memory storage disks started with a 14-in. diameter, then briefly went to 8 in., then had a surge of 5¼-in. substrates for magnetic data storage. Silicon wafers started to be mass produced with 2-in. diameters, then 4 and 5 in., and currently are being produced at 450 mm. Polygon mirror wheels combining optical and mechanical tolerances for their drive bearings and motors became a real challenge to precision engineering. These developments prompted efforts in both automatic sorting and fast visual sorting of bad samples. (The fast-changing market was a welcome development to small businesses supplying dedicated hardware.)

The amount of effort involved in optical/instrumental testing can be reduced if the mere view of the reflection off of a substrate surface (e.g., of a collimated beam) produces a light distribution on a screen, as in Fig. 8.1. Sunlight or a bright beam of light from a tungsten lamp suffices when visually judging the sample's quality by reflected light distribution on the spot. The light distribution, as viewed in Fig. 8.1, might offer a quick qualitative *in situ* check without the need for handling and aligning. Also, adjusting the chucking vacuum will quickly produce evidence of elastic deformations (dirt on chuck) directly on the machine.

Figures 8.2(a) and (b) show two interferograms, each indicating specularity but with forms far from acceptable. Initial flatness errors will be perpetuated (beyond the possibility for correction) in further finishing. Automatic fringe evaluation for each of such samples will be unnecessary and too expensive to apply. The desire for a quick sorting check in 100% cassette-to-cassette operation has led to observation of the defocusing plane.

Surfaces having rendered interferograms such as that in Fig. 8.2(b) produce foci in the Fizeau interferometer such as those reproduced in Figs. 8.3(a) and (b),

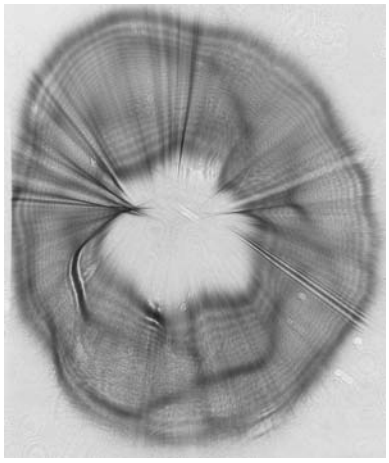

Figure 8.1 Collimated beam reflected (not focused) off of a freshly diamond-turned aluminum surface. The shiny, specular finish is completely useless in meeting any flatness tolerances.

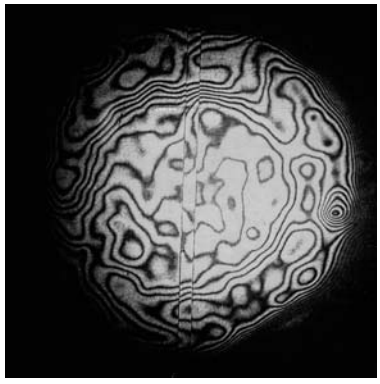

Figure 8.2(a) Fizeau interferogram of a 5-in. Si wafer after lapping and flash polishing, prior to final polishing. Such a gross deformation has no chance of being removed by continued polishing, regardless of the duration of the polishing. (Incidentally, this interferogram is representative of one from a prism interferometer with 2-μm fringe equivalent). This figure correlates with Fig. 8.3(a).

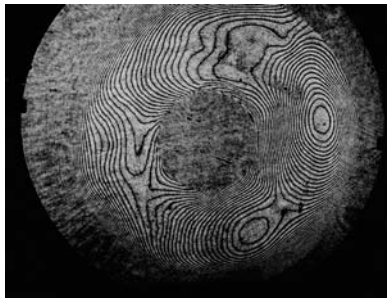

Figure 8.2(b) Fizeau interferogram ($\lambda = 0.63$ μm) of a 5¼-in. magnetic storage disk substrate of diamond-turned metal Al6061 of ~ 2-mm thickness. The interferogram represents a flat while still chucked and presents a view that is completely useless after dechucking. This figure correlates with Fig. 8.3(b).

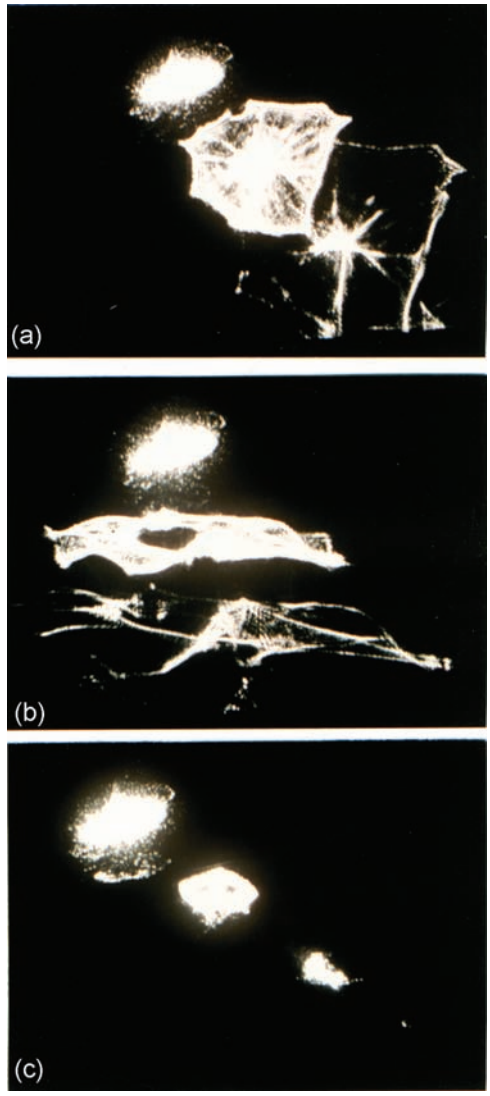

Figure 8.3 The defoci in a Fizeau interferometer of (a) the sample in Fig. 8.2(a), (b) the sample in Fig. 8.2(b), and (c) a flat sample mirror.

where the upper bright spot shows the defocus by reflection off of the reference mirror, and the first and second reflections result from the sample. For comparison, flat-sample-mirror-generated foci are shown in Fig. 8.3(c). The general-utility beamsplitter coating on the Fizeau reference mirror was chosen to reduce the relative brightness of successive multiple reflected beams (Section 2.5.1). An interferogram is obtained only after aligning the sample or reference to have foci (however cloudy) coinciding.

The two different substrates represented by the interferograms of Figs. 8.2(a) and (b) offer quite different opportunities for in-process control. The wafer needs to be cleaned before presenting a naked surface, regardless of what test ensues. This is not the case for the diamond-turned surface; it can be—and should be—tested on the machine prior to removal, possibly even while turning. The inspection of the beam reflected off of the work (target) can be in a location somewhat remote from the actual machining, as in the case of using the handheld hairline interferometer (Section 4.3.5). Focus inspection is closely related to techniques for obtaining a sample's information by mechanically interfering in the focus, as in phase contrast and strioscopy (the Foucault method).

8.1.1 Strioscopy: Is it quantitative?

We recall classical pre-laser times with optical inspection methods and names such as M. Françon, H. Wolter, and H. Schardin, contributors to *The Encyclopedia of Physics*.[1] Strioscopy visualizes relatively gross phase objects (specular surfaces) of the type just discussed. The simplicity of the method has for a long time contributed to its stigma of not being quantitative, despite the fact that generations of astronomers tested their mirrors using Foucault strioscopy by evaluating the surface shape based on the brightness distribution. The light sources used were incoherent (tungsten band lamps).

The transition from incoherent to coherent illumination allows one to characterize light deviations by a so-called phase object within a collimated beam, using countable interference patterns. This transition away from tungsten lamps to coherent light sources was achieved using spectral lamps, such as mercury vapor lamps focused onto a slit with controllable width. Such illumination is used in the classical strioscopy and phase contrast setup shown in Fig. 8.4(a).

For illustration we chose a gross phase object: a flame whose gas refractive index changes in the combustion zone. Such an object, placed in a collimated light path, will deviate light out of collimation, bypassing the stop and preventing the undeviated light from propagating to the image plane. Only *object* light is used to form the image of the object. Illumination by the

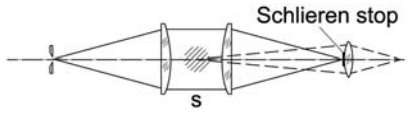

Figure 8.4(a) Observation of phase objects in a classical strioscopic setup. Illumination is by mercury vapor lamp onto a slit of controllable width. A central stop is deposited onto the imaging lens (a small drop of black ink). The only adjustment needed is for the collimated light to be focused onto this stop.

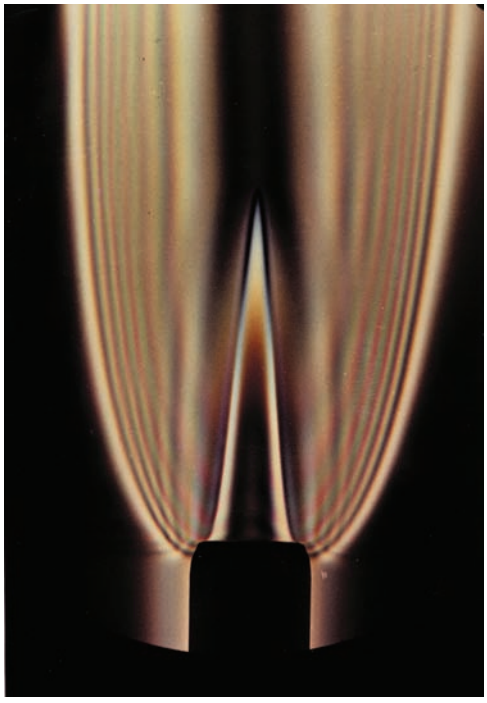

Figure 8.4(b) Image of a gas flame in interference strioscopy. The center of the image is equally dark as the ambient area for lack of dn/dx, where n is the refractive index within the flame. What may be expected from application of color strioscopy to samples such as those in Figs. 8.2(a) and (b)? The objective of the search is a fast, low-cost sorting optic. The preferred answer would be a simple criterion, such as *color there* (undesired) or *color not there* (desired).

mercury spectral lamp through an open slit produces a bright so-called shadow image, which becomes quite distinct after stopping the collimated light surrounding the object. Upon reducing the slit width (approaching Verdet's criterion), colored interference fringes begin to appear in the image of the flame [Fig. 8.4(b)]. The colors represent the spectral lines of mercury, and the interference develops because the reduced slit width ($\sin \Delta u < \lambda/4$) causes the illumination to fulfill Verdet's coherence condition.

8.1.2 Further review of strioscopy

For repetitive samples, the optical setup in Fig. 8.4(a) can be operated at increased speed only in a transmission case (such as flame *off*, flame *on*, or, sample *in* or *out*). Thus, samples differing in reflection need to be aligned for their evaluation. For instance, diamond-turned substrates are aligned by remaining chucked after machining. Or, samples on a transporting conveyor belt might be given a brief nutation, enough for the defocus to traverse the

stop, briefly allowing electro-optical image evaluation. A stretched, blackened wire will reduce the 2D engineering task to a 1D task.

The setup in Fig. 8.5(a) allows comparison of strioscopy to regular Fizeau interferometry. Samples on a tilt table allow positioning of the decollimated focus onto the stop for strioscopy. Insertion of a Fizeau beamsplitter plate and removal of the focal plane stop allows one to obtain the interferogram that correlates with the strioscopy record. For demonstration, a flat mirror was polished to carry an error of size and depth typical for the anticipated deformations.

The half-plane stop (a shaving blade, after Foucault) is easier to arrange but has an associated uncertainty about the optimal blade position. The verification of the proper blade position is a symmetrical dark field, as obtained by a blackened wire (acting as 1D), replacing the black stop on the

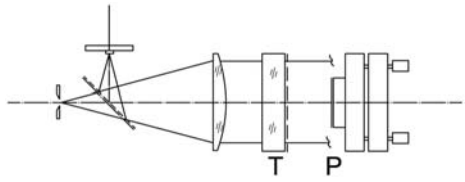

Figure 8.5(a) Classical strioscope setup combined with Fizeau interferometer for comparing both methods on one sample. Illumination for the Fizeau case was a HeNe laser and for strioscopy was a mercury-vapor lamp with a green filter, transferred by fiber cable. The two methods produce qualitatively equivalent results, shown in Fig. 8.5(b).

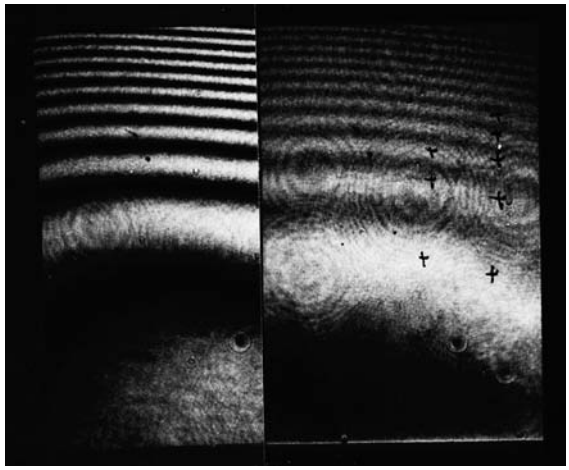

Figure 8.5(b) Comparing Fizeau interferometry to strioscopy. (Left): Fizeau interferogram (laser, $\lambda = 0.63$ μm) of a sample, with the stop in the defocusing plane removed. (Right): Strioscopy of the same sample, with central stop inserted as indicated in Fig. 8.5(a). The Fizeau transmission reference mirror is removed.

center of the imaging lens (acting as 2D). The symmetrical dark field is a convenient indication of the correct placement of the stop. The term *correct* needs definition at this point: One will soon recognize an undefined variety of possible Foucault half-plane settings, each one resulting in a different (however similar) fringe pattern. For some samples, the criterion *fringes present* or *no fringes* might suffice.

The low cost of strioscopy makes it most useful for detection of such small defects, whose diffraction spectrum extends widely around the central zeroth order (the stop). However, regardless of which method is chosen, neither interferometry nor strioscopy will operate without good sample alignment; any alignment should take place instantaneously, regardless of the engineering quality of the instrumentation.

8.1.3 Interference in strioscopy: the origin of coherent background (reference)

In the experiment shown in Figs. 8.5(a) and (b), the sample was alternatively viewed by Fizeau interference and by strioscopy. Simultaneous superposition of both methods, as shown in Fig. 8.6, starts with a common two-beam Michelson interferometer setup, using two flat mirrors M_1 and M_2. The interferogram between the mirrors is reproduced in Fig. 8.7(a). M_2 has a low-reflection coating, while M_1 is Al coated as usual (resulting in low-contrast,

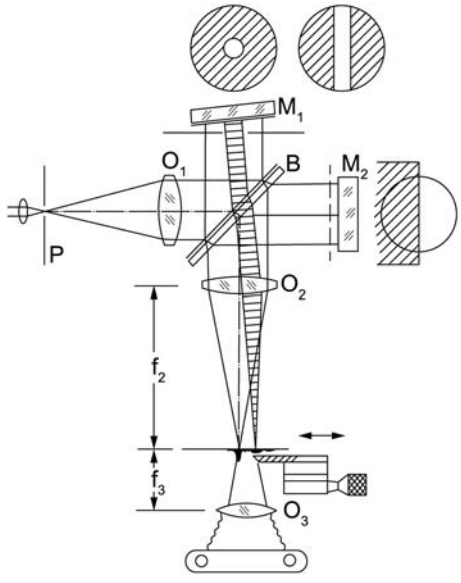

Figure 8.6 Simultaneous implementation of Michelson interferometry and strioscopy for demonstrating the origin of the coherent white-light background (coherent reference) in the strioscope [Fig. 8.4(b)].

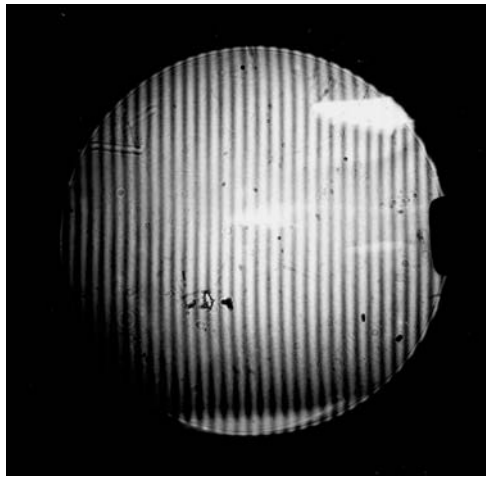

Figure 8.7(a) Michelson interferogram taken by the setup in Fig. 8.6 with no stops inserted yet.

but still recognizable, two-beam fringes). The angular setting M_1/M_2 is large enough to have each mirror's decollimation image P_1' and P_2' of the point source P sufficiently separated for the planned interaction upon only one of the decollimation images (P_1'). Therefore, the fringes in the image [Fig. 8.7(a)] will be narrowly spaced.

A screen covering one-half of the field placed in front of M_2 permits one to observe one-half of the interferogram, as in Figs. 8.6 and 8.7(d). The complete field of M_1, however, gets reduced in size by alternative stops, as shown in Fig. 8.6. The residual beam represents one that might be used in a strioscope and is cross-hatched in Fig. 8.6. The resulting image [Fig. 8.7(b)] shows a half-section on the lower part and the plain field of M_1 in the upper part.

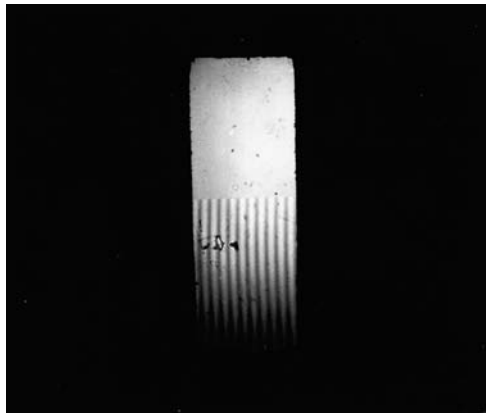

Figure 8.7(b) Michelson interferogram taken by the setup in Fig. 8.6 but now with three screens (stops) inserted in both interferometer arms: two vertical and one horizontal.

Insertion of a black half-plane (blade) into the P_1' image generates Figs. 8.7(c) and (d), representing two minutely different blade positions [Fig. 8.7(e) was generated in the same way but using a circular field stop]. Thus, the origin of the reference light for interference in a strioscope is evidenced, be it by the benign or malign coherent background that is produced by interaction in the focal plane. The effect will be beneficial, as will be seen in Section 8.2. After this experiment, one may understand the generation of interference patterns in the striogram of the flame [Fig. 8.4(b)]. The zero-angular-deflection light zones right, left, and central to the flame (dark in the image) produce their own central diffraction image of the point source. The partial stop leaves a light distribution, representing a smaller secondary light source, which causes a more widely spread coherent light distribution in the image space. The interpretation of Fig. 8.5(b) is as follows: Gross wavefront errors (more than one interference order, allowing fringes to be counted) can be interpreted in higher interference orders ($m + \Delta m$) with an uncertainty of $\Delta m < 1$. This uncertainty is certainly acceptable with a *go* / *no go* sorting apparatus. The number and slope of orders m of interference will be quite useful for testing if m is large, e.g., more than 3. What will be the hardware consequences, in this case?

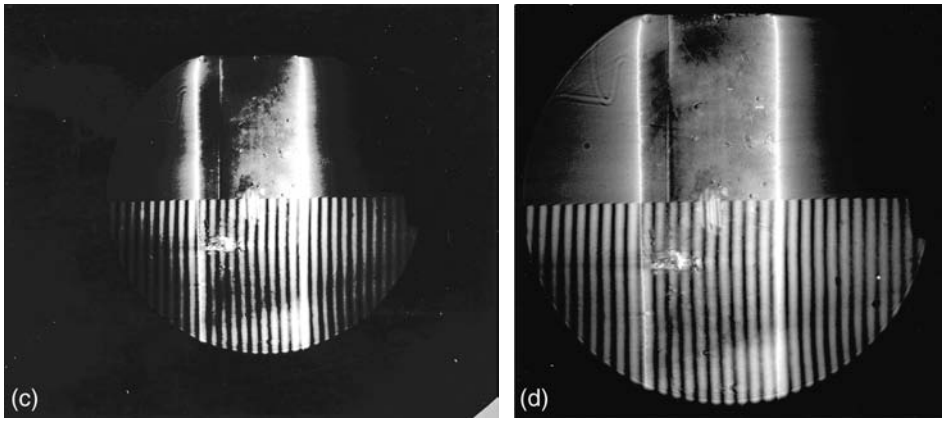

Figure 8.7 (c) and (d) (c) A focal plane stop (a blade) is driven into the defocus of a cross-hatched beam (Fig. 8.6). (d) The blade inserted in a minutely different position. The upper parts of both images show the striogram; the lower parts show the striogram superimposed by the Michelson reference. This experiment illustrates the generation of the coherent background: the width of the image of the light source is much reduced by the intrusion of the focal plane stop. Therefore, the zeroth-order-diffracted light spreads into a wider angle, as seen in Figs. 8.7(b) and (c). Referring to Fig. 8.4(a), the dark zones in the image of the flame show the collimated light passing through the two zones beside the flame and along a slim path through the center of the flame.

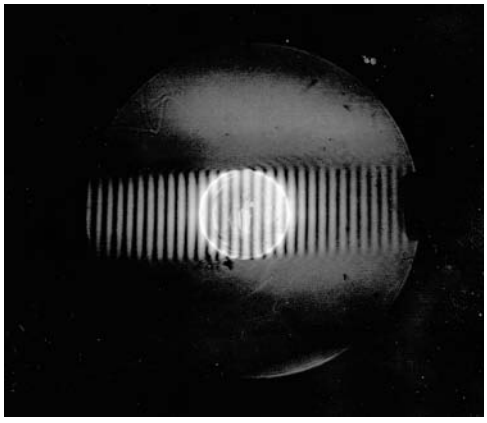

Figure 8.7(e) As in Figs. 8.7(c) and (d) but with a circular stop replacing the rectangular field stop.

8.1.4 Mechanical focal-plane interaction

After having solved the sample alignment, let us check what the interaction in the focal plane has to offer. Of the sample foci shown in Figs. 8.3(a)–(c), we select the first one. Its x'/y' location in the focal plane of the decollimating objective will be determined only by the sample's angular alignment, irrespective of its lateral and rotary orientation.

The sequence of interaction by a Foucault half-plane, as shown in Fig. 8.6, will start with a bright field (represented by the upper half in Fig. 8.7(a), will become somewhat shadowed, as in Fig. 8.7(b), and will be succeeded by Fig. 8.7(c), as the Foucault blade moves further (a few microns) across. Finally, the image will appear dark, with residual small defects becoming visible on the dark background (like stars in a night sky). Obviously, the 1D Foucault blade offers acceptable simplicity, whereas a dark spot would require a 2D micrometric positioning and would not substantially increase the information; the overshoot into any direction will be difficult to control. The linear movement need not be by the Foucault blade; it might be a nutation of the sample while being transported.

One will encounter two distinct types of errors that can be detected by the Foucault method:

1. microdefects, pits, grooves, scratches, even granularity, the limit of which will be the resolution on the lower defect of size and,
2. substantial extension of error zones (out of flatness), causing defocused light to spread such as to bypass the main, zeroth-order defocused light from the residual good (flat) zones of the sample; let us call these macro-defects.

So far, the anticipated method will be dynamic. Testing in quantity, as in samples on a moving belt, will (regardless of their alignment) allow the defocused image to pass by the Foucault blade and produce strioscopic information for a brief moment.

8.1.5 Optical interaction: color coding

Preselection of a certain bandwidth of different angular directions in the illuminating beam is offered by longitudinal, chromatic aberration, as provided by a monochromatic defocusing objective. Within white-light illumination, the blue focus is located closer to the objective and the red focus farther away.

A 2D circular dark spot, thence, will be placed to block out the blue, while letting pass the red. Needless to re-emphasize is that the stop's and sample's alignments need to be on axis. Samples (memory substrate disks) were recorded with a setup as described in Fig. 8.5(a). Figure 8.8 proves this method.

Sample substrates for the following records were 5¼-in. substrates for magnetic memory disks: Figs. 8.9(a) and (b) and 8.10(a) and (b) were recorded in the Foucault setup (central focal plane disk replaced by half-plane). These records allow instant visual disqualification for obvious lack of rotary symmetry.

Substrates for 5¼-in. magnetic storage disks were the typical sample, requiring QC in cassette-to-cassette operation. A good sample is shown in Fig. 8.10(b), which shows almost-uniform red with a minute green ring at the inner clamping diameter. By contrast, Fig. 8.10(a) shows annular defects that look like machining marks. However, the latter are beyond resolution with about 5000 cuts per radius. The grooves in the image result from irregular depths of cut, caused either by superimposed tool vibration or by substance buildup on the diamond tool.

The cloudy surface profiles seen in Fig. 8.9(a) are typical for ductile material being polished; the depth of the cloudy profile became known to be around 15 nm (information supplied by BASF—a large German chemical company). One also

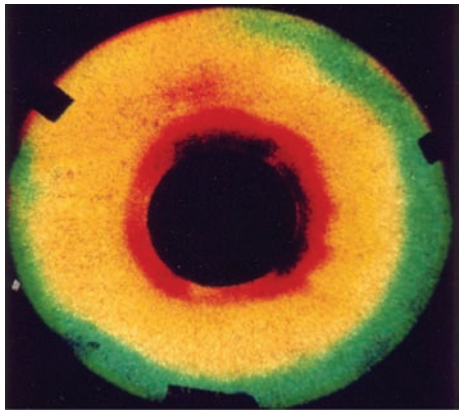

Figure 8.8 Striogram of 5¼-in. lapped/polished substrate exhibiting natural colors; the coding zones are deformed out of flatness and are characterized by yellow.

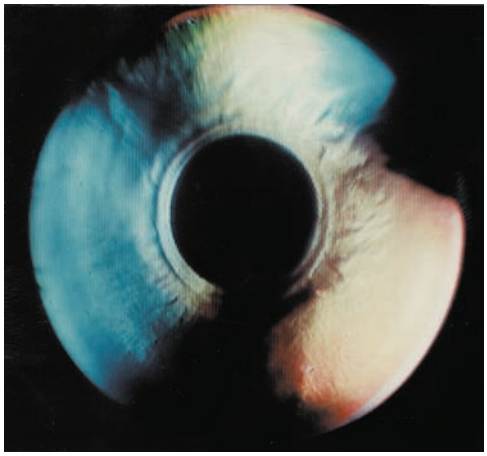

Figure 8.9(a) Lapped/polished aluminum substrate disk. The three dark zones do not deviate light aside the central focal-plane stop. They might be tracked back to irregular chucking or kneading of the ductile material. The inner ring shows ductile-material deformation due to clamping on the test spindle.

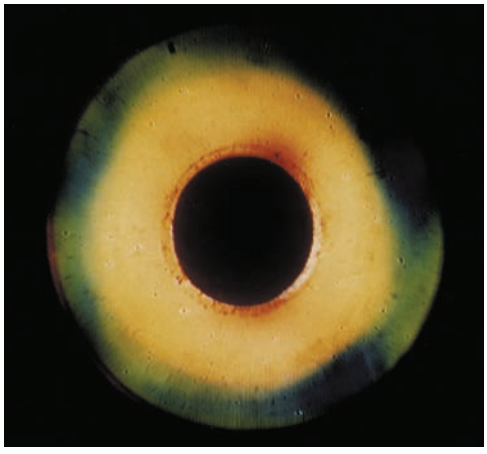

Figure 8.9(b) Another disk lapped/polished like the one shown in Fig. 8.10(b). The error zones can be judged as still being triangular, comparable to those in Fig. 8.9(a). The circumferential acceleration value seems to be smaller; thus, the sample is immediately judged to be unacceptable.

recognizes the triangular out-of-flat areas and the impression (red) due to clamping; the other areas show acceptable smoothness. Good rotary symmetry (small acceleration values) is displayed by the two micromachined samples shown in Figs. 8.10(a) and (b). In Fig. 8.10(b), the clamping trace is not so obvious, and the smoothness is acceptable; the sample in Fig. 8.10(a) exhibits a machining

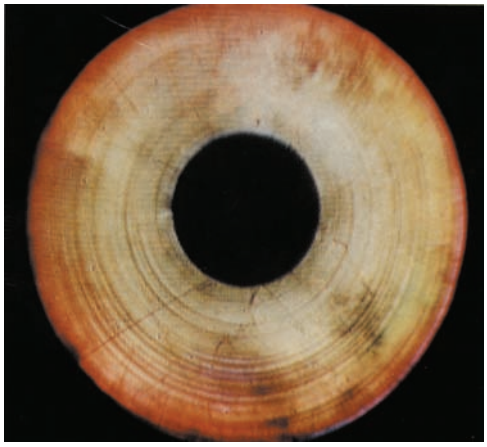

Figure 8.10(a) A substrate that has been micromachined with a defective tool; the grooves result from edge buildup on the tool.

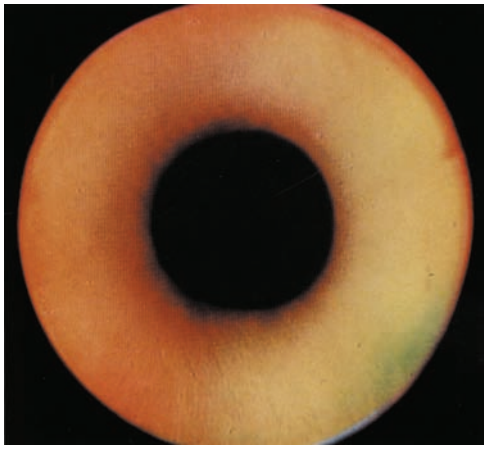

Figure 8.10(b) A micromachined sample at the limit of being acceptable.

profile that is much coarser than might be seen due to a feed of 7 μm/rev. The instrumental resolution does not allow one to view the cutting marks. However, the peripheral gross traces signal an interaction of the profile as cut with vibrations between the tool and the work, the cause of which starts with initial tool alignment (burnishing) prior to lubricant application.

8.1.5.1 Further comments on striograms

The information obtained by strioscopy is surprising in its sensitivity, both macroscopic (acceleration values) and microscopic (kneading). The only adjustment after a sample's mild vacuum chucking is the lateral shift of the

Foucault stop, or of the stretched wire. The latter has the advantage of signaling its symmetric position, thereby reducing the time until conclusive record taking.

Samples that are not pre-oriented, such as disks immediately after having been machined on their chuck, need an auxiliary means, such as autoleveling, for expedient quantity testing. An alternative to autoleveling for this testing takes place in the process of transportation on a linear conveyor belt, where, in a suitable location, the disk is given a brief nutation. This nutation allows the focus to walk by the stop, a movement that is equivalent to adjusting the focal plane stop. The sample nutation trick allows instant electro-optic evaluation.

8.2 The One-Arm Interferometer

Occasionally, one needs to analyze a plain beam, transmitted by, or reflected at, an object. One device applied to such a task is the differential shearing interferometer [Figs. 4.4, 5.1, and 5.2(b)], which provides the utmost in ease of handling but is inversely complex in evaluation. Occasionally, one also needs instant visual interpretation, such as is provided by strioscopy or a hairline ruler. Converting a shear interferometer into an absolute interferometer, one obtains a one-arm interferometer. The one-arm interferometer measures an input beam much like a shearing interferometer, but it neutralizes one of the two beams provided by any shearing interferometer, as explained schematically in Fig. 8.11.

Q_1 and Q_2 in Fig. 8.11 are two secondary laser light sources illuminating the objective O_1 to be analyzed. A small pinhole stop in the $2f$ plane of O_1 is aligned to transmit a small amount of light focused on Q_2' only, which, thereby, is neutralized of any errors on O_1. The pinhole stop placed near the edge of a blade thus allows passage of the nonobstructed bundle producing Q_1'. Due to the necessary wide angular separation of these two bundles, the interference fringes will be spaced quite narrowly. A moiré grating Gr_2 placed into the image plane transforms the fine fringes P into wide moiré fringes of spacing M, allowing convenient evaluation by the relation $\Delta P/P = \Delta M/M$. A brief schematic of moiré evaluation is seen in Fig. 8.12.

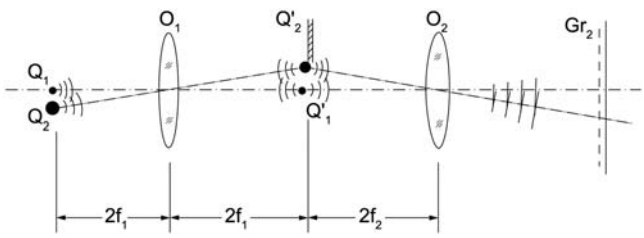

Figure 8.11 Schematic view of a one-arm interferometer (reprinted from Ref. 2).

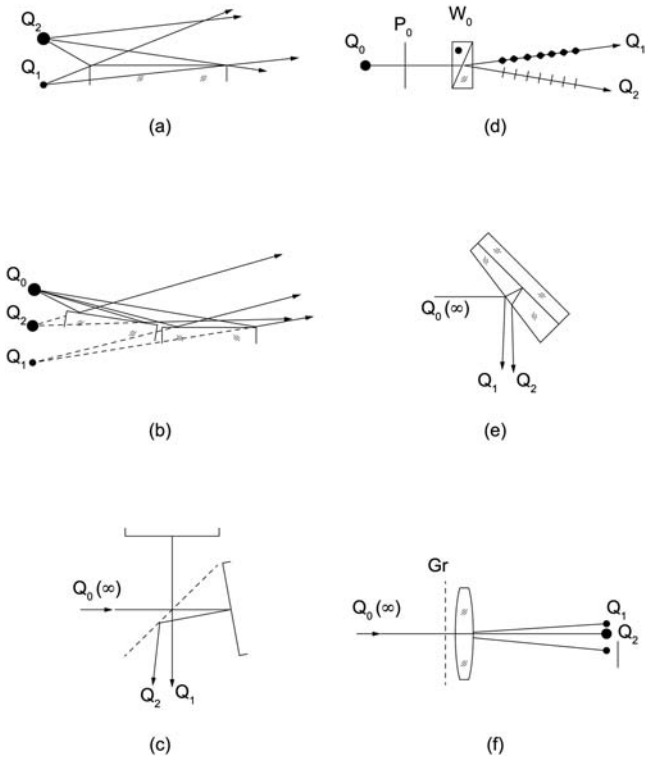

Figure 8.12 Methods for producing a double light source Q_1 and Q_2 from one source Q_0: (a) the most simple setup to use, Lloyd's mirror; (b) the most flexible setup to use; (c) a mini two-beam setup; (d) a setup providing easy brightness control; (e) a small two-beam interferometer with high reflectance on one mirror and low reflectance on the other mirror; (f) a Ronchi ruling [∞ indicates that the light source is at infinity (collimated illumination)].

The pinhole stop covering Q_2' in Fig. 8.12 produces a coherent neutral second beam next to the object beam, passing alongside the stop at Q_1'. The separation between Q_1' and Q_2' will be large enough to prevent any strioscopic influence of the truncated stop upon Q_1. The Q_2 bundle off axis is given brightness sufficiently larger than that of Q_1 so that, after passing the pinhole stop, the two brightness values will be balanced for convenient interference contrast.

In Fig. 8.11, Q_1 transmits both beams in a $4f$ configuration. For practical purposes, any ratio Q_1/Q_1' may be chosen. The pinhole stop is on the order of 5 μm, about 0.2 mm from the edge. From the pinhole stop on, there will be an object beam and a reference beam.

For experimental proof, we look at a sample in a two-beam Michelson interferometer (Fig. 8.13). The sample, a parallel glass plate with an approximately λ/2 deep groove, is placed in front of mirror M. Reference

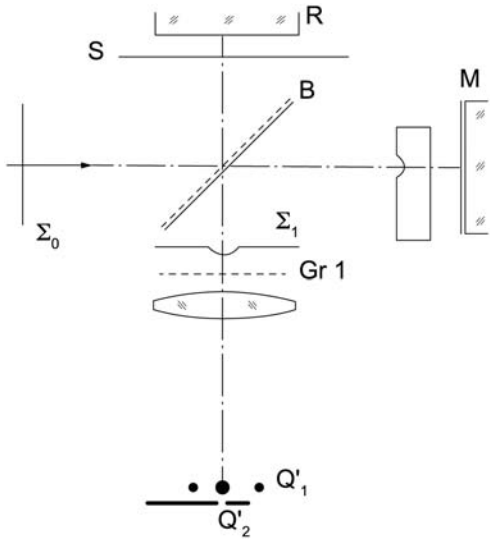

Figure 8.13 Experimental Michelson two-beam interferometer setup for comparing a one-arm interferogram with the equivalent Michelson interferogram and the shearing interferogram of the same sample.

mirror R is covered by a screen S. Without S, without the neutralizing focal plane stop, and without grating Gr_1, one obtains a regular two-beam transmission Michelson interferogram [Figs. 8.14(a)–(c)]. Figure 8.14(a) shows part of interferometer's empty field and the sample.

For the one-arm interferogram (Fig. 8.13), one introduces screen S, leaving a section free for reference, and a diffraction grating Gr_1. The latter produces two series of diffraction foci of the object beam and of the reference beam. The only function of Gr_1 is to produce two-light-source images: the zeroth order and the first order. Q_2', the brighter of the two, is to be neutralized by the pinhole. Q_1' will be the object beam (off axis, here). The resulting one-arm interferogram, after insertion of the pinhole, is reproduced in Fig. 8.14(b); this so-called one-arm interferogram is nearly equivalent to the Michelson interferogram in Fig. 8.14(a). The fine fringes P were converted into moiré fringes, which were adjusted to have a spacing of $M = P$. A second grating Gr_2 was used for this conversion, as previously described.

The setup in Fig. 8.13, after retracting the pinhole stop to clear Q_2', yields a shearing interferogram between Q_1' and Q_2' (the zeroth and first diffraction order). The fine interference fringes, transformed by the grating Gr_2, are not resolved in the image. Ways to double a primary point light source Q_0 into secondary light sources Q_1 and Q_2 are shown in Fig. 8.12.

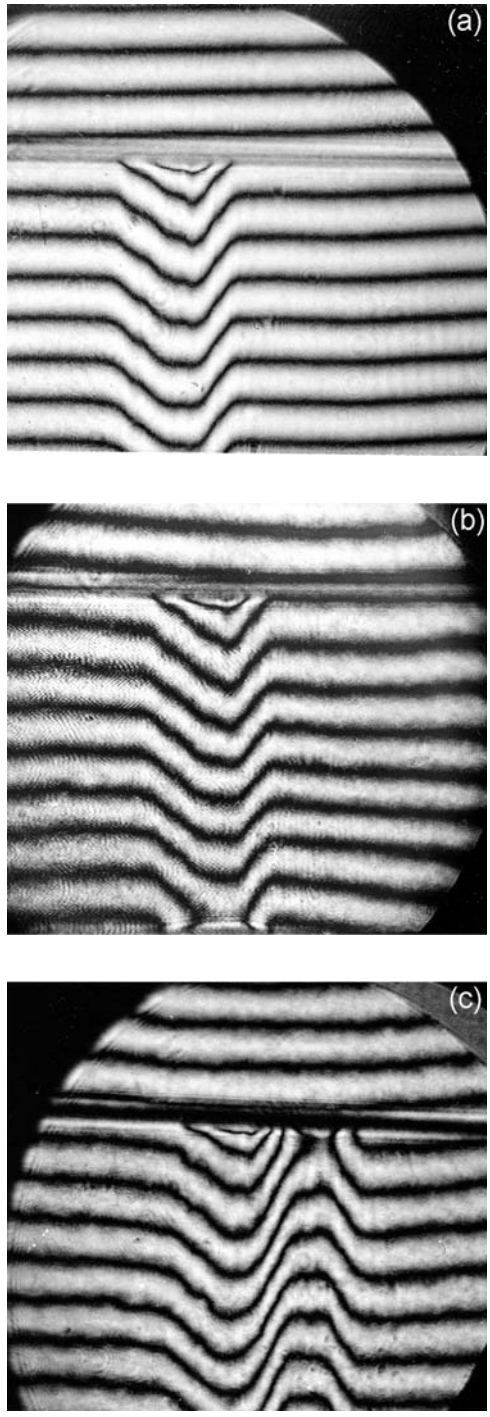

Figure 8.14 Three interferogram types of the same sample enabled by the setup in Fig. 8.13: (a) a plain Michelson interferogram, (b) the one-arm interferogram, and (c) the shearing interferogram.

8.2.1 Comments on the one-arm interferometer

1. Precise navigation to ensure that the pinhole does not touch Q1′ allows one to align the fringes to suit. A practical range of final fringe spacing control is provided by low-cost light-source doubling devices, some of which are shown in Fig. 8.12.
2. The one-arm object should be illuminated on axis by the weaker beam; the brighter off-axis beam is the beam to be neutralized.
3. A very ingenious one-arm solution was described by Smartt in Ref. 3.
4. The following is the way in which a pinhole can be used for beam neutralizing: The pinhole sits amidst a beamsplitter coating and is laser pinched into a pellicle beamsplitter. The transmitted light serves as a reference, as shown schematically in Fig. 8.13. The fringe pattern (related to a deformed wavefront) cannot be chosen deliberately, as it is determined only by the sample, much like the fringe pattern of the flame in Fig. 8.4(b).

8.2.2 Removing the spatial carrier frequency

Methods for doubling the light source Q_0 into Q_1 and Q_2 with a substantial brightness difference are summarized in Fig. 8.12. These methods allow one to match the light sources' angular separations with the grating constants of available larger-size moiré gratings. The twin bundle of zeroth order and one first order is impregnated with the fine fringe pattern that will continue to be recognizable in the image plane. Removal of this spatial carrier frequency, leaving behind a clean two-beam interferogram, might be desirable.

In the simplest situation, the grating Gr_2 is just an ordinary moiré-fringe-producing device (Ronchi ruling). In a more sophisticated practice, the same grating may be used for three purposes: (1) to remove the fine spatial-carrier-frequency fringes, thereby, (2) generating pure two-beam fringes, and (3) allowing aligning fringes to suit interpretation. The procedure is illustrated in Fig. 8.15(a). An objective O_4 recollimates the light sources Q_1' and Q_2'. A grating Gr_2 is placed into the collimated sections of the two beams, producing two diffraction spectra that are mutually offset. The grating's lateral and rotary displacements allow one to set the moiré fringes between Gr_2 and the interference pattern to suit that particular arrangement. Those moiré fringes are in the same arrangement as will suit for the demonstration in Figs. 8.14(a) and (c), both having the same orientation and spacing.

Referring to Fig. 8.15(a), the objectives O_3/O_4 include grating Gr_2 and refocus the light sources Q_1' and Q_2' to Q_1'' and Q_2''. The grating constant of Gr_2 is chosen to produce clearly separated diffraction orders [these can be

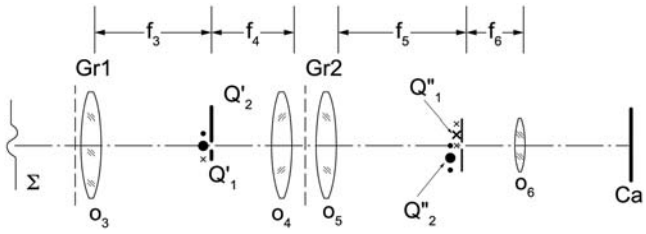

Figure 8.15(a) Removing the carrier frequency for observing a "clean" two-beam interferogram, representative of one arm.

checked from Fig. 9.4(b)]. The lateral separation of the two zeroth orders of Q_1'' and Q_2'' is controlled at the entry of the one-arm interferometer by the angle given by the point-source-doubling device, e.g., such as to have $\pm$ orders coincide. Each of the matched pairs shows the same two-beam interference at different brightness and contrast. A controllable slit is positioned to allow passage of the most opportune pair of diffraction orders.

8.2.2.1 Summary

The one-arm interferometer described here can be applied to the analysis of a collimated beam that has acquired some deformation of its wavefront. The deformation of the wavefront might be acquired at the reflection off of a sample, or in transmission through a sample lens. Experimental, high-quality components, including lenses and moiré gratings that are available in any optical laboratory, are usually considerably less expensive than optical flats and beam splitters.

Certain precautions need to be pointed out here. The neutralizing pinhole needs to be small enough to act as a true point source, independent of its location within the zeroth order (focus), and not as a field stop. Additionally, the pinhole-carrying thin sheet should not act as a strioscopy stop on the neighboring focus of the sample beam. Recognizing the sign of the wavefront deformation requires source shifting (momentary fringe movement).

8.2.3 Other interactions in the defocal plane

A unique way to generate a coherent background was introduced by Smartt and is found in Ref. 3.

A thin glass plate with a beamsplitter coating is given a small pinhole, which acts as a point source and thus provides a neutral reference wavefront as soon as it is navigated into the high spot of a defocus. Figure 8.15(b) shows the schematic of the Smartt interferometer. This is quite similar to the symmetric dark field, where that same high spot is completely obscured. The interested reader might enjoy the early literature on phase contrast microscopy by M. Françon.[4]

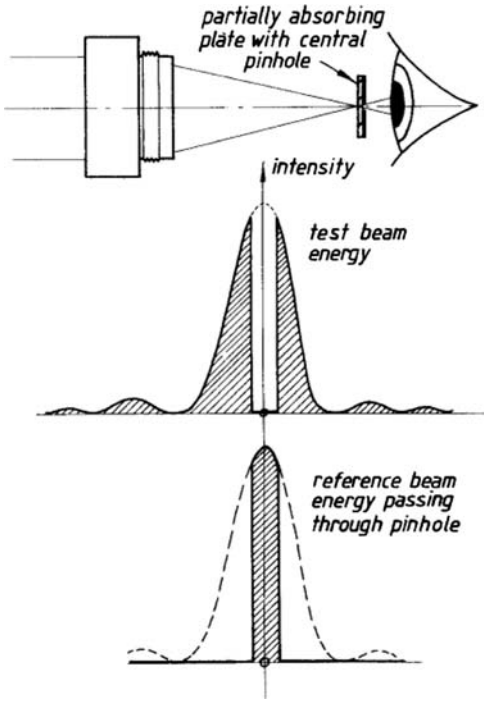

Figure 8.15(b) The Smartt one-arm interferometer illustration (reprinted with permission from Ref. 3).

References

1. H. Wolter, "Schlieren– Phasenkontrast – und Lichtschnittverfahren, " in *Encyclopedia of Physics*, Vol. **5/**24, S. Flügge, Editor, Springer Verlag, Berlin, pp. 555–645 (1956).
2. P. Langenbeck, "Modifying a shear interferometer to obtain a neutral reference beam," *J. Optical Society of America* **61**(2), 172–175 (1971).
3. W. Zschommler, Editor, *Precision Optical Glassworking: Manual for Craftsmen and Designers*, *Proc. SPIE* **0472**, Chapter 15 (1984).
4. M. Françon, "Interférences, Diffraction, et Polarisation," in *Fundamentals of Optics*, S. Flügge, Editor, Springer Verlag OHG, Berlin, p. 171 (1956).

Chapter 9
Nonspecular, Near-Flat, Mass-Produced Surfaces

9.1 Degenerate One-Arm Interferometer: The Lloyd Interferometer

The purpose of the classic Lloyd mirror was to duplicate a point source by specular reflection into a second source (which thereby becomes coherent to the first) and to then observe interference. Figure 9.1(a) illustrates the scheme. In fact, interference can be observed at the end of a flat component (not to say mirror), covering the entire length of the component, and on some surface areas to the right and left of the plane of incidence. Fringes first run parallel to the surface and soon take on a hyperbolic slope to both sides of the incident plane. Therefore, a meaningful evaluation is restricted to zones near the incident plane. There is a temptation to use this evaluation for metrology; however, due to the variable angle of incidence, the applications would be restricted to very undemanding tasks.

That situation changes with the use of collimated illumination, in which one-half of a collimated beam is reflected off of the component and intersects the other half, as shown in Fig. 9.1(b). The two beam fringes, still narrow to the point of being unreadable, will be converted to readable wide moiré fringes by a moiré (Ronchi-type) grating. The availability of sufficiently large gratings determines the average fringe spacing, which can be arranged by the included angle α between the direct and the reflected halves of the collimated beam. Fringe spacing P will be determined by the angle of incidence α as follows: with angle $\varepsilon = (90 \text{ deg} - \alpha)$, $P = \lambda/2\varepsilon$.

The Lloyd interferometer shown schematically in Fig. 9.1(b) found some application in the machine tool industry. The fringe spacing is constant for a flat mirror and varies as a function of departure from flatness. The fringe equivalents, $\lambda/2 \cos(90 - \varepsilon)$, in terms of μm for a given λ are listed in Table 9.1. The grating constant can be selected accordingly, or the angle α adjusted, and vice versa.

The reflected portion of the wavefront becomes reverted with respect to the unreflected portion. Because of wavefront reversion, perfect collimation

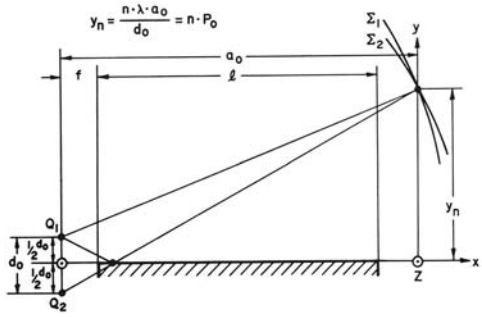

Figure 9.1(a) The simplest version of the Lloyd interferometer.

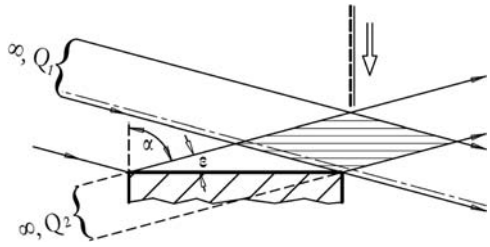

Figure 9.1(b) Lloyd interferometer with collimated light (reprinted from Ref. 1).

Table 9.1 Fringe equivalents with corresponding angles of incidence. In any oblique incidence interferometer applied to flatness testing, there exists a relationship between the angle of incidence, wavelength, and fringe equivalent that is valid in the plane of incidence, although only within a few interference orders.

Fringe equivalent ($\lambda = 0.63$ μm)	Angle of incidence
0.3 μm	0 deg
0.6 μm	60.0 deg
1.0 μm	71.5 deg
2.0 μm	81.0 deg
3.0 μm	84.0 deg
4.0 μm	85.5 deg
5.0 μm	86.3 deg
6.0 μm	86.9 deg
7.0 μm	87.4 deg
8.0 μm	87.7 deg
9.0 μm	88.0 deg
10.0 μm	88.2 deg

will be needed for practical applications of this simple configuration. The fringes from this setup always run parallel to the component. Departures from flatness will manifest as changes in fringe spacing. The fringe interpretation by moiré technique is illustrated in Fig. 9.2(a).

The low reading accuracy of moiré fringes formed between a Ronchi-type grating and two-beam interference fringes (first-order moiré with $P = g$) can be improved by a factor of 2 by applying a moiré grating with $P = g/2$. This is explained graphically in Fig. 9.2(b).

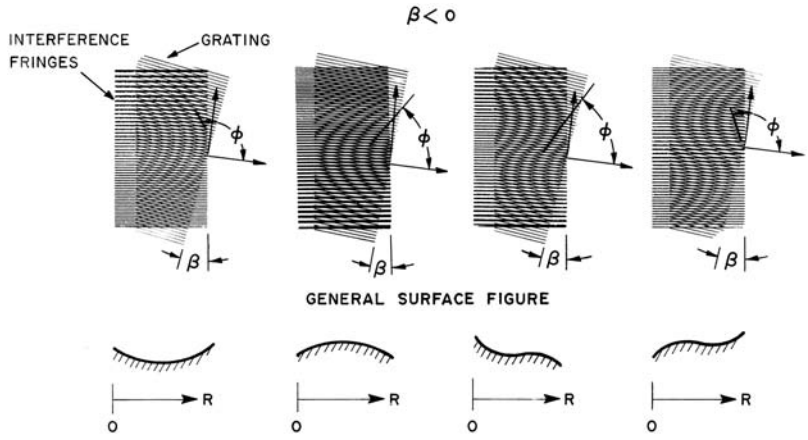

Figure 9.2(a) Schematic representation of Lloyd moiré fringes formed between a commercially available Ronchi grating (line spacing g) and artificial gratings with variable spacing, as would have occurred in real interferograms (of fringe spacing P). The relation between P and M is $\Delta P/P = \Delta M/M$. M is controlled by the angle between the fringes and the grating. A null field occurs when interference fringes and grating lines run parallel to each other and are equally spaced (reprinted from Ref. 1).

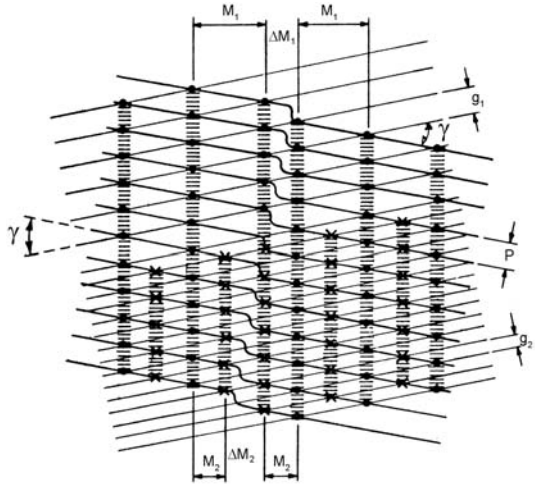

Figure 9.2(b) Generation of second-order moiré fringes M_2 by doubling the spatial frequency of the moiré grating lines: $g_1 = 2g_2$. N^{th}-order moiré fringes are interpreted as $\lambda/2n$ contour lines.

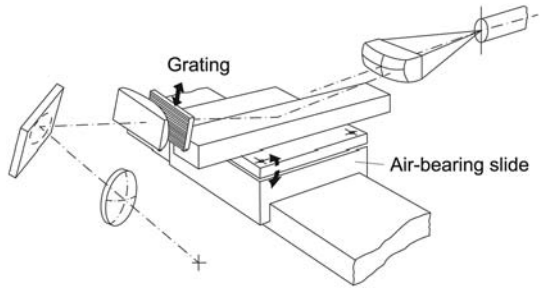

Figure 9.3 Lloyd moiré interferometer in scanning mode. The sample might be a linear rail, as shown, or an extended flat plate (not shown).

In one of its most basic forms (see Fig. 9.3), the Lloyd interferometer is appealing for its simplicity and low cost. Cases where the fringe equivalents range from 6 to 20 μm have numerous applications in quality control of mechanical parts. Smaller fringe equivalents do not require the Lloyd technique.

Operation with angle ε coinciding with the gloss angle causes good interference contrast, but this angular coincidence will be pure luck; grating constants are not available with enough variety to suit the gloss angle of any substrate. However, the angular zones neighboring the gloss angle provide sufficient reflectance.

9.1.1 Higher-order Lloyd interferometer

In Fig. 9.4(a) one recognizes the typical Lloyd interferometer setup: the test surface T, serving as Lloyd's mirror, is illuminated from one end by a monochromatic λ point source Q. At the other end of T are two interfering bundles of light, one direct bundle and one reflected at T, both emanating from the virtual light source Q′. For convenient interferogram evaluation, the angle of incidence α should be uniform throughout T, and Q should be placed at infinity, this placement being achieved by illuminating T with collimated light.

The grating G is used in the Lloyd moiré interferometer to transform the very narrowly spaced Lloyd interference fringes into more-conveniently visible broad moiré fringes. This grating will now function as a diffraction grating or beamsplitter. Due to diffraction, the grating splits a transmitted beam into a multiplicity (higher order of diffraction) of beams that are grouped in periodic angular distances on both sides of the directly transmitted, zeroth-order beam.

The Lloyd interferometer generates two beams: one from the real light source Q and one from the virtual light source Q′. The beams include an angle $2\varepsilon = 2(90 - \alpha)$; therefore, the grating produces two series of diffracted beams that also include an angle 2ε. An objective O placed behind the grating focuses the diffracted beams, as indicated in Fig. 9.4(a),

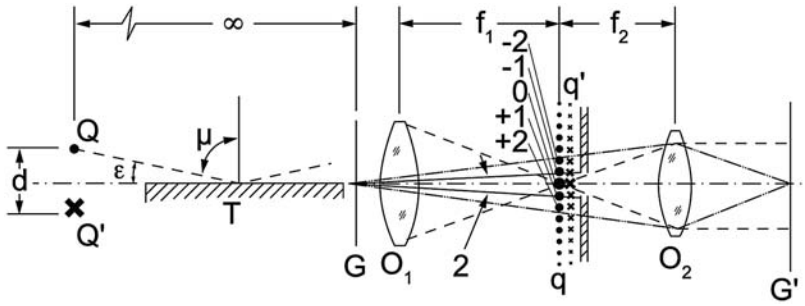

Figure 9.4(a) Lloyd interferometer upgraded to a higher-order Lloyd interferometer.

where the series of dots (labeled q) corresponds to Q and the series of crosses (labeled q′) to Q′.

Certain angles of incidence can be adjusted such that the angular direction of the zeroth-order Q beam coincides with the angular direction of the N^{th}-order, diffracted Q′ beam, as shown in Fig. 9.4(b). An adjustable slit is inserted behind the focal plane of the objective for the purpose of selecting a pair of diffraction orders consisting of one order q of the real and one order q′ of the virtual light source. Two-beam interference fringes are observed in the path behind the stop.

An advantage over the Michelson-type interferometer is the lack of expensive interferometric components. The advantages over the simple Lloyd moiré interferometer are the possibility of selecting higher sensitivity by going to a smaller angle of incidence, and the almost-perfect interference contrast. All of this is possible without changing the alignment of the receiving optic. A disadvantage is the impossibility to obtain a sharp image of the test surface.

9.1.2 Alignment and interpretation

In the basic alignment, the grating is oriented with its lines (x axis) perpendicular to the line connecting the real with the virtual light source (y axis). Two diffraction series appear in line, on top of each other. This displacement is controlled by the difference between the angles of incidence of the two beams on the grating, a difference which, in turn, is solely controlled by the angle of incidence α to the surface T. From there, controlling the angle of incidence allows one to match pairs of diffraction orders, such that the zero diffraction order of the virtual source combines with either the first, second, or third, etc., diffraction order of the real source [Fig. 9.4(b)].

In a given configuration, any pair of matched diffraction orders will produce the same interferogram, and by means of a slit-stop in the focal plane, one can select the one pair that produces the best contrast and brightness. Assuming a negligible loss of light due to reflection in oblique incidence at the test surface, one might select symmetric orders, e.g., the (–1,+1) or (–2, +2);

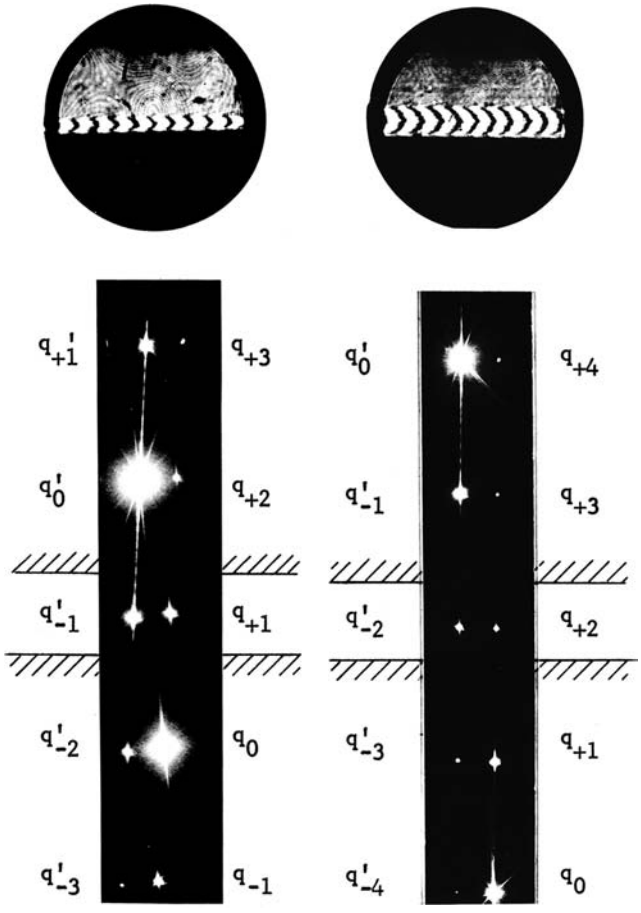

Figure 9.4(b) A grating produces two sets of diffraction orders, defocused by O_1 in Fig. 9.4(a). The offset between the two diffraction orders is controlled by the angle of incidence. Matching $\pm$ higher orders permits the selection of one matched couple to form two-beam-interference fringes. Bottom left: $\pm$ first orders; bottom right: $\pm$ second orders; top: the associated interferograms. Each pair of diffraction orders presents an identical fringe pattern; the best contrast is obtained with diffraction orders selected as shown.

for such combinations, the focal plane stop can be kept in a stationary position, centered on the optical axis.

After insertion of the pinhole stop, one practically deals with a two-beam interferometer. Any small variation in spacing and orientation of the two point sources, as by change of angle of incidence, causes a change in spacing and orientation of the interference fringes. Interference fringes observed at infinity will change their spacing P inversely proportionally to distance d between the real and virtual light source [see Fig. 9.4(a)] and will be parallel to the orientation of the grating (and perpendicular to d).

As the grating is rotated in its plane, which is equivalent to around the optical axis, the two diffraction series each rotate the same angle around their respective zeroth orders. This rotation of the grating introduces a lateral separation of the two diffraction orders that is chiefly in the x direction but also minutely in the y direction. The y displacement can be compensated for by adjustment of the angle of incidence α. With these two adjustments, the fringes can take on any desired orientation and spacing.

The angle of incidence must be known in order to define the fringe equivalent and can be obtained directly from the angular separation of the two defocused diffraction orders. The separation of the two zeroth orders, however, is best measured in units of the diffraction angle ε, which is predetermined by λ and the grating period g. Whenever the interferometer is aligned as described above, pairs of diffraction orders will match up, and one can count an integer number N of orders between the two zeroth orders. The angle 2ε between the two beams incident on the grating and the angle of incidence α is therefore related as

$$2\varepsilon = \frac{N\lambda}{g} = 2(90 \text{ deg} - \alpha). \tag{9.1}$$

In the case of a (+2,–2) interferogram, one has $N = 4$ [see Fig. 9.4(b)]. In order to adjust α to best comply with a count of N, one first adjusts for fringes parallel to the grating and then controls α in order for fringes to become as wide as possible (null field). Afterward, fringe spacing should be controlled only by means of rotating the grating (to keep α constant).

Evaluation of the height contours h of the surface investigated is performed using

$$h = \pm\left[\frac{\lambda}{2\sin\left(\frac{N\lambda}{2g}\right)}\right]\left(\frac{\Delta P}{P}\right), \tag{9.2}$$

which becomes

$$h = \pm\left(\frac{g}{N}\right)\left(\frac{\Delta P}{P}\right), \tag{9.3}$$

as long as $\varepsilon \approx \sin\varepsilon$. ($\Delta P/P$ is the relative fringe displacement.)

The direction of the zeroth order of interference is found by looking from the plane of observation toward the focal plane, when fringes are aligned nearly perpendicular to the grating. The zeroth order of interference lies on the side where the image of the real light source appears. For easier observation, one may rotate the grating so as to enhance the separation of the diffraction series in the x direction. However, for consistent evaluation, one must take care not to over-rotate the grating in the opposite direction when re-adjusting for broader fringes.

9.1.3 Reduced interferometric sensitivity allows for broader adaptation

To demonstrate the higher-order Lloyd technique in a qualitative way, a nominally flat mirror blank of 18-cm diameter was chosen. The optical setup was according to Fig. 9.4(a), with diverging illumination ($\alpha = 1587$ cm) and with a Ronchi-type grating having a period of 1/400 cm. The angle of incidence was decreased in order to obtain a focal plane image, as shown in Fig. 9.4(a), where +1 and –1 orders of diffraction are almost matched. The associated (+1,–1) interferogram is shown on the left side of Fig. 9.4(b). Similarly, the right side of Fig. 9.4(b) shows a (+2,–2) Lloyd interferogram of the same surface and the accompanying focal plane image. The decreased angle of incidence causes the image height to be increased. Thus, the image will be more suitable for fringe interpolation. Simultaneously, the fringe equivalent $\Delta P/P$ is greater, due to the improved sensitivity at the smaller angle of incidence. Contrast is unity, and fringe orientation and spacing are controlled as previously described. A limit to the continued decrease in angle of incidence is set by the diameter of the optics involved.

9.1.4 Lloyd interferometer for dynamic testing

Figure 9.5 illustrates the dynamic testing of 5¼-in memory substrates on an ultraprecise test air-bearing spindle—a setup called scan interferometry. This test serves the detection of acceleration values, the change in flatness ($\Delta^2 Z / \Delta U^2$), where Z is the normal to the substrate (parallel to axis of

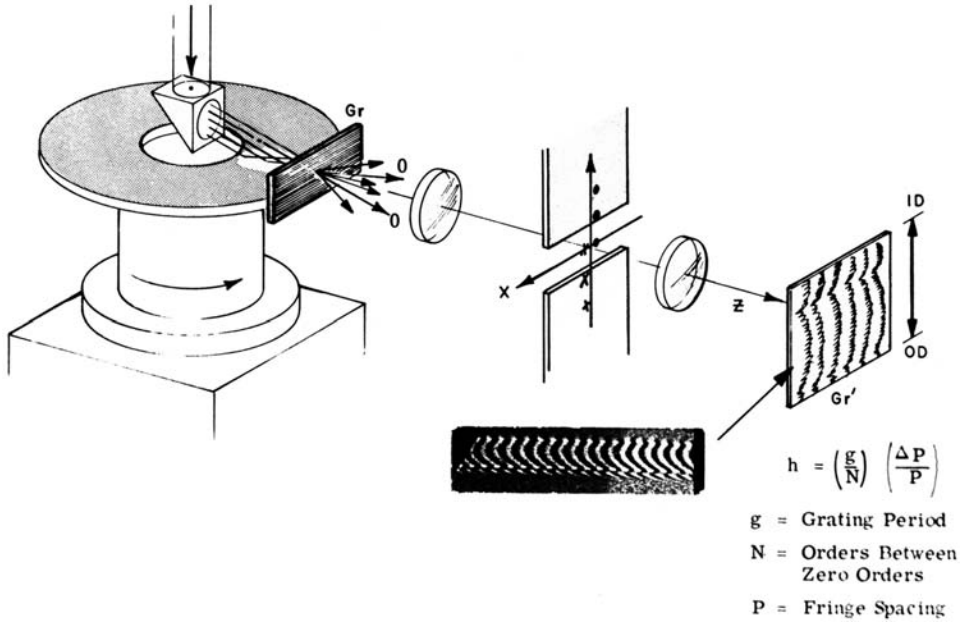

Figure 9.5 The Lloyd interferometer for higher orders (LIHO) applied to memory substrate testing on a motorized air-bearing spindle. The substrate can be with or without a magnetic layer.

rotation), and U is the angular velocity. The fringe equivalent may be selected from 2 to 10 μm, depending on the grating and angle of incidence. Fringes from the setup in Fig. 9.5 have a 3-μm equivalent. Observation is possible from stationary to high speed with electronic fringe counting. Errors of the spindle are an integral part of the information. Skewed insertion of the sample onto the spindle, likewise, will be part of the information. Separation of error sources is performed by separate measurement of the chucking zone.

Rotating disks for lapping or for polishing flat works allow for great adaptability, including changing shape with different loads, varying speed of rotation, varying temperature during operation, changing the viscosity of the lapping/polishing slurry, and variable duration of a work cycle, a parameter that varies with every optical fabrication. Frequent checking of the surface of witness glasses during testplating (as in Fig. 1.2) informs the operator of the necessary parameter changes. That checking procedure would be shortened if one could continuously measure the shape of the lapping of the interferogram or polishing plate. Figure 9.6(a) shows a typical polishing plate after the polishing slurry is removed and the plate is dried. In an experimental interferometric setup with an 80-deg angle of incidence, it was found that evaluable fringes of 20-μm fringe equivalent could be obtained. Installation of a Lloyd interferometer using the angle of incidence found permits continuous monitoring of the interference fringes and, thereby, of the tendency of the lapped surface to change its shape [Fig. 9.6(b)].

In any shop involved in the production of optical flat work using continuous-polishing machines, the question arises time and again: Can the in-process-occurring changes of the pitch's shape away from producing flat surfaces be detected prior to the time those changes are detected in the normal testplating method (Section 1.1)? The answer is: Yes, with the Lloyd-type interferometer. A setup much like that shown in Fig. 9.6(a) with a 50-mm-wide beam covering a 400-mm-long radial swath on a polishing plate produces interferograms of the rotating polishing plate. The interferograms can be picked up by a TV camera

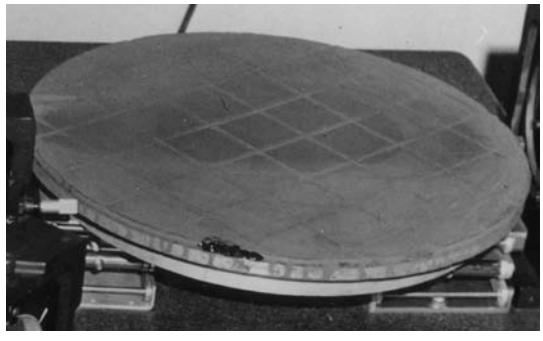

Figure 9.6(a) A typical optical polishing plate (polishing pitch), after removing the works and cleaning off the polishing slurry. The plate is removed from its machine for a feasibility test in a grazing incidence interferometric setup that allows one to vary the angle of incidence from 90 deg on (found by autocollimation off of a 90-deg prism placed onto the plate), until an interpretable (however, awkward to understand) interferogram is obtained.

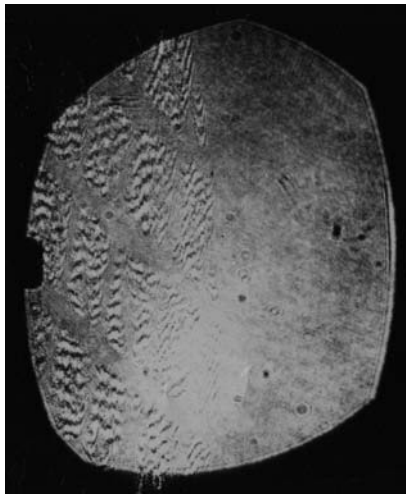

Figure 9.6(b) 30-μm fringe equivalent interferogram of a pitch polishing plate. The fringes have a fringe equivalent of 30 μm, as taken from Table 9.1.

and displayed on a monitor [Fig. 9.6(c)]. Obviously, the challenge of keeping the swath free of superfluous, abundant slurry must be addressed.

Some intuitive interpretation is needed here to understand the process: The angular motion error of the rotating lapping plate causes the fringes to show variable, repeatable orientation. The essential information on the change in lap flatness is revealed by the fringe curvature.

As seen in Fig. 9.6(c), continuous in-process observation also allows one to see the fringes, but not as distinctly. Of the six examples shown, only (i) indicates a very acceptable flat path; the others show a curvature of about one fringe along the path on the pitch surface, combined with shorter flat zones [(iii) and (v)] with a convex bow of 25-μm height. During further inspection, the conclusion reached is that the entire polishing disk nutates, creating an angular effect that involves a minor variation of the fringe equivalent. Application of two electronic spirit levels (rotating with the plate, and stationary on the machine frame) confirm the suspicion that the poor quality of the machine's main spindle bearing is the cause. The remedy involves using a sufficiently wide air-bearing rotary table.

9.1.5 Measuring the flatness of lapped granite plates/machine beds

A typical T-slot granite machine bed for an air-bearing linear slide is shown in Fig. 9.7(a). A beam that is collimated by a 400-mm-diameter spherical mirror ($F = 6$ m) is shone onto the stone at grazing incidence. The angle of incidence is controlled by a steel beam collimator with a mirror on one end and an expanded laser beam that starts at the front of the steel beam. Additional fine control of ε is provided by supports under the stone. The grating is mounted

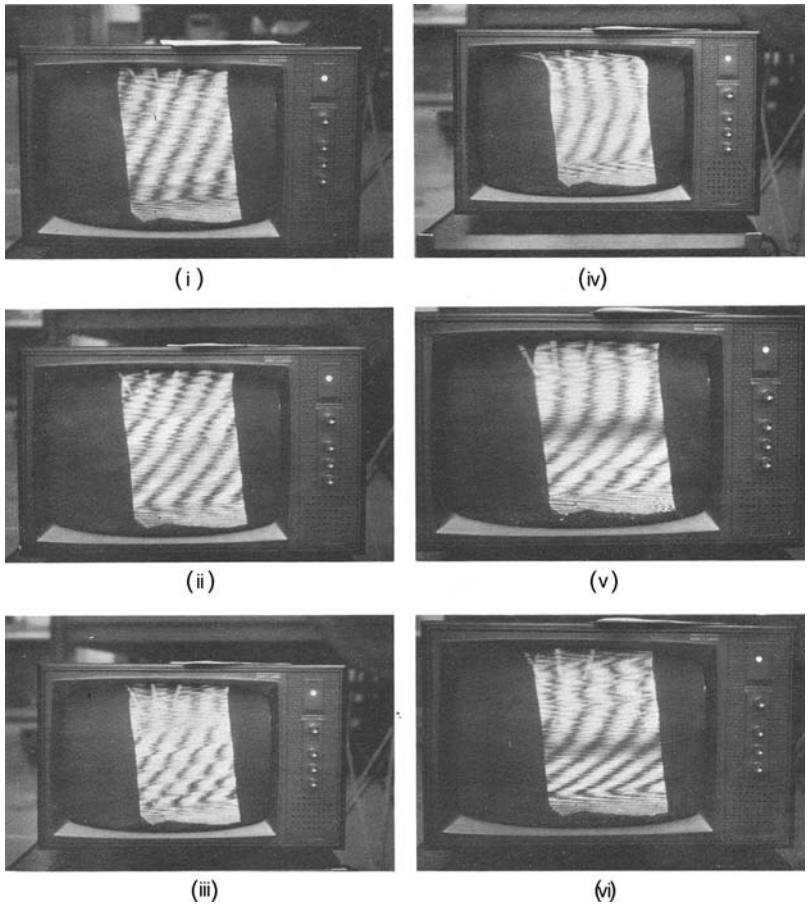

Figure 9.6(c) Six records taken during two hours of operation of the LIHO applied in process to a precision lapping machine, on a 50-mm-wide path from center to periphery (the height of the image). The length of the path is 400 mm, and the fringe equivalent is 25 μm. The records as shown are typical for the application and require a temporary cleaning of the light path using an ordinary windshield wiper.

between PVC plates to facilitate its angular adjustment. In the focal plane of the defocussing lens, one will see the separate diffraction orders of the direct beam and of the beam reflected by the polishing pitch, as in Figs. 9.4(b) and 9.5, respectively. The interferogram on the monitor can be observed while working on the surface.

The decollimation objective, a plano-convex lens ($F = 1.5$ m), is cut in a rectangle to match the grating and is mounted on the grating frame (as presented in Ref. 2). The interferogram shows fringes of 6.2 μm because $N = 4$. The Ronchi grating has 400 lines/cm and a size of 10 × 40 cm, according to Ref. 3. Fine adjustment of angle β is accomplished by minutely rotating the grating within the frame.

Figure 9.7(a) Granite air-bearing machine bed tested by LIHO during the final lapping. The TV monitor display is shown in Fig. 9.7(b).

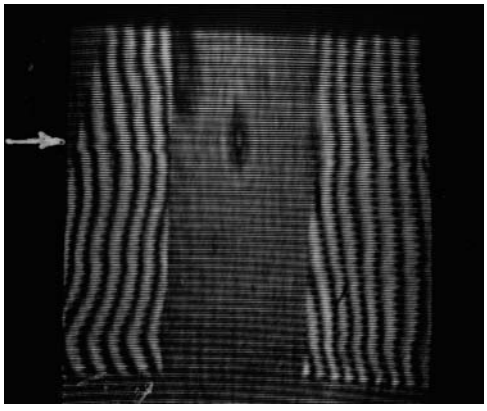

Figure 9.7(b) LIHO interferogram of granite stone seen with 6.2-μm fringes, as displayed from a TV monitor. The nose, marked by the white arrow, is produced by a brief cold spray, which causes it to be deep and point toward the zeroth order.

The LIHO offers instant overall information compared to information gathered by other metrology tools, such as electronic spirit levels or auto-collimators, which come in physical contact with the surface being lapped. The

LIHO surface needs only moderate cleaning, whereas the other instruments become degraded relatively quickly by residual lapping grains.

9.1.6 High or low?

The fine corrective lapping of a problem surface as shown in Fig. 9.7(b) is based on the knowledge of the "lows" and the "highs" (see Section 5.1.4, which describes certain artifacts as being high or low). The best-fit reference plane will be represented by two or more straight equidistant fringes, or at least part thereof. Warming the stone locally by placing hands on it, or cooling the stone by a brief cold spray will produce momentary high and low zones, respectively. An example of a cold-spray-induced momentary low is seen in Fig. 9.7(b).

Surfaces that are separate but need to be coplanar are typically the two flanks of the granite T-slot bed, another view of which is shown in Fig. 9.7(c). Without additional information, the sign of the inclination between the two flanks remains unknown. The cold-nose test informed us that on both flanks, the zeroth orders of incidence were located outside; the extrapolated surfaces meet in a ridge somewhere above the T-slot. Therefore, the flanks are quasi-convex.

9.1.7 Summary of Lloyd interferometry

The higher-order Lloyd interferometer, like the Lloyd moiré interferometer, can be used for testing the flatness of large surfaces or the straightness of long paths (for example, on lathe beds or on precision surface plates). Generally, surfaces for which oblique incidence of the test beam is the best method to measure straightness can be observed during the process of finishing. The

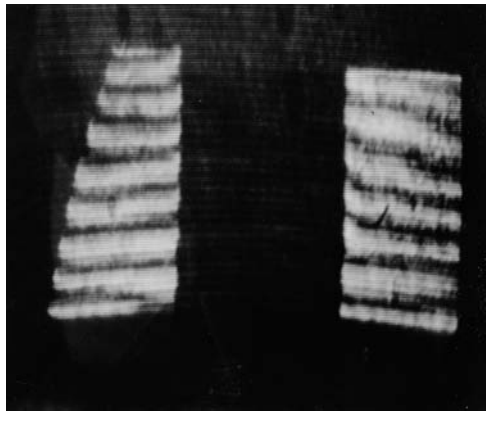

Figure 9.7(c) Fringes realigned from Fig. 9.7(b) for convenient interpretation of the bend between the two flanks. The two flanks are skewed toward each other for approximately one fringe.

oblique incidence method might be required because of roughness, size, or geometric requirements. It might also be used while the test surface is being worked on (in-process control).

It should be noted that wavelength λ does not appear directly in the evaluation Eq. (9.3); λ is hidden in the previous determination of the grating constant. Simplicity is also provided by $\varepsilon = \sin\varepsilon$, which is applicable for most grazing-incidence situations.

9.2 Instrumentation for Grazing Incidence Interferometry

Oblique incidence and even grazing incidence are practical methods for interferometric inspection of technical, nonspecular, nominally flat surfaces. Samples that have been diamond sawed, lapped, and fine lapped to polish require different interferometric sensitivity in order to safely operate in their individual ranges; different fringe equivalents require different angles of incidence. A salient outcome was the design of special sample holders that adapt to any standard instrumentation, even to some old-fashioned instruments, which were often, in fact, of high professional quality. An example schematic of such instrumentation is shown in Fig. 9.8, where collimated light shone obliquely onto the sample is reflected back by a 90-deg fold mirror. The resulting image will consist of two symmetric halves, as in the testing of 90-deg roof angles.

The dedicated sample holder (Fig. 9.9) allows one to set a 90-deg angle between the sample surface and the reverting reference-quality mirror. The incident angles to be sampled can be chosen to suit (for instance, a 3-μm fringe equivalent) by inclining the entire sample holder. The 90-deg apex will remain on the instrument's optical axis. With a flat reference mirror in the reference path, one will see a double image, as in Fig. 9.10(a). Using two mirrors in the reference arm (as shown in Fig. 9.8) reduces potential reversion effects; of the twin images, only one can be in focus.

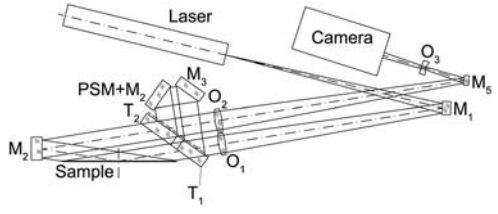

Figure 9.8 Michelson two-beam interferometer. In both arms, the customary flats are replaced by a 90-deg roof-angle/mirror combination for avoiding reversion effects. In one arm, the sample/fold-mirror combination can be inclined around the 90-deg apex for alignment of the desired angle of incidence. The height of the apex above ground level is chosen according to the sample diameter and thickness. [PSM is phase-shift mechanism (or motor), and $T_1 + T_2$ is transmission mirror 1 and transmission mirror 2.]

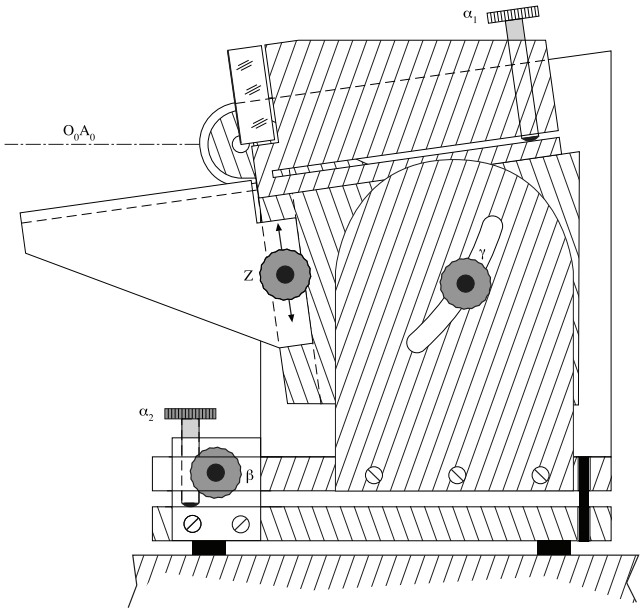

Figure 9.9 A sturdy sample holder, applicable to instrumentation such as that in Fig. 9.8, allows one to set different angles of incidence between 88 and 40 deg. It has a height-adjustable platform to carry vacuum chucks [see Fig. 9.10(a)].

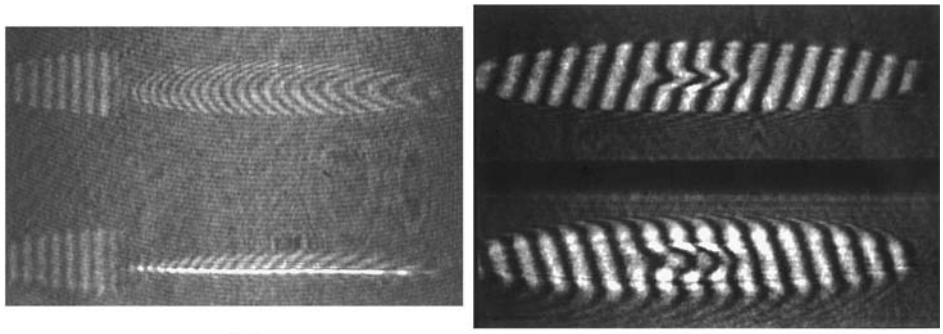

Figure 9.10 (a) Lapped wafer on a chuck with the reference zone elevated for a given thickness value of the specific wafer type. (b) 4-μm fringe equivalent witness sample, with its two partial images from an instrument as in Fig. 9.8. The portion of the sample beam producing the unsharp image can be used for observing the defocus plane (checking alignment).

Calibration of fringe equivalence is achieved using a calibration master having an artificial defect. In normal incidence, the same master shows the artificial defect in an interferogram as in Fig. 9.11. The complete calibration procedure of the witness samples (masters) for oblique and grazing incidence is described in Section 1.6.2.

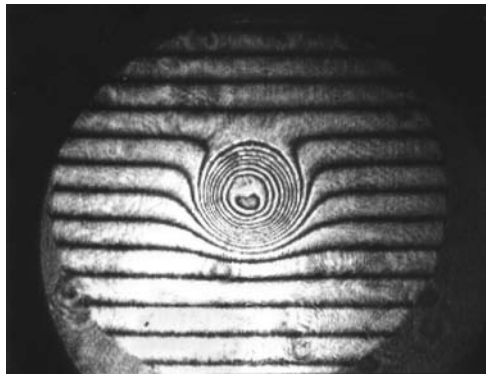

Figure 9.11 Calibration flat in a normal-incidence Fizeau interferometer. A Michelson two-beam breadboard setup was used for automatic PC fringe evaluation (using ISTRA software from ITO[4]).The reader may refer to Section 1.6.2, Fig. 1.15.

Figure 9.12(a) A chuck with reference zone in a reverting two-beam interferometer (Fig. 9.8). The chuck holder rests on three height-controllable anvils. The wafer-holding chuck area is plane parallel to the reference zone; the height difference between the two plateaus equals the specific proprietary wafer thickness. The reference zone serves in the computer-aided evaluation of thickness and its variation and tilt between the wafer surfaces.

Thin wafers are held on a vacuum chuck that must be carried by the holder's Z slide. The chucks (of any brand) are interferometrically flat, and some are available with an integral reference zone alongside the chuck pattern; the two are strictly parallel. Figure 9.12(a) shows the chuck carried by both the sample

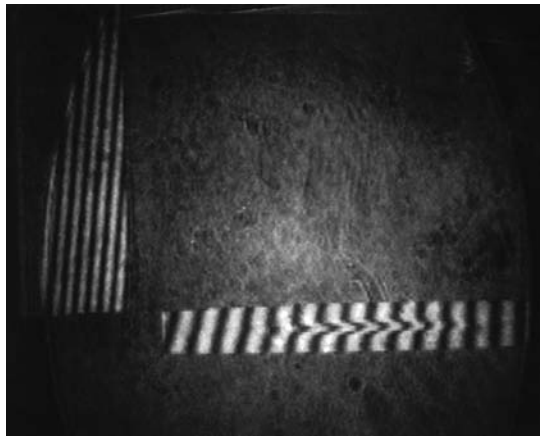

Figure 9.12(b) Interferogram of the reference zone (left side), an integral part of the bulk quartz-glass compact chuck. The interferogram to the right of the reference shows the calibration master. Due to its 10-mm thickness, its image appears to be shifted away from the location of an interferogram of a wafer having the specified thickness (coplanar to the reference).

holder and the 90-deg fold mirror, both being part of the inclinable sample holder. The 10-mm-thick calibration master will be placed onto the chuck in the same location as the wafer sample; therefore, its interferogram is offset, as seen in Fig. 9.12(b).

A wafer chuck such as those produced in author's lab had a reference zone that was strictly parallel to the chuck and elevated for the given standard thickness of the wafer. Such a wafer sample and a reference zone for automatic evaluation are seen in one plane [Fig. 9.10(a)]. The elevated reference zone serves as a lateral stop to position the wafer in its holding pattern.

The angle of incidence is calibrated either by a sample with known error [Fig. 9.10(b)] or by the perspective foreshortening of the image of a circular or rectangular sample. An image that is produced by a decollimator can be expected to be sharpest only along the meridian line. An exact, 90-deg setting is obtained by a set screw, labeled λ in Fig. 9.9. In the case of a good 90-deg setting, the fringes in both images will be aligned (like the 90-deg in a roof angle test). As the angle of incidence is altered (by nutating the entire sample holder), the calibrating nose [Fig. 9.12(b)] will be shown at different lengths; a value of $\Delta P/P = 1$ indicates the fringe equivalent marked on the calibration master.

Figure 9.13 emphasizes the need for collimation testing. The interferogram shows a ceramic sealing ring that is flat across its width and has no rolled-off edges. However, the slowly changing fringe spacing and orientation from left to right indicates either a warping of the sample or poor collimation. Changing to different fringe equivalents produces the answer: the irregularity

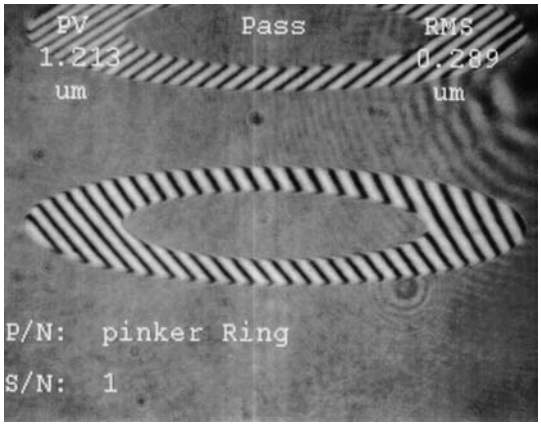

Figure 9.13 Interferogram from a sample that was a nominally flat ceramic seal. The interferogram is locally flat with no roll off on its edges, suggesting either cylindrical warping [fringe spacing changing from left (P_1) to right ($P_2 = \alpha P_1$)] or collimation error.

will remain if it was caused by lack of collimation. In the case of Fig. 9.13, the reference arm of the interferometer did not revert the wavefront because the instrument was a two-beam Michelson type.

9.2.1 The prism interferometer

The prism interferometer first gained widespread acceptance in wafer production, which called for ever tighter QC at prepolishing phases. The 5-μm fringe equivalent was most desirable. The prism interferometer was found to produce inconsistent results with samples fed at some safe distance (approximately 0.5 mm). The author's lab (supplier of this type of instrument in the 1970s and 1980s) confirmed that that error amount depended both on the distance between the sample and the reference plane and on the quality of collimation. The hypotenuse of the 90-deg prism was proved to be not culpable. The inconsistencies were traced to larger gaps between the sample and the reference, gaps that were permitted with the introduction of safe leveling systems (Section 2.3). As a consequence, the collimation test, as described in Section 4.3, was developed; this collimation test is dedicated to the prism interferometer in its final alignment phase.

Qualitatively, the effects are explained by the large shear between the reference beam and the sample beam at grazing incidence, as seen in Figs. 4.6(b)–(e). The beam that is repeatably reflected by the sample migrates (via walkoff) from one side to the other side of the reference field, as the gap of the cavity is slightly increased.

The prism interferometer is the only one among the grazing-incidence interferometers for which the collimating beam's full aperture comes into use.

Only one-half of this aperture is used in the Lloyd setups. If collimation is perfect, the shear, regardless of its large size, will not be recognized in terms of fringe deformations on flat samples. That is the essence of collimation testing.

However, the error contribution grows as one operates the prism of the prism interferometer near the angle of total internal reflection. Figure 4.6(a) illustrates the effect graphically: if α is the initial direction of the parallel rays exiting the prism's hypotenuse, then the exiting path length between the reference and the sample will rapidly increase, as the incoming ray at the hypotenuse grows close to the angle of total reflection. Consequently, more interference orders will fit onto the path within the cavity. This unilateral effect causes the asymmetry of the interferograms in Fig. 4.4(d). The sidebands to the fringes mark the open side of the cavity.

Multiple beams, or their wavefronts, not only produce side bands (pointing to the open end of the wedge base/sample) but also cause *some* shift of the fringes' center. This fringe shift is observed in near-orthogonal incidence as well. Therefore, it is good practice in prism interferometers to orient the wedge reference/sample such that the incoming beam walks toward the apex. Finding a retroreflective angle and making the beam walk out of the wedge from there on [see Fig. 10.3(a)] is possible only in normal Fizeau interferometers.

As with any Fizeau interferometer, errors on the reference (the hypotenuse of the prism interferometer's prism), which has a beamsplitting function, will propagate in both directions and recombine additively in the image. Briefly, the hypotenuse of the Flatest interferometer, being both the beamsplitting surface and reference simultaneously, needs a flatness specification of $\lambda/20$ in order to be worth only $\lambda/10$.

9.2.2 The image in a prism interferometer

The obliquely illuminated sample will appear foreshortened on a screen (or on the plane of a CCD camera) if placed orthogonal to the optical axis. Images are obtained without distortion by placing a projection screen made of ground glass obliquely into the beam for visual inspection, as in Fig. 1.2(d). This low-cost viewing method instantly provides a good integral impression.

Recording the image by an inexpensive digital camera [Fig. 9.14(a)] allows inexpensive, fast, flexible ways to electronically compensate for the uniaxial perspective dilation foreshortening in the image for documentation. There will be no need for *optical* compensation for that same foreshortening in the image; for this reason, oblique-incidence interferometers [Figs. 9.14(b) and (c)] become viable with electronic phase-shift evaluation. Figure 9.14(c) shows a large Dove prism with its hypotenuse serving as reference and beamsplitting surface. Neither the sample nor reference mirror has any contact with the precision surfaces, as was described in Chapter 1 of this book.

The Dove prism in Fig. 9.14(c) can be used for sample inspection in orthogonal incidence ($\lambda/2$ fringes), and, alternatively, in the oblique-incidence

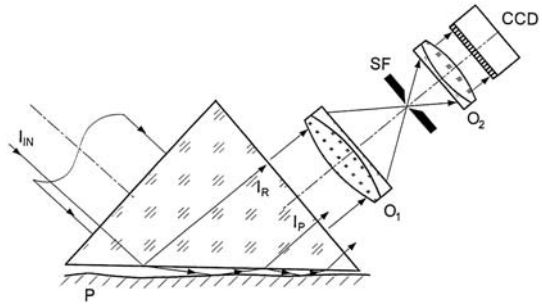

Figure 9.14(a) Schematic view of a prism Flatest interferometer for technical surfaces. A CCD camera replaces observer viewing and provides documentation. Note that the illumination is shone *into* the wedge for reduction of walkoff (reprinted with permission from Ref. 5).

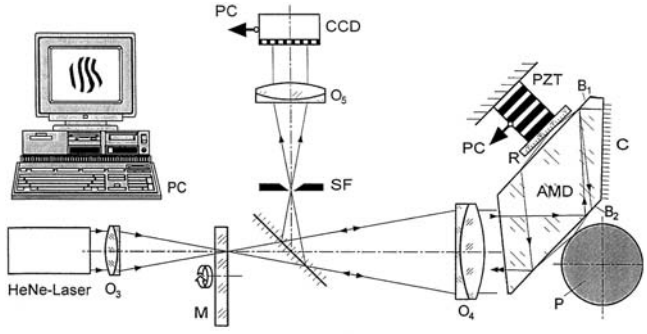

Figure 9.14(b) The two-beam Flatest solution for application of automatic fringe evaluation, using phase shifting developed by Körner et al. (reprinted with permission from Ref. 5).

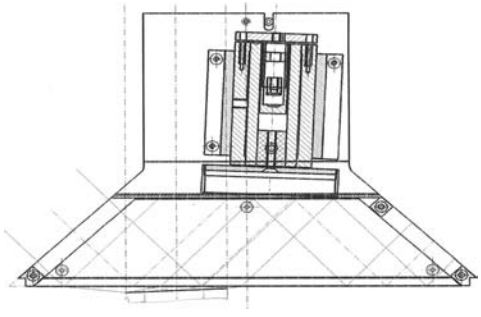

Figure 9.14(c) The Flatest interferometer, using a Dove prism's hypotenuse for reference, with a phase-shift mirror (reprinted from Ref. 7).

mode on the same sample. The salient point in favor of the Dove prism over the less-costly 90-deg prism is the fact that pure two-beam interference is obtained from both the reference mirror and the sample, both being located some millimeters from the prism's surfaces. With pure two-beam interference, an automatic phase-shift interferogram evaluation becomes possible.[4] And, because of the reversal of the perspective image foreshortening upon re-entry of the well-collimated beams to the hypotenuse, the compensation for this foreshortening is greater than it would be with plain grazing incidence. M. MacBean[6] designed the dimensions of the Dove prism to be sufficiently long as to not allow the first walkoff-reflected beam to become part of the image formation. Consequently, he could operate with large clearances of the sample and reference to the prism.

9.2.3 Parameters influencing $\Delta P/P$ reading accuracy

Any adjustment of the useful fringe spacing P and its orientation is accompanied by uncertainties. Obviously, this uncertainty is greatest when $P = \infty$. When $P <<$ the diameter of the sample, ΔP will be small and $\Delta P/P$ will be difficult to measure. An optimal P follows from C. Synborski[8] as well as from the vast experience of this book's author. The empirical range of opportune P values is $P = 1/5$ to $1/11$ of the diameter of the FOV G. A consequence of sample feeding, be it manual or automatic, is an angle ε between the reference and the sample as the sample rests on whatever carrier is used *ad hoc* upon feeding. The useful range of ε thus is between

$$\varepsilon_1 = \frac{\lambda}{P_1} = \frac{5\lambda}{G} \text{ and } \varepsilon_2 = \frac{\lambda}{P_2} = \frac{11\lambda}{G}, \text{or } \varepsilon_{1/2} = \pm 7 \text{ arcsec at } G = 50 \text{ mm}. \quad (9.4)$$

Section 2.3 described one of the many solutions for automatic sample alignment, providing both the distance to the reference and the wedge angle. In this case, the reference points are the three anvils surrounding the sample platform. A spherical, free-floating air bearing carries the platform and is locked (air off) after being aligned by the truing plate.

The sample will undergo a small lateral shift upon being leveled and will be pushed into the correct angle ε and height. Therefore, the truing plate is a porous plate functioning under different circumstances as a shallow, flat air bearing. The truing-plate material is either porous carbon Purbone,[9] as is used for air bearings, or a sinter brass filter plate, both of which are micromachineable by diamond turning. Figure 9.14(d) shows the truing plate's approximately 2.5-μm concave shape. An air film of approximately 4 μm provides a safe cushion to push the sample into the desired position without touching it.

In conclusion, finding the closest possible proximity of a sample to the prism Flatest interferometer by autolevel devices in the shortest possible duration can be a challenging engineering task.

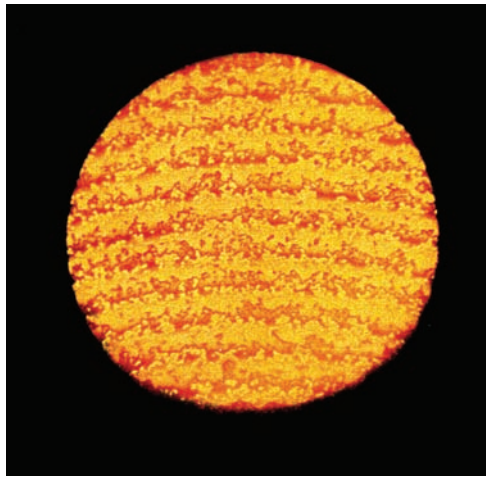

Figure 9.14(d) 50-mm OD air-bearing truing plate made of micromachined sinter brass, with a fringe equivalent of 2.5 μm [a component of the autolevel shown in Fig. 2.4(a)].

References

1. P. Langenbeck, "Lloyd interferometer applied to flatness testing," *Applied Optics* **6**(10), 1707–1714 (1967).
2. P. Langenbeck, "Higher-order Lloyd interferometer," *Applied Optics* **9**(8), 1838–1841 (1970).
3. Max Levy Autograph, Inc., 2710 Commerce Way, Philadelphia, PA 19144, USA: Ronchi gratings.
4. H. J. Tiziani, ISTRA Fringe Shifting Program, ITO Institut für Technische Optik, Universität Stuttgart.
5. K. Körner, W. Stadthaus, and L. Nyarsik, "Messung des Makroprofils mit einem Echtzeit-Interferometer," *Feingerätetechnik* **39** (1990).
6. M. D. A. MacBean, "Oblique incidence interferometry of rough surfaces using a novel Dove-prism spectrometer," *Applied Optics* **23**(22), 4024–4028 (1984).
7. M. Bartelt and P. Langenbeck, "Topographie rauher Oberflächen," *Feinwerktechnik, Mikrotechnik, Messtechnik* **101**(1–2), 44–46 (1993).
8. C. E. Synborski, "Interferometric analysis of flatness by eye and computer," *Proc. SPIE* **135**, 104–110 (1978) [doi: 10.1117/12.956119].
9. Purbone: Trade-name of a porous graphite material: Shanghai Gongtao Ceramics Co, Ltd., Shanghai, China.

Chapter 10
Enhancing Regular Interferometric Sensitivity

10.1 Multiple Reflections

A technical realization for enhancing regular interferometric sensitivity is shown in Fig. 10.1(a). The errors of a Fizeau beamsplitter T, rear mirror M (usually the sample), and included medium (air) are accumulated both longitudinally (wanted) and, inseparably, laterally (unwanted). The resulting error summation upon each passage of the initially collimated beam is a successive wavefront deformation (Fig. 10.2) and the associated phase shift. The effect of increasing phase shift is demonstrated in the vector diagrams in Figs. 3.5(a) and (b). The depth of an error Δt appears as $2n\Delta t$ on the n^{th} wavefront. Errors seen in the summation are determined by the relation of the error gradient to the amount of beam walkoff tW_n, where W is walkoff. W_n is determined by wedge angle β and by the T-to-M distance t (thought to be small). With small values of $2n\Delta t$, multiple beam fringes are seen. Only the contrast profile of the fringes becomes modified. Side lobes develop, and the maximum of the amplitude becomes shifted as a function of increasing angle β. The side lobes indicate the direction away from the zeroth order of the interference.

Both the depth and the width of the error zones on a nominally flat problem surface, assumed to be small enough for their representation in the defocal plane, will not extend into the neighboring orders of reflection (see Fig. 8.3). With these qualitative limitations, one may expect to visualize slow slope errors with gradually enhanced sensitivity. In the experimental setup shown in Figs. 10.1(a) and (b), wedge angle β is shown to be large enough to have successive beams defocused in positions clearly separated from each other, allowing beam selection by a slit in the stop. The stop is arranged in the defocal plane, as shown in Fig. 10.1(b).

The fold mirror in Fig. 10.1(a) allows the zeroth-order beam to be reflected at a non–mirror-coated zone, whereby its brightness becomes closer to that of a selected higher-order beam. Reflection at Brewster's angle allows

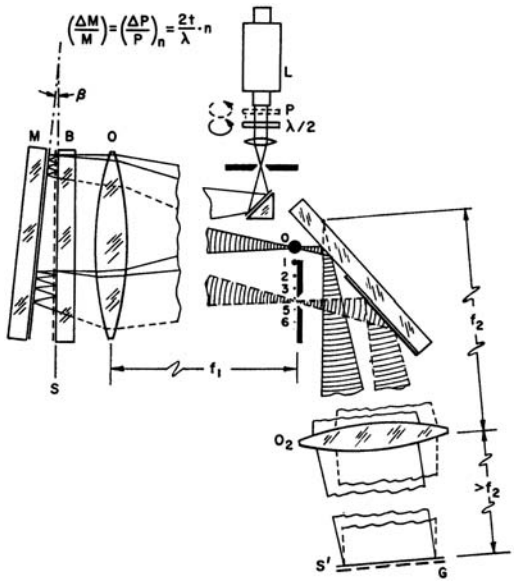

Figure 10.1(a) Fizeau interferometer aligned with a large cavity angle allows for separation of orders of reflection in the defocal plane [see Fig. 10.1(b)].

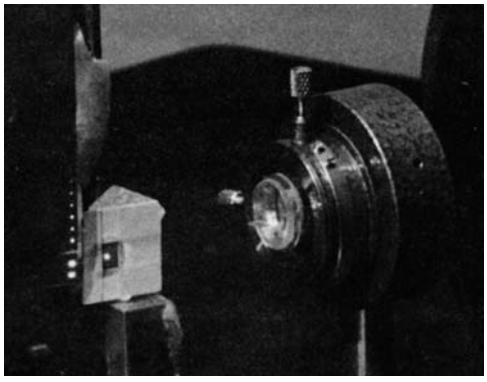

Figure 10.1(b) Experimental realization of the focal plane stop as in Fig. 10.1(a). The bright spot on the hypotenuse of the 90-deg prism is a 5-μm pinhole (secondary light source). The row of light spots seen on a blade fixed to the prism is the first, second, fourth, fifth, and seventh, etc. orders of reflection from the distant Fizeau interferometer. The zeroth and third orders are not seen because they pass by the stop when forming the interference fringes in the image plane.

some fine control of amplitude in the reflected zeroth order by rotating the plane of polarization at the illuminating side.

The stop in the defocal plane [Fig. 10.1(b)] allows two beams to pass: the zeroth-order reference beam and the selected n^{th} order of the reflection beam.

Objective O_2 produces two images of S at location S′. A grating G in this location is used for generating two diffraction spectra, much like in the higher-order Lloyd interferometer [Fig. 9.4(b)]. With this procedure, the unreadable fine fringes can be converted into conveniently evaluable two-beam interference fringes. Figure 10.1(c) presents in (i) the common Fizeau interferogram of the sample; (ii) is the two-beam interferogram between the reference and the first order of reflection; (i) and (ii) are equivalent. (iii) is the second-order, two-beam interferogram, and so on. Figure 10.1(c) shows the interferograms up to the fifth order of reflection.

There are inherent practical restrictions to a routine application of the multipass technique suggested in Fig. 10.1(a). An alternative method for sensitivity enhancement by multipass technique is shown in Fig. 10.1(d): Two Fizeau configurations are coupled in a Michelson setup in a way that allows the superimposition of two quasi-identical adjustments with the two

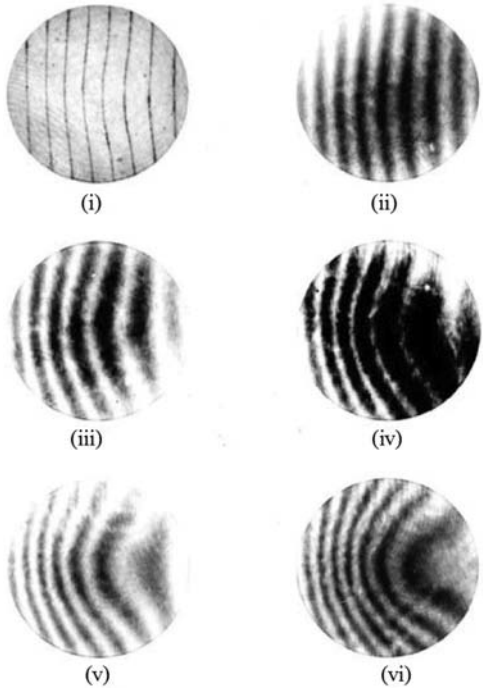

Figure 10.1(c) Interferograms of the same surface, taken in the setup of Fig. 10.1(a). The regular Fizeau interferogram (all beams) is seen in (i). (ii) is the two-beam interferogram between the zeroth and first order, and represents the same fringe deformation of 0.5 fringe, as does (i). (iii)–(vi) are the higher-order Fizeau interferograms. The beams wallk off into the open wedge between mirrors M and B; therefore, the evaluation of the surface profile of both mirrors might be misleading. The following statement is applicable to (vi): $\lambda/10$ fringes being straight to, for instance, $\lambda/10$ is equivalent to flatness departure under $\lambda/100$.

respective defoci spectra spread widely enough to permit the separation of the pairs of reflection orders. One of the two Fizeau back mirrors, e.g., M_2, will be the problem sample. After initial alignment of a problem sample, and having fixed all essential hardware interfaces, one may substitute other samples and align them as in any Fizeau interferometer. A translatable slit in the defocal plane allows one to select the desired order of reflection, without needing to reset the interferogram. Each interferogram of a higher order of reflection is a two-beam Michelson interferogram, with the reference in one arm and the work in the other arm. No moiré grating will be needed.

The uncommon illumination system shown here is described in Section 3.9. The error on the nominally flat sample surface is—in the professional optician's language—one-ring spherical, convex, indicated by the first-order-of-reflection interferogram and, for comparison, by the common multiple-beam Fizeau interferogram of the same surface. The optical technician may now continue the polishing work, watching (in the third order) fringes of $\lambda/6$ instead of the $\lambda/2$ fringe equivalent.

The multipass technique, as shown in Fig. 10.1(d), provides the ability to rapidly change the sensitivity in the pursuit of very stringent tolerances for flatness or sphericity. In this solution, the evaluation relies on fringe following and the customary fringe evaluation but with enhanced sensitivity. Other interferometric techniques rely on scanning and fringe counting, as in, e.g., measuring the tilt motions of an ultraprecise air-bearing spindle carrying an optical flat whose inclinations are picked up by a small

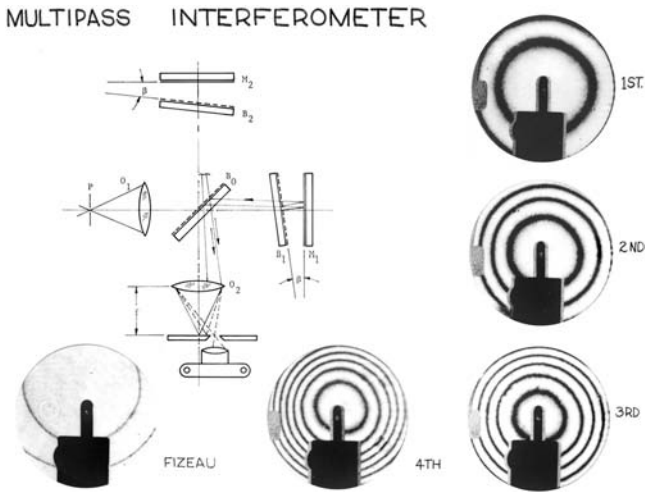

Figure 10.1(d) Two identical Fizeau configurations combined in a Michelson setup, and a comparison between the Fizeau interferogram and a regular Michelson interferogram, the latter, successively, in four reflection orders.

multipass Fizeau interferometer. The approximately 10-mm-diameter front transmission mirror of the Fizeau interferometer is given an approximately 3-mm-diameter dip with approximately 0.5 μm of concavity (compare to Fig. 1.16). In the third order of reflection, one deals with interference of 0.1-μm fringe equivalent!

Figure 10.1(e) shows higher-order Fizeau moiré interferograms displaying three effects produced by multipass interferometry:

1. the stepwise increase in the wavefront's longitudinal deformation (wanted);
2. likewise, the increasing wavefront's lateral extension (unwanted); and
3. the direction of walkoff into the open wedge between the Fizeau reference and the target (an optical flat).

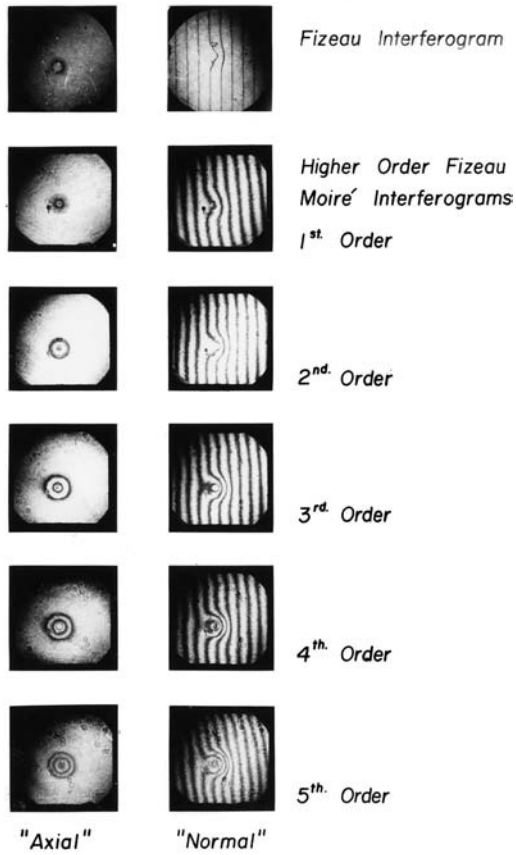

Figure 10.1(e) Multipass moiré Fizeau interferograms in an axial alignment (moiré grid parallel to the interference fringes) and a normal alignment (moiré grid at an angle to the interference fringes). The moiré diffusion screen was fixed in the image plane and photographed from behind.

10.2 Advantages and Disadvantages of Multipass Interferometers

As previously mentioned, the walkoff of the higher-order beams between mirrors M and B allows an error on the sample mirror M to be successively collected in the longitudinal direction (wanted); however, likewise, the lateral extension of a defective zone will appear widened after each successive reflection (unwanted). Thus, application of multipass interferometry is restricted to a few cases. The wanted and unwanted parts of the wavefront deformation by walkoff are illustrated in Fig. 10.2.

Lateral and longitudinal walkoff are inseparably coupled to each other. Only a small reduction of the lateral extension of the effective beam walkoff can be obtained by a slight off-axis illumination, as illustrated in Fig. 10.3(a). The wedge angle ε and angle θ of incidence to the transmission flat T can be

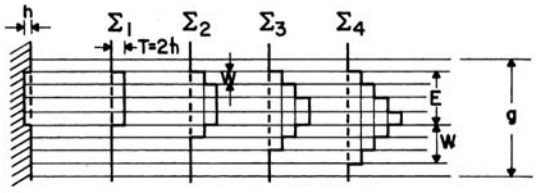

Figure 10.2 The effect of longitudinal (wanted) and lateral (unwanted) walkoff.

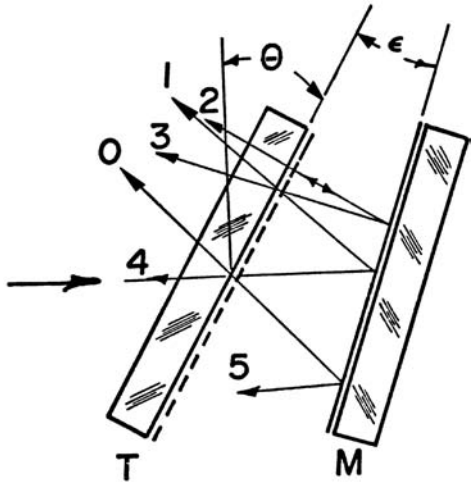

Figure 10.3(a) Schematic representation of the reduction of path length of the accumulating walkoff in a Fizeau interferometer (T/M) if using off-axis illumination. Line 4 represents the optical axis around which the system can be rotated. The incoming beam 4 is split by T into the system's reference 0; on the left and right side, the beam is reflected into the Fizeau cavity, finding a retroreflection.

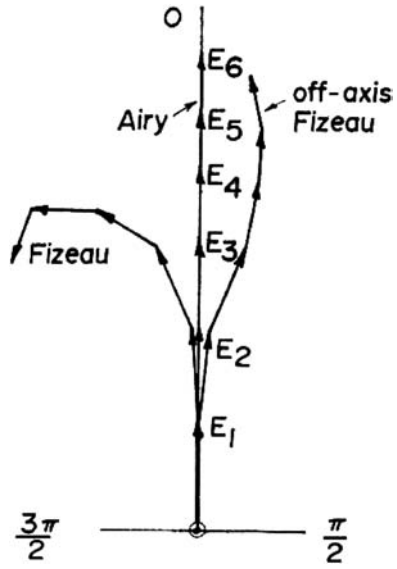

Figure 10.3(b) Vector addition representing the periodic maximum of the summed amplitudes for the classical and off-axis illumination of a Fizeau interferometer. The Airy sum relates to the plane-parallel Fabry–Pérot case.

chosen experimentally such as to retroreflect the beam after n reflections at either mirror M or T. In Fig. 10.3(a), the retroreflected beam, having integrated four reflections at M, used less walkoff path on M than would be used in a customary Fizeau technique.

A vector addition along the zero-deg (with respect to 360 deg) axis is shown in Fig. 10.3(b) for the customary Fizeau case, the off-axis Fizeau case, and the Airy case. The Airy case results from a Fabry–Pérot plane-parallel interferometer. A remarkable fringe sharpening or improvement of finesse can be predicted for the off-axis illumination of a Fizeau interferomter.[1]

One plausible beneficial application of multipass interference testing is the production of reference plates and precision flats. Figure 1.5(b) shows a mild twist on the white-light fringes. In the fifth order of reflection, this twist will appear five times more pronounced than was required in the specification.

Notes for the practitioner

1. Separation of errors on M and T, joined in the so-called empty interferometer, may be attempted by moiré technique. The grating lines will form moiré fringes with a record of the Fizeau fringes. Since the grating can be considered to be representing a perfect interferometer cavity, straight moiré fringes will be indicative of a perfect Fizeau cavity as well.

2. Tilting the assembly T/M against the optical axis of the collimator allows the beam inside the cavity to attain successive positions of zero degrees of incidence, identical to retroreflection. Retroreflection alternates between mirrors T and M. As angle Θ becomes further reduced, the loci of retroreflection converge to the position of the first beam entering the cavity [beam 4 in Fig. 10.3(a)]. As a result, one may produce a second-order interferogram with $\lambda/4$ fringes, using a single reference mirror in a Michelson configuration. In that configuration, a simple half-plane stop (a Foucault blade) in the defocal plane suffices.

10.3 Relevance of Multiple-Reflection and Off-Axis Illumination

Lasers allow the operation of very long interferometer cavities (e.g., for machine tool inspection), and multipass configurations are used for testing thin-window homogeneity. Testing corner cubes [Fig. 5.20(a)] with interferograms as distinctly clear as those in Fig. 5.20(b) became possible by experimentally optimizing off-axis illumination. The reader's attention is drawn to Figs. 5.22(a)–(c).

10.4 Multipass Applications

Applications of multipass interferometers for the metrology of changes of distances or of angles are of interest here. These applications use high-quality mirrors without surface errors, which would be multiplied and would interfere with the objective of the metrology.

10.4.1 Multipass in comparator interferometry

The beamsplitting Köster prism shown in Fig. 10.4(a) is the core of classical interferometers that are used for following and measuring (by fringe counting) the distance a sample has moved. White light is used to indicate coplanarity between stationary reference surfaces and the target's upper and lower surfaces. Targets can be, for instance, slip gauges or length standards. A more detailed description of the Köster comparator function is given in Sections 1.3 and 3.7. Here, in connection with multipass techniques, we address the task of more precisely identifying the start and stop signal of a moving target: A retroreflective wedge can be arranged as shown in Fig. 10.4(a) to allow three reflections on the rear stationary mirror. One fringe equivalent applicable to the distance change between the two mirrors is $(\lambda/2 \times 3) = 0.1\ \mu m$. The observer will see in one image of the comparator one fringe pattern pertaining to the target [the left side of Fig. 10.4(b)] with the white-light interference as in Fig. 1.7(a). On the right side of the figure is the interference fringe pattern (with 0.1-μm fringe equivalent) of the traveling reference mirror.

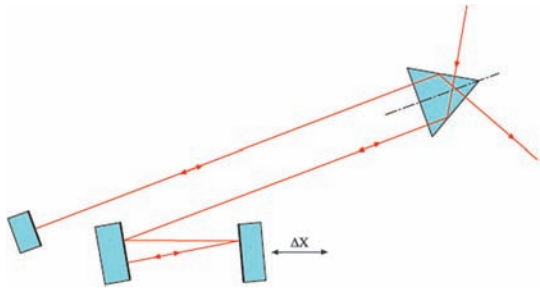

Figure 10.4(a) The Köster comparator interferometer with a multipass cavity (retroreflective wedge) in one arm.

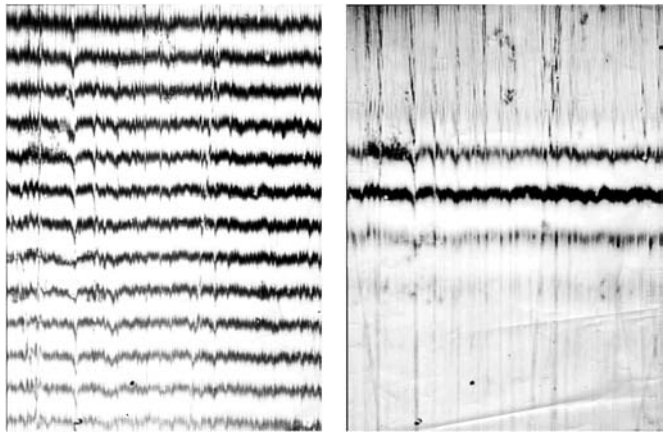

Figure 10.4(b) Left: Measuring long-distance changes by fringe counting using a laser diode. Right: measuring the zero position with white light and multiple reflections with a λ/6 fringe equivalent.

The mirror's Z movement is also measured by fringe counting. Replacing the flat mirror in one arm by two flat mirrors, as shown in Fig. 10.4(a), allows one to pick up (n times) a reflection from a retroreflective wedge cavity. The figure shows a double pickup of change in distance within the cavity. The wedge angle can be arranged for $n = 3, 4, 5$, etc. The laterally walked-off beam in the long cavity will meet surface sections of unknown quality and will integrate unknown errors.

10.4.2 Angular metrology

Referring back to Fig. 10.3(a), a compound off-axis Fizeau interferometer may serve to measure tilt errors below 1 arcsec. The objective of dynamic angular metrology is a compound multireflection mirror that will retroreflect

a beam of collimated light after, for instance, four reflections at mirrors M and T, as shown in Fig. 10.5. Once such alignment is found experimentally, the two mirrors M and T will be fixed in a frame, which will allow one to mount the same on a spindle to be tested. Upon rotation of the M/T fixture, the retroreflected (4×) beam will exhibit its total angular deviation in an interferometer.

Figure 10.5 shows two flat mirrors forming a wedge that becomes retroreflective in one plane only: the plane of incidence. While this is trivial for a 90-deg angle, the retroreflection also occurs at angles of 45, 22.5, 11.25 deg., etc. These angles can be conveniently ascertained interferometrically (see Section 6.2, Fig. 6.7). The retroreflective wedge may be aligned, as shown in Fig. 10.5, to retroreflect an optical beam into any other direction, for instance,

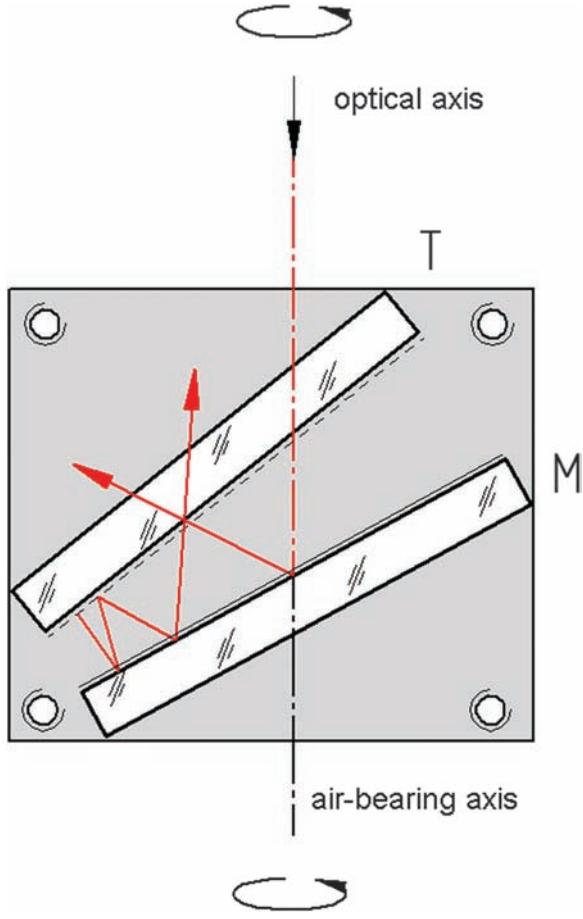

Figure 10.5 The compound wedge between two mirrors M and T becomes retroflective for certain discrete wedge angles. Within the plane of incidence orthogonal to the wedge's apex, this is a useful uniaxial metrology device.

one being colinear with the optical axis of an interferometer. Under interferometric control, one may incline the wedge around its apex such as to successively obtain the null-field interferogram for the second, third, or fourth order of retroreflection—except for the then *n*-times-smaller fringe equivalent. The retroreflective wedge might look like a Fizeau interferometer, as the surfaces have a beamsplitting and a full-reflection coating. In the intended configuration, the beam retroreflected by the wedge assembly acts like the orthogonal to the rear plane mirror in a common Fizeau interferometer, whose optical axis is aligned to coincide with the axis of rotation of a problem air-bearing spindle, as in Fig. 4.2(d). The alignment of the wedge reflector follows the scheme shown in Fig. 4.2(e).

The essential feature of the compound retroreflecting wedge is the change in optical path length, occurring upon minute changes of inclination relative to the axis of rotation. The latter depends on the separation between the mirrors T and M, which is not measurable; the device needs calibration. For the wedge mounted atop the rotor of a problem spindle, the zero fringe count signifies a perfectly tiltless axis of rotation.

Compared to a multipass interferometer, the defoci of the unused reflections out of the wedge are separated from the online defocus widely enough to make an extra stop in the defocusing plane superfluous. For measurement of angular error motions of the problem spindle, the initial wedge inclination must be found and fixed.

References

1. P. Langenbeck, "Fizeau interferometer—fringe sharpening," *Applied Optics* **9**(9), 2053–2058 (1970).

Index

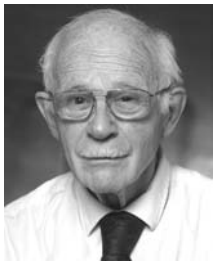

Peter Langenbeck graduated in 1959 with a Diploma in Physics from the University of Saarbrücken, Institute for Experimental Physics, under Prof. C. von Fragstein. He was a faculty assistant for three years at the Physikalisch Technisches Entwicklungs-Büro Laing in Stuttgart, where he led a laboratory for experimental physics and led an industrial study on enhancing light emission of thorium ceramic structures at elevated temperatures. At the same institute he became a project engineer for infrared optics and cryogenics. Langenbeck's presentation at a solar energy conference in Boston, of a Laing project on transmission-controllable plastic structures for greenhouses, prompted P. F. Forman (who later founded Zygo Co.) to offer him a position in optical engineering at PerkinElmer, Electro Optical division. There, Langenbeck soon became a senior engineering physicist with the optical physics group of PerkinElmer, specializing in industrial measurements and interferometry. His work led to new developments in laser instrumentation and new methods of optical testing, such as sensitivity enhancement in interferometry. The author set up an Apollo 11 retroreflector test program, using his newly developed multipass interferometry technique. With this subject, he completed a Ph.D. degree in optical engineering from the Technical University of Berlin, Optical Institute, under Prof. Slevogt. Dr. Langenbeck also developed an incremental cross-axis motion detector for the PerkinElmer laser distance interferometer.

As air bearings began to play an increasingly important role in the design of ultraprecise equipment for production and test of optical surfaces, Dr. Langenbeck became fascinated by his then superior's, Gordon J. Watt's, teachings on air-bearing techniques and their benefits to engineering. Spindles, involving only spherical and flat surfaces, and their compatibility with optical wavefronts supplied by interferometers, promised enormous progress in precision engineering. In 1970 Watt started his own business, PanTek, and Langenbeck, likewise, started InTop-Entwicklungen with its first contracts from Laing/Stuttgart. For the production of cylindrical Fresnel lenses from diamond-machined acrylic glass, InTop, as a very small unknown firm, received 100% financing to build a linear fly cutter. Further financing for the development of interferometers for use in industry QC was enabled by the U.S. company Kollmorgen, which established the InTop Division of Kollmorgen in Wallingford, Connecticut and the Intop division of Kollmorgen GmbH in Germany. With the assistance of Dr. Langenbeck, the German division of Kollmorgen was integrated into the U.S. business.

Toward the end of his career, Dr. Langenbeck was a consultant and taught optical metrology at the University of Kaiserslautern, Institute of Feinwerktechnik.